Radiance Interpolants for Interactive Scene Editing and Ray Tracing

by

Kavita Bala

B. Tech., Indian Institute of Technology, Bombay (1992)
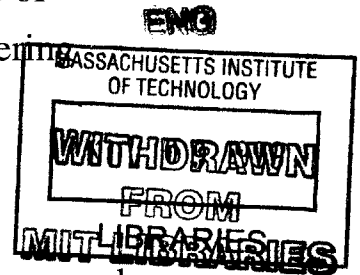S.M., Massachusetts Institute of Technology (1995)

Submitted to the Department of Electrical Engineering and Computer Science
in partial fulfillment of the requirements for the degree of

Doctor of Philosophy in Computer Science and Engineering

at the

Massachusetts Institute of Technology

September 1999

Author . . . .
Department of Electrical Engineering and Computer Science
September 9, 1999

Certified by . . . .
Julie Dorsey
Associate Professor
Thesis Supervisor

Certified by . . . .
Seth Teller
Associate Professor
Thesis Supervisor

Accepted by . . . .
Arthur C. Smith
Chairman, Departmental Committee on Graduate Students

Radiance Interpolants for Interactive Scene Editing
and Ray Tracing

by

Kavita Bala

Abstract

Ray tracers are usually regarded as off-line rendering algorithms that are too slow for interactive use. This thesis introduces techniques to accelerate ray tracing and to support interactive editing of ray-traced scenes. These techniques should be useful in many applications, such as architectural walk-throughs, modeling, and games, and will enhance both interactive and batch rendering.

This thesis introduces *radiance interpolants*: radiance samples that can be used to rapidly approximate radiance with bounded approximation error. Radiance interpolants capture object-space, ray-space, image-space and temporal coherence in the radiance function. New algorithms are presented that efficiently, accurately and conservatively bound approximation error.

The *interpolant ray tracer* is a novel renderer that uses radiance interpolants to accelerate both primary operations of a ray tracer: shading and visibility determination. Shading is accelerated by quadrilinearly interpolating the radiance samples associated with a radiance interpolant. Determination of the visible object at each pixel is accelerated by *reprojecting* interpolants as the user's viewpoint changes. A fast scan-line algorithm then achieves high performance without sacrificing image quality. For a smoothly varying viewpoint, the combination of lazily sampled interpolants and reprojection substantially accelerates the ray tracer. Additionally, an efficient cache management algorithm keeps the memory footprint of the system small with negligible overhead.

The interpolant ray tracer is the first accelerated ray tracer that reconstructs radiance from sparse samples while bounding error conservatively. The system controls error by adaptively sampling at discontinuities and radiance non-linearities. Because the error introduced by interpolation does not exceed a user-specified bound, the user can trade performance for quality.

The interpolant ray tracer also supports interactive scene editing with *incremental* rendering; it is the first incremental ray tracer to support both object manipulation and changes to the viewpoint. A new hierarchical data structure, called the *ray segment tree*, tracks the dependencies of radiance interpolants on regions of world space. When the scene is edited, affected interpolants are rapidly identified and updated by traversing these ray segment trees.

Thesis Supervisor: Julie Dorsey
Title: Associate Professor

Thesis Supervisor: Seth Teller
Title: Associate Professor

Acknowledgments

There are many people I should thank for supporting me through my Ph.D. First, I would like to thank my advisors, Prof. Seth Teller and Prof. Julie Dorsey, who gave me a chance; I entered the field of graphics four years ago with no prior experience, and they took me on and were patient as I learned the ropes. Working with them has been a wonderful learning experience; I have benefited greatly from their knowledge of the field. They have taught me how to articulate my ideas and how to step back to see the bigger picture and to aim high. I particularly appreciate the freedom they gave me to explore my ideas; while this freedom has taken me down some garden paths, it has taught me a lot about the research process and strengthened my skills as a researcher.

I would also like to thank my readers Prof. Eric Grimson and Prof. Leonard McMillan for their useful feedback and suggestions on my thesis. I appreciate the time and effort they have taken to improve my thesis.

I would like to thank Justin Legakis and Mike Capps, my first office-mates in the graphics group, and Satyan Coorg and Neel Master for their conversations and company.

There are several friends who I should thank for making my stay at MIT enjoyable: Donald Yeung for being such a wonderful listener and loyal friend to me over the years, even supporting me in my off-key efforts at learning to play the violin; Carl Waldspurger for being my friend and unofficial mentor through my Master's thesis; Kathy Knobe for being around to talk and share research experiences with; Ulana Legedza for always making the time to give me suggestions on talks and drafts of papers and being fun to hang out with; Jim O'Toole for being a good friend and supporter over the years; and Patrick Sobalvarro for explaining to me why people behave the way they do.

My relationship with the programming methodology group (PMG) started when I first got to graduate school and worked on programming language problem sets with three members of PMG, Atul Adya, Phil Bogle, and Quinton Zondervan. We spent hours discussing problem sets and probably drove other, more seasoned veterans in the group (Mark Day, Sanjay Ghemawat, Bob Gruber and Andrew Myers) up the wall. However, they were too nice ever to tell us to put a sock in it. Over the years since, I have enjoyed countless discussions with members of the group on topics ranging over magic tricks, movies, politics, puzzles, the Gulag, and the general meaning of life. Unfortunately, space restrictions do not permit me to describe all the resulting insights, but they are very much a part of my experience as a graduate student and I will miss the group. I would like to thank all the members of the group, particularly Atul Adya, Phil Bogle, Miguel Castro, Jason Hunter, Andrew Myers, Radhika Nagpal and Quinton Zondervan, for those conversations. I would also like to thank Barbara Liskov for creating an environment in which we could fully enjoy the

Contents

List of Figures

13

Chapter 1

Introduction

A long-standing challenge in computer graphics is the rapid rendering of accurate, high-quality imagery. Rendering algorithms generate images by simulating light and its interaction with the environment, where the environment is modeled as a collection of virtual lights, objects and a camera. The rendering algorithm is responsible for computing the path that light follows from the light sources to the camera. The goal of this thesis is to develop a fast, high-quality rendering algorithm that can be used in interactive applications.

Renderers that offer interactive performance, such as standard graphics hardware engines, permit the scene to change dynamically and the user's viewpoint to change. Hardware rendering has become impressively fast; however, this interactive performance is achieved by sacrificing image quality. Most hardware renderers use *local* illumination algorithms that render each object as though it were the only one in the scene. As a result, these algorithms do not render effects such as shadows or reflections, which arise from the lighting interactions between objects.

Global illumination algorithms, on the other hand, focus on producing the most realistic image possible. These systems produce an image by simulating the light energy, or *radiance*, that is visible at each pixel of the image. These algorithms improve rendering accuracy and permit higher scene complexity than when a hardware renderer is used. However, computing the true equilibrium distribution of light energy in a scene is very expensive. Therefore, practical global illumination algorithms typically compromise the degree of realism to provide faster rendering. Two commonly used global illumination algorithms span the spectrum of options: ray tracing and radiosity.

At one end of the spectrum, ray tracing [Whi80] is a popular technique for rendering high-quality images. Ray tracers support a rich set of models and capture view-dependent specular effects, as well as reflections and transmission. However, the view-dependent component of radiance is expensive to compute, making ray tracers unsuitable for interactive applications.

At the other end, radiosity methods [GTGB84] capture view-independent diffuse inter-reflections in a scene; however, these methods restrict the scene to pure diffuse, polygonal objects. Radiosity systems pre-compute *view-independent* radiosity for all polygons in the scene, allowing the scene to be rendered in hardware at interactive rates as the viewpoint changes.

Ideally, a rendering system would support interactive rendering of dynamically-changing scenes, generating realistic, high-quality imagery. This thesis demonstrates an approach to *accelerating ray tracing so that a user can interact with the scene while receiving high-quality, ray-traced imagery as feedback.* Two kinds of interactions are permitted: changes to the viewpoint, and changes to the scene itself.

1.1 Applications

The rendering techniques presented in this thesis should be useful in a variety of different applications that incorporate interactive rendering, such as computer-aided design, architectural walk-throughs, simulation and scientific visualization, generation of animations, virtual reality, and games. In this section, a few of these applications are discussed.

For computer-aided design and modeling, a fast, high-quality renderer would allow the designer to obtain accurate, interactive feedback about the objects being modeled. This feedback would improve the efficiency of the design process. Architecture is one area of design where accurate feedback on appearance is particularly useful, because the appearance of the product is central to the design process. Because lighting effects such as shadows and reflections have a significant impact on appearance, a renderer that takes global illumination into account is required.

Animated movies and computer-generated visual effects are usually produced using ray tracers, and considerable computational expense is incurred to ensure that the rendered results do not contain visible errors. The techniques introduced in this thesis are particularly appropriate for the problem of rendering animations because they improve performance most when accelerating a sequence of frames in which the scenes rendered in each frames are similar to one another. For cinematic animations, it is important that rendering error be strictly controlled; this thesis also introduces useful techniques for controlling error. The rendering techniques presented here should improve the interactive design process for animations, and also accelerate rendering of the animation itself, although it is unrealistic at present to expect real-time rendering of the animation.

Faster rendering techniques would also be of use for scientific visualization and simulation. High-quality rendering of results of a simulation—for example, an aerodynamic simulation or a detailed molecular simulation—can make the results easier to grasp intuitively, both during the
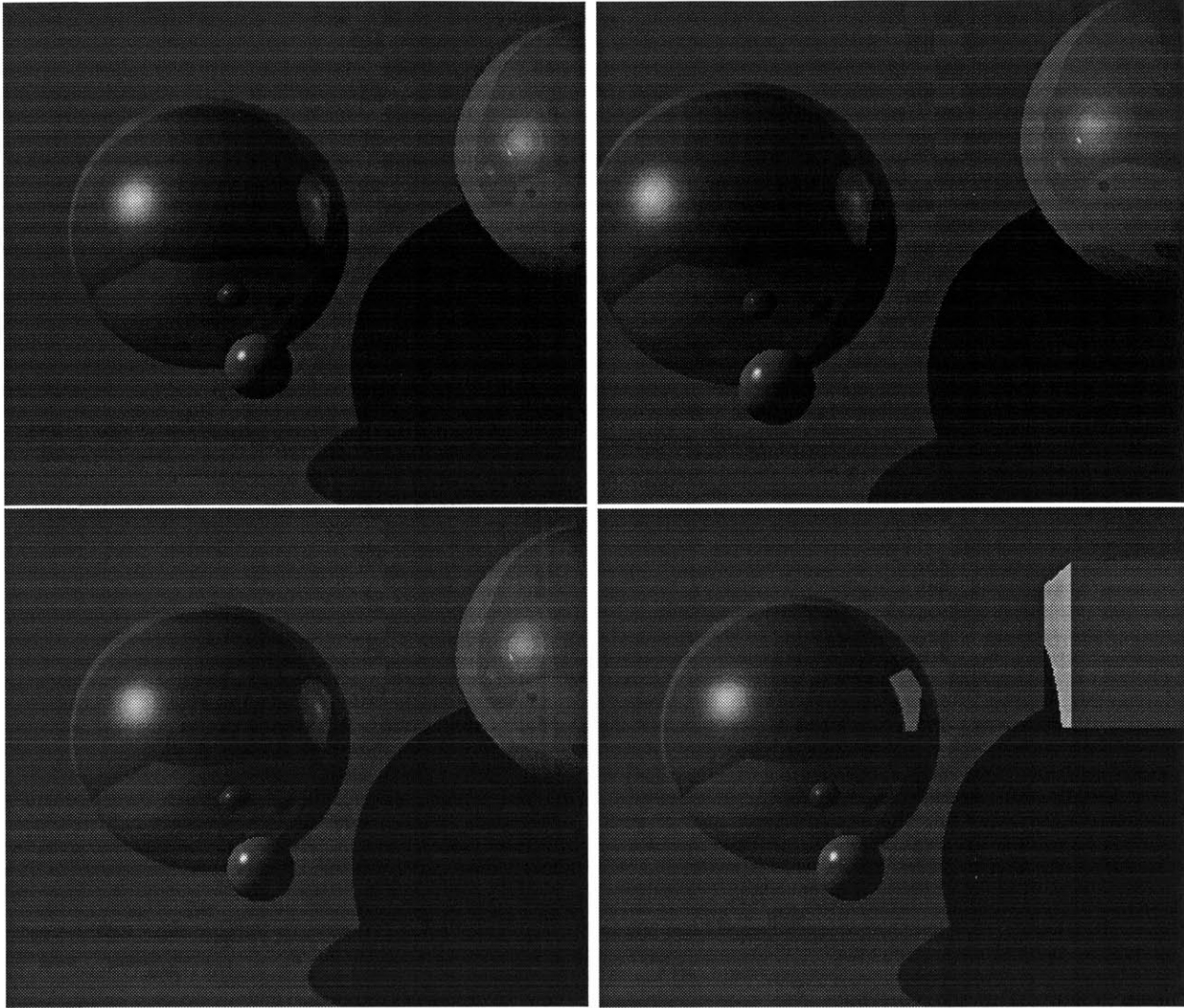
Figure 1-1: Coherence and the localized effect of an edit.

research process and for presentation purposes. Faster rendering of both static and dynamic scenes would be useful for this application.

Virtual reality applications and computer games have similar requirements from the standpoint of rendering. Both kinds of applications have an increasing demand for realism in rendering, and also a requirement that rendering feedback be interactive. For these applications, a guarantee on rendering quality is not as important as for cinematic animations. However, any technique that accelerates high-quality rendering is likely to be of use in these domains.

1.2 Intuition

The key observation for acceleration of ray tracing is that radiance tends to be a smoothly varying function. A ray tracer ought to be able to exploit this smoothness in radiance to compute radiance without doing the full work of ray tracing every pixel in the image independently.

This central intuition is illustrated in Figure 1-1. In this thesis, all figures containing rendered images are reproduced in color in Appendix B. On the top row are two images shown from two nearby viewpoints. On the bottom row are two images shown from the same viewpoint; these images show a scene that is edited by replacing the green sphere with a yellow cube. There are several points of interest:

- First, consider only the image on the top left. Radiance varies smoothly along the objects in the image except at a few places such as specular highlights and silhouettes. This smoothness is called *object-space coherence*.

- When these objects are rendered to produce an image, nearby pixels in the image have similar radiance values. This is called *image-space coherence*.

- Now consider the image on the top right, where the viewpoint has changed with respect to the image on the top left. If the viewpoint changes by a small amount, the radiance information computed for the previous frame can be reused in the new frame. This is called *temporal coherence*.

- Finally, when the user edits the scene shown in the bottom row of the figure, only a small part of the ray-traced image is affected: the green sphere and its reflection. The rest of the image remains the same. The effect of the edit is localized; this property will be referred to as the *localized-effect property*.

This thesis introduces new mechanisms that allow a ray tracer to exploit object-space, image-space, and temporal coherence to accelerate rendering. Coherence allows the radiance for many pixels in the image to be approximated using already-computed radiance information. Using these various intuitions, rendering can be accelerated in various ways:

- Ray tracing of static scenes can be accelerated by exploiting object-space and image-space coherence within a single frame. Further acceleration can be achieved by exploiting temporal coherence across multiple frames, as the user's viewpoint changes.
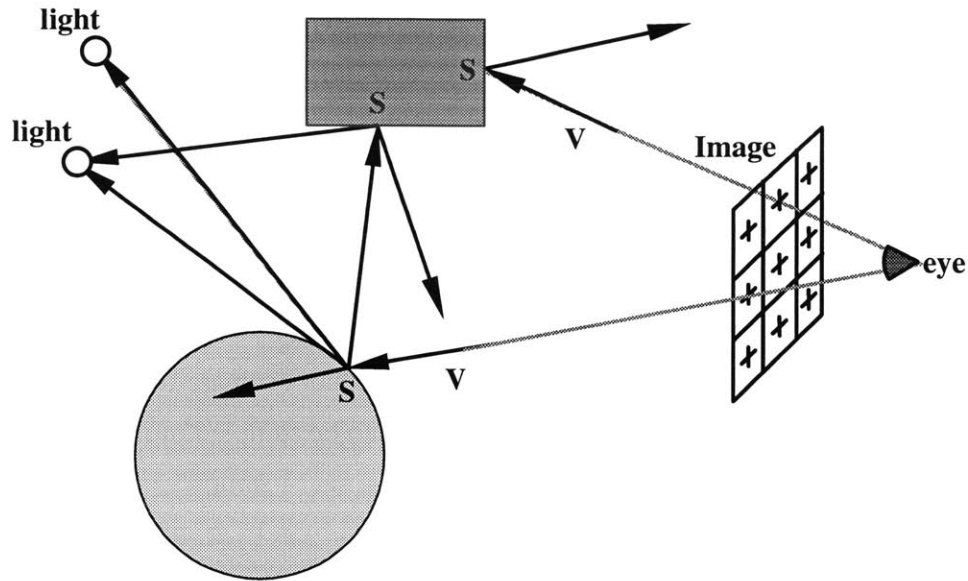
Figure 1-2: Whitted ray tracer.

- When the scene is not static, the localized-effect property allows the scene to be *incrementally* re-rendered even when the scene is allowed to change. These changes may include moving, adding, or deleting objects in the scene.

1.3 Ray tracers

A brief review of ray tracing algorithms may help in understanding the new mechanisms to be introduced. A classic Whitted ray tracer [Whi80] computes an image by tracing a ray from the eye through each pixel in the image (shown in Figure 1-2). Radiance at each pixel is computed as follows: a ray from the eye through the pixel, called an *eye ray*, is intersected with the scene to determine the closest object visible along the eye ray. The radiance along the eye ray is the sum of the radiance computed by local and global shading. The local radiance component consists of diffuse and specular contributions from each visible light in the scene. The global shading component is computed by recursively tracing reflected and refracted rays, if they exist, through the scene. The two operations of a ray tracer that dominate performance are the visibility computation that determines the closest visible object along an eye ray (indicated as **V** in the figure), and the shading computation for the visible point so identified (indicated as **S**). Because shading involves recursively tracing rays through the scene, with consequent intersection and shading operations, shading is usually more expensive than visibility determination.

Accelerating ray tracing has long been an important area of computer graphics research. This

thesis introduces a system that accelerates ray tracing by exploiting spatial and temporal coherence in a principled manner. This system decouples and independently accelerates both primary operations of a ray tracer: visibility determination and shading.

1.4 Radiance interpolants

The intuition about the smoothness of radiance can be exploited by viewing radiance as a function over the space of rays that pass through a scene. Rather than evaluate the radiance function for every eye ray, as an ordinary ray tracer would, radiance can be sampled more sparsely. This thesis introduces the notion of a *radiance interpolant*, which is a set of samples of the radiance function that allows the radiance function to be reconstructed for nearby rays to *any desired accuracy*.

Radiance interpolants are used by my rendering system, the *interpolant ray tracer*, to accelerate rendering in several ways. When radiance for a pixel can be approximated using an interpolant, the expensive shading operation is eliminated. As described later, radiance interpolants can also be used to accelerate other aspects of rendering: specifically, visibility determination and scene editing.

A small fraction of the pixels in any image cannot be approximated using a radiance interpolant, because these pixels do not lie in regions where radiance varies smoothly. For example, pixels at the silhouettes of objects fall into this category. One important new feature of the interpolant ray tracer is a fast, accurate *error bounding algorithm* used to prevent interpolation from a set of samples that would result in unacceptable rendering error. Previous ray tracing systems have largely ignored the problem of error in rendering.

For pixels that cannot be approximated using a radiance interpolant, the interpolant ray tracer uses an ordinary ray tracer, the *base ray tracer*, to render the pixel. The base ray tracer is a standard Whitted ray tracer with some extensions and optimizations, and is described in more detail in Chapters 4 and 7. The base ray tracer is also used by the interpolant ray tracer to collect the samples that make up interpolants. The interface between these two ray tracers is depicted in Figure 1-3. The goal of the interpolant ray tracer is to produce an image that closely approximates the image produced by the base ray tracer, but more quickly than the base ray tracer would.

Figure 1-4 shows images of how successful interpolants are at exploiting coherence. In the left column, rendered output of the ray tracer is shown. In the right column, color-coded images show in blue the pixels that are reconstructed using interpolants. Green, yellow, and pink pixels show where interpolants are not used, because radiance was not known to vary smoothly. Two important observations can be made about the color-coded images. First, most of the pixels are blue, so

Render pixel

**approximate
radiance for pixel**

```
┌─────────────────────────────┐
│   Interpolant ray tracer    │
└─────────────────────────────┘
```

**collect
radiance samples**

**render
failed pixels**

```
┌─────────────────────────────┐
│      Base ray tracer        │
└─────────────────────────────┘
```
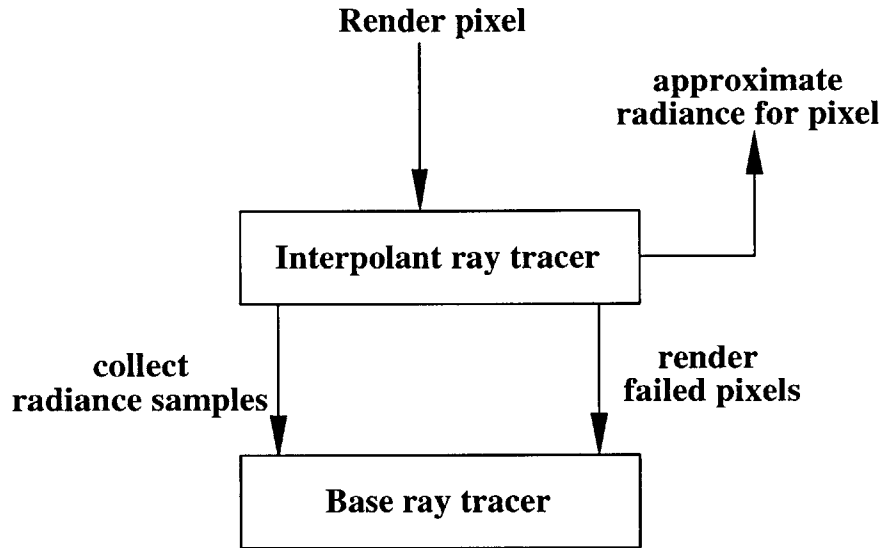
Figure 1-3: High-level structure of the interpolant ray tracer.

rendering is accelerated; for this image, rendering is about 5 times faster with the interpolant ray tracer. Second, interpolation is correctly avoided where it would produce inaccurate results.

The second row shows the same scene from a nearby viewpoint. The red pixels on the right show pixels for which no previously computed radiance interpolant (from the image on top) was suitable for computing their radiance. These pixels are rendered using radiance interpolants that are computed on the fly as the image is being rendered; despite the computation of new interpolants, the rendering of these pixels is still accelerated when compared to the base ray tracer. Note that the radiance for most pixels can be computed using radiance interpolants from the image on top. Thus, temporal coherence is effectively exploited in this example.

The bottom row shows results for a scene edit. Note that most of the image is unaffected by the edit and is rendered using previously constructed interpolants. Radiance is affected by the edit only for the pixels marked in red, which are correctly identified by the ray tracer. The image is then rendered incrementally, reusing all the unaffected radiance interpolants computed earlier.

Radiance interpolants are the central mechanism used by the interpolant ray tracer. They are used to accelerate both primary operations of a ray tracer: visibility determination and shading. They are also useful when incrementally re-rendering a dynamic scene. The next three sections discuss these uses of radiance interpolants in more detail.
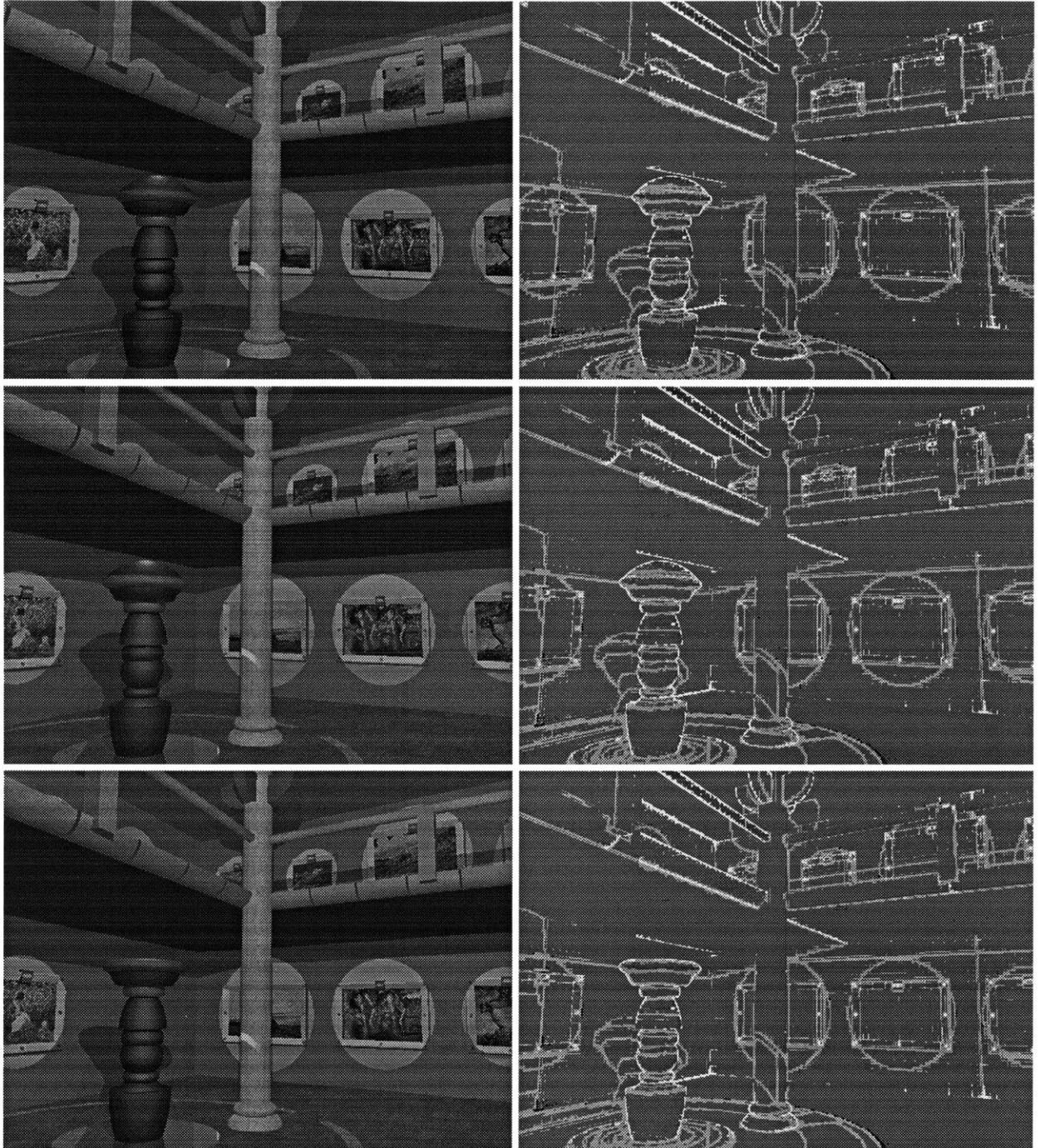
Figure 1-4: Results illustrating the effectiveness of radiance interpolants.

1.4.1 Accelerating shading

As described, the interpolant ray tracer accelerates shading by using a suitable interpolant to approximate the radiance of the pixel, rather than performing the usual shading operation. If no information is available about the radiance function, interpolating radiance samples can introduce

arbitrary errors in the image. Therefore, it is necessary to characterize how radiance varies over ray space. Systems that exploit coherence to accelerate rendering have traditionally used *ad hoc* techniques to determine where to sample radiance; these systems have no correctness guarantees. The error bounding algorithm introduced in this thesis characterizes the error introduced by interpolation; this characterization permits the interpolant ray tracer to sample radiance densely where radiance changes rapidly, and to use sparse sampling where radiance is smooth. The system uses this *adaptive sampling* to guarantee that interpolation error does not exceed a user-specified error bound ϵ. The user can use ϵ to control performance-quality trade-offs.

1.4.2 Accelerating visibility

Visibility determination is accelerated by exploiting frame-to-frame temporal coherence: when the viewpoint changes, objects visible in the previous frame are still typically visible in the current frame, as discussed in Section 1.2. This occurs because eye rays from the new viewpoint are close (in ray space) to eye rays from the previous viewpoint. When the interpolant ray tracer is used to render a sequence of frames from nearby viewpoints, interpolants from one frame are *reprojected* to the next frame. A reprojected interpolant covers some set of pixels in the new frame; these pixels are rendered using the interpolant. Rendering is substantially accelerated because neither visibility nor shading is explicitly computed for these pixels.

1.4.3 Incremental rendering with scene editing

Conventional ray tracers are too slow to be used for interactive modeling. In this application, when a user edits a scene, he should quickly receive high-quality rendered imagery as feedback. Rapid feedback in such scenarios is a reasonable expectation because the effect of an edit is typically localized (as described in Section 1.2); therefore, rendering a slightly modified scene could be much faster than rendering the original image. However, conventional ray tracers do not exploit this fact. An *incremental* renderer that efficiently identifies and updates the pixels affected by an edit would enable the user to get rapid high-quality feedback.

Identifying the pixels affected by an edit is not easy; therefore, researchers have supported scene editing with ray tracing by restricting the viewpoint to a fixed location [SS89, BP96]. These systems permit a limited set of edits, such as color changes and object movement. However, if the user changes the viewpoint, the whole frame is re-rendered, incurring the cost of pre-processing to support edits from the new viewpoint. This restriction on the viewpoint limits the usefulness of these systems.

This thesis describes how radiance interpolants can be used to support incremental rendering with scene editing, while allowing the viewpoint to change. The interpolant ray tracer constructs interpolants, which are useful for scene editing for the following two reasons. First, an interpolant represents a bundle of rays. Therefore, updating an interpolant efficiently updates radiance for all the rays represented by the interpolant. Second, an interpolant does not depend on the viewpoint. Therefore, interpolants are not invalidated when the viewpoint changes.

The incremental renderer supports edits such as changing the material properties of objects in the scene, adding/deleting/moving objects, *and* changing the viewpoint. When the user edits the scene, the system automatically identifies the interpolants that are affected by the edit. Unaffected interpolants are used when re-rendering the scene.

1.5 System overview

This section describes the flow of control in the interpolant ray tracing system and the data structures built during rendering. Some limitations of the system are also discussed.

1.5.1 Interpolant ray tracer

The interpolant ray tracer is the core of the system; it accelerates rendering by substituting interpolation of radiance for ray tracing when possible. This section briefly describes how the interpolant ray tracer accelerates ray tracing; the next section describes how the rest of the system is built around the interpolant ray tracer.

Radiance samples collected by invoking the base ray tracer are used to construct interpolants, which are stored in a data structure called a *linetree*. Each object has a set of associated linetrees that store its radiance samples. The linetree has a hierarchical tree organization that permits the efficient lookup of interpolants for each eye ray. Chapter 3 presents linetrees in detail.

Figure 1-5 shows the rendering algorithm of the interpolant ray tracer. Each pixel in the image is rendered using one of three rendering paths: the *fast path*, the *interpolate path*, or the *slow path*. Along the fast path, the system exploits frame-to-frame temporal coherence by reprojecting interpolants from the previous frame; this accelerates both visibility and shading for pixels covered by reprojected interpolants. Rendering of pixels that are not reprojected may still be accelerated by interpolating radiance samples from the appropriate interpolants (interpolate path). If both reprojection and interpolation fail for a pixel, the base ray tracer renders the pixel (slow path).

The fast path, indicated by the thick line, corresponds to the case when reprojection succeeds. When a reprojected interpolant is available for a pixel, the system finds all consecutive pixels in
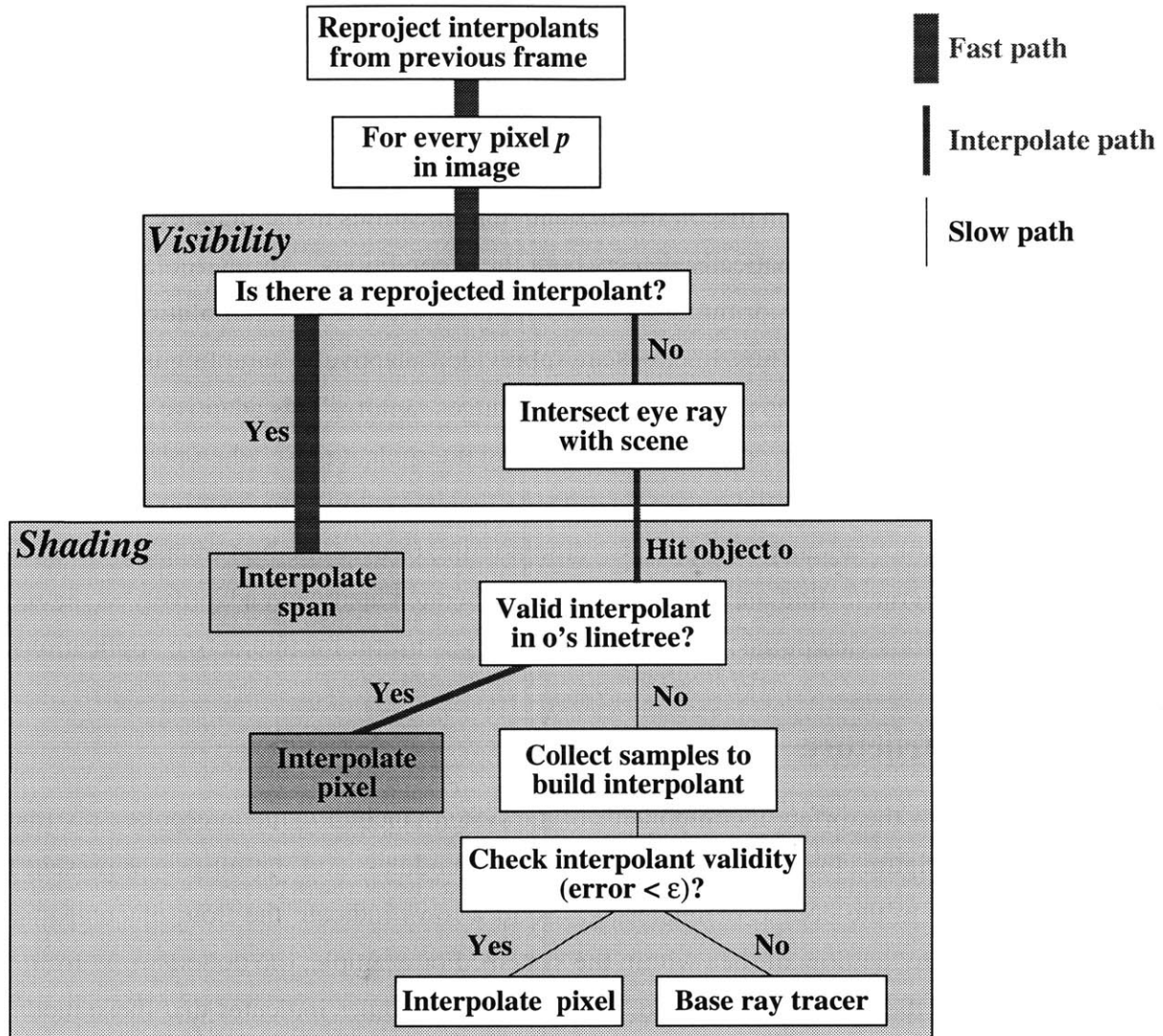
Figure 1-5: Algorithm overview.

that scan-line covered by the same interpolant, and interpolates radiance for these pixels in screen-space; neither the visibility nor shading computation is invoked for these pixels. This fast path is about 30 times faster than the base ray tracer (see Chapter 7 for details), and is used for most pixels.

If no reprojected interpolant is available, the eye ray is intersected with the scene to determine the object visible at that pixel. The system searches for a valid interpolant for that ray and object in the appropriate linetree; if it exists, the radiance for that eye ray (and the corresponding pixel) is computed by quadrilinear interpolation. This interpolate path, indicated by the medium-thick line, is about 5 times faster than the base ray tracer.

If an interpolant is not available for a pixel, the system builds an interpolant by collecting

radiance samples. The error bounding algorithm checks the validity of the new interpolant. If the interpolant is valid, the pixel's radiance can be interpolated, and the interpolant is stored in the linetree. If it is not valid, the linetree is subdivided, and the system falls back to shading the pixel using the base ray tracer. This is the slow path indicated by the thin black line.

Interpolation errors arise from discontinuities and non-linearities in the radiance function. The error bounding algorithm automatically detects both these conditions. An interpolant is not constructed if the error bounding algorithm indicates conservatively that its interpolation error would exceed a user-specified bound. Thus, linetrees are subdivided adaptively: sampling is sparse where radiance varies smoothly, and dense where radiance changes rapidly. This adaptive subdivision of linetrees prevents erroneous interpolation while allowing interpolant reuse when possible.

The interpolant ray tracer has the important property that it is entirely on-line: no pre-processing is necessary to construct radiance interpolants, yet rendering of even the first image generated by the ray tracer is accelerated. Radiance interpolants are generated lazily and adaptively as the scene is rendered from various viewpoints. This on-line property is useful for interactive applications.

1.5.2 System structure

Figure 1-6 shows how the different components of the system, including the interpolant ray tracer, fit together. In the figure, the rectangles represent code modules, and the ellipses represent the data structures built in the course of rendering. Solid arrows indicate the flow of control, and dotted arrows indicate the flow of data within the system. For example, the dotted arrow from the "Linetree" ellipse to the "Reprojection" and "Interpolation" modules indicates that these modules read data from the linetree, as described in Section 1.5.1. The dotted arrow from "Interpolant construction" to "Linetree" indicates that this module writes data into the linetree.

The user interface module processes user input. Two kinds of user input are of interest: changes in the viewpoint, and edits to the scene. If the user's viewpoint changes, the interpolant ray tracer renders an image from the new viewpoint, as described in Section 1.5.1. If the user edits the scene, by changing the material properties of objects, or deleting objects, the "Scene Editing" module is invoked.

The "Interpolant Ray Tracer" module has already been described in some detail. One additional component is the memory management module, which bounds the memory usage of the ray tracer. This module is invoked when the ray tracer requires more memory to construct interpolants than is available. Using a least-recently-used scheme described in Chapter 7, the memory management module identifies and frees linetree memory that can be reused.

The "Scene Editing" module provides the ability to incrementally update interpolants after a
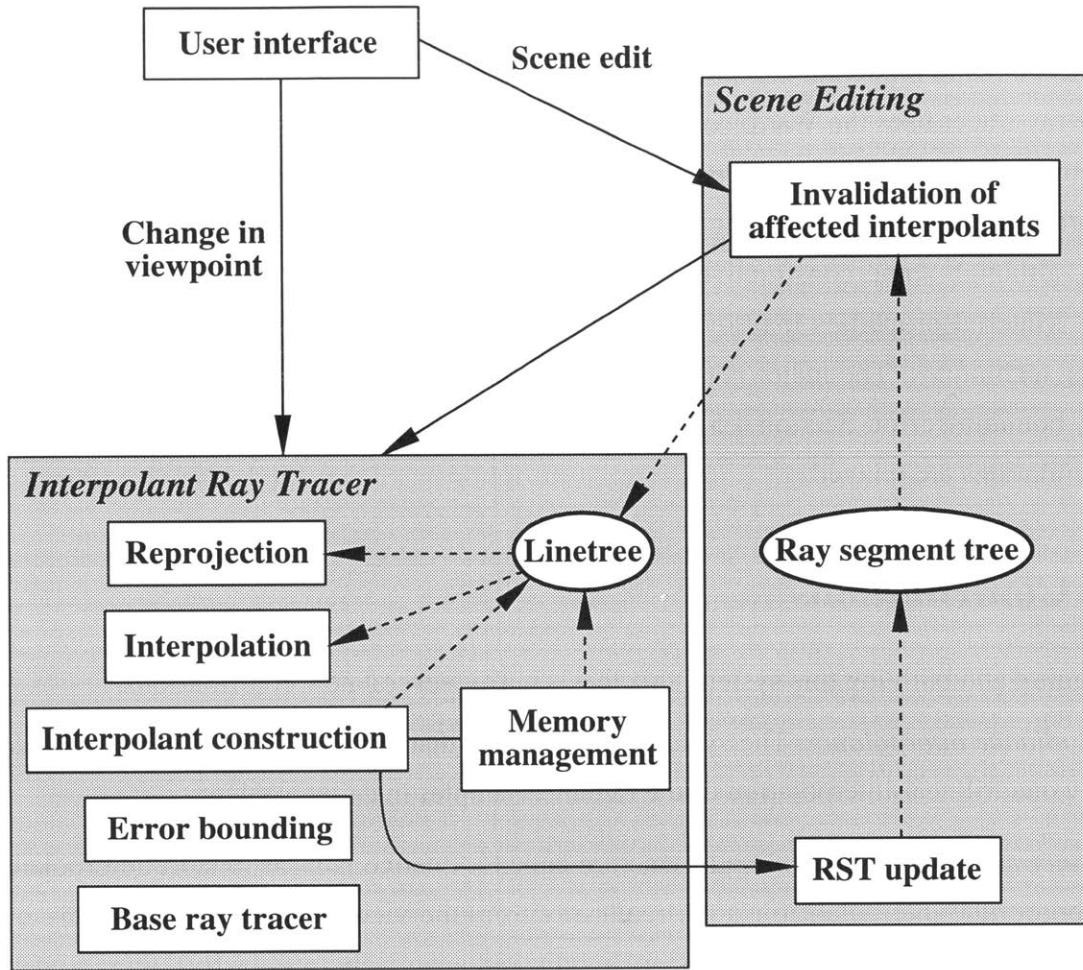
Figure 1-6: System overview.

user-specified change to the scene. A data structure called a *ray segment tree* (RST) is used to record the regions of world space on which each interpolant depends. When an interpolant is constructed, the "RST Update" module records the dependencies of the interpolant in ray segment trees. When the user edits the scene, the ray segment trees are traversed to rapidly identify the affected interpolants and invalidate them, removing them from the containing linetree. The new image can then be rendered by the interpolant ray tracer, making use of any interpolants unaffected by the edit.

1.5.3 Limitations

To bound interpolation error the interpolant ray tracer makes several assumptions about the shading model and geometry of objects in the scene. These assumptions are discussed in detail in Section 4.1.2. Because the interpolant ray tracer is an accelerated version of a Whitted ray tracer,

it inherits some of the limitations of a Whitted ray tracer. It also places some additional restrictions on the scene being rendered.

The ray tracer uses the Ward isotropic shading model [War92]. While this is a more sophisticated model than that of Whitted, it does not model diffuse inter-reflections and generalized light transport. Also, the error bounding algorithm described in Chapter 4 requires that all objects be convex, although some constructive solid geometry operators (union and intersection) are permitted. Material properties may include diffuse texture maps, but not some more sophisticated texturing techniques. The major reason for these limitations is to simplify the problem of conservatively bounding error. Section 4.5 discusses approaches for bounding error in a system in which these limitations are relaxed.

1.6 Contributions

In designing and building this system, this thesis makes several new contributions:

- *Radiance interpolants:* The system demonstrates that radiance can be approximated rapidly by quadrilinear interpolation of the radiance samples in an interpolant.

- *Linetrees:* A hierarchical data structure called a linetree is used to store interpolants. The appropriate interpolant for a particular ray from the viewpoint is located rapidly by walking down the linetree. Linetrees are subdivided adaptively (and lazily), thereby permitting greater interpolant reuse where radiance varies smoothly, and denser sampling where radiance changes rapidly.

- *Error bounds:* New techniques for bounding interpolation error are introduced. The system guarantees that when radiance is approximated, the relative error between interpolated and true radiance (as computed by the base ray tracer) is less than a user-specified error bound ϵ. The user can vary the error bound ϵ to trade performance for quality. Larger permitted error produces lower-quality images rapidly, while smaller permitted error improves image quality at the expense of rendering performance.

  Interpolation error arises both from discontinuities and non-linearities in the radiance function. An error bounding algorithm automatically and conservatively prevents interpolation in both these cases. This algorithm uses a generalization of interval arithmetic to bound error.

- *Error-driven sampling:* The error bounding algorithm is used to guide adaptive subdivision; where the error bounding algorithm indicates rapid variations in radiance, radiance is sampled more densely.

- *Visibility by reprojection:* Determination of the visible surface for each pixel is accelerated by a novel reprojection algorithm that exploits temporal frame-to-frame coherence in the user's viewpoint, but guarantees correctness. A fast scan-line algorithm uses the reprojected linetrees to further accelerate rendering.

- *Memory management:* Efficient cache management keeps the memory footprint of the system small, while imposing a negligible performance overhead (1%).

- *Interpolants for scene editing:* The system demonstrates that interpolants provide an efficient mechanism for incremental update of radiance when the scene is edited. This is possible because the error bounding algorithm guarantees that each interpolant represents radiance well for a region of ray space.

- *Ray segment trees:* The concept of ray segment space is introduced for scene editing. A shaft in 3D space is represented simply as a bounding box in this five-dimensional space. This concept is used to identify the regions of world space that affect an interpolant. An auxiliary data structure, the ray segment tree, is built over ray segment space; when the scene is edited, ray segment trees are rapidly traversed to identify affected interpolants.

1.7   Organization of thesis

The rest of the thesis is organized as follows: Chapter 2 discusses previous work. Chapter 3 describes the interpolant building mechanism and the linetree data structure in detail. Chapter 4 presents the error bounding algorithm, which validates interpolants and guarantees that interpolation error does not exceed a user-specified error bound. Chapter 5 describes how reprojection is used to accelerate visibility. Chapter 6 extends the interpolant ray tracer to support incremental rendering with scene editing. Finally, Chapter 7 presents results and Chapter 8 concludes with a discussion of future work.

Chapter 2

Related Work

This chapter presents the related work in accelerating ray tracing and incremental scene editing. Section 2.1 discusses the most relevant prior work on accelerating high-quality renderers. Section 2.2 presents related work on incremental rendering for scene editing with global illumination. The contributions of this thesis are discussed in the context of previous work in Section 2.3.

2.1 Accelerating rendering

Accelerating rendering is a long standing area of research. Many researchers have developed techniques that improve the performance of rendering systems: adaptive 3D spatial hierarchies [Gla84], beam-tracing for polyhedral scenes [HH84], cone-tracing [Ama84], and ray classification [AK87]. A good summary of these algorithms can be found in [Gla89, CW93, SP94, Gla95]. In this chapter, the related work most relevant to this thesis is presented.

Ray tracers perform two major operations: visibility determination and shading. Most systems presented here focus on accelerating shading, though a few systems exclusively accelerate visibility determination. The distinction between these two objectives is often blurred, since both improve the performance of rendering. Systems that accelerate rendering by approximating radiance typically differ in the following ways:

- the correctness guarantees (if any) provided for computed radiance,

- the shading model supported,

- the use of pre-processing (if any), and

- the hardware expectations for performance.

Some of these systems also approximate visibility by polygonalizing the scene, or by using images instead of geometry.

2.1.1 Systems with error estimates

Some rendering systems trade accuracy for speed by using error estimates to determine where computation and memory resources should be expended. Some radiosity systems use explicit error bounds to make this trade-off [HSA91, LSG94]. Ray tracers typically use stochastic techniques to estimate error in computed radiance [Coo86, PS89] but do not rigorously bound error.

Ward's RADIANCE ray tracer estimates error for diffuse radiance [WH92]. RADIANCE uses ray tracing to produce high-quality images that include view-dependent specular effects, as well as diffuse inter-reflections [WRC88, War92]. RADIANCE assumes that the diffuse component of radiance varies slowly, and can be sampled sparsely. Therefore, the RADIANCE ray tracer computes the specular radiance at each pixel, but lazily samples diffuse inter-reflections. The system uses gradient information to guide the sparse, non-uniform sampling of the slowly-varying diffuse component of radiance. However, RADIANCE does not interpolate the view-dependent components of radiance, nor does it bound error incurred by its interpolation of sparse samples.

Several researchers exploit image coherence to accelerate ray tracing [AF84]. These systems typically use error estimates based on the variance in pixel radiance to determine where to expend computational resources. Recently, two systems that exploit image coherence for the progressive refinement of ray-traced imagery have been developed [Guo98, PLS97]. These systems do not use explicit error estimates, but implicitly try to decrease perceived error in the image by detecting discontinuities in screen space. Guo [Guo98] samples the image sparsely along discontinuities to produce images for previewing. For polyhedral scenes, Pighin et al. [PLS97] compute image-space discontinuities, which are used to construct a constrained Delaunay triangulation of the image plane. This Delaunay triangulation drives a sparse sampling technique to produce previewable images rapidly. The traditional problem with screen-space interpolation techniques is that they may incorrectly interpolate across small geometric details, radiance discontinuities, and radiance non-linearities. While both these systems alleviate the problem of interpolation across discontinuities, neither system bounds error. Since they do not guarantee error bounds, they are useful for previewing; however, the user cannot be sure of obtaining an accurate image until the entire image is rendered. Also, both systems detect discontinuities in the image plane; therefore, when the viewpoint changes, discontinuities have to be recomputed from scratch.

2.1.2 Systems without error estimates

Several systems accelerate rendering by approximating visibility and shading, but do not use error estimates or guarantee bounded error.

Hardware-based rendering. Some systems exploit the graphics hardware to obtain some of the realism of ray tracing. Diefenbach's rendering system [DB97] uses multiple passes of standard graphics hardware to approximate ray-tracing effects such as shadows, reflections, and translucency at interactive rates. Ofek and Rappoport [OR98] consider a particular sub-problem, reflections of objects in curved reflectors, and compute better approximations for this sub-problem. Both systems use the graphics hardware to merge approximated reflections, shadows etc. with images at interactive rates. While both these systems approximate ray-tracing effects, neither provides any correctness guarantees. These systems are also restricted to polygonal scenes.

Parker et al. [PMS$^+$99] use a "brute-force" approach to support interactive ray tracing on multi-processors. Their approach focuses on software engineering issues in constructing a fast ray tracer. Note that this approach does not approximate shading and computes accurate radiance at each pixel, but relies on the computational power of multiprocessor hardware to accelerate rendering.

Image-based rendering. The goal of image-based rendering [MB95] is to support interactive rendering of scenes where radiance samples are collected by acquiring images of the scene in a pre-processing phase. The idea is to eliminate the scene model, and use images as the input to the rendering engine. The interpolant ray tracer differs in its goals substantially from these systems; however, IBR systems such as the Light Field [LH96] and the Lumigraph [GGSC96] have similarities to the interpolant ray tracer because they also collect radiance samples over a four-dimensional line space and quadrilinearly interpolate the samples to approximate radiance. Both these IBR systems construct uniformly subdivided 4D arrays whose size is fixed in the pre-processing phase. This fixed sampling rate does not guarantee that enough samples are collected in regions with high-frequency radiance variations, and may result in over-sampling in regions where radiance is smooth. Also, these systems typically constrain the viewpoint to lie outside the convex hull of the scene.

Recently, Lischinski and Rappoport use layered depth images (LDIs) to rapidly render both diffuse and specular radiance for new viewpoints [LR98]. They represent diffuse radiance with a few high-resolution LDIs and specular radiance with several low-resolution LDIs. When the scene is rendered, these LDIs are rapidly recombined to produce approximations to the correct image. For small scenes, this approach has better memory usage and visual results than the light field or Lumigraph. However, scenes with greater depth complexity could require excessive memory. Also,

though this technique alleviates artifacts for specular surfaces, it still relies on radiance sampling that is not error-driven.

Mark et al. [MMB97] apply a 3D warp to pixels from reference images to create an image at the new viewpoint. They treat their reference image as a mesh and warp the mesh triangles to the current viewpoint. Their system does not handle view-dependent shading such as specular highlights and does not guarantee correct results for arbitrary movements of the eye.

Chevrier [Che97] computes a set of key views used to construct a 3D mesh that is interpolated for new viewpoints. If a pixel is not covered by one key view, several key views are used. To handle specularity, one 3D mesh per specular surface is built, and the specular coefficient is linearly interpolated from multiple key images. While this algorithm decreases some aliasing artifacts, it still may interpolate across shadows or specular highlights.

None of these image-based systems bounds the error introduced by approximating visibility or radiance. Also, all these techniques require a pre-processing phase in which light fields, LDIs, reference images, or key views are computed to be reused later. The memory requirements of these systems is proportional to the number of reference images obtained in the pre-processing phase; some systems use compression to alleviate this problem. Note that the reliance of these systems on pre-processing precludes their use in interactive applications in which the scene changes.

2.1.3   Accelerating animations

By reusing information from frame to frame, several systems accelerate animations. Algorithms that exploit temporal coherence to approximate visibility at pixels can be categorized by the assumptions they make about the scene and the correctness guarantees they provide. Chapman et al. use the known trajectory of the viewpoint through the scene to compute continuous intersection information for rays [CCD90, CCD91]. However, because the system assumes that the scene is polygonal and the paths of objects through the scene is known *a priori*, this system is not useful in applications where the user interacts with the scene.

Several systems reuse pixels from the previous frame to render the current frame without any prior knowledge of the viewpoint's trajectory [Bad88, AH95]. Adelson and Hodges [AH95] apply a 3D warp to pixels from reference images to the current image. Diffuse radiance is reused in the warped pixels, but specular radiance is computed by casting rays as necessary. Their system achieves modest performance benefits (on the order of 50%-70%), and exhibits aliasing effects because pixels are not warped to pixel centers in the current frame.

Nimeroff et al. [NDR95] use IBR techniques to warp pre-rendered images in animated environments with moving viewpoints. However, their system does not provide any correctness

guarantees.

2.1.4 Higher-dimensional representations

Another related area of research is the use of line or ray space to accelerate rendering in global illumination algorithms. Arvo and Kirk [AK87] represent bundles of rays as 5D bounding volumes that are used to accelerate ray-object intersections. However, the focus of their work is to improve the performance of visibility determination, and they do not accelerate shading or editing.

2.1.5 Radiance caching

Like the interpolant ray tracer, some systems cache radiance while rendering a frame and reuse these cached radiance values to render interactively. Ward [War98] uses a 4D *holodeck* data structure that is populated as the RADIANCE system computes an image. Walter et al. [WDP99] store radiance samples in a *render cache*, and reproject these samples when the viewpoint changes. With varying success, these systems use heuristics to fill in pixels not stored in their caches. These systems focus on rendering speed, and so they do not characterize or bound the rendering errors introduced by the heuristics they use.

2.2 Interactive scene editing

Recently, there has been increased interest in the problem of accelerating scene editing with various global illumination algorithms. Work on both incremental ray tracers and incremental radiosity algorithms is relevant to this thesis.

2.2.1 Ray tracing

Strides have been made in facilitating interactive scene manipulation with ray tracing. Several researchers have developed ray tracers supporting scene editing that incrementally render only those parts of the scene that might be affected by a change.

Cook's *shade trees* [Coo84] maintain a symbolic evaluation of the local illumination at each pixel of a frame. When an object's material properties are changed, the shade trees are re-evaluated with the new material properties, if they remain the same. Séquin and Smyrl [SS89] extend shade trees to include reflections and refractions. Their *ray trees* represent the entire radiance contribution by the scene at each pixel. When the user changes the material properties of objects (e.g., color,

specular coefficient) or changes light intensities, the affected trees are re-evaluated. However, this approach assumes that the trees do not change by the scene edit; therefore, edits such as moving an object or changing the viewpoint are not supported.

Murakami and Hirota [MH92] and Jevans [Jev92] extend these techniques to support geometry changes such as moving an object in the scene, or deleting objects. Rays that are traced through the scene during rendering are associated with the voxels they traverse. When the scene is edited, the affected voxels and their associated rays are found. Radiance along the rays is then updated to reflect the edit.

Recently, Brière and Poulin [BP96] introduced a system that supports incremental rendering for a fixed viewpoint. Their system supports the most comprehensive set of edits to date. These edits are categorized into two major types: attribute changes which involve adjustments to an object's color, reflection coefficient, and other material properties; and geometry changes, which include changes such as moving an object. *Color trees* and *ray trees* are maintained for each pixel in the image. These trees are used to separately accelerate updates to object attributes and geometry; attribute edits typically only affect the color trees, while geometry edits affect both types of trees. For efficiency, their system groups these trees and maintains hierarchical bounding volumes to rapidly identify the pixels affected by an edit. Their system reflects attribute changes in about 1-2 seconds, and geometry changes in 10-110 seconds.

All of the above systems are completely view-dependent because they assume that the viewpoint is fixed; while a user can edit the scene, he cannot adjust the viewpoint. Since the viewpoint is fixed, all the techniques are *pixel-based*; that is, additional information, such as ray trees, are maintained for each pixel in the image and used to recompute radiance as the user edits the scene. Most of these systems use compression techniques to alleviate memory usage; even so, for high resolution images, the memory requirements of these systems can be large.

2.2.2 Radiosity

In the context of radiosity, several researchers have studied the problem of dynamic editing [Che90, GSG90, FYT94]. Recently, Dretakkis and Sillion [DS97] augment the link structure of hierarchical radiosity with additional line-space information to track links affected by the addition or deletion of objects. The hierarchical link structure, and hence the implicit line space, makes it possible to identify affected regions rapidly when an object is edited. Their system is not pixel-based; therefore, a user can change the viewpoint after an update. However, their algorithms apply only to radiosity systems for scenes with diffuse materials.

36

2.3 Discussion

This thesis differs from previous work in several ways. The most important difference is that radiance interpolants approximate radiance while *bounding* interpolation error conservatively and accurately. This thesis presents several novel geometric techniques and a generalization of interval arithmetic to bound approximation error. These techniques are instrumental in making the interpolant ray tracer the first accelerated ray tracer to reconstruct radiance from sparse samples while bounding error conservatively.

The interpolant ray tracer is an on-line algorithm: no pre-processing is required. This property makes the system suitable for interactive applications, and also makes it possible to use memory management techniques to bound the memory use. When memory management is used, recently unused radiance samples are discarded, and the system acts as a cache of radiance samples—though one that provides guarantees on rendering quality.

Another contribution of this system is that reprojection is used to accelerate visibility determination by exploiting temporal coherence in visibility, *without* introducing visual artifacts. Visibility determination by this algorithm is guaranteed to be correct.

This thesis also presents an incremental rendering system that supports scene editing *while permitting changes in the viewpoint*. This thesis builds on the work of Brière and Poulin, Dretakkis and Sillion, and the interpolant ray tracer, while providing additional functionality. This is the first system that supports incremental ray tracing of non-diffuse scenes while permitting the user's viewpoint to change. A novel data structure, the ray segment tree, and efficient algorithms to solve this problem are introduced.

The error guarantees of the interpolant ray tracer make interpolants useful for interactive rendering, because each interpolant is guaranteed to accurately represent the radiance of every ray covered by the interpolant. Therefore, when the scene is edited, updating an interpolant updates all the rays it represents, which is important for efficiency. Previous pixel-based systems are unable to support moving viewpoints because they cannot determine how radiance along every ray will change when the viewpoint changes.

Chapter 3

Radiance Interpolants

Radiance is a function over the space of all rays. As mentioned in Chapter 1, the interpolant ray tracer is based on the assumption that radiance is a smoothly varying function. Therefore, radiance can be sampled sparsely, and these sparse samples can be reconstructed to approximate radiance while rendering an image. There are several issues that must be considered when sampling and reconstructing a function. These issues are explored in the remainder of this chapter:

- What is the domain of the function being sampled?

  The domain of the radiance function is the space of all rays. Section 3.1 presents a coordinate system that uses four parameters to describe all rays intersecting an object. Therefore, the domain of the radiance function is a four-dimensional space called *line space*.

- Where in the domain of the function are samples collected?

  Section 3.2 describes how samples are collected adaptively at the corners of hypercubes in linespace. The radiance samples collected are stored in a hierarchical data structure, called a *linetree*, built over line space. As described in Chapter 1, the interpolant ray tracer is built on top of the base ray tracer. Samples are collected by invoking the base ray tracer.

- When rendering the scene, how can the original function be reconstructed?

  For each eye ray, the system finds and interpolates an appropriate set of radiance samples, called an *interpolant*, to approximate radiance. Section 3.3 describes how quadrilinear interpolation of the samples stored in an interpolant is used to approximately reconstruct the radiance function for a given eye ray. Samples are located rapidly by traversing linetrees.

- Do the samples collected permit accurate reconstruction of the function?

39

Section 3.3 describes how the radiance function can be adaptively sampled. The error bounding algorithm described in Chapter 4 is used to identify when the samples approximate radiance accurately, and when denser sampling is required.

The rest of this chapter discusses the mechanisms for sampling, storing and reconstructing radiance. The problem of determining *when* samples can be used to accurately reconstruct the radiance function is deferred until Chapter 4.

3.1 Ray parameterization

To interpolate over the domain of rays, we require a coordinate system describing rays. In this section, a coordinate system is introduced that uses four parameters to describe all rays intersecting an object. This ray parameterization is used to index into the space of rays when searching for and storing samples: the linetree data structure stores samples using their ray parameters as keys. For simplicity, the discussion is initially restricted to 2D rays, and then extended to 3D rays.

3.1.1 2D ray parameterization
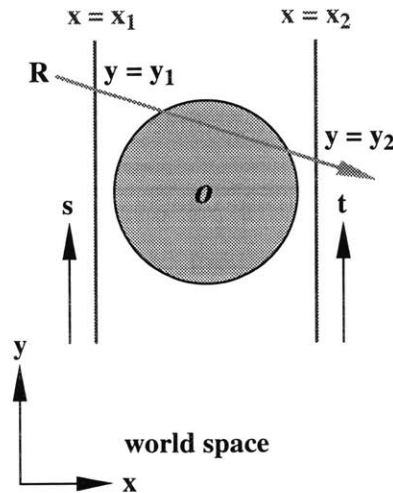
Figure 3-1: A segment pair (dark gray) and an associated ray R (light gray).

Every 2D ray can be parameterized by the two intercepts, s and t (see Figure 3-1), that it makes with two parallel lines (assuming the ray is not parallel to the lines). For example, consider two lines parallel to the y-axis at $x = x_1$ and $x = x_2$, on either side of an object o. Every ray **R** intersecting o that is not parallel to the y-axis can be parameterized by the y-intercepts that
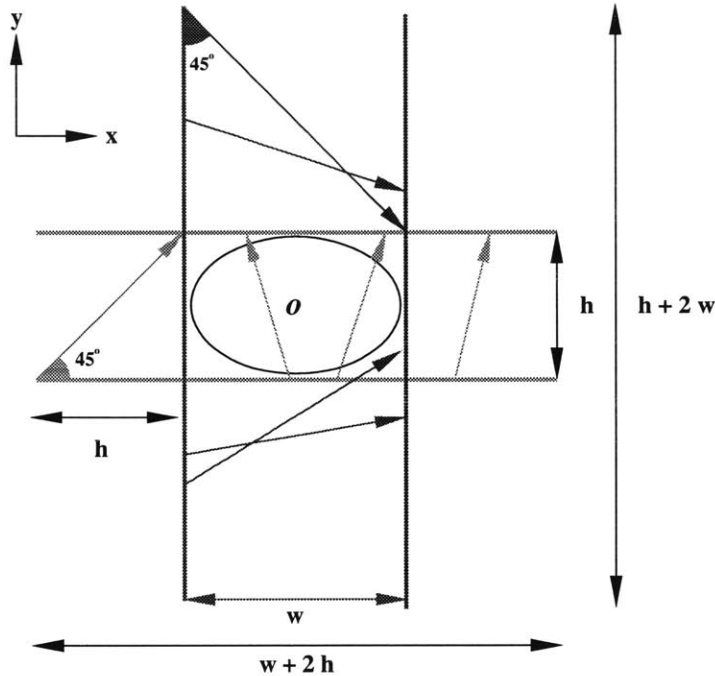
Figure 3-2: Two segment pairs (dark gray and light gray) and some associated rays.

R makes with the two parallel lines; i.e., $(s, t) = (y_1, y_2)$. There are three problems with this parameterization: rays parallel to the y-axis cannot be represented; the intercepts of rays nearly parallel to the y-axis are numerically imprecise and could be arbitrarily large; and the orientation (right or left) of the ray is not specified by the parameterization.

These problems are avoided by parameterizing each 2D ray with respect to one of four *segment pairs*. A segment pair is defined by two parallel line segments and a principal direction that is perpendicular to the line segments. The four segment pairs have the principal directions $+\hat{x}$, $-\hat{x}$, $+\hat{y}$, and $-\hat{y}$. In each segment pair, the principal direction vector 'enters' one of the line segments (called the *front* segment) and 'leaves' the other line segment (called the *back* segment). The segment pairs with principal directions $+\hat{x}$ and $-\hat{x}$ have the same parallel line segments and only differ in the designation of front and back line segments. The same is true for the segment pairs with principal directions $+\hat{y}$ and $-\hat{y}$.

Every ray intersecting o is uniquely associated with the segment pair whose principal direction is closest to the ray's direction: the principal direction onto which the ray has the maximum positive projection. Once the segment pair associated with a ray is identified, the ray is intersected with its front and back line segments to compute its s and t coordinates respectively.

To ensure that every ray associated with a segment pair intersects both parallel line segments, the line segments are sized as shown in Figure 3-2. In the figure, an object o with a bounding

41
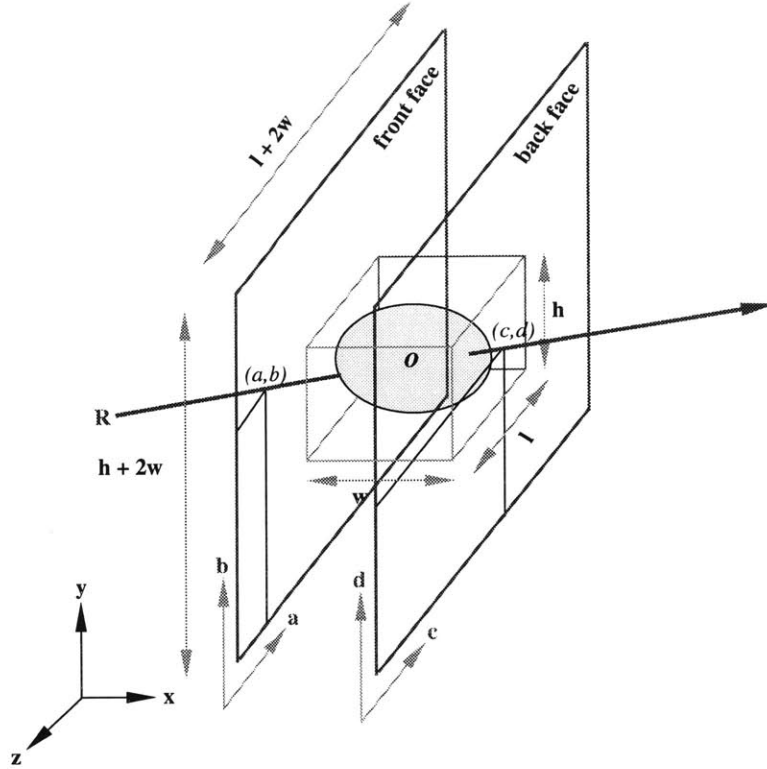
Figure 3-3: Ray parameterization in 3D. The face pair is shown in dark gray. The dark gray ray intersects the front face at (a, b), and the back face at (c, d), and is parameterized by these four intercepts.

rectangle of size $w \times h$ is shown with two of its four segment pairs. The segment pairs with principal directions $\pm \hat{x}$ have line segments of length $(h + 2w)$, while the segment pairs with principal directions $\pm \hat{y}$ have line segments of length $(w + 2h)$. This sizing ensures that the most extreme rays (rays at an angle of $45°$ to the principal direction) intersect both line segments of the segment pair with which they are associated. The dark gray segment pair with principal direction $\hat{x}$ represents all rays $r = (r_x, r_y)$ with $|r_x| > |r_y|$ and $sign(r_x) > 0$; i.e., all normalized rays with r_x in $[\frac{1}{\sqrt{2}}, 1]$ and r_y in $[-\frac{1}{\sqrt{2}}, \frac{1}{\sqrt{2}}]$. The light gray rays are associated with the light gray segment pair whose principal direction is $\hat{y}$. This segment pair represents all rays with r_x in $[-\frac{1}{\sqrt{2}}, +\frac{1}{\sqrt{2}}]$, and r_y in $[\frac{1}{\sqrt{2}}, 1]$. Rays that have the same projection on two segment pairs (e.g., $r_x = r_y = \frac{1}{\sqrt{2}}$) can be represented by either of the segment pairs when interpolating radiance.

The four segment pairs represent all rays intersecting the 2D object o. The maximal component of the direction vector of a ray and its sign identify the segment pair with which the ray is associated. The ray is intersected with this segment pair to compute its intercepts (s, t); these (s, t) coordinates parameterize the ray.

42
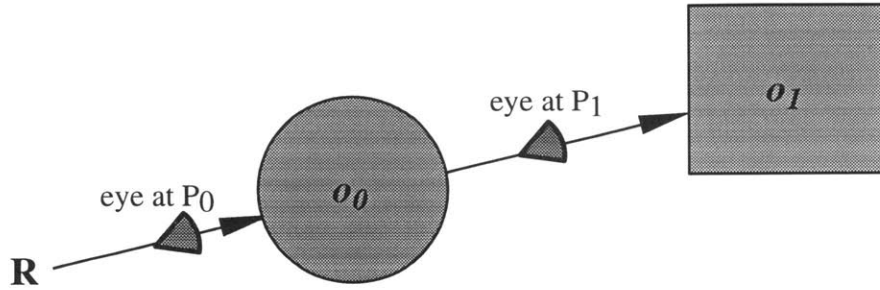
Figure 3-4: Radiance along ray **R** depends on the eye position.

3.1.2 3D ray parameterization

The parameterization of the previous section is easily extended to 3D rays. Every ray intersecting an object o can be parameterized by the ray's four intercepts (a, b, c, d) with two parallel bounded *faces* surrounding o (see Figure 3-3). This parameterization is similar to some previous schemes [GGSC96, LH96, TBD96].

Six pairs of faces surrounding o are required to represent all rays intersecting o. The principal directions of the six face pairs are $+\hat{x}$, $+\hat{y}$, $+\hat{z}$, $-\hat{x}$, $-\hat{y}$, and $-\hat{z}$. As in the 2D case, the faces are expanded on all sides by the distance between the faces, as shown in Figure 3-3. In the figure, a face pair with principal direction $\hat{x}$ is shown. The distance between the faces is w. Therefore, the face pair is of dimensions $(h + 2w) \times (l + 2w)$. This face pair represents all normalized rays with $|r_x| > |r_y|$, $|r_x| > |r_z|$, and $sign(r_x) > 0$.

A ray's coordinates are computed by intersecting it with the two parallel faces of the associated face pair. For example, in Figure 3-3, the dark gray ray **R** is associated with the face pair with principal direction $\hat{x}$. **R** is intersected with the two parallel faces perpendicular to the x-axis, and its y and z coordinates with respect to each face are its (a, b) and (c, d) coordinates respectively. An additional translation and rescaling of the intercepts is done such that (a, b, c, d) always lie in the range $[0, 1]$.

Thus, the dominant direction and sign of a ray determine which of the six face pairs it is associated with. The ray is parameterized by its four intercepts (a, b, c, d) with the two parallel faces of that face pair.

3.1.3 Line space vs. ray space

Note that ray space is actually a five dimensional space in which the fifth dimension is the position of the eye along the ray. For example, in Figure 3-4, the radiance along the ray **R** is different depending on whether the eye is at position P_0 or P_1. Assuming the medium of propagation of

rays is transparent, radiance changes along the fifth dimension only when there is a discontinuity in the dielectric properties of the medium, such as at an object surface. Therefore, radiance along a ray is mostly constant and changes only when there is a change in visibility along the ray.

To avoid representing the fifth dimension explicitly, a separate ray coordinate system is introduced for every object in the scene. In the parameterization described in the previous section, every ray R is parameterized with respect to the object it intersects. For example, in Figure 3-4, if the eye is at P_0, R intersects o_0 and if the eye is at P_1, R intersects o_1. The ray is then parameterized with respect to the face pair of the appropriate object. This four-parameter representation used by the interpolant ray tracer is not a parameterization of rays, but rather an object-space parameterization of directed lines. Using an object-space parameterization of line space eliminates the need to explicitly represent the fifth dimension of ray space.

3.2   Interpolants and linetrees

The ray parameterization presented in the previous section can be used to define a simple way to interpolate radiance over the domain of rays. The linetree data structure is used to store and look up the samples used for interpolation. This section describes how interpolants and linetrees are built and used to approximate radiance when rendering a frame. Again, 2D rays are considered first.

3.2.1   2D line space

Every 2D ray is associated with a segment pair and is parameterized by its (s, t) coordinates. On the left, in Figure 3-5, a segment pair in 2D world space is shown. On the right, a Cartesian representation of s-t line space is shown. All rays associated with the segment pair in world space are points that lie inside a square in s-t space; the ray R, shown in dark gray, is an example. The extremal points at the four corners of the s-t square, R_{00}, R_{01}, R_{10}, and R_{11}, correspond to the rays in light gray shown on the left.

Radiance for any ray R inside the s-t square can be approximated by bilinearly interpolating the radiance samples associated with the four rays at the corners of the square. These four rays are called the *extremal rays*. If $R_{00}, R_{01}, R_{10}, R_{11}$ represent the radiance along rays $R_{00}, R_{01}, R_{10}, R_{11}$, radiance along ray R is given as $f(R)$:

$$f(R) = (1 - s)(1 - t)R_{00} + s(1 - t)R_{10} + (1 - s)tR_{01} + stR_{11}$$

world space   s-t line space
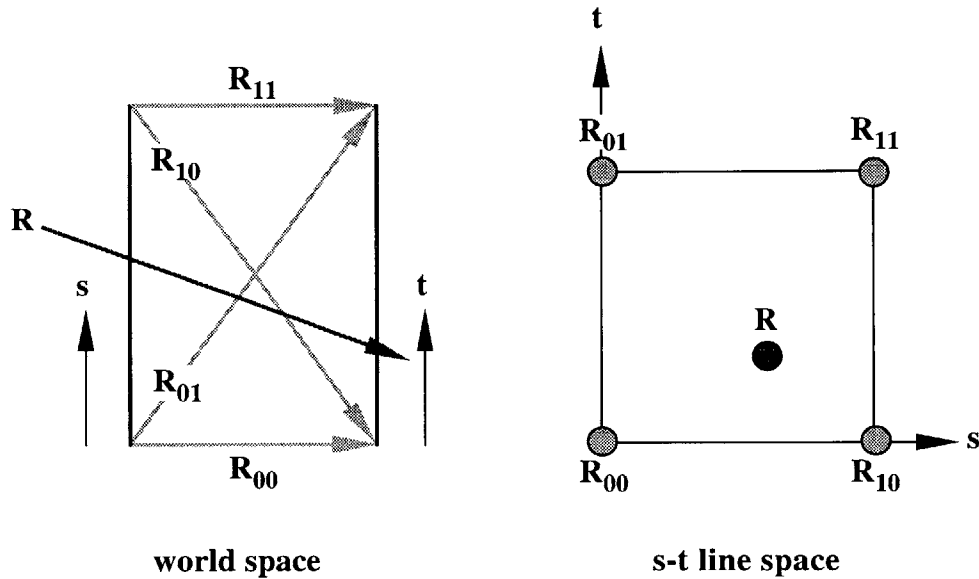
Figure 3-5: A segment pair and its associated s-t line space.

Bilinear interpolation is a standard technique for interpolation of a function over a rectangular domain [Gla95]. The set of four radiance samples associated with the extremal rays is called an *interpolant*.

Radiance interpolants are stored in a hierarchical data structure called a *linetree*; each of the four segment pairs has an associated linetree. In 2D, the linetree is a quadtree built over line space; the root of the linetree represents all the rays that intersect the segment pair. An interpolant is built at the root of the linetree by computing the radiance along the extremal rays, R_{00}, R_{01}, R_{10}, and R_{11}, that span the s-t square in line space. An error bounding algorithm (described in Chapter 4) determines if the interpolant is valid; i.e., if the interpolant can be used to approximate radiance to within a user-specified error bound. If the interpolant is valid, it is used to bilinearly interpolate radiance for every eye ray R inside the s-t square. If the interpolant is not valid, the 2D linetree is subdivided at the center of both the s and t axes, as in a quadtree, to produce four children.

Subdividing the s and t axes in line space corresponds to subdividing the front and back line segments of the linetree cell in world space. The rays represented by the linetree cell can be divided into four categories depending on whether the rays enter by the top or bottom half of the front line segment and leave by the top or bottom half of the back line segment. These four categories correspond to the four children of the linetree cell. Therefore, rays that lie in the linetree cell are uniquely associated with one of its four children.

In Figure 3-6, a segment pair and its associated s-t line space are depicted. On the top left, the segment pair is shown with some rays that intersect it. The four children of the subdivided segment

45
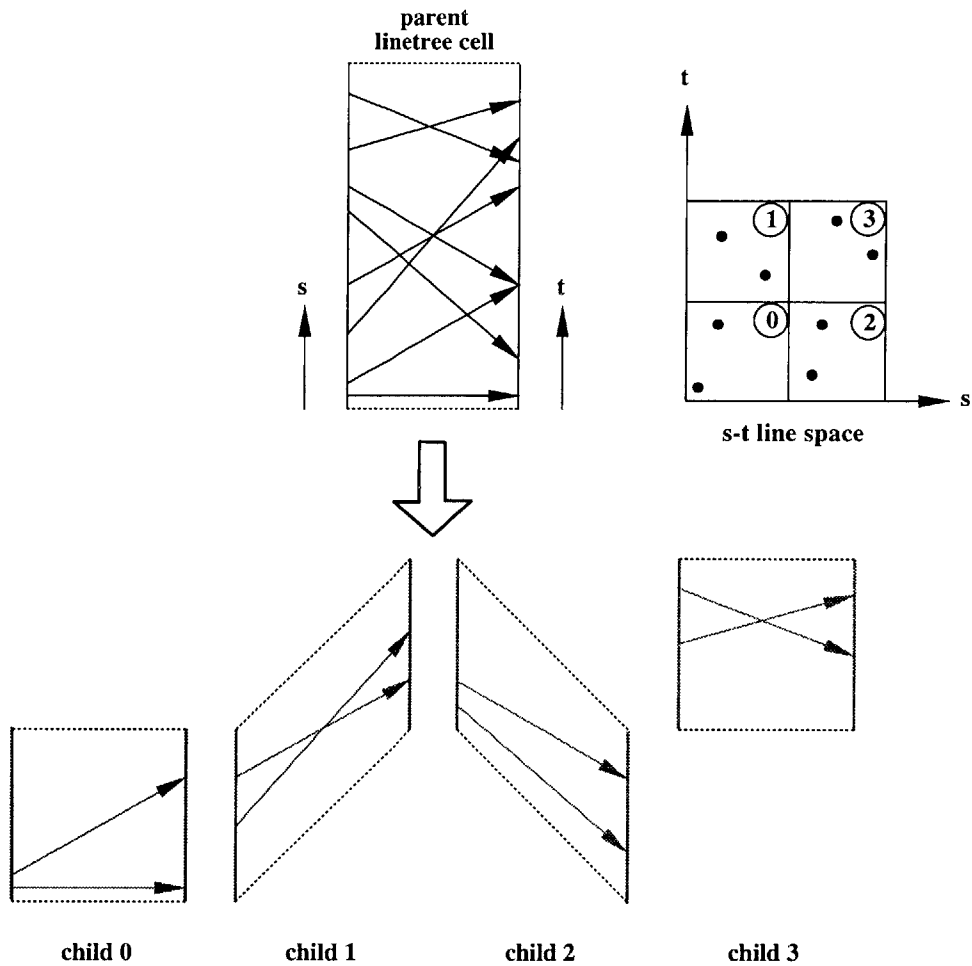
Figure 3-6: A 2D segment pair and its children. Every ray that intersects the segment pair (represented as a point in s-t space) lies in one of its four subdivided children.

pair are shown on the bottom. Each of the four children is represented by the correspondingly numbered region of line space shown in the top right. The dotted lines show the region of world space intersected by the rays represented by that linetree cell.

3.2.2 4D line space

Now consider rays in 3D, which are parameterized by four coordinates (a, b, c, d). Each face pair corresponds to a 4D hypercube in line space that represents all the rays that pass from the front face to the back face of the face pair. Each face pair has a 4D linetree associated with it that stores radiance interpolants. The root of the linetree represents all rays associated with the face pair. When an interpolant is built for a linetree cell, samples for the sixteen extremal rays of the linetree cell are computed. In line space, these sixteen rays are the vertices of the 4D hypercube
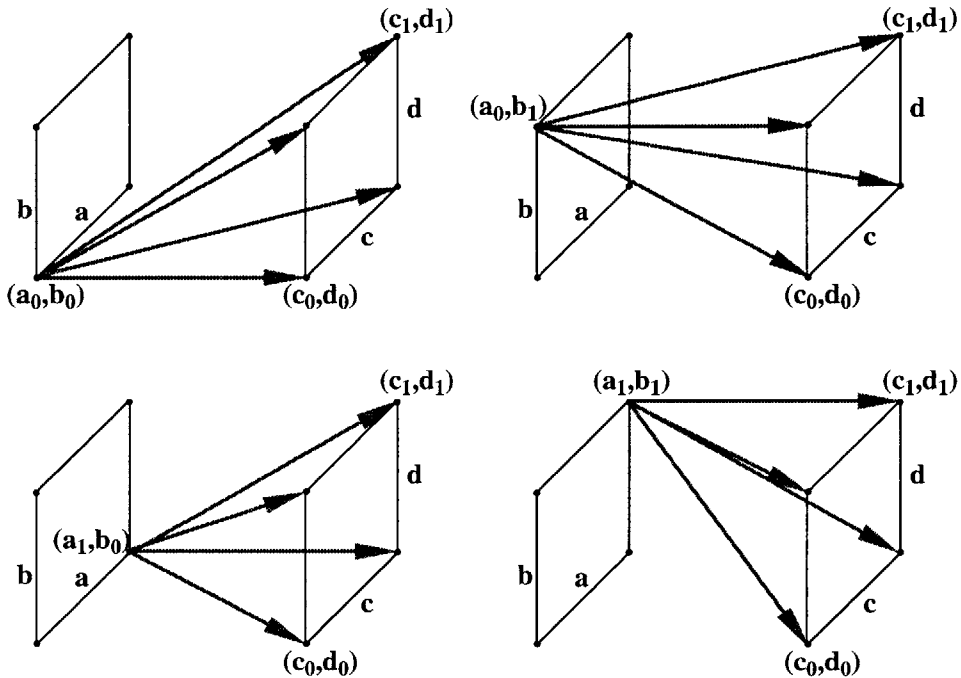
Figure 3-7: A 4D linetree cell and its sixteen extremal rays.

represented by the linetree cell, and in world space they are the rays from each of the four corners of the front face of the linetree cell to each of the four corners of its back face. Figure 3-7 shows a linetree cell and its sixteen extremal rays.

If the error bounding algorithm (see Chapter 4) determines that an interpolant is valid, the radiance of any eye ray represented by that linetree cell is quadrilinearly interpolated using the stored radiance samples, where quadrilinear interpolation is the natural 4D extension of bilinear interpolation. If the interpolant is not valid, the linetree cell is subdivided adaptively; both the front and back faces of the linetree cell are subdivided along the a, b and c, d axes respectively. Thus, the linetree cell is subdivided into sixteen children; each child represents all the rays that pass from one of its four front sub-faces to one of its four back sub-faces. A ray that intersects the linetree cell uniquely lies in one of its sixteen children. The sixteen children of the linetree cell are shown in Figure 3-8. Note that each of the sixteen children shares one extremal ray with the parent linetree cell. This subdivision scheme is similar to that in [TH93].

3.3   Using 4D linetrees

Linetrees are used to store and look up interpolants during rendering. When rendering a pixel, the corresponding eye ray is constructed and intersected with the scene. If the eye ray intersects an

47
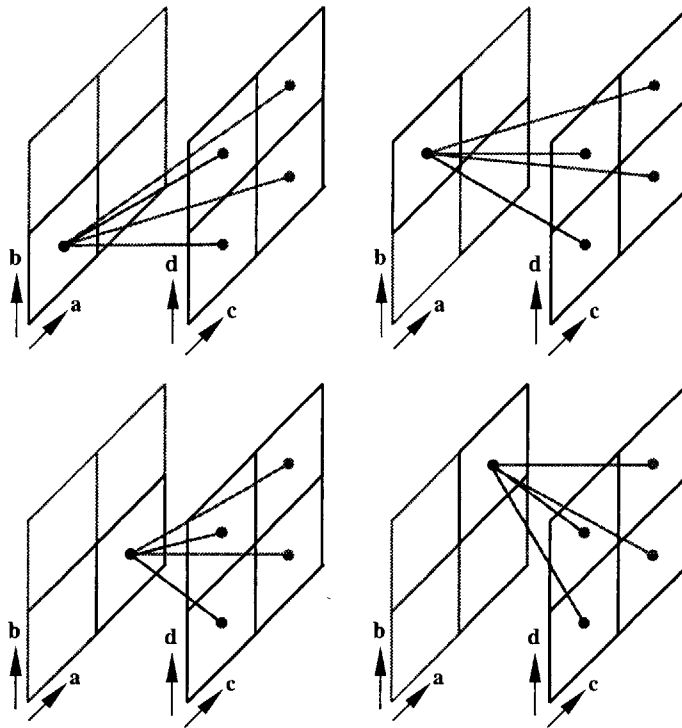
Figure 3-8: Linetree cell subdivision.

object, its four intercepts (a, b, c, d) are computed with respect to the appropriate face pair of that object. The linetree associated with that face pair of the object is traversed to find the leaf cell containing the ray. This leaf cell is found by walking down the linetree performing four interval tests, one for each of the ray coordinates. If the leaf cell contains a valid interpolant, radiance for that pixel is quadrilinearly interpolated. If a valid interpolant is not available, an interpolant for the leaf cell is built by computing radiance along the sixteen extremal rays of the linetree cell. The error bounding algorithm determines if the samples collected represent a valid interpolant. If so, the interpolant is stored in the linetree cell.

If the interpolant is not valid, the front and back faces of the linetree cell are subdivided. An interpolant is lazily built for the child that contains the eye ray. Thus, linetrees are adaptively subdivided; this alleviates the memory problem of representing 4D radiance, by using memory only where necessary. More samples are collected in regions with high-frequency changes in radiance. Fewer samples are collected in regions with low-frequency changes in radiance, saving time and memory.

Figure 3-9 shows an image of a specular sphere (on the left), and the linetree cells that contribute to the image (on the right). A linetree cell can be shown as a shaft from its front face to its back face; however, this visualization is cluttered. To simplify the visualization, only the front

48
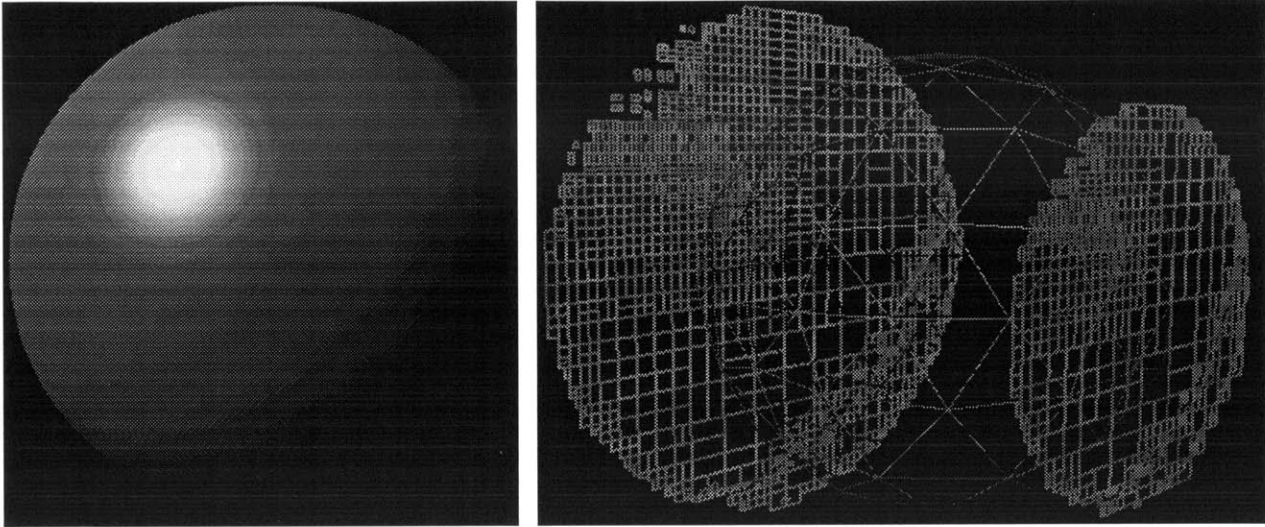
Figure 3-9: Linetree visualization. On the left is an image of a sphere rendered using the interpolant ray tracer. On the right is a visualization of the corresponding linetree cells.

(blue-green) and back face (pink) of each linetree cell are shown. Each subdivision of a linetree cell corresponds to a subdivision of its front and back face. Therefore, small, highly subdivided front and back faces in the visualization correspond to highly subdivided linetree cells, as can be seen around the specular highlight of the sphere. Chapter 4 describes how the error bounding algorithm determines which linetree cells to subdivide.

3.4   Comparing the base and interpolant ray tracers

Figure 3-10 illustrates the difference between the base ray tracer and the interpolant ray tracer. This figure explains pictorially why the interpolant ray tracer accelerates ray tracing.

When a frame is rendered, the ray tracer collects a set of radiance samples for each eye ray in the image. These samples are shown as light gray points. When the viewpoint changes, a different set of samples are collected, shown as dark gray points. Note that for a particular viewpoint, the points in line space that represent eye rays for that viewpoint lie on a line in line space [GGC97]. Since the base ray tracer does not exploit coherence, when the viewpoint changes, it has no information about the radiance along the new eye rays.

On the right in the figure, a line space representation of the interpolant ray tracer is shown. Each interpolant, shown as a shaded rectangle, represents radiance for some region of line space. This figure illustrates two intuitions about interpolants:

- For a particular viewpoint, interpolants can be reused to approximate radiance for several

49
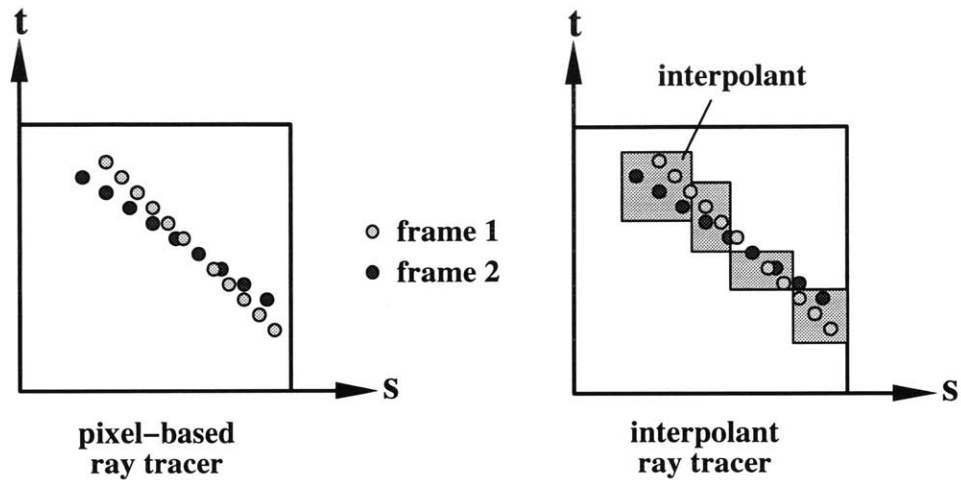
Figure 3-10: Comparing the base ray tracer and the interpolant ray tracer.

eye rays. Thus, interpolants exploit image-space and object-space coherence.

- When the viewpoint changes to a nearby location, interpolants built in the previous frame can still be reused to approximate radiance for eye rays from the new frame. Thus, interpolants exploit temporal coherence.

3.5 Discussion

This chapter presents an object-space ray parameterization used to index into the space of rays. Every eye ray intersecting an object is parameterized by its four coordinates (a, b, c, d). Linetrees are used to store radiance samples used in interpolation. This section discusses some design decisions and optimizations that improve performance.

3.5.1 Efficient quadrilinear interpolation

Quadrilinear interpolation can be accelerated by appropriately factoring the expressions computed. This factoring is useful even for bilinear interpolation. Bilinear interpolation computes the following expression:

$$f(s, t) = (1 - s)(1 - t)R_{00} + (1 - s)tR_{01} + s(1 - t)R_{10} + stR_{11}$$

50

Evaluating this expression sequentially, as written, requires eight multiplications and five additions, assuming that the values of $(1-s)$ and $(1-t)$ are computed only once. It is well-known that bilinear interpolation can be computed faster using the following factorization [Pra91]:

$$f(s,t) = (1-s)\left[(1-t)R_{00} + tR_{01}\right] + s\left[(1-t)R_{10} + tR_{11}\right]$$

This formula can be expressed in terms of a linear interpolation function L:

$$L(x, y_0, y_1) = (1-x)y_0 + xy_1 = y_0 + x(y_1 - y_0)$$

The function L can be computed using one multiplication and two additions using the rightmost expression. The bilinear interpolation can be expressed using L as follows:

$$
\begin{aligned}
f(s,t) &= (1-s)L(t, R_{00}, R_{01}) + sL(t, R_{10}, R_{11}) \\
&= L(s, L(t, R_{00}, R_{01}), L(t, R_{10}, R_{11}))
\end{aligned}
$$

The function f is computed with three applications of L, so the total cost is three multiplications and six additions. Multiplication is usually slower than addition, so this computation is an improvement. This factoring is even more effective for quadrilinear interpolation, where the number of multiplications is decreased from 64 to 15, while the number of additions is increased from 19 to 30. In general, for interpolation in n dimensions, this factoring allows us to trade $(n-1)2^n + 1$ multiplications for $2^n - n - 1$ additions, which is always a speedup if multiplication is at least as slow as addition.

3.5.2 Adaptive linetree subdivision

A linetree cell is subdivided if the sixteen extremal samples associated with the cell do not approximate the radiance function over the cell acceptably. When a linetree cell is subdivided, all four axes of the cell are subdivided. If no information is available about the form of the radiance function that the cell represents, this greedy subdivision makes sense. However, if information about how the radiance function varies *is* available, this information can be used to drive adaptive subdivision. This concept is reminiscent of the use of information about the distribution of objects in a 3D scene to build optimal spatial subdivisions of the scene [FI85, Jan86, Gla89].

The subdivision algorithm presented earlier in this chapter greedily splits a linetree cell into sixteen children. The interpolant ray tracer implements a 4-way split algorithm that splits only two of the axes (a, c) or (b, d) at a time; each linetree cell is subdivided into four children. The pair of
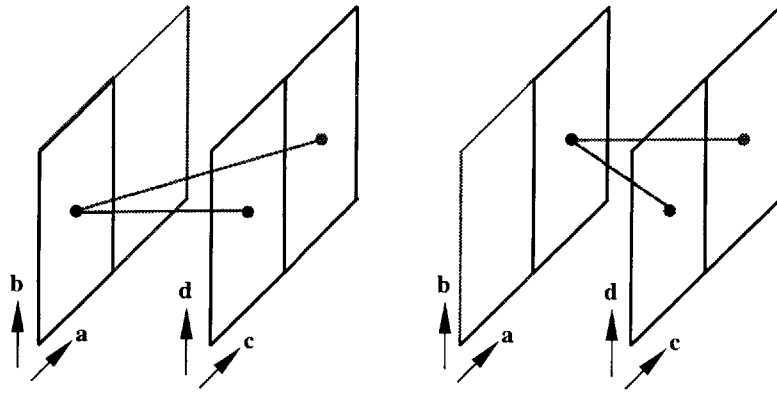
Figure 3-11: 4-way split of linetree cell.

axes to subdivide is decided using information about the error in the radiance approximation from the error bounding algorithm. This error-driven subdivision is described in detail in Section 4.4.1. Figure 3-11 shows the four children of a linetree cell that is subdivided along the a and c axes.

A 2-way split algorithm that splits only one of the four axes, in a manner similar to the kd-tree and BSP tree [FvDFH90], has also been implemented in the interpolant ray tracer; however, it did not result in performance gains. Note that unlike the kd-tree and BSP tree, linetree cells are always split at the center of the axis being subdivided. This is because it is hard to predict the shape of the radiance function over the linetree cell. This problem will become more clear in Chapter 4.

3.5.3   Sharing sample rays

The cost of building interpolants can be decreased by noticing that linetree cells share many rays. In the 4-way split algorithm, each child of a linetree cell shares four of its sixteen rays with its parent. Similarly, siblings in the linetree share common rays. For example, consider two sibling linetree cells L_0 and L_1 that have the same front face F_0, but different back faces, B_0 and B_1, as shown in Figure 3-12. These two linetree cells share eight of the sixteen extremal rays (shown in black). The bottom of the figure shows the sixteen extremal rays of L_0 on the left and L_1 on the right. Again the common rays are shown in black.

When building interpolants, it is desirable to reuse samples that have already been computed; a fast algorithm is required that finds and reuses these samples. These shared samples can be found by computing the common rays between siblings and parents analytically [TH93]. However, the problem with this analytical solution is that a ray can be shared between linetree cells that are far from each other in the tree. For example, common rays are shared by siblings, or between the children of siblings, or between the children of the children of siblings, etc. Finding the linetree cell with which rays are shared could be slow, eliminating the benefits of this optimization. Instead,

52
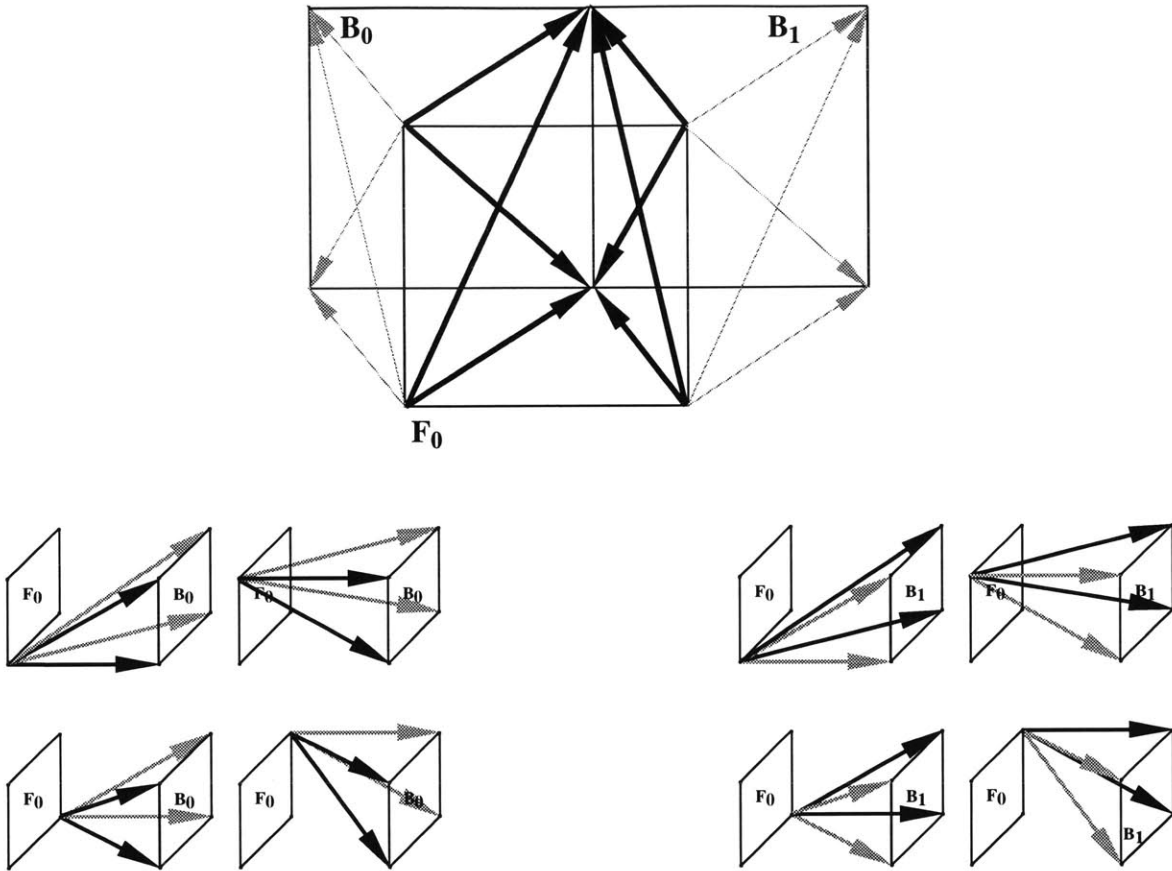
Figure 3-12: Common rays.

the interpolant ray tracer uses hash tables to track common rays; the average amortized search time is constant. The hash tables are indexed by the four parameters of the ray; one hash table is associated with each face pair of an object.

The precise amount of ray sharing depends on the sparsity of the linetree structure and is therefore scene-dependent. Empirical measurements for various scenes suggest that storing common rays in a hash table eliminates about 65% of the intersection and shading computations while building interpolants.

3.5.4 Linetree depth

The interpolant ray tracer builds interpolants adaptively only if the benefits of interpolating radiance outweigh the cost of building interpolants. It achieves this by evaluating a simple cost model when deciding whether to subdivide a linetree cell. Linetree cells are subdivided on the basis of the number of screen pixels that they are estimated to cover. This estimate is computed using an algorithm similar to that used for reprojection (see Figure 5-3 in Chapter 5). The front face of the

53

linetree cell is projected onto its back plane, and clipped against its back face. When this clipped back face is projected on the image plane, its area is a good estimate of the number of pixels covered by the linetree cell for that frame. Thus, when the observer zooms in on an object, interpolants for that object are built to a greater resolution if required by the error bounding algorithm; if an observer is far away from an object, the interpolants are coarse, saving memory. This cost model ensures that the cost of building interpolants is amortized over several pixels. The best results are found empirically to occur when an interpolant is built only if it covers at least twelve pixels on the image plane. It makes sense that this setting delivers the best performance because building an interpolant is roughly twelve times more expensive than shooting a single ray. This follows because four of the sixteen samples associated with the interpolant have already been computed for its parent linetree cell and are reused, as explained in the previous section.

3.5.5 Linetree lookup cache

Ray space and screen space coherence are exploited by the following optimization. For every eye ray in the image, the algorithm finds the object intersected by the ray, and then walks down the appropriate linetree of the object, starting at the root of the linetree. Linetrees are subdivided to a depth of 8 to 16 for typical scenes; traversing these linetrees from the root to the leaf takes time.

However, because of screen space and ray space coherence, a linetree leaf cell typically contributes to the radiance of multiple pixels in an image. Therefore, a linetree cache per object can be maintained that stores the linetree leaf cell last used to satisfy a query for this object. As the frame is rendered, for each new ray R, this cache is checked to see if R lies in the cached leaf linetree cell. If it does, no traversal of the linetree from the root is required. This cache is effective: its hit rate is 70-75%. As an additional optimization, when the cache lookup fails, the system walks up from the cached linetree cell to the linetree cell of the closest ancestor that includes R and then walks down from that ancestor. Since there is ray space coherence, the closest ancestor is typically close to the cached leaf. This walk up and down the tree is faster than walking down from the root. Eliminating the traversal from the root to the leaf of a linetree decreases the average time to find a linetree cell from $9\mu s$ to $3.5\mu s$ on a 194MHz MIPS R10000 processor.

3.5.6 Alternative data structures

This section considers alternatives for storing and interpolating radiance samples, and their expected impact on performance. Building interpolants is expensive; it would be beneficial to use a smaller number of samples to interpolate radiance. In order to interpolate a function over a region

2D

R₀

R₁

R

R₂

$R = w_0 R_0 + w_1 R_1 + w_2 R_2$

3D

R₀

R

R₃

R₁

R₂

$R = w_0 R_0 + w_1 R_1 + w_2 R_2 + w_3 R_3$
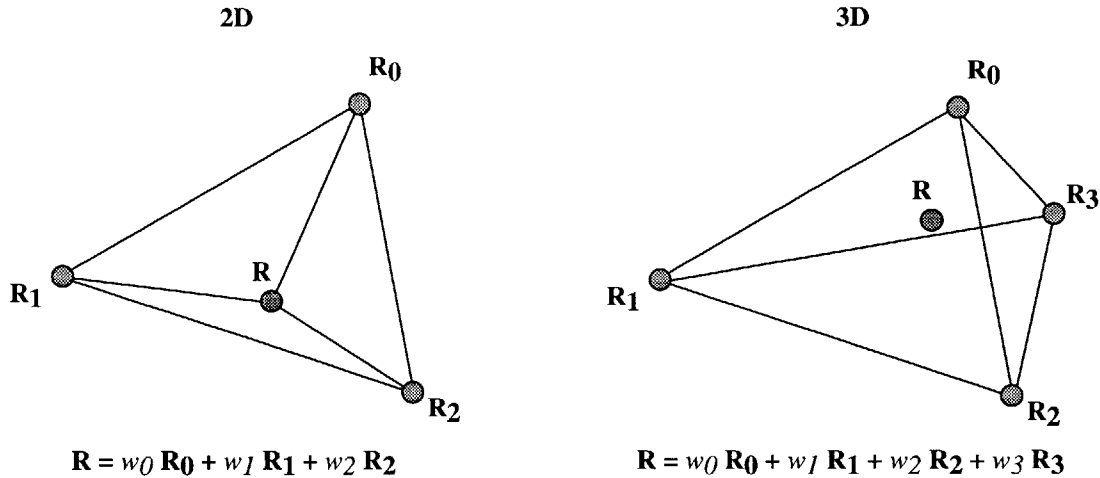
Figure 3-13: A simplex in 2D and 3D: triangle and tetrahedron.

of n-dimensional space, at least $n + 1$ linearly independent samples are required; these samples form a *simplex*. A 2D simplex is a triangle and a 3D simplex is a tetrahedron. Therefore, in 2D, the smallest number of samples required to interpolate a function is three, shown in Figure 3-13; in 3D, it is four.

Interpolation of a function over a simplex is usually done using barycentric interpolation, in which the radiance samples from each of the simplex vertices are weighted according to the barycentric coordinates of the point being interpolated. This interpolation technique results in a linear dependence of the interpolating function on each of the coordinates of the point. For example, in Figure 3-13, the radiance for the 2D ray R is interpolated using the radiance of rays R_1, R_2, and R_3 with weights w_1, w_2, and w_3 that sum to 1. If the ray R has coordinates (s, t), the interpolated radiance will have the form $A + Bs + Ct$ for some constants A, B, C that can be computed from the sample coordinates using matrix inversion.

Extending this discussion to 4D line space, a simplex in 4D line space has five vertices and is called a *pentatope* [Cox69, Gar84]. Therefore, at least five samples are required to interpolate radiance. The following problems have to be addressed to construct a simplicial subdivision of line space:

- A new data structure to store pentatope interpolants is needed, since the simple linetree data structure is not sufficient. It should support efficient identification of the interpolant containing a ray.

- A scheme for pentatope subdivision is needed that is efficient and also avoids creating simplices that are nearly linearly dependent (and thus cover a negligible portion of line space).

55

The vertex-splitting approach proposed by Popović and Hoppe for lower-dimensional simplex meshes may be applicable [PH97].

- Visibility acceleration is more difficult with pentatope interpolants than with 4D hypercubes, because there is no obvious analog to the front and back face clipping algorithm that is used to identify pixels covered by an interpolant (see Chapter 5).

The interpolant ray tracer described in this thesis opts for the simple approach of computing samples at the corners of a hypercube, and interpolating them using quadrilinear interpolation. The price to pay for this simplicity is that sixteen samples are required to represent an interpolant instead of five. Thus, interpolant construction and quadrilinear interpolation are correspondingly more expensive (see Section 3.5.1). Pentatope interpolation requires only 4 floating point multiplies and 4 additions. However, computation of the weighting factors used in pentatope interpolation requires inversion of a 5×5 matrix, which quadrilinear interpolation does not require. A more complete comparison of the two approaches would be of interest.

3.5.7 Alternative ray parameterizations

In recent work [CLF98], a spherical parameterization of rays has been presented in which a ray intersecting o is parameterized with respect to the two triangular patches of a tesselated sphere surrounding o that the ray intersects. This parameterization samples line space more uniformly than the two-plane parameterization presented in this chapter. It also has the benefit that only 9 samples are required to construct an interpolant.

It should be straightforward to integrate this parameterization into the interpolant ray tracer; however, it is not obvious that there would be much benefit. The spherical parameterization can be considered to have front and back faces: the regions of the sphere around the intersection points of the ray with the sphere. Each of these regions must be subdivided roughly as finely as the front and back faces in the two-plane parameterization. The total number of samples acquired in the two schemes is expected to be within a small constant factor of each other.

Chapter 4

Error Bounds

The interpolant ray tracer samples radiance adaptively, collecting more samples where radiance varies rapidly and fewer samples where radiance varies smoothly. To enable this adaptive division, the system must determine how radiance changes over the domain of rays. This chapter presents an error bounding algorithm that characterizes how radiance varies over line space and determines whether each interpolant built approximates radiance well.

4.1 Overview

The error bounding algorithm described in this chapter is used to determine when an interpolant is valid; an interpolant is valid if it can be used to interpolate radiance sufficiently well over the associated linetree cell. For example, if radiance changes discontinuously over a linetree cell, interpolation across the cell would result in the blurring of the sharp discontinuous edge; the corresponding interpolant is therefore invalid. When the error bounding algorithm determines that an interpolant is invalid, the ray tracer subdivides the linetree cell associated with the interpolant as described in Chapter 3.

In providing this error bounding algorithm, this thesis makes several contributions to the problem of bounding radiance interpolation error:

- It categorizes interpolation error into two major classes: error due to discontinuities and error due to non-linear radiance variations.

- It describes the various ways in which radiance discontinuities can cause interpolation error and presents geometric techniques to conservatively identify each type of radiance discontinuity.

- It introduces a novel use of a multi-variate generalization of interval arithmetic to conservatively bound interpolation error arising from non-linear variations in radiance.

Together, these techniques provide the first complete, conservative characterization of interpolation error; importantly for the acceleration of ray tracing, the error bounds derived are accurate and can be computed efficiently.

4.1.1 Interpolant validation

First, we must consider how interpolation error can arise. The interpolant ray tracer uses quadrilinear interpolation to approximate radiance for all rays represented by a linetree cell. Quadrilinear interpolation is accurate as long as radiance within the cell has a linear dependence on the line space coordinates (a, b, c, d). Interpolation error arises only if there is a non-linear variation in the radiance over the cell.

Interpolation error can arise in two ways:

- Interpolation over a radiance discontinuity (for example, due to shadows, occluding objects or total internal reflection).

- Interpolation over regions of line space in which radiance varies non-linearly (for example, due to diffuse or specular peaks).

Discontinuities are treated as a special case because the human eye is sensitive to discontinuous changes in radiance [Gla95]. Therefore, interpolating across a radiance discontinuity is perceived as erroneous by the human eye, even if the resultant interpolation error is less than ϵ.

Thus, the error bounding algorithm receives as input the sixteen radiance samples of the extremal rays of a linetree cell, and determines if the interpolant is valid by answering the following two questions conservatively:

1. Does radiance change discontinuously *anywhere* in the region of line space represented by the linetree cell?

2. If radiance does not change discontinuously, is the quadrilinearly interpolated radiance within ϵ of the radiance computed by the base ray tracer for *every* ray represented by that linetree cell?

If either answer is no, the interpolant is invalid, and the linetree cell is subdivided.

This chapter presents techniques to identify both discontinuities and non-linearities. Together, these techniques completely specify the error bounding algorithm.

58

4.1.2 Assumptions and limitations

The error bounding algorithm is based on certain assumptions about the scene being rendered and the rendering model. These assumptions affect the difficulty of bounding error in various ways. The assumptions are as follows:

1. The scene is composed of convex objects: spheres, cubes, polygons, cylinders and cones and the CSG union and intersection of these primitives [Rot82] are supported. This assumption simplifies the detection of certains kinds of discontinuities; for example, discontinuities arising from shadow edges.

2. The base ray tracer implements a classical Whitted ray tracer, sampling the reflected and refracted directions. The local shading model used is the Ward isotropic shading model [War92].

3. Textures for the diffuse color of a surface are supported.

4. Lights are assumed to be either infinite light sources, local light sources, or spotlights.

Each of these assumptions imposes limitations on the system; some of these limitations are easily addressed, while others are areas for future research. Note that the interpolation mechanism described in Chapter 3 is applicable to a broader range of scenes and rendering models; only the error bounding algorithm, described in this chapter, is tied closely to this set of assumptions. Section 4.5 discusses extensions to address these limitations.

The rest of this chapter is organized as follows. Section 4.2 presents a taxonomy of the different types of radiance discontinuities and shows how to detect and avoid interpolation over each type of discontinuity. Section 4.3 describes how interpolation error can arise from non-linear variations in radiance and introduces the use of multi-variate linear interval arithmetic to bound interpolation error over non-linear radiance variations. Section 4.4 presents various optimizations. Section 4.5 discusses extensions to the error bounding algorithm to support more complex scenes and rendering models. Finally, Section 4.6 discusses alternatives to bounding error.

4.2 Radiance discontinuities

Radiance discontinuities arise because the scene is composed of multiple objects that occlude and cast shadows on each other. First, this section presents the invariant that should be maintained to ensure that an interpolant does not include any discontinuities. Then, a taxonomy of the different kinds of radiance discontinuities is presented. Finally, geometric techniques to detect each possible discontinuity are presented.
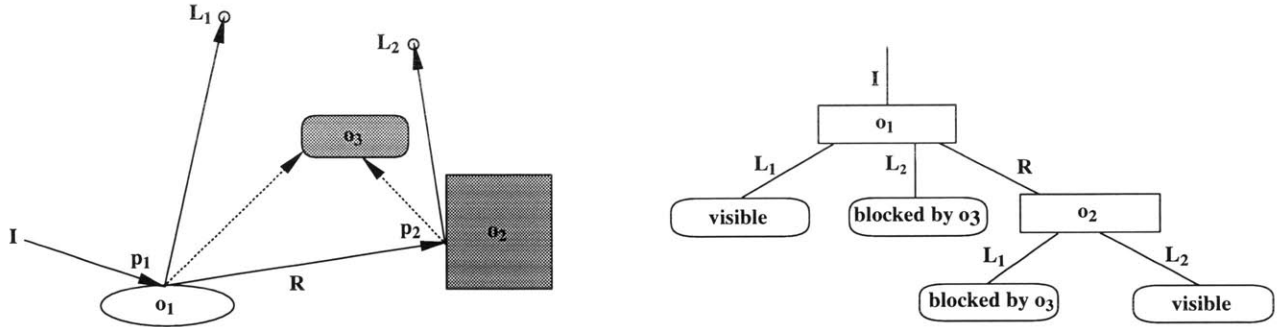
Figure 4-1: A ray **I** traced through the scene and its associated ray tree.

4.2.1 Ray trees

Ray trees [SS89] are a convenient mechanism for identifying and characterizing interpolant discontinuities. When a ray is traced through the scene, an associated ray tree can be built that records all sources of radiance that contribute to the total radiance of the ray [BDT99b, BP96, SS89]. The ray tree tracks all objects, lights, and occluders that contribute to the radiance of the ray, including both direct contributions from lights and indirect contributions through reflections and refractions.

A ray tree node associated with a ray stores the object intersected by the ray in addition to the lights and occluders visible at the point of intersection. The children of the node are pointers to the ray trees associated with the corresponding reflected and refracted rays (if they exist); these trees are computed recursively.

For example, in Figure 4-1, on the left a ray **I** is traced from the eye through the scene, and on the right, the ray tree associated with **I** is shown. The ray **I** intersects the object o_1 at the point p_1. The local shading component of radiance at p_1 is computed by shooting rays from p_1 toward the lights L_1 and L_2; L_1 is visible, while L_2 is blocked by the object o_3. Since the object o_1 is reflective, a reflected ray **R** is constructed. This ray is then traced recursively through the scene, intersecting object o_2 at point p_2. The light L_2 contributes to the local shading at p_2, but L_1 does not contribute, since L_1 is blocked by object o_3. In the ray tree (shown on the right), each edge of the ray tree represents a ray, and each internal node (shown as a rectangle) represents the intersection of the incoming ray at that node with some surface in the scene; the node stores the identity of this surface. The leaves in the ray tree (rounded rectangles) represent the sources of radiance: lights. The leaf records whether the light is self-shadowed[1], visible, or blocked by some object. The identity of each blocker is also stored in the ray tree. An edge in the ray tree from a parent to a child corresponds to some ray from the surface represented by the parent to the surface (or light)

---

[1]A light is self-shadowed by an object at some point on the object's surface if the light is not visible at that point because the object itself occludes the light. For convex objects, this can occur only if $\mathbf{N} \cdot \mathbf{L} < 0$.

60

represented by the child.

The radiance along the incoming ray of a ray tree can be expressed as a local shading term that uses the lights visible at that node, plus a weighted sum of radiance from the reflected and refracted child nodes, if any. The radiance computed at the root of the ray tree is a weighted sum of all of the local shading terms computed within the tree.

Note that a ray tree can be split into two components: a *position-independent* component that includes the object intersected by the ray, a list of every light that contributes to the radiance at that point, and a list of every occluder that blocks light; and a *position-dependent* component that includes the point of intersection of the ray, the normal at that point, and texture coordinates (if any). These two components will be referred to as the *position-independent ray tree* and the *position-dependent ray tree*, respectively.

4.2.2 Invariant for discontinuities

Let us assume that every ray represented by a linetree cell L is ray traced, and the corresponding ray trees are constructed. Of course, constructing all the ray trees for *every* ray represented by L is not feasible. But thinking about the problem in terms of ray trees gives the invariant that should be maintained to avoid interpolation across discontinuities. The following observation is crucial:

> *Radiance changes discontinuously over a linetree cell only when some rays within the cell have different position-independent ray trees.*

Therefore, to guarantee that interpolants do not erroneously interpolate over a radiance discontinuity, the error bounding algorithm must check that the position-independent ray trees for *all* rays in the 4D hypercube represented by a linetree cell are the same.

Textured surfaces are an exception to the observation above because radiance can change discontinuously across the texture. However, the argument above can be made about the *incoming* radiance at the textured surface: it changes discontinuously when the position-independent ray trees differ (see Section 4.4.3). Therefore, to allow interpolation over textured surfaces, texture coordinates are interpolated separately from incoming radiance at the textured surface.

Therefore, the invariant that should be maintained is that *the position-independent ray trees of all rays represented by L should be the same*. This is true even for textured surfaces since the texture does not affect the shape of the ray tree.
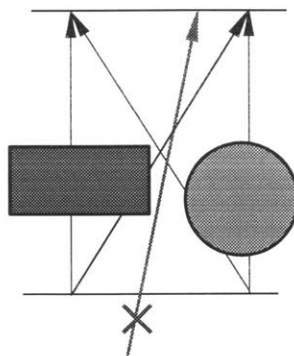
Figure 4-2: Visibility changes. Interpolation for the ray marked with the × would be erroneous.

4.2.3   A taxonomy of discontinuities

Now let us consider the different ways in which the position-independent ray trees could differ, causing radiance discontinuities.

Object geometry. Interpolation across object edges, such as the edges of a cube, could result in erroneous interpolation; this is because there is a discontinuous change in the normal of the cube at its edges. To prevent erroneous interpolation over object edges, the system treats different surfaces of a single object as different objects for the purpose of discontinuity detection.

Each object is considered to be built of a finite number of smooth (possibly non-planar) faces. For example, a cube has six faces, a cylinder has three faces, and a sphere has one face. This face index is also stored in the ray tree node and used in ray tree comparisons. Note that a single set of six linetrees, common to all the faces of an object, is built for each object. The faces are considered to be different objects only for the purpose of ray tree comparisons.

The two CSG operators supported are union and intersection. The union is treated straightforwardly by considering each component of the union as a separate object. The CSG intersection of a set of objects consists of some set of faces: each face in the CSG intersection corresponds to a face from one of the constituent objects. Therefore, the intersection is represented by this set of faces for ray tree comparisons.

Scene geometry and visibility changes. Consider a two-dimensional linetree cell L with its four extremal rays (black) as shown in Figure 4-2. The gray ray is a query ray that is represented by L. In the figure, the extremal (black) rays hit different objects while the query (gray) ray misses the objects completely. It would be incorrect to interpolate radiance for the gray ray because the ray trees associated with the extremal rays differ; i.e., the extremal rays do not all hit the same object. A simple check that catches many invalid interpolants is to compare the position-independent
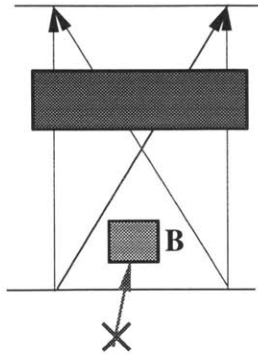
Figure 4-3: Erroneous interpolation due to occluders.
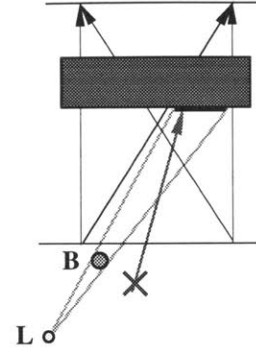
Figure 4-4: Erroneous interpolation due to shadows.

ray trees of the extremal rays. If they differ, the interpolant is invalid because it must include a discontinuity.

Ensuring that the extremal rays have the same position-independent ray trees is necessary, but not sufficient, to detect all discontinuities. For example, in Figure 4-3 the extremal rays all hit the same object, but the query ray hits an occluding object. In Figure 4-4, the extremal rays and the query ray all hit the same object, but the circle B casts a shadow on the rectangle. While the extremal rays are illuminated by the light L, the query ray is not. In each of these cases, it would be incorrect to interpolate radiance using the samples associated with the extremal rays.

There are several ways in which the position-independent ray tree of a ray can differ from the position-independent ray trees of the extremal rays. Consider an interpolant L with extremal rays $R_{00}, R_{01}, R_{10}, R_{11}$, and a query ray R. Let us assume that the error bounding algorithm has already checked that the position-independent ray trees of the extremal rays are the same. Consider the standard shading algorithm for a ray tracer, as shown in Figure 4-5. Discontinuities can only arise from conditionally executed code in the shading algorithm, or from recursive calls to the shading algorithm; the relevant lines in the shading algorithm are marked. For each of the cases, only one level of the ray tree is considered, i.e., a ray R intersecting a surface S and being lit (or blocked) by some set of lights. The reflected and refracted components of the ray trees are also ray trees and are considered recursively.

Discontinuities may be introduced at each of the lines numbered from 1 to 6. Each case can be described intuitively:

1. Ray R intersects a different object than the extremal rays.

2. A light L is self-shadowed for the extremal rays R_{ij}, but not for R; or conversely, light L is self-shadowed for R, but not for the extremal rays R_{ij}.

Radiance Trace(Ray I) { // *returns the radiance along ray I*
(1)   (p,o,N) = Intersect(I, S) // *I intersects object o in scene S at point p, with normal N at p*
       return Shade(I,o,p,N);
}

Radiance Shade(Ray I, Object o, Point p, Vector N) {
       // *o is object visible along ray I*
       // *p is point of intersection, N is normal to o at p*
       Radiance r;
       // *Local shading*
       for (each light L)
(2)   **if** (!self−shadowed(L,o,p) &&
(3)   visible(L,p))
                // *determine visibility by shooting a ray from p to L*
(NL)   r += Diffuse + Specular radiance at p
       // *Global shading*
(4)   **if** (reflective(o)) { // *reflected*
           Ray R = ReflectedRay(I,N); // *build reflected ray R*
(A)   r += Trace(R);
       }
(5)   **if** (refractive(o)) { // *refracted*
           Ray T = RefractedRay(I,N) // *build refracted ray T*
(6)   **if** (!TIR(T)) r += Trace(T);
(B)   **else** {tirT = TIRray(R,N); r += Trace(tirT);}
       }
       return r;
}

Figure 4-5: Shading algorithm

3. A light L visible to the extremal rays is not visible to R; or conversely, a light L visible to R is not visible to the extremal rays.

4. The extremal rays have reflected rays while the query ray R does not, or vice-versa.

5. The extremal rays have refracted rays while the query ray R does not, or vice-versa.

6. If the surface is transparent, ray R is totally internally reflected while the extremal rays are not; or conversely, the extremal rays are totally internally reflected while ray R is not.

Additionally, discontinuities can arise recursively in the component of radiance reflected from or refracted by the surface; any of the cases 1–6 may occur recursively for the reflected or refracted rays. These cases correspond to the lines marked A and B in the figure.
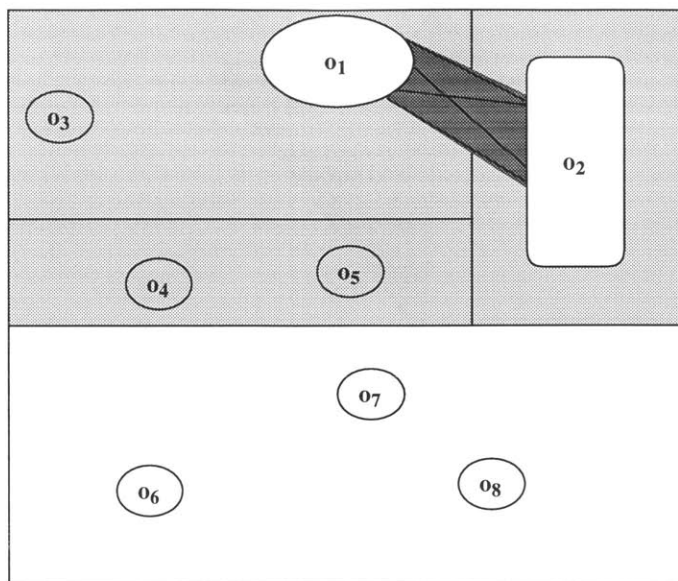
Figure 4-6: Least-common ancestor optimization for shaft culling.

4.2.4 Detecting discontinuities

The algorithm for detecting discontinuities proceeds as follows. First, all rays from the front face to the back face of the appropriate linetree cell are checked for the discontinuities described in cases 1–6. Then, if the surface is reflective, the same discontinuity detection algorithm is applied recursively to detect discontinuities in rays reflected from the surface of the object for which the interpolant is being built (case A). Refracted rays are tested similarly (case B). This recursive algorithm reduces the problem of determining discontinuities in radiance to the problem of detecting local discontinuities arising from cases 1–6.

Case 1: Occluders. There could be occluding objects between the extremal rays, as shown in Figure 4-3, so that ray R intersects a different object than the extremal rays.

These occluders are detected using a variant of shaft-culling [HW91, TBD96]. Bounding boxes are constructed around the source of the extremal rays and the destination of the extremal rays. A shaft is constructed between these two bounding boxes, and the bounding boxes of all objects in the scene are intersected with this shaft. If the bounding box of any object intersects the shaft, that object is a potential occluder, and the interpolant is invalid. If no objects intersect the shaft, the interpolant is valid.

Intersecting each shaft with all the objects in the scene could be expensive. Since the scene is augmented with a kd-tree to accelerate ray-scene intersections [Gla89] (see Chapter 7), the following optimization is used to decrease the cost of the shaft cull: the algorithm finds the least

65
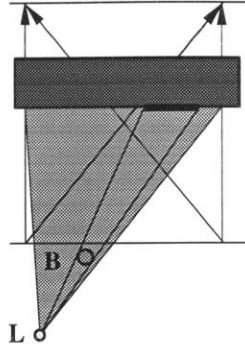
Figure 4-7: Shaft-culling for shadows. The shaft from the light to the surface of the object is checked for occluders that could cast a shadow on the object.

common ancestor in the kd-tree of the source and destination objects of the shaft. The shaft is then propagated recursively down from the least common ancestor to the leaves, ignoring subtrees that do not intersect the shaft. Objects in the leaves are then tested individually against the shaft. As before, if any object intersects the shaft, the interpolant is invalid. Note that this test is conservative because the shaft may intersect some object bounding box without actually intersecting the object.

This least common ancestor optimization is depicted in Figure 4-6. In the figure, the shaft is the dark gray shaded region between objects o_1 and o_2. The least common ancestor of objects o_1 and o_2 in the kd-tree is indicated by the light gray shaded rectangle. Since the least common ancestor does not include objects o_6, o_7 and o_8, no shaft cull is needed against that entire part of the scene. The shaft is propagated down from the least common ancestor. Since the kd-tree node that includes object o_4 and o_5 does not intersect the shaft, that sub-tree of the kd-tree is pruned away. Only object o_3 is tested against the shaft.

Case 2: Self-shadowing. A discontinuity can arise if the extremal rays are self-shadowed (for each extremal ray e, $\mathbf{N}_e \cdot \mathbf{L}_e < 0$), but some internal ray $\mathbf{R}$ is not. In Section 4.3, it is shown that linear interval arithmetic can be used to bound the range of $\mathbf{N} \cdot \mathbf{L}$. If the range includes the value 0, the interpolant is invalid. Conversely, a discontinuity occurs if the extremal rays are not self-shadowed, but an internal ray $\mathbf{R}$ is. The same interval test prevents this condition as well.

Case 3: Shadows. If the light L is visible to the extremal rays it could be blocked for some query ray $\mathbf{R}$ by some blocker B, as shown in Figure 4-4. This condition is detected by shaft-culling the light against the surface for which the interpolant is constructed as shown in Figure 4-7. A bounding box is constructed around the points of intersection of all rays represented by the interpolant. This bounding box p is constructed by using the interval arithmetic techniques described in Section 4.3. A shaft, shown in light gray in the figure, is constructed from each visible

66
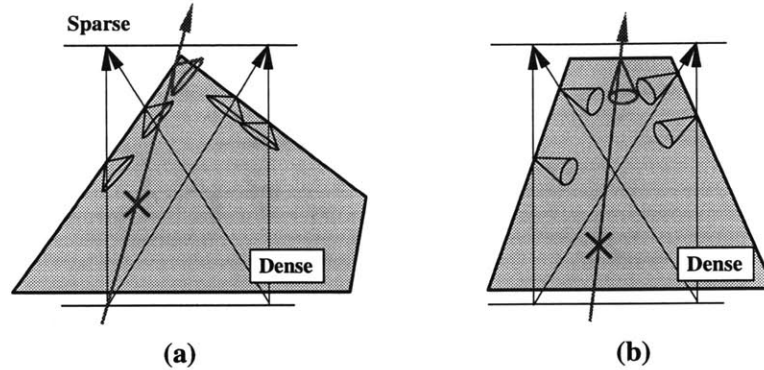
Figure 4-8: Erroneous interpolation due to total internal reflection.

light to the bounding box p. If any objects lie inside the shaft, the interpolant is invalidated. Note that this test is conservative since the shaft cull is conservative. As in Case 1, the least common ancestor of the light and the bounding box can be used to optimize the performance of the shaft-cull.

A radiance discontinuity could result from a shadow if the light L is not visible to the extremal rays, but is visible to $\mathbf{R}$. This situation can be detected by ensuring that all rays from p to the light L are shadowed by the same blocker b. Because b is convex, it is only necessary to test the rays from the corners of p to the light. If the corner rays are all blocked by b, every ray $\mathbf{R}$ that intersects the surface at some point subsumed by the extremal rays, has a light vector L_R that is also blocked by b.

Case 4: Reflective surface. A discontinuity results if the extremal rays hit a reflective object, while $\mathbf{R}$ does not, or vice-versa. The ray-tree equality test of Case 1 already guarantees that the extremal rays and $\mathbf{R}$ all hit the same object o. The system assumes that surfaces are made of homogeneous materials; i.e., the reflective properties of any object in the scene do not vary over the surface. Therefore, all the rays intersecting o are reflected or not, and this discontinuity cannot arise.

Case 5: Refractive surface. The extremal rays hit a transparent object, while $\mathbf{R}$ does not, or vice-versa. Using the same argument as in Case 4, this case cannot arise.

Case 6: Total internal reflection (TIR). Figure 4-8 depicts discontinuities that arise due to total internal reflection (TIR). For a ray traversing different media, TIR occurs when the angle θ between the incident ray and normal is greater than the critical angle θ_c which is determined by the relative indices of refraction of the two media. All rays outside the TIR cone (rays with $\theta > \theta_c$) undergo total internal reflection. In Figure 4-8-(a), the extremal rays lie in the TIR cone but the query ray
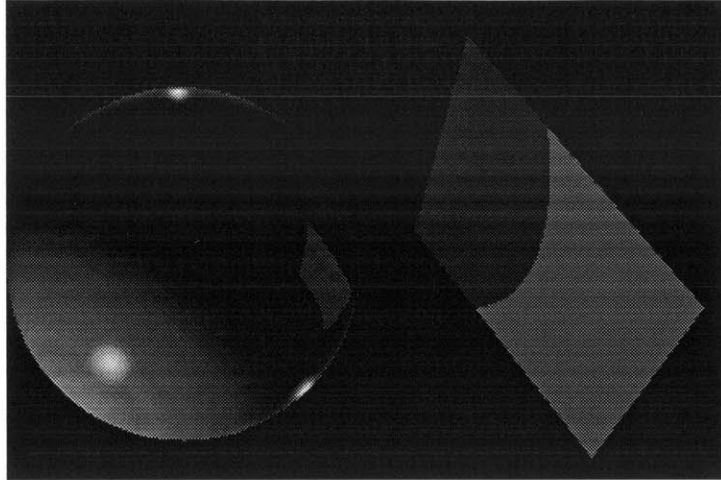
Figure 4-9: Reflection of a convex object.

does not; in Figure 4-8-(b), the extremal rays lie outside the TIR cone while the query ray lies in the cone. In both cases, interpolation would produce incorrect results [TBD96].

A conservative test for TIR is to invalidate an interpolant if its extremal ray trees include an edge representing rays traveling between different media. However, this rule prevents interpolation whenever there is refraction, which is too conservative. The main problem is that the extremal rays do not indicate whether or not a query ray could undergo TIR. Section 4.3 describes how linear interval arithmetic can be used to conservatively bound the angle θ between the normal and incident ray to a range $[\theta_-, \theta_+]$. If θ_c (the critical angle at which TIR occurs) is outside this range, the interpolant is valid: either all rays represented by the interpolant undergo TIR or none do. The error bounding algorithm uses this interval test to detect interpolation error caused by TIR.

Cases A and B: recursive reflections and refractions. Discontinuities can arise recursively by tracing reflected or refracted rays, when the discontinuities are due to the incoming reflected or refracted radiance. These discontinuities correspond to the lines marked (A) and (B) in the rendering algorithm. One simple and usually effective test for discontinuities is to compare the ray trees of the sixteen extremal rays. Most discontinuities in the incoming reflected radiance are manifested as ray trees that differ in their reflected subtrees, and similarly for refracted radiance.

Ray tree comparison is sufficient to detect all discontinuities in incoming reflected radiance for 2D rays, but not for 3D rays. To see why, consider the reflected image of a convex polygon in a spherical surface. As shown in Figure 4-9, the reflected image is not always convex; the reflected image of a straight line bends away from the center of the reflecting sphere. Now, suppose that for some linetree cell of a spherical object, the outer twelve sample rays (all the sample rays other than the long diagonal rays) happen to have intersection points that coincide with the vertices of
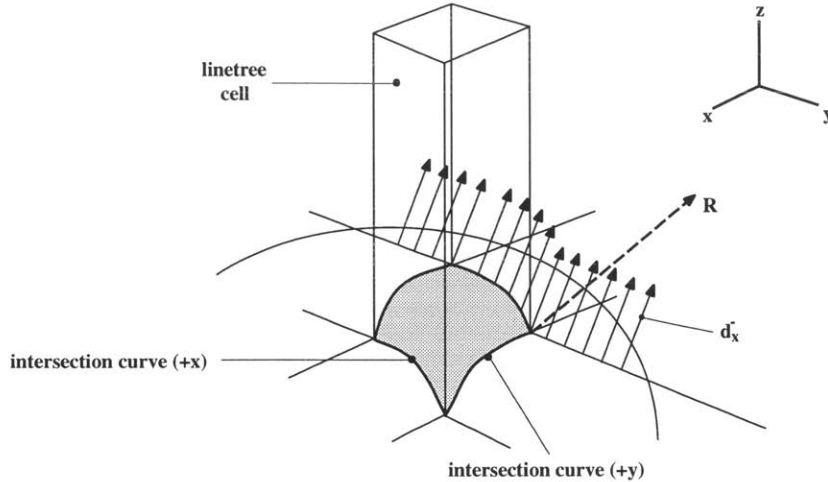
Figure 4-10: Construction of a bounding volume for reflected rays.

the image of a convex polygon P that is reflected in the sphere. A ray $\mathbf{R}$ that lies halfway between two of the sample rays might not hit P when reflected. The discontinuity created by the edge of P does affect the linetree cell, yet the ray trees of the extremal rays are identical.

To test conservatively for discontinuities in reflected radiance, it is necessary to compute a set of *test rays* leaving the reflective surface, with the property that if all the test rays strike some convex surface P, then the reflections of *all* incident rays from the linetree cell also strike P. This set of test rays comprises four rays that leave the reflective surface from the intersections of the four corner sample rays. The corner sample rays are the sample rays that connect (a_0, b_0) to (c_0, d_0), (a_0, b_1) to (c_0, d_1), (a_1, b_0) to (c_1, d_0), and (a_1, b_1) to (c_1, d_1). Because the object is convex, the intersection points of the corner sample rays are the most extremal of any of the intersection points; it is sufficient for correctness to shoot test rays only from these points.

The direction of the four test rays can be determined using the construction process depicted in Figure 4-10. In the figure, a linetree cell with a principal axis of $-\hat{z}$ intersects a reflective surface. The intersection of the linetree cell edges with the surface is a four-sided curve whose projection on the plane of the non-principal axes is a rectangle, but whose edges have some curvature in the dimension of the principal axis. The interval arithmetic techniques described in Section 4.3 are used to find the maximal and minimal values of the x and y components of reflected rays for the entire interpolant. For each of the four sides of this curve, these maximal and minimal values can be used to construct a direction vector that leans outward from the direction of the negative principal axis as much as any reflected ray produced by the linetree cell. For example, on the $+\hat{x}$ side of the linetree cell, this direction vector $\mathbf{d}_x^+$ has no y component, but an x component that is as large as that of any of the reflected rays within the cell. On the $-\hat{x}$, the direction vector $\mathbf{d}_x^-$

69

has no y component, but an x component that is at most as large as that of any reflected ray. The x components that satisfy these conditions are the maximum and minimum computed by interval analysis.

Now, imagine sliding the direction vector $\mathbf{d}_x^-$ associated with the $-\hat{x}$ side of the intersection curve along that side, generating a surface consisting of all the points in space that are in the given direction from some point along that side of the intersection curve. If the direction vector is allowed to continue past the corners of the intersection curve at the same z value as the corner it slides past, it generates an infinite surface. Repeating this process for all four sides of the curve, a set of four surfaces is obtained. Together, these four surfaces bound all reflected rays from the linetree cell.

Fortunately, the ray tracer does not need to construct an actual representation of these four rather complex bounding surfaces. Each of the four surfaces intersects the two surfaces corresponding to the adjacent sides of the intersection curve; the interface of any two of these surfaces is a ray extending outward from a corner of the intersection curve. For each of the corners of the intersection curve, there is such a ray; these rays are the four test rays. For example, consider the intersection of the $-\hat{x}$ surface depicted in the figure with the $+\hat{y}$ surface. The direction of the test ray that is the intersection of these surfaces is indicated by the dashed ray $\mathbf{R}$ in the figure. Its coordinates (x, y, z) can be computed from the coordinates for the $\mathbf{d}_x^-$ and $\mathbf{d}_y^+$ rays, which have the form $(x^-, 0, z')$ and $(0, y^+, z'')$ respectively. The following equations uniquely define the intersection ray $R = (x, y, z)$ for this corner of the intersection curve:

$$
\begin{aligned}
x^2 + y^2 + z^2 &= 1 \\
\frac{x}{x^-} &= \frac{z}{z'} \\
\frac{y}{y^+} &= \frac{z}{z''}
\end{aligned}
$$

The solution to these three equations is straightforward:

$$
\begin{aligned}
(\frac{zx^-}{z'})^2 + (\frac{zy^+}{z''})^2 + z^2 &= 1 \\
x &= \frac{zx^-}{z'} \\
y &= \frac{zy^+}{z''}
\end{aligned}
$$

70
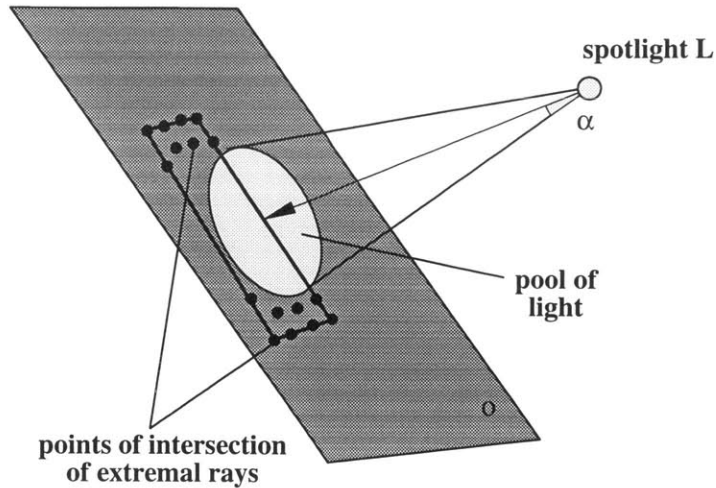
Figure 4-11: Problem with spotlights.

$$z = \left(1 + \left(\frac{x^-}{z'}\right)^2 + \left(\frac{y^+}{z''}\right)^2\right)^{-\frac{1}{2}}$$

For each of the four corners of the intersection curve, similar equations are used to compute the direction of the corresponding test ray.

Now suppose the test rays all intersect the same convex object o. Because the reflective object is convex, the object o will seal off the volume enclosed by the four bounding surfaces, and all reflected rays from the linetree cell will hit o (unless they encounter some closer occluder, which would be detected by Case 1). Therefore, the reflected ray test is conservative.

Spotlights. Spotlights are a special case of lights: spotlights have a principal direction and a cut-off angle α. A spotlight lights a surface only if the vector from the surface to the spotlight is within α of the principal direction of the spotlight. This condition is enforced by the test at line (3) in the shading algorithm in Figure 4-5, which is also the test that checks whether a light is shadowed. In fact, a spotlight is equivalent to an ordinary light source that is blocked by an object that wraps around it and contains a circular aperture. However, the discontinuity created by the α test is more difficult to detect conservatively than ordinary shadows are, because the "blocker" is not a convex object.

Figure 4-11 illustrates the problem. The spotlight **L** casts a pool of light on the plane o. If all sixteen samples lie in the pool of light, then the interpolant is valid because the pool of light is convex. If some of the sixteen samples lie inside and some outside, the interpolant will be rejected by ray tree comparison. Thus, the standard ray tree comparison usually, but not always, detects the spotlight discontinuity. More testing is required only when all sixteen samples lie outside the

71
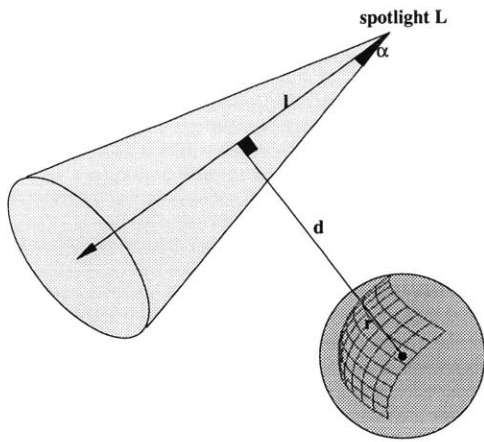
Figure 4-12: Spotlight: Test 1.
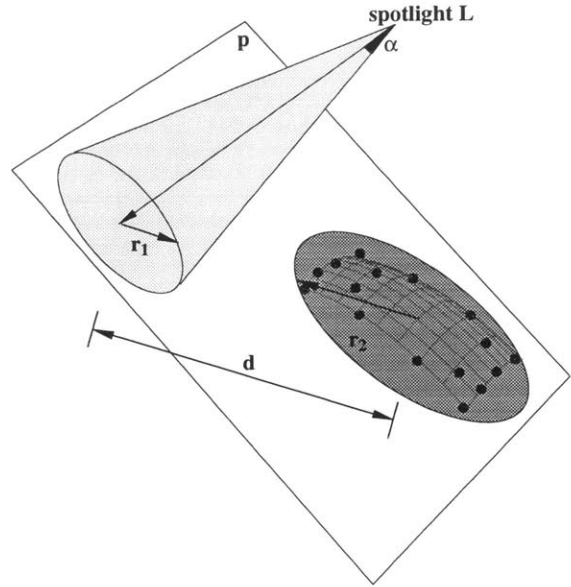
Figure 4-13: Spotlight: Test 2.
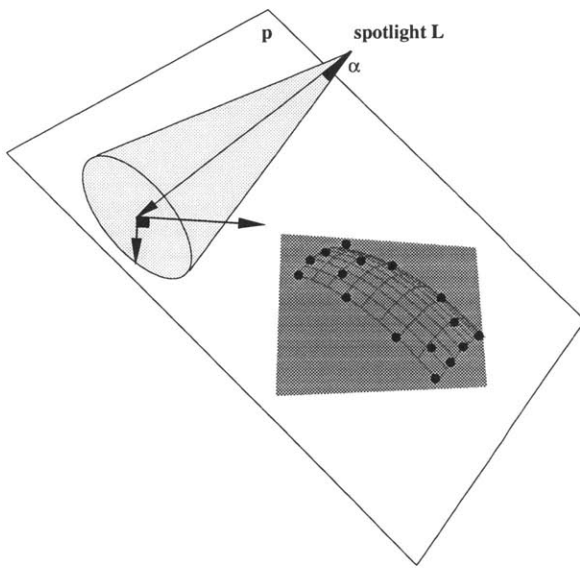
Figure 4-14: Spotlight: Test 3.
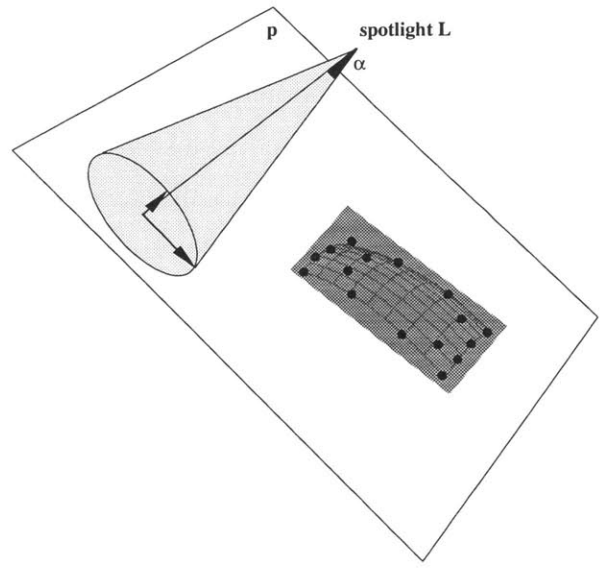
Figure 4-15: Spotlight: Test 4.

pool of light; in this case, it is possible that some interior ray lies inside the pool of light, and interpolation would yield incorrect results. The figure demonstrates how this can happen. The sixteen samples lie outside the pool of light, but some interpolated rays lie inside.

One approach that would yield correct results would be to reject all interpolants whose samples all lie outside the spotlight. However, this choice would result in invalidation of most interpolants, since most interpolants lie outside any given spotlight. A more accurate test is needed for determining when all rays in the interpolant lie outside the spotlight. The interpolant ray tracer performs

72

a series of four tests to detect this condition. If any of the tests succeed, further testing is not necessary because the interpolant is valid. If all the tests fail, the interpolant is considered invalid. The ray tracer performs these tests in the order given below—from least expensive to most expensive, and correspondingly, from most conservative to most accurate.

Test 1: The spotlight can be considered as an infinite cone in 3D. When an interpolant is built, a sphere including all the points of intersection of the extremal rays is constructed, centered on the center of mass of these points, as shown in Figure 4-12. A test that the cone and the sphere do not intersect can be done quickly; the test is that $d > r\cos\alpha + l\tan\alpha$ [Ama84]. If the sphere and cone do not intersect each other, the interpolant is valid. Otherwise, more testing is required.

Test 2: Test 1 is conservative because the sphere enclosing the intersection points can be quite large. A more precise test is used when Test 1 fails. The sixteen points of intersection are projected onto a plane perpendicular to the principal direction of the spotlight, as shown in Figure 4-13. The spotlight casts a perfectly circular region of light on this plane, with some radius r_1. A circle with some radius r_2 is constructed that contains the sixteen projected points. If $d > (r_1 + r_2)$, there is no overlap between the spotlight's pool of light and the interpolant, and the interpolant is valid.

Test 3: Consider the case where the projected points lie along a thin long rectangle; the circle that contains all the points can be too conservative. Therefore, if Test 2 fails, a two-dimensional coordinate system is set up for the plane constructed in Test 2. The origin of this coordinate system is at the point where the principal direction of the spotlight intersects the plane, and the spotlight's light is a circle with radius r_1 around this origin. The projected points are translated into this coordinate system and a bounding rectangle is constructed for the translated points as shown in Figure 4-14. If the bounding rectangle does not intersect the spotlight's circle, the interpolant is valid.

Test 4: The size of the bounding rectangle in Test 3 depends on the axes of the new coordinate system; therefore, Test 3 might fail because a suboptimal bounding rectangle is computed. Test 4 addresses that problem by computing a new coordinate system with the same origin, but different axes, to give a tight bounding rectangle around the projected points as shown in Figure 4-15. This new coordinate system minimizes the average square distance of the projected points from one of the new axes; its basis vectors are computed by diagonalizing the 2×2 inertia tensor for the projected points [LL76]. While Test 4 is more expensive than

Test 3, it produces a tighter bounding rectangle for the points, as can be seen in Figure 4-15. The same intersection test as in Test 3 is performed again with the new bounding rectangle.

The most accurate test would be to compute the convex hull of the projected points in the plane and test whether the convex hull intersects the circle. This test would be more expensive and complex than Test 4, and seems unlikely to improve accuracy substantially.

4.3 Non-linear radiance variations

The previous section has shown how the various sources of discontinuities in an interpolant can be detected conservatively. Once discontinuities are detected, the only remaining source of interpolation error is the computation of the local diffuse and shading component itself (indicated as NL in the shading algorithm shown in Figure 4-5). Quadrilinear interpolation approximates radiance well in most regions of line space that are free of discontinuities, but it is not accurate where radiance varies in a significantly non-linear fashion; for example, at specular highlights and diffuse peaks.

This section shows how a generalized interval arithmetic can be used to conservatively and tightly bound the deviation between interpolated radiance and base radiance for all rays represented by a linetree cell (where base radiance is the radiance computed by the base ray tracer).

4.3.1 Motivation

Radiance can vary non-linearly across a surface; this effect is particularly noticeable at radiance peaks such as specular highlights and diffuse highlights. If interpolation is performed without testing for these non-linear radiance variations, images will have visual artifacts like those shown in Figure 4-16. On the top row of the figure, images depict a specular highlight for a shiny sphere and a diffuse highlight for a plane. The bottom row of the figure shows images in which the ray tracer does not correctly identify the non-linear radiance variations, and the specular and diffuse highlights are rendered incorrectly.

The reason that interpolation error can arise is depicted in Figure 4-17 for the case of diffuse radiance in two dimensions. Similar scenarios can be constructed for specular radiance. In the figure, the incoming eye ray R strikes the surface at the diffuse radiance peak, because the normal at that point on the surface points directly at the light source, and diffuse radiance is proportional to N · L. Now, consider the four intersection points of the sample rays of the linetree cell containing the incoming eye ray. None of the surface normals at these intersection points are directed at the light. Therefore, bilinear interpolation across this linetree cell will result in the eye ray being

74
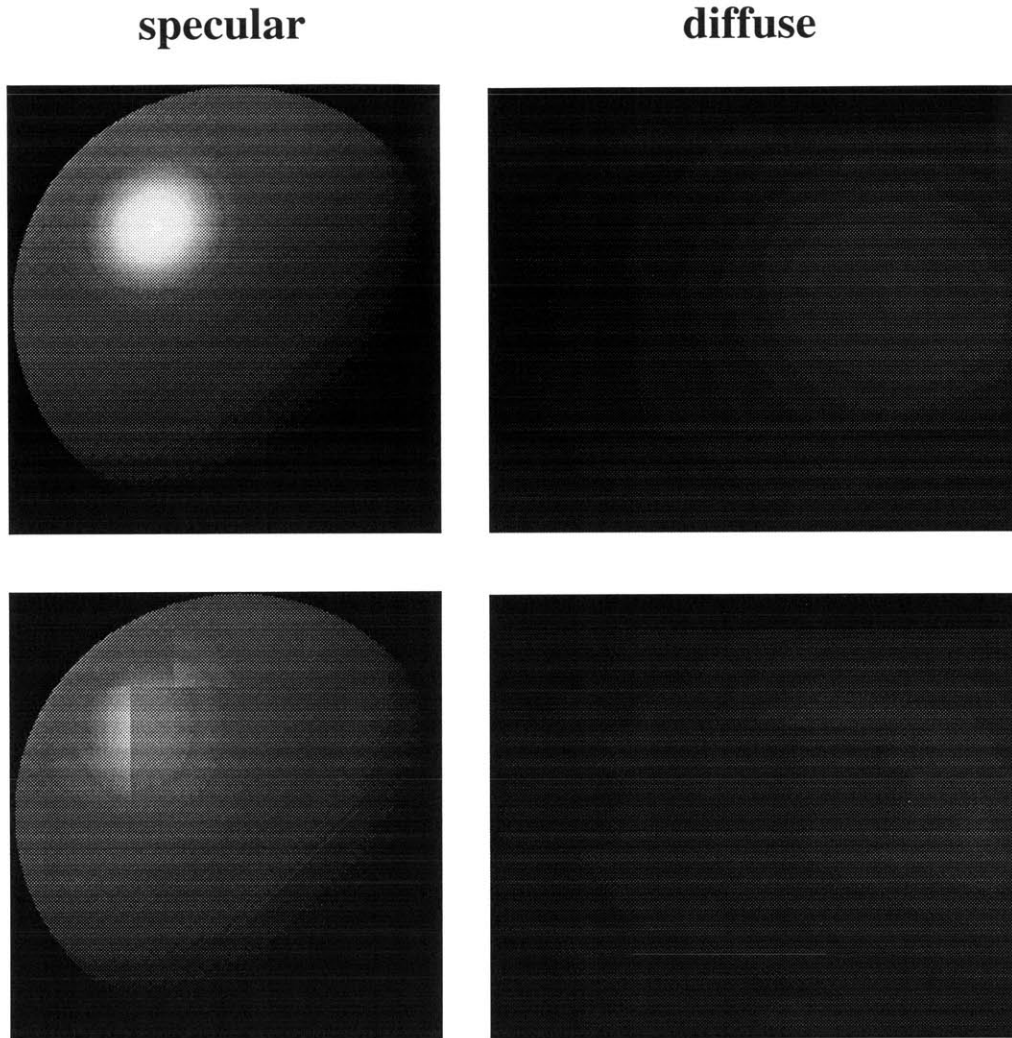
specular　　　　　　　　**diffuse**

Figure 4-16: Non-linear radiance variations. The top row shows specular and diffuse highlights for a shiny sphere and a red plane. The bottom row shows erroneous interpolation that would result if the non-linear variations in radiance are not detected.

assigned a radiance value that is too small: the diffuse peak will not appear in the image.

4.3.2　Local shading model

In general, non-linear radiance variations other than discontinuities arise from the diffuse and specular radiance computed by the local shading model. The local shading model used by the interpolant ray tracer is the Ward isotropic model [War92]. Given an incident ray **I** (Figure 4-18) that intersects an object at a point $\vec{p}$, the diffuse radiance for that ray in the Ward model is
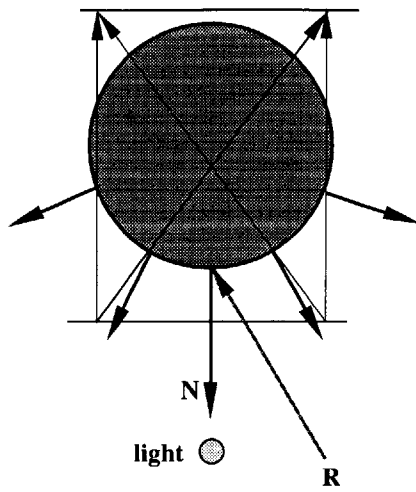
Figure 4-17: Erroneous interpolation across diffuse peak.
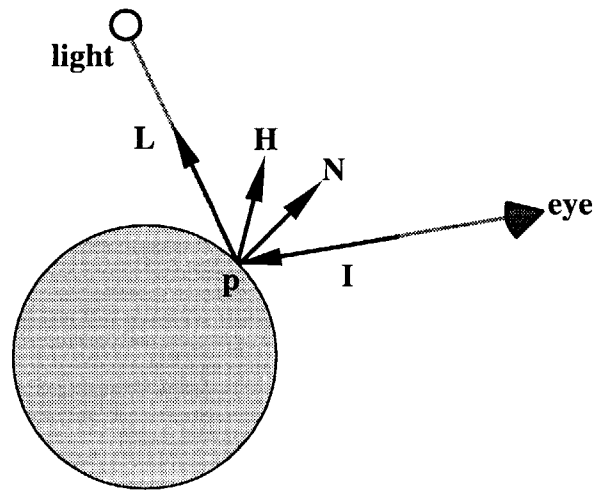
Figure 4-18: Ray geometry.

$$R_d = \rho_d(\mathbf{N} \cdot \mathbf{L}) \tag{4.1}$$

and the specular radiance is

$$R_s = \frac{\rho_s}{4\sigma^2} e^{\frac{-\tan^2 \alpha}{\sigma^2}} \sqrt{\frac{\mathbf{N} \cdot \mathbf{L}}{\mathbf{N} \cdot (-\mathbf{I})}} \tag{4.2}$$

where

- $\mathbf{N}$ is the normal to the surface at $\vec{p}$,

- **L** is the vector to the light source at $\vec{p}$,

- **I** is the incident ray direction,

- **H** is the half-vector (**H** $= \frac{\mathbf{L} - \mathbf{I}}{||\mathbf{L} - \mathbf{I}||}$) [FvD82] (**H** represents the normal direction that would reflect the light along the incident ray),

- α is the angle between **N** and **H**,

- ρ_d, ρ_s are the diffuse and specular coefficients of the surface respectively, and

- σ is a measure of surface roughness.

For an infinite light source, the light vector **L** is independent of the point of intersection $\vec{p}$ and is given as **L** $= (l_x, l_y, l_z)$, where $l_x^2 + l_y^2 + l_z^2 = 1$. For a local light source, the definition of **L** is **L** $= \frac{\mathbf{L}_p - \vec{p}}{||\mathbf{L}_p - \vec{p}||}$, where $\mathbf{L}_p$ is the position of the light source. Thus, **L** is not constant over the linetree cell in this case.

4.3.3 Goal: bounding interpolation error

The remainder of this section describes how the error bounding algorithm computes a conservative bound on the radiance interpolation error. Radiance is interpolated using quadrilinear interpolation, but for simplicity, linear interpolation of a one-dimensional function $f(x)$ is first considered. This treatment is then generalized to consider quadrilinear interpolation of the four-dimensional radiance function.

Let us assume that the function $f(x)$ is approximated over some domain D that is defined as $D = [x_0 - \Delta x, x_0 + \Delta x]$. Without loss of generality, the value of x_0 can be set to 0. For the purpose of bounding radiance interpolation error, the domain of the function will be the region of line space that is represented by the linetree cell for which the interpolant is being built.

Linear interpolation approximates the function $f(x)$ by the function

$$\tilde{f}(x) = \frac{1}{2}(f(\Delta x) + f(-\Delta x)) + \frac{x}{2\Delta x}(f(\Delta x) - f(-\Delta x))$$

The goal of the error bounding algorithm is to bound the maximum difference, ϵ_R, between $f(x)$ and $\tilde{f}(x)$, where

$$\epsilon_R = \max_{x \in D} |f(x) - \tilde{f}(x)| \tag{4.3}$$
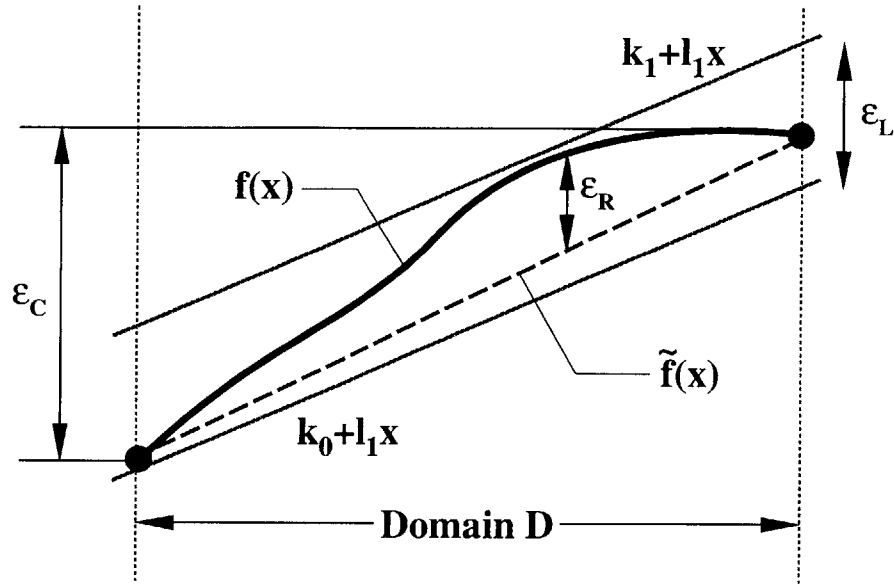
Figure 4-19: Interpolation error. The thick black curve is the base radiance function $f(x)$. The dark shaded circles at the end-points of the domain D are the samples that are interpolated, and the dotted line at the bottom of the curve is the interpolated radiance function $\tilde{f}(x)$. ϵ_R is the interpolation error, ϵ_C is the error computed by standard (constant) interval arithmetic, and ϵ_L is the error computed by linear interval arithmetic.

This maximum difference is shown in Figure 4-19, and is also the L_∞ distance between the functions $f(x)$ and $\tilde{f}(x)$.

4.3.4 Interval arithmetic

There are several ways in which the error term in Equation 4.3 can be computed, including interval arithmetic [Moo79], Hansen's generalized interval arithmetic [Han75] and variants [Tup96], and affine arithmetic [ACS94]. The simplest approach is to use interval arithmetic: values in a computation are replaced by intervals that are conservative representations of the sets of values that might occur at that point in the computation. Arithmetic operators and other functions are applied to and yield intervals that are conservative representations of sets of values. For example, the sum of two numbers represented by intervals $[a, b]$ and $[c, d]$ respectively is equal to $[a + c, b + d]$, because this is the smallest interval containing all possible sums of the two numbers. Similarly, $\exp([a, b]) = [\exp(a), \exp(b)]$, because the function exp monotonically increases. More complex functions can be evaluated by composing primitive operators such as these.

Interpolation error can be bounded by evaluating the radiance function $f(x)$ using interval arithmetic. The result is a bound on the minimum and maximum value of $f(x)$ over the domain of interpolation D. In this approach, the true bound, $\epsilon_R = \max_x |f(x) - \tilde{f}(x)|$, is approximated con-
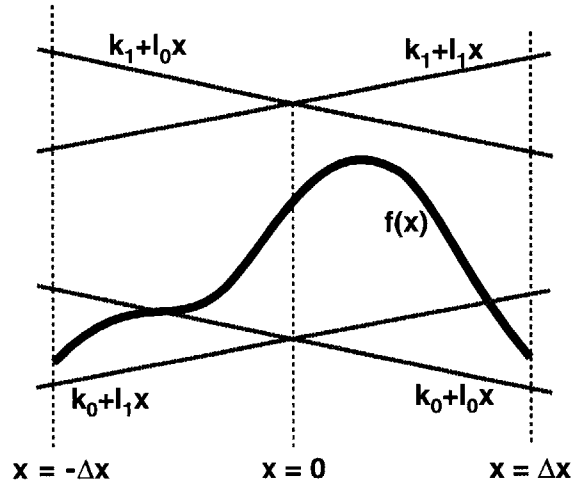
Figure 4-20: The four linear bounding functions specified by a linear interval.

servatively by the bound $\epsilon_C = |(\max_x\ f(x)) - (\min_x f(x))|$. This bound is conservative because for all x in D, $\tilde{f}(x) \in [(\min_x\ f(x)), (\max_x f(x))]$. However, this error bound is typically *too* conservative because it does not take into account the ability of linear interpolation to approximate the linear component of the function f. If standard linear interval arithmetic is used by the error bounding algorithm, it causes excessive subdivision and thus performance degradation.

4.3.5 Linear interval arithmetic

This thesis shows how *linear interval arithmetic* can be used to obtain tighter bounds on interpolation error than standard interval arithmetic does. Linear interval arithmetic generalizes standard interval arithmetic by constructing linear functions that bound f over its domain D. The insight developed here is that because the function $\tilde{f}(x)$ lies between these linear functions, the maximum difference between the bounding linear functions conservatively bounds the interpolation error, $\max_{x \in D} |f(x) - \tilde{f}(x)|$. In Figure 4-19, the bounds computed by standard and linear interval arithmetic are ϵ_C and ϵ_L respectively, while the real error bound is ϵ_R. As can be seen, linear interval arithmetic can bound error more tightly than standard interval arithmetic; it is also never worse [Han75].

Hansen's *generalized interval arithmetic* is a variety of linear interval arithmetic that was chosen over other variants of interval arithmetic because of its simplicity and ease of generalization to multiple dimensions. This thesis follows Tupper [Tup96] in use of the term "linear interval arithmetic", though it should not be confused with *linear interval analysis*, which refers to the use of standard interval arithmetic for systems of linear equations.

In Hansen's linear interval arithmetic, the value of $f(x)$ is bounded at each x by an interval
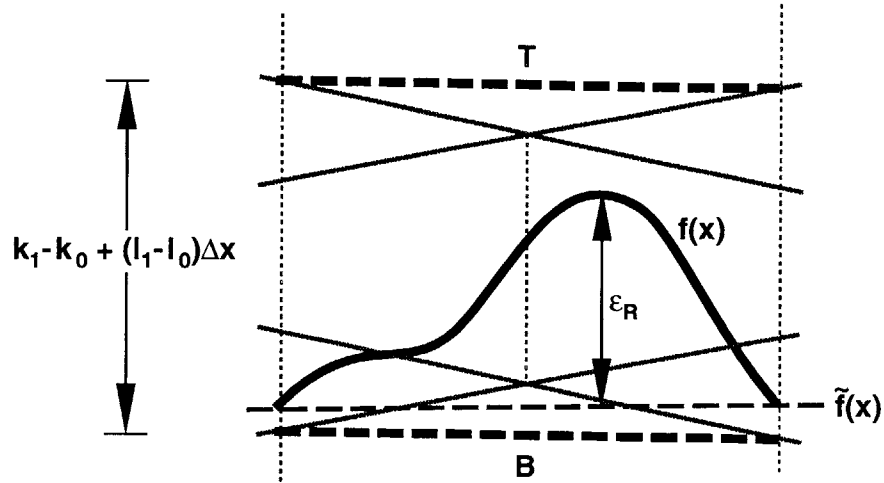
Figure 4-21: Bounding maximum interpolation error.

$F(x) = K + Lx$, where F is an interval-valued function and L, K are simple intervals $[l_0, l_1]$ and $[k_0, k_1]$. The addition of K and Lx is performed using standard interval arithmetic. The interval-valued function $F(x)$ bounds $f(x)$ if for all $x \in D$, $f(x) \in F(x)$. Expanding the definition of $F(x)$, this means that for $x \in D$, $f(x)$ lies in the interval $[k_0, k_1] + [l_0, l_1]x$, evaluated using interval arithmetic.

In general, the interval-valued function $F(x)$ represents four linear functions that together bound $f(x)$: the line $y = k_0 + l_0 x$, the line $y = k_0 + l_1 x$, the line $y = k_1 + l_0 x$, and the line $y = k_1 + l_1 x$. As x varies over its domain D, different pairs of these four lines bound $f(x)$. For $x > 0$, $f(x)$ is bounded below by $k_0 + l_0 x$ and above by $k_1 + l_1 x$. For $x < 0$, it is bounded below by $k_0 + l_1 x$ and above by $k_1 + l_0 x$. These bounding lines are depicted in Figure 4-20. Together they constrain $f(x)$ to lie within a bow-tie shape. Note that the maximum interval computed by $F(x)$ over D occurs at either the right-hand or left-hand side of the domain D.

It does not directly follow that bounding $f(x)$ bounds $\epsilon_R = \max_{x \in D} |f(x) - \tilde{f}(x)|$, because the interpolation function $\tilde{f}(x)$ is not necessarily bounded by the four lines that bound $f(x)$ as shown in Figure 4-21. However, this error bound can be proved as follows.

Claim: The maximum linear interpolation error, $\epsilon_R = \max_{x \in D} |f(x) - \tilde{f}(x)|$, is bounded by the maximum interval computed by $F(x)$ over D.

Proof: Figure 4-21 shows $f(x)$ and $\tilde{f}(x)$ where $\tilde{f}(x)$ is not bounded by the four lines that bound $f(x)$. The figure shows two additional lines T and B. The line T connects the maximum bounds on $f(x)$ at $x = -\Delta x$ and $x = \Delta x$; considered as a function of x, it is always at least as large as the four linear bounding functions over the domain D. Similarly, the line B connects the minimum bounds on $f(x)$ at the endpoints of D, and is at most as large as the linear bounding functions

80

over D. Because **T** and **B** bound the linear bounding functions, **T** and **B** also bound $f(x)$. Also, **T** and **B** bound the linear interpolation function $\tilde{f}(x)$. Therefore, the distance between $f(x)$ and $\tilde{f}(x)$ is at most as large as the distance between **T** and **B**, which is $k_1 - k_0 + \Delta x(l_1 - l_0)$ for all x. Therefore, the maximum linear interpolation error is bounded by this distance, which is the maximum interval computed by $F(x)$ over D.

This proves that the maximum interpolation error ϵ_R is bounded by the maximum interval computed by $F(x)$ over D, which occurs at either the right-hand or left-hand side of the domain D.

This approach generalizes to functions of several variables x_i. Given a function $f(x_1, \ldots, x_n)$ where each of the variables x_i varies over $[-\Delta x_i, \Delta x_i]$, a multi-variate linear interval-valued function can be constructed that bounds it. This function takes the form

$$F(x) = K + \sum_i L_i x_i$$

where K and all of the L_i are intervals. For compactness, the set of $n + 1$ intervals specifying a linear interval-valued function are called a *linear interval* for the function f that they bound. For all points $\mathbf{x} = (x_1, \ldots, x_n)$ such that $x_i \in [-\Delta x_i, \Delta x_i]$, the value of the function f is bounded by the interval produced by F: $f(\mathbf{x}) \in F(\mathbf{x})$.

The goal of the ray tracer is to bound radiance, a function of four variables: $f(a, b, c, d)$. A linear interval F that bounds radiance can be specified as a constant interval K and four intervals L_a, L_b, L_c, L_d. Just as in the single-variable case, the maximum error introduced by quadrilinear interpolation is at most as large as the size of the largest interval produced by F over its domain. This largest interval occurs at one of the sixteen corner points of the domain, so it can be computed as the size of the largest interval computed by evaluating F at the sixteen corner points of D.

Arithmetic operators on linear intervals. A linear interval that bounds the radiance function can be produced using the standard approach for interval arithmetic: the shading computation performed by the ray tracer is broken down into a series of simple operations, and these operations are performed on linear intervals rather than on ordinary scalars. This approach requires rules for propagating linear intervals through each of the operations being performed.

For example, consider the multiplication of two quantities for which linear intervals are known: the product of two functions $f(\mathbf{x})$ and $g(\mathbf{x})$. Suppose that these two functions are bounded by linear intervals $K_f + \sum L_{fi} x_i$ and $K_g + \sum L_{gi} x_i$, respectively. The product $h(\mathbf{x}) = f(\mathbf{x})g(\mathbf{x})$ is bounded

by a linear interval with components K_h and L_{hi} that are computed as follows [Han75]:

$$K_h = K_f \cdot K_g + \sum_i [0, \Delta x_i^2] L_{fi} L_{gi}$$

$$L_{hi} = K_f \cdot L_{gi} + K_g \cdot L_{fi} + L_{fi} \sum_{j \neq i} [-\Delta x_j, \Delta x_j] \cdot L_{gj}$$

Similar rules are derived for the other operations needed to compute shading: $\frac{1}{f(x)}$, $\sqrt{f(x)}$, and $e^{f(x)}$. For example, the reciprocal of a linear interval $h(x) = \frac{1}{f(x)}$ is computed as follows:

$$K_h = 1/K_f$$

$$L_{hi} = \frac{-L_{fi}}{K_f \cdot (K_f + \sum_j [-\Delta x_j, \Delta x_j] L_{fj})}$$

General functions on linear intervals. Hansen's approach to more general functions such as e^x is to use the first-order Taylor expansion of the function to generate a rule for propagating linear intervals. The error bounding algorithm presented here improves on this approach by using second-order Taylor expansions that result in tighter error bounds.

According to Taylor's theorem [DB69], when n terms of the Taylor series are used to approximate $f(x)$ over the domain $D = [-\Delta x, \Delta x]$, the remainder R_n is the error that results from using this truncated approximation:

$$\forall_{x \in D} \exists_{\xi \in D} \quad f(x) = f(x_0) + f'(x_0)(x - x_0) + \ldots + f^{(n-1)}(x_0)\frac{(x - x_0)^{n-1}}{(n-1)!} + f^{(n)}(\xi)\frac{(x - x_0)^n}{n!}$$

$$R_n(x) = f^{(n)}(\xi)\frac{(x - x_0)^n}{n!}$$

For each x in the domain D, ξ is some other point in the domain D; ξ is a function of the x chosen. The same theorem generalizes to functions of several variables.

Consider the expression $f(y(\mathbf{x}))$ where $y(\mathbf{x})$ is a function of $\mathbf{x}$ and f is a scalar function. This expression is a function of $\mathbf{x}$. Assume that the function $y(\mathbf{x})$ is bounded by the linear interval $K + \sum L_i x_i$. A rule is needed for producing a linear interval for $f(y(\mathbf{x}))$. In Hansen's approach, this linear interval is computed conservatively by expanding $f(y(\mathbf{x}))$ around $\mathbf{x} = 0$ to terms linear in x_i ($n = 1$ in Taylor's theorem). For the moment, this result is presented without justification:

$$f(y(\mathbf{x})) \in f(K) + f'(Y) \sum L_i x_i$$

The expression on the right-hand side is evaluated using standard interval arithmetic. In this equation, the interval variable Y is a standard interval capturing the maximum range of the variable y:

that is, $Y = K + \sum L_i[-\Delta x_i, \Delta x_i]$. This formula leads directly to the rule for the resulting linear interval K_f, L_{fi}:

$$K_f = f(K)$$
$$L_{fi} = f'(Y)L_i$$

For example, with this rule the expression $\exp(K + Lx)$ produces a new linear interval $e^K + e^Y Lx$. Of course, exponentiation is particularly convenient for this rule because $f = f'$.

Hansen does not prove this general rule to be sound, though it can be done as follows.

Claim: The function $f(y(\mathbf{x}))$ is bounded by the linear interval

$$f(K) + f'(Y) \sum L_i x_i$$

if $y(\mathbf{x})$ is bounded by the linear interval $K + \sum L_i x_i$, and $Y = K + \sum L_i[-\Delta x_i, \Delta x_i]$.

Proof: Consider the evaluation of the function $f(y(\mathbf{x}))$ at some particular point $\mathbf{x}^*$. Because $y(\mathbf{x})$ is bounded by the linear interval $K + \sum L_i x_i$, there is some scalar $k \in K$ and $l_i \in L_i$ (for each i) such that $y(\mathbf{x}^*) = k + \sum_i l_i x_i^*$. Now, define a new function y^* that is equal to y at the point $\mathbf{x}^*$: $y^*(\mathbf{x}) = k + \sum_i l_i x_i$. To evaluate $f(y(\mathbf{x}))$ at the point $\mathbf{x} = \mathbf{x}^*$, the function $f(y^*(\mathbf{x}))$ can be evaluated at $\mathbf{x} = \mathbf{x}^*$ instead. This function $f(y^*(\mathbf{x}))$ can be expanded in a first-order Taylor series:

$$
\begin{aligned}
f(y^*(\mathbf{x})) &= f(y^*(0)) + \sum_i x_i \left. \frac{\partial f(y^*(\mathbf{x}))}{\partial x_i} \right|_{\mathbf{x}=\xi(\mathbf{x})} \\
&= f(k) + \sum_i x_i f'(y^*(\xi(\mathbf{x}))) \left. \frac{\partial y^*(\mathbf{x})}{\partial x_i} \right|_{\mathbf{x}=\xi(\mathbf{x})} \quad \text{(using the chain rule)} \\
&= f(k) + \sum_i x_i f'(y^*(\xi(\mathbf{x}))) l_i
\end{aligned}
$$

Now, observe that $k \in K$, $y^*(\xi(\mathbf{x})) \in Y$, and $l_i \in L_i$. Therefore, $f(y^*(\mathbf{x})) \in f(K) + f'(Y) \sum L_i x_i$. The interval Y effectively allows the variable ξ in Taylor's theorem to take on any value in D; this is a conservative position to take, since it assumes nothing about ξ. At the point $\mathbf{x}^*$, it is also the case that $f(y(\mathbf{x}^*)) \in K + f'(Y) \sum L_i x_i^*$. Since this is the case for any $\mathbf{x}^* \in D$, it is proved that the expression $f(y(\mathbf{x}))$ is bounded by the linear interval $K + f'(Y) \sum L_i x_i$.

Hansen's approach yields conservative intervals, but the resulting error estimates are often overly conservative because the rule expands the intervals L_{fi}. The approach presented above can

83

be extended to a second-order Taylor expansion that usually results in tighter intervals. Using reasoning similar to that for the first-order expansion, the following relation is derived:

$$f(y(\mathbf{x})) \in f(K) + f'(K) \sum L_i x_i + \sum_i \sum_j \frac{1}{2} f''(Y) L_i L_j x_i x_j$$

Note that the new terms linear in x_i are tighter than in the first-order formulation because f' is applied to K rather than to the wider interval Y. However, this result does not directly lead to a rule for computing the linear interval for $f(y)$, because the second-order terms $f''(Y) L_i L_j x_i x_j$ must be dealt with. To arrive at a linear interval, these terms must be folded into either the constant or linear terms of the linear interval. For tight bounds, it is important to fold the diagonal second-order terms $(i = j)$ into the constant term of the resulting linear interval. This approach allows the use of the tighter interval arithmetic rule for squaring a number [Moo79]. (The rule is applied to the term $(L_i x_i)^2$.) The other, non-diagonal second-order terms $(i \neq j)$ can be folded into either the constant term or the linear terms. Empirically, it seems not to make much difference which approach is taken.

The non-diagonal terms are folded into the constant term as follows:

$$
\begin{aligned}
f(y(\mathbf{x})) \in f(K) \quad &+ \quad f'(K) \sum_i L_i x_i \\
&+ \quad \frac{1}{2} f''(Y) \sum_i L_i^2 [0, \Delta x_i^2] \\
&+ \quad f''(Y) \sum_i \sum_{j<i} L_i L_j [-\Delta x_i, \Delta x_i][-\Delta x_j, \Delta x_j]
\end{aligned}
$$

Using the definition $l_i = \max(|L_i|)$, the rule for applying f to the linear interval y can be expressed in a computationally efficient form that is used by the error bounding algorithm:

$$
\begin{aligned}
K_f &= f(K) + \left[0, \frac{1}{2} \sum_i l_i^2 \Delta x_i^2\right] f''(Y) + [-1, 1] f''(Y) \sum_i \sum_{j<i} l_i l_j \Delta x_i \Delta x_j \\
L_{fi} &= f'(K) L_i
\end{aligned}
$$

Alternatively, the non-diagonal terms can be folded into the linear terms of the result by factoring out x_i and shifting the mixed term into the corresponding linear term for x_i:

$$f(y(\mathbf{x})) \in f(K) + f'(K) \sum L_i x_i + \left[0, \frac{1}{2} \sum_i \Delta l_i^2 x_i^2\right] f''(Y)$$

84

$$+ \quad \sum_i x_i \left(\frac{1}{2} f''(Y) L_i \sum_{j \neq i} L_j [-\Delta x_j, \Delta x_j] \right)$$

$$K_f \quad = \quad f(K) + \left[0, \frac{1}{2} \sum_i \Delta l_i^2 x_i^2 \right] f''(Y)$$

$$L_{fi} \quad = \quad f'(K) L_i + [-1, 1] l_i f''(Y) \sum_{j \neq i} l_j \Delta x_j$$

The application of either of these rules to the various functions used in the computation of radiance is straightforward. All that is required is standard interval arithmetic operations for the function f, and for its first and second derivatives.

4.3.6 Comparison of interval-based error bounding techniques

The rules developed in the previous section can be used to compare the various interval-based error bounding techniques. For simplicity, these rules will be compared for a function of one variable, e^y.

For example, when the second-order interval rule developed in the previous section is applied to the function $\exp(K + Lx)$, where $K = [k_0, k_1]$ and $L = [l_0, l_1]$, the resulting linear interval is

$$e^K + L^2 [0, \frac{1}{2} \Delta x^2] e^Y + e^K Lx$$

Assuming $L > 0$, the maximum interpolation error computed by the second-order rule is as follows:

$$e^{k_1} - e^{k_0} + \frac{1}{2} l_1^2 \Delta x^2 e^{k_1 + l_1 \Delta x} + \left(e^{k_1} l_1 - e^{k_0} l_0 \right) \Delta x$$

Hansen's first-order rule gives a usually less tight error bound:

$$e^{k_1} - e^{k_0} + \left(l_1 e^{k_1 + l_1 \Delta x} - l_0 e^{k_0 + l_0 \Delta x} \right) \Delta x$$

In this bound, the presence of $l_1 \Delta x$ and $l_0 \Delta x$ in the exponents that appear in the linear term often cause the error bound to become large. In the second-order linear interval, by contrast, these terms appear only in the exponents of the term multiplied by Δx^2.

The best possible error bound that could be computed is the difference between two exponential functions at $x = \Delta x$. This difference is $e^{k_1 + l_1 \Delta x} - e^{k_0 + l_0 \Delta x}$. Hansen's approach computes a first-order approximation to this error bound, and the extension developed in this thesis computes a second-order approximation. Both of these bounds are tighter than the bound computed using
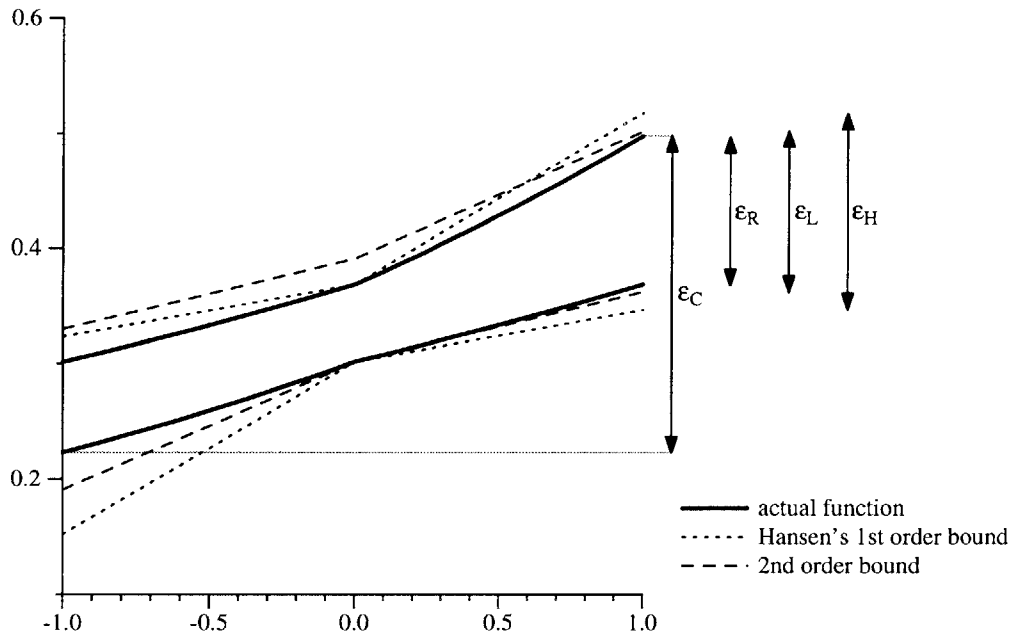
Figure 4-22: Comparison of various error bounding techniques for $\exp([-1, -1.2] + [0.2, 0.3]x)$.

constant interval arithmetic: $e^{k_1 + l_1 \Delta x} - e^{k_0 - l_0 \Delta x}$.

These bounds are plotted in Figure 4-22 for comparison. In the figure, the tightest possible bounds on the interval-valued function $\exp([-1.2, -1.0] + [0.2, 0.3]x)$ are shown, along with the bounds computed by various techniques that have been described. The bound computed by standard (constant) interval analysis is shown as ϵ_C; the tightest conservative bound on interpolation error is shown as ϵ_R. Compared to constant interval arithmetic, both the first- and second-order linear interval techniques approximate this optimum bound better. This example shows that the bound computed by the second-order technique, ϵ_L, is tighter than the bound computed by Hansen's rule, ϵ_H; in fact ϵ_L is only slightly larger than ϵ_R itself.

Note that Hansen's rule results in a linear interval that bounds the function tightly at the point $x = 0$, whereas the second-order technique does not. This occurs because the second order error terms are folded into the constant term of the interval. Alternatively, the second order terms may be folded into the linear term, resulting in a tight bound at $x = 0$ but a less tight estimate of interpolation error (it is intermediate between ϵ_L and ϵ_H).

4.3.7 Application to the shading computation

The linear interval framework developed in the previous sections can be used to derive error bounds for interpolated radiance. The total error bound for a linetree cell is computed using its associated ray trees. Since there are no radiance discontinuities in the linetree cell, the sixteen extremal

86
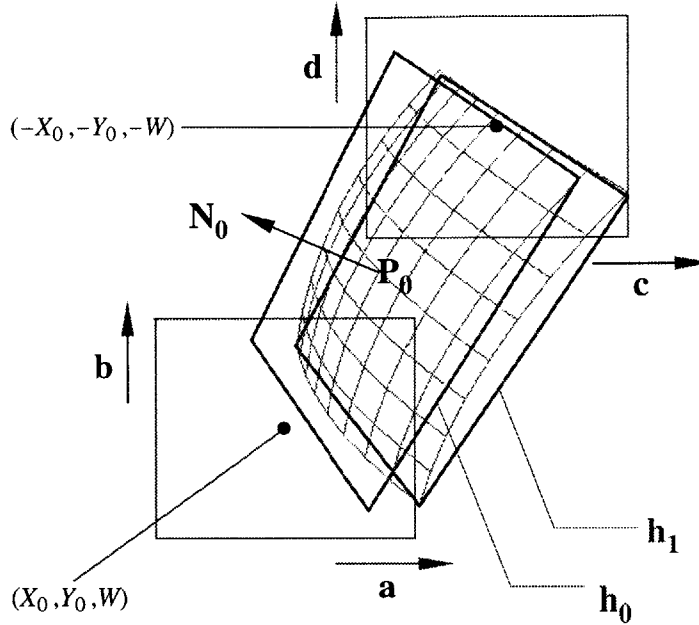
Figure 4-23: A linetree cell for a surface patch in 3D.

position-independent ray trees of the cell are the same; that is, the sixteen rays hit the same objects, are illuminated by the same lights, and are blocked by the same occluders. The radiance associated with a ray tree node is computed as a local shading term plus a weighted sum of the radiance of its children, as explained in Section 4-1. Therefore, error in the radiance of the ray tree is bounded by the error in its local shading term plus the weighted sum of the error bounds for its children, which are computed recursively. This observation allows the error bounding problem to be reduced to that of bounding error for the local shading computation.

The first step is to compute linear intervals for the various inputs used in the computation of radiance: the incident ray I, the light ray L, and the normal N. These intervals are propagated by evaluating the Ward model for diffuse and specular radiance, but using the linear interval arithmetic operations described above in place of ordinary scalar operations, to produce a linear interval for radiance. Relative or absolute interpolation error is then computed using this linear interval.

Consider a linetree cell associated with a surface for which an interpolant is being constructed (shown in Figure 4-23). Without loss of generality, the principal direction of the linetree cell is $-\hat{z}$, and the origin is located in the center of the cell. Note that the ray from the center of the front face to the center of the back face of a linetree cell is, in general, not aligned with the principal direction of the linetree cell. Therefore, to describe a general linetree cell, it is necessary to introduce parameters X_0 and Y_0 representing the x and y coordinates of the center of the front face of the

linetree cell. The linetree cell is assumed to extend along the principal direction from $-W$ to W. Because the origin is at the center of the cell the cell's front face is centered on (X_0, Y_0, W) and its back face is centered on $(-X_0, -Y_0, -W)$.

Incident ray I. Since the front and back faces of the linetree cell are at $z = W$ and $z = -W$ respectively, a ray parameterized by (a, b, c, d) represents a ray in 3D space from $(a+X_0, b+Y_0, W)$ to $(c - X_0, d - Y_0, -W)$. Therefore, the unnormalized incident ray is:

$$\mathbf{I} = (c - a - 2X_0, d - b - 2Y_0, -2W)$$

Since each component of $\mathbf{I}$ is a simple linear function of the variables (a, b, c, d), the corresponding linear intervals are computed trivially. For example, the x-component of $\mathbf{I}$ is $\mathbf{I}_x = -2X_0 + (-1)a + (-1)c$, and the linear interval representation for $\mathbf{I}_x$ is $[-2X_0, -2X_0] + [-1, -1]a + [1, 1]c$. The incident ray is normalized by computing the linear interval for $\frac{1}{\sqrt{I_x^2 + I_y^2 + I_z^2}}$, where each of the operations used—division, square, square root, and addition—are the linear interval operations defined in the previous section.

Light ray L. For an infinite light source, the light vector is $\mathbf{L} = (l_x, l_y, l_z)$, where $l_x^2 + l_y^2 + l_z^2 = 1$. The linear interval representation for the x-component of $\mathbf{L}$ is trivial: $[l_x, l_x]$. For a local light source, $\mathbf{L} = \frac{\mathbf{L}_p - \vec{p}}{\|\mathbf{L}_p - \vec{p}\|}$, where $\mathbf{L}_p$ is the position of the light source. The linear interval representation for $\mathbf{L}$ is computed from the linear interval for $\vec{p}$ using the interval operations described in the previous section. The linear interval representation for the point of intersection $\vec{p}$ is computed as below.

Point of intersection $\vec{p}$. The point of intersection $\vec{p}$ of the incident ray $\mathbf{I}$ with the surface lies on $\mathbf{I}$, and can be parameterized by its distance t from the front face:

$$\vec{p} = (X_0 + a, Y_0 + b, W) + t\,\mathbf{I} \tag{4.4}$$

A conservative linear interval for the components of $\vec{p}$ can be constructed in several ways with varying degrees of precision. First, a simple way of conservatively bounding the intersection point for any convex surface is described. Consider the ray $\mathbf{R}_0$ from the middle of the linetree's front face to the middle of its back face. $\mathbf{R}_0$ intersects the surface at the point $\mathbf{P}_0$, and the normal at that point is $\mathbf{N}_0$. Figures 4-24 and 4-23 depict this construction in 2D and 3D respectively. The plane
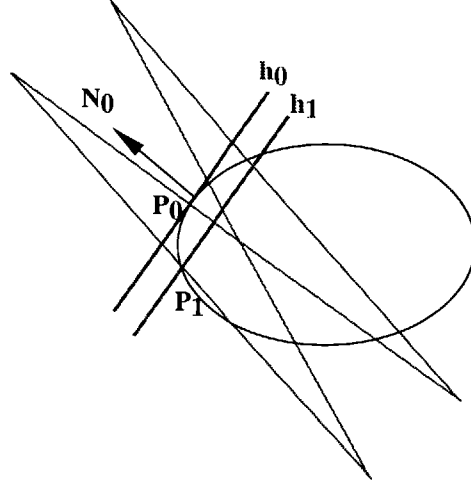
Figure 4-24: A linetree cell for a surface patch in 2D.

h_0 tangent to the surface at $\mathbf{P}_0$ is defined by the equation:

$$\mathbf{N}_0 \cdot (x, y, z) - \mathbf{P}_0 \cdot \mathbf{N}_0 = 0$$

Another plane h_1 can be constructed parallel to h_0, passing through the farthest point of intersection of any ray covered by the interpolant. Because the object is convex, the point of intersection of one of the sixteen extremal rays is guaranteed to be this farthest point. Let $\mathbf{P}_1$ be this farthest point of intersection of the sixteen extremal rays; that is, the point with the most negative projection on the surface normal $\mathbf{N}_0$. The equation of h_1 is:

$$\mathbf{N}_0 \cdot (x, y, z) - \mathbf{P}_1 \cdot \mathbf{N}_0 = 0$$

If the points of intersection of the incident ray $\mathbf{I}$ with planes h_0 and h_1 are at $t = t_{\text{near}}$ and $t = t_{\text{far}}$ respectively, then, $t \in [t_{\text{near}}, t_{\text{far}}]$, where:

$$t_{\text{near}} = \frac{\mathbf{N}_0 \cdot (P_0 - (X_0 + a, Y_0 + b, W))}{\mathbf{N}_0 \cdot \mathbf{I}}$$
$$t_{\text{far}} = \frac{\mathbf{N}_0 \cdot (P_1 - (X_0 + a, Y_0 + b, W))}{\mathbf{N}_0 \cdot \mathbf{I}}$$

These equations for t_{near} and t_{far} are converted into linear interval representations and used to compute a linear interval for the parameter t:

$$t = t_{\text{near}} + [0, 1] \cdot (t_{\text{far}} - t_{\text{near}}) \tag{4.5}$$

The linear interval for $\vec{p}$ is then computed by substituting Equation 4.5 into Equation 4.4.

There is another option for computing linear intervals for $\vec{p}$ when the point of intersection can be computed analytically. For example, consider a general quadric surface in three dimensions, defined by the following implicit equation:

$$Ax^2 + By^2 + Cz^2 + Dxy + Eyz + Fxz + Gx + Hy + Iz + J = 0 \qquad (4.6)$$

Substituting $\vec{p} = (x, y, z) = (X_0 + a, Y_0 + b, W) + t\,\mathbf{I}$, gives a quadratic in t, which can be solved to give a linear interval for $\vec{p}$.

Normal N. The vector $\mathbf{N}$ normal to the surface at the intersection point is used in the computation of diffuse and specular radiance: it appears in the terms $\mathbf{N \cdot I}$, $\mathbf{N \cdot L}$, and $\mathbf{N \cdot H}$. The surface normal at the intersection point varies across the linetree cell; it is a function of (a, b, c, d). There are various options for constructing the linear intervals that conservatively approximate $\mathbf{N}$. If little information about the surface within the linetree cell is available, the normal can be bounded using a constant interval bound. While this characterization is not precise, it will bound error conservatively.

For quadric surfaces and other surfaces that can be characterized analytically, tighter bounds can be obtained for the normal by normalizing the gradient of the implicit equation defining the surface. For the quadric surface described by Equation 4.6, the unnormalized normal vector is

$$(2Ax + Dy + Fz + G, 2By + Dx + Ez + H, 2Cz + Ey + Fx + I)$$

As described earlier, the point of intersection $\vec{p} = (x, y, z)$ can be expressed as a linear interval. This solution is substituted into the normal vector formula, allowing the normal vector to be bounded by linear intervals.

This approach can be extended to support spline patches. The surface intersection point can be bounded by the two-plane technique described above. Normals can be bounded to varying degrees of precision. A simple approach is to use constant intervals to bound the normals; a more accurate approach is to compute linear intervals for the surface parameters (u, v) using interval-based root finding [Han75]. The normal can then be computed using these parameters.

Other issues. One important technique to improve the precision of interval analysis for radiance is to treat the term $\exp(\frac{1}{\sigma^2} \tan^2 \alpha)$, which appears in the formula for specular radiance, as a primitive linear interval operator. Although $\exp$ and $\tan$ are both functions that tend to amplify error, this term computes a Gaussian function over $\tan \alpha$, and Gaussians are well-behaved regardless of the domain of evaluation. A primitive linear interval operator can exploit this property of a Gaussian

function.

Because α is the angle between the vectors $\mathbf{N}$ and $\mathbf{H}$, this term can be evaluated more simply by using the following equality:

$$\tan^2\alpha = 1 - \frac{1}{(\mathbf{N}\cdot\mathbf{H})^2}$$

For this reason, a new linear interval operator is added that computes the function $\exp(\frac{1}{\sigma^2}(1-\frac{1}{x^2}))$, which is applied in the computation of radiance with $x = \mathbf{N}\cdot\mathbf{H}$. The linear interval rule for this function is obtained using the second-order Taylor expansion technique described in Section 4.3.3.

This approach yields a much tighter error bound than simple composition of the linear interval rules for exponentiation and division does. Without this optimization, the error bound often diverges even for small linetree cells, preventing interpolation. Thus, this optimization is crucial for good performance.

4.3.8 Error refinement

Figures 4-25 and 4-26 demonstrate the error refinement process for a specular sphere and a diffuse plane. The top row of each figure shows the sphere and plane rendered without testing for non-linearity; visible artifacts can be seen around the specular and diffuse highlights. The bottom row shows the sphere and plane rendered with non-linearity detection enabled and $\epsilon = 0.2$ and 0.1 respectively. The system automatically detects the need for refinement around highlights and refines interpolants that exceed the user-specified error bound. The image quality improves (bottom row) and the linetrees are increasingly subdivided, as shown in the linetree visualization on the right. Figure 4-27 shows a more complex scene containing many primitives (described in Section 7). Non-linearity detection substantially reduces error and eliminates visual artifacts (shown in the bottom row). The difference images in the right column show the error in interpolated radiance for the images on the left. Because this error is subtle, the difference images have been scaled by a factor of 4 for the purpose of visualization.

An interesting observation is that the error intervals can be used to subdivide linetree cells more effectively. The error bound computed for an interpolant specifies intervals for each of the four axes; the axes with larger intervals (that is, more error) are subdivided preferentially. This *error-driven subdivision* is discussed further in the next section.

Figure 4-28 shows the actual and interpolated radiance for one scan-line of the image in Figure 4-26; Figure 4-29 depicts actual and bounded error for that scan-line. The scan-line passes through the diffuse peak of that image. The x-axis represents the pixels of the scan-line, and the y-axis measures error in radiance. The image was generated with a user-specified error of 0.1, as
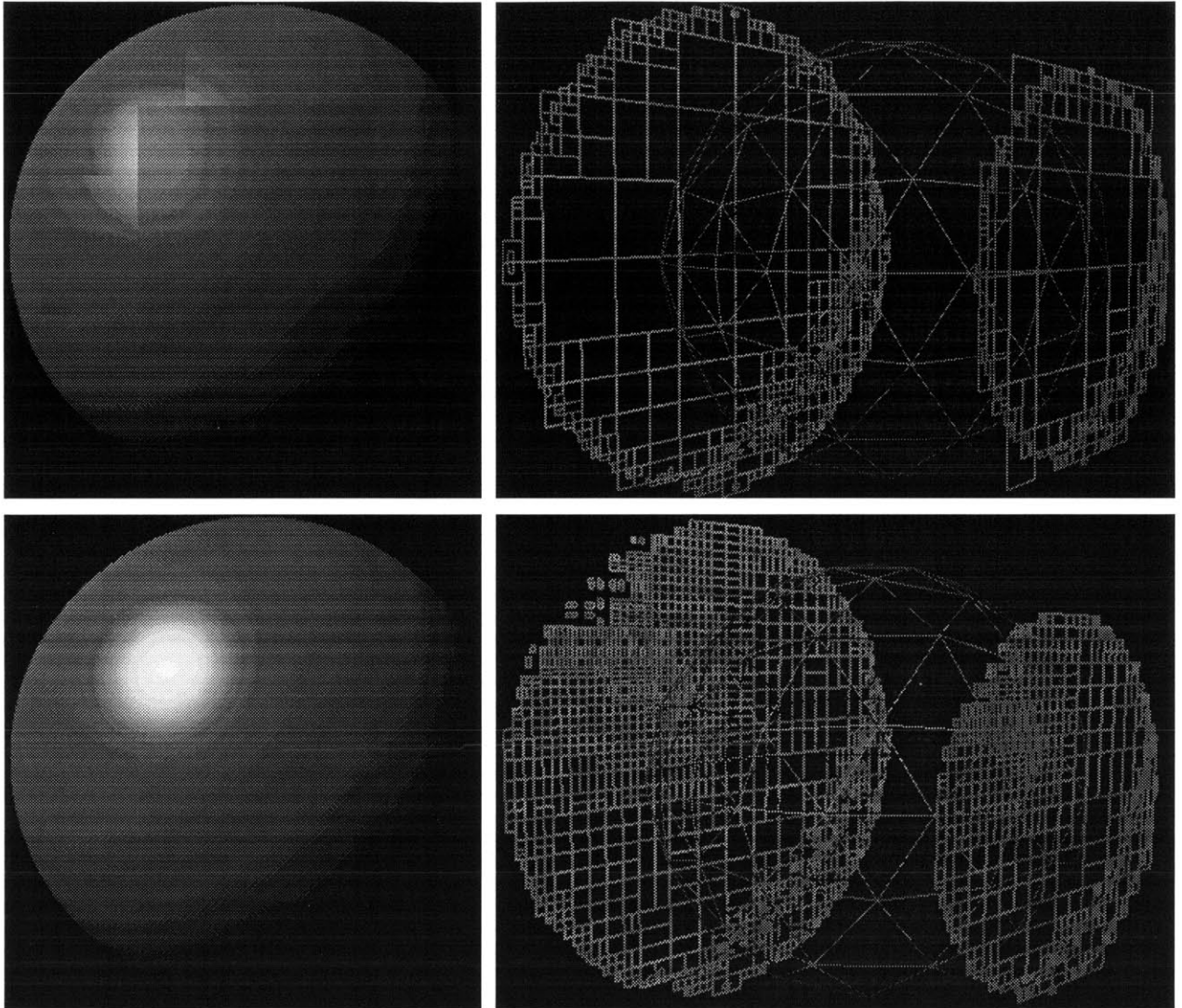
Figure 4-25: **Error refinement for a specular highlight**. A visualization of the front (blue) and back (pink) faces of the sphere's linetrees is shown on the right (the eye is off-screen to the right). Notice the error-driven adaptive subdivision along the silhouette and at the specular highlight. Top row: without non-linearity detection. Bottom row: with non-linearity detection and $\epsilon = 0.2$.

shown by the horizontal dashed line in the figure. The black trace is the actual error for each pixel in the scan-line, computed as the difference between interpolated and base radiance. The solid gray trace is the error bound computed by linear interval analysis for the interpolants contributing to the corresponding pixels in the scan-line. The dotted gray trace is the error bound computed by constant interval analysis. Since each linetree cell contributes to multiple consecutive pixels, both the linear and constant interval traces are piece-wise constant.

The graph illustrates two interesting facts:

- both linear and constant interval analysis conservatively bound error for the pixels; and
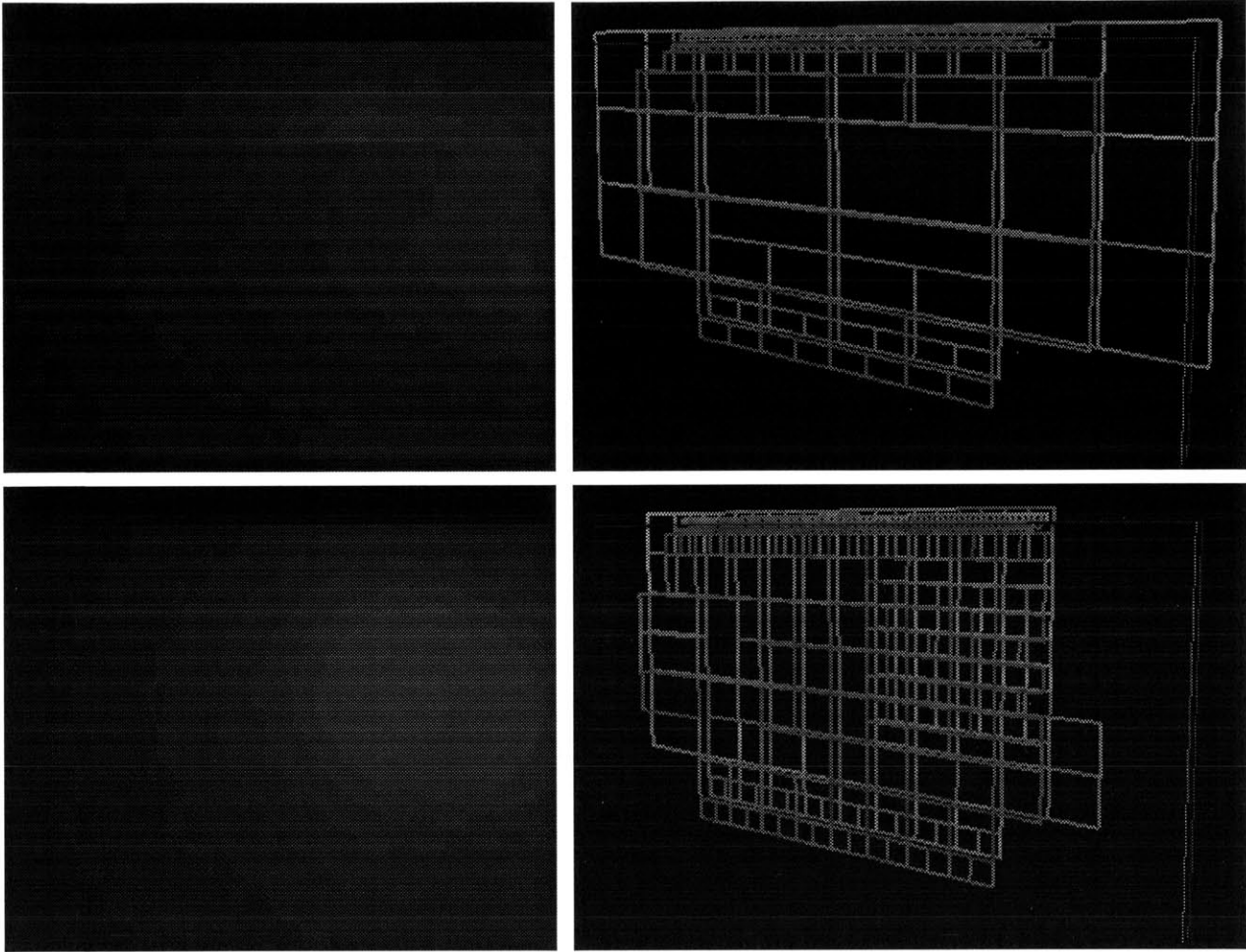
Figure 4-26: **Error refinement for a diffuse highlight**. A visualization of the front (blue) and back (pink) faces of the plane's linetrees is shown on the right (the eye is off-screen to the left). Notice the error-driven adaptive subdivision along the silhouette and at the diffuse highlight. Top row: without non-linearity detection. Bottom row: with non-linearity detection and $\epsilon = 0.1$.

- linear interval analysis computes tighter error bounds than constant interval analysis.

Several factors make linear interval error bounds more conservative than necessary:

- The error bound is computed for the entire linetree cell, whereas any scan-line is a single slice through the linetree cell and usually does not encounter the point of worst error in the interpolant.

- The bound is computed assuming simple linear interpolation, but the actual interpolation technique is quadrilinear interpolation, which interpolates with less error.

- Linear interval analysis is inherently conservative.
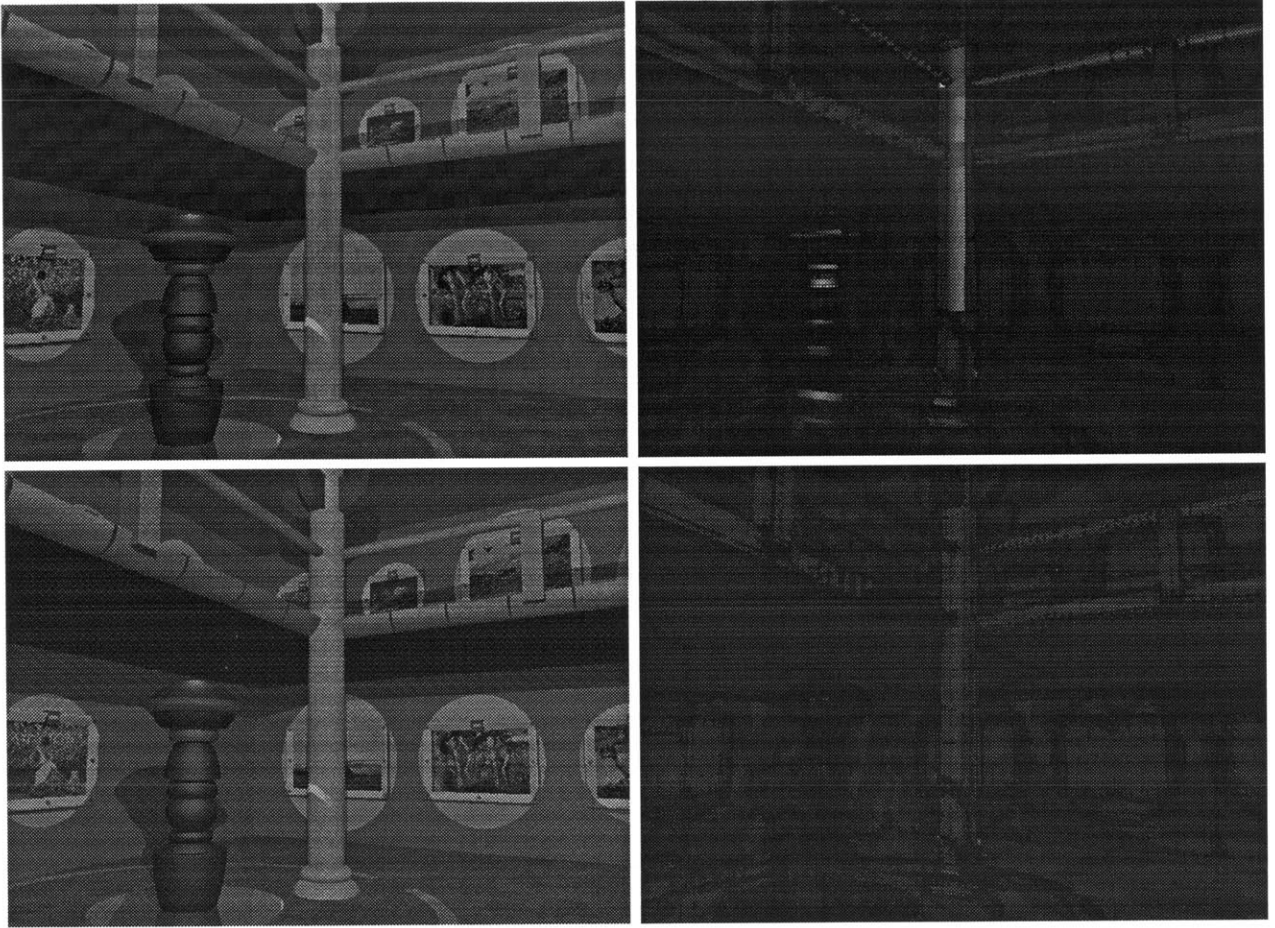
Figure 4-27: **Error refinement for the museum scene**. Top row: without non-linearity detection. Bottom row: with non-linearity detection and $\epsilon = 0.5$. Right column: scaled difference images.

4.4 Optimizations

This section presents some important performance optimizations and features of the system.

4.4.1 Error-driven subdivision

The error analysis presented in the previous section suggests that uniformly subdividing a linetree cell along all four axes is too aggressive (as mentioned in Chapter 3). The error bounding algorithm has information about how the radiance function varies over the linetree cell; this information can be used to drive adaptive subdivision.

The interpolant ray tracer implements a four-way split algorithm that splits each linetree cell into four children, using the error bounding algorithm to guide subdivision. The split algorithm uses the information about the sixteen ray trees associated with the interpolant to subdivide ei-
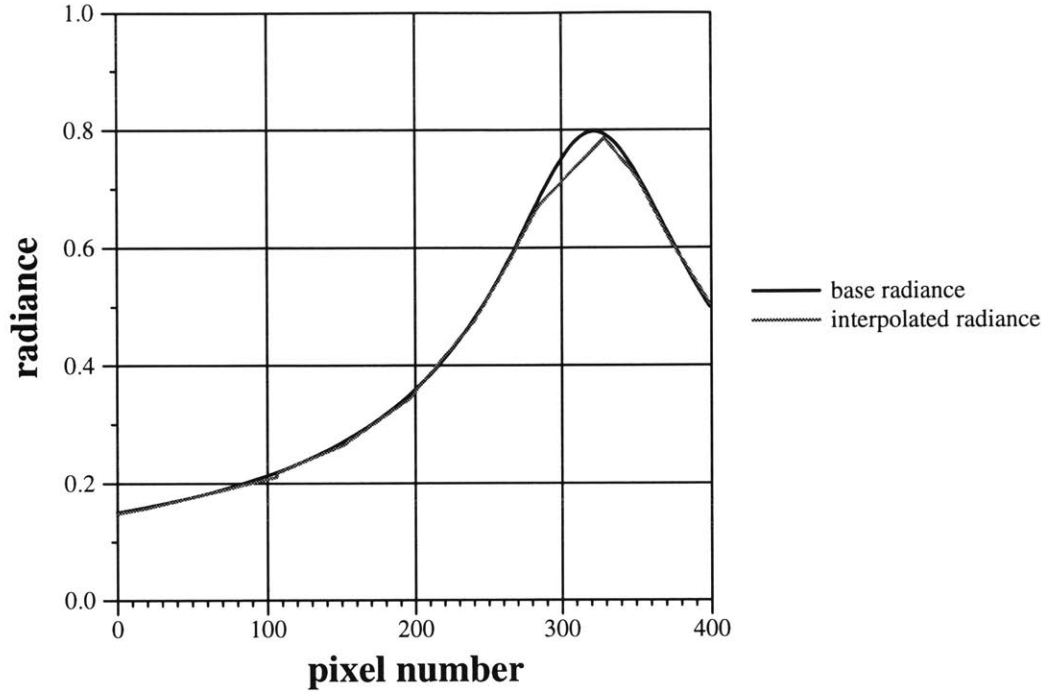
Figure 4-28: Actual and interpolated radiance for one scan-line of the image in Figure 4-26.
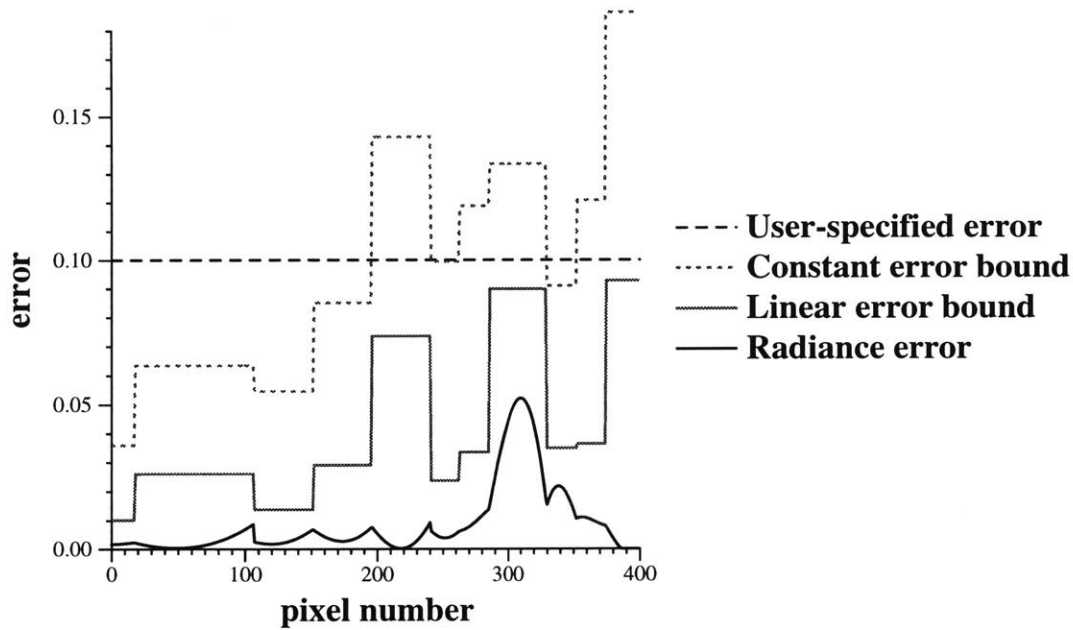
Figure 4-29: Actual and conservative error bounds for the scan-line in Figure 4-28.

ther the a and c axes or the b and d axes. This error-based adaptive subdivision results in fewer interpolants being built for the same number of successfully interpolated pixels.

The interpolant ray tracer adaptively subdivides across radiance discontinuities as follows: when a linetree cell is subdivided, the sixteen ray trees of the extremal rays associated with the

95

cell are considered. If all sixteen ray trees are the same, the cell is simply subdivided on the basis of aspect ratio. However, if the sixteen ray trees differ, the algorithm splits the cell on that pair of axes that maintains the maximum coherence. Coherence is destroyed if splitting an axis spreads rays with the same position-independent ray tree to different children. When picking the pair of axes to split, that pair is picked that spreads the least number of ray trees to different children. For the museum scene, using error-driven subdivision results in a 35% speedup. This is because maintaining the coherence in a cell results in fewer subdivisions of the linetree for the same image quality and in turn, results in fewer interpolants being built.

This technique could also be applied to adaptive subdivision across regions with non-linear radiance variation. The linear interval terms L_i constructed by the error bounding algorithm represent the variation in the corresponding axis $i \in \{a, b, c, d\}$. The pair of axes that has the largest L_i's would be selected for subdivision.

4.4.2 Unique ray trees

Storing radiance samples and their associated ray trees could result in substantial memory usage. However, all valid interpolants and a large number of invalid interpolants are associated with similar ray trees. Therefore, the interpolant ray tracer uses hash tables to avoid storing duplicate ray trees, resulting in substantial memory savings.

4.4.3 Textures

The interpolant ray tracer supports textured objects by separating the texture coordinate computation from texture lookup. Texture coordinates and incoming radiance at the textured surface are both quadrilinearly interpolated. In general, multiple textures may contribute to the radiance of an interpolant. The texture coordinates of every contributing texture, and the appropriate weighting of each texture by the incoming radiance are recorded in the interpolant for each of the sixteen extremal rays and are separately interpolated. For reflected textures, an additional ray must be shot for each contributing texture from the point of reflection to compute the texture coordinates used in interpolation.

4.5 Extensions to scene and lighting models

The error bounding algorithm is based on certain assumptions about the scene model and lighting model supported by the interpolant ray tracer, as described in Section 4.1.2. The interpolant

ray tracer can be applied to more general scenes and lighting models, but in these cases the error bounding algorithm presented in this chapter does not guarantee that error is bounded. It is interesting to consider the difficulty of extending the error bounding algorithm to support more general models. A few possible extensions are discussed here.

- **Parametric surfaces**: It would be useful for the ray tracer to support a more general model of surfaces, such as bicubic spline patches. Support for non-convex surfaces would also be useful. In both cases the non-linear variations in radiance can be bounded by applying the linear interval techniques from this chapter. The intersection and normal for parametric surfaces can be bounded by using root finding on linear intervals [Han75]. The assumption of convexity is more difficult to eliminate because it is used in various ways during the detection of discontinuities. One possibility is to use interval-based techniques to bound the degree to which a surface is non-convex; another is to bound the surface on the inside and outside using convex surfaces.

- **Generalized shading model**: The interpolant ray tracer uses the isotropic Ward model for local shading, and the Whitted ray tracing model for global illumination. The techniques discussed in this chapter can be extended to other local shading models such as non-isotropic Ward [War92], Cook-Torrance [CT82], He [HTSG91], and others [Gla95, WC88]. Only the linear interval techniques that identify non-linear radiance variations would need to be modified. Because these linear interval techniques are very general, application to these other models should be straightforward.

  It would be desirable for the ray tracer to include a global illumination model that supports more generalized light transport paths such as diffuse inter-reflections and caustics. Diffuse inter-reflections often produce a smoother distribution of light energy within the scene, so one would expect radiance interpolation to be more successful. Techniques for bounding error in radiosity systems [LSG94] may be useful. Bounding error from caustics is more difficult.

- **Textures**: Using the existing algorithm, the system can be extended straightforwardly to support texturing of the specular or reflective coefficients of surfaces. Bump maps [Bli78] could also be supported without difficulty. Some more sophisticated texturing techniques that change object geometry, such as displacement maps [Coo84], are more difficult to support.

- **Light sources**: Support for area light sources or other clusters of lights would be useful. Like

diffuse inter-reflections, area light sources are expected to make interpolation more success-ful. However, for the purposes of bounding error, it is important to accurately characterize the partial occlusion of area light sources and clustered light sources. This characterization is well known to be difficult [CW93, SP94].

Chapter 8 further discusses how the interpolant ray tracer can be extended to address each of these limitations.

4.6 Discussion: error approximation

Another approach that can be used to detect non-linear radiance variations in place of interval arithmetic is error approximation. While error approximation can occasionally result in erroneous interpolation, it can be used to produce good image quality at a lower cost. In [BDT98], I pre-sented an algorithm that uses error approximation to guide sampling. This algorithm computes the components of the second-order Taylor expansion of the radiance function around the center of the linetree cell. These second-order terms of the Taylor expansion, which are the interpolation error at the center of the cell, are used to estimate error over the rest of the linetree cell. This technique is effective because the maximum interpolation error typically occurs near the center of the linetree cell. By measuring interpolation error at the center of the linetree cell, this technique typically produces a more accurate estimate of error than interval arithmetic does, though it is not conservative.

Chapter 5

Accelerating visibility

Using interpolants to approximate radiance eliminates a significant fraction of the shading computations and their associated intersections invoked by a ray tracer; however, the number of intersections computed for determining visibility remains the same. Once interpolants accelerate shading, the cost of rendering a frame is dominated by the following three operations:

- determining visibility at each pixel—constructing a ray from the eye through the pixel and intersecting that ray with the scene to find the closest visible object,

- for pixels that can be interpolated, computing the 4D intercepts for the ray and evaluating radiance by quadrilinear interpolation, and

- for pixels that cannot be interpolated (because valid interpolants are unavailable), evaluating radiance using the base ray tracer.

This chapter presents techniques to accelerate visibility determination and interpolation by further exploiting temporal and image-space coherence, reducing the cost of these operations.

5.1   Temporal coherence

For complex scenes, determining visibility at each pixel is expensive. However, if multiple frames of a scene are being rendered from nearby viewpoints, temporal coherence can be exploited to reduce the cost of determining visibility. For small changes in the viewpoint, objects that are visible in one frame are often visible in subsequent frames. This temporal coherence occurs because eye rays from the new viewpoint are close (in ray space) to eye rays from the previous viewpoint. For the same reason, linetree cells that contribute to one frame typically contribute to subsequent

99

frames. This section presents a reprojection algorithm that exploits this temporal coherence to accelerate visibility determination, while guaranteeing that the correct visible surface is always assigned to each pixel.

Consider a pixel that is rendered in one frame using a particular interpolant; the linetree cell for the interpolant is said to *cover* the pixel in that frame. A linetree cell typically covers a number of adjacent pixels on the image plane; this set of pixels can be computed by a simple geometric projection. When rendering a series of frames, this property is used to identify pixels covered by linetree cells. For each frame, linetree cells that contributed to the previous frame are reprojected to the current viewpoint to determine which pixels are covered by these cells.

Using reprojection to determine visibility accelerates rendering in the following way. If a pixel in the new frame is covered by a linetree cell, it is not necessary to compute visibility or shading for that pixel: the radiance of the pixel can be computed directly from the interpolant associated with that cell. Since a linetree cell typically covers multiple pixels, the cost of reprojecting the cell is amortized across many pixels. Reprojection also enables scan-line interpolation, further accelerating rendering (see Section 5.2).

There are two important issues to be considered:

1. how to reproject linetree cells efficiently, and

2. how to guarantee that a cell is reprojected to a pixel only if it covers that pixel in the new frame. Note that the reprojection algorithm is conservative since it never incorrectly assigns a linetree to a pixel.

These two issues are discussed in detail in the following sections: Section 5.1.1 shows how linetree cells can be efficiently reprojected using the graphics hardware, and Section 5.1.2 describes how shaft-culling is used to ensure that the correct visible surface is always assigned to each pixel.

5.1.1   Reprojecting linetrees

First, we consider reprojecting linetrees in 2D. In 2D, each linetree cell represents all the rays that enter its front line segment and leave its back line segment. For a given viewpoint, a cell covers some (possibly empty) set of pixels; the rays from the viewpoint through these pixels are a subset of the rays represented by the linetree cell. Given a viewpoint, the pixels covered by a linetree cell and their corresponding rays can be found efficiently as shown below.

On the left in Figure 5-1, a linetree cell, L, of an object is shown; the front segment of L is shown in light gray and its back segment is shown in black. In this frame, the viewpoint is at the point **eye**. A ray from the viewpoint that lies in L must intersect both its front and back segment.

100
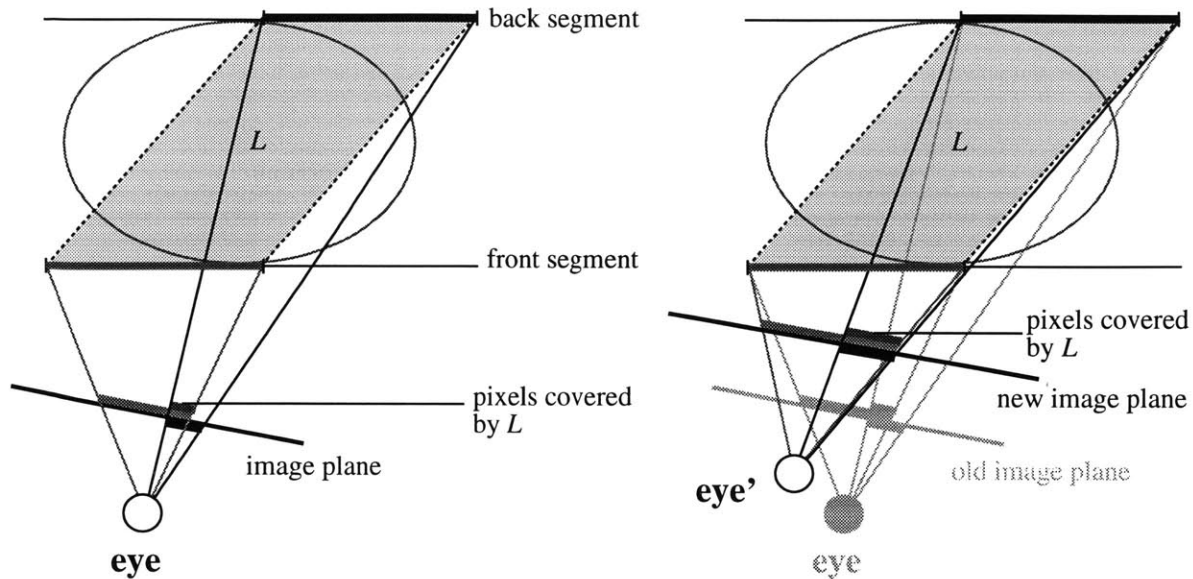
Figure 5-1: Pixels covered by a linetree cell. A linetree cell with its front face (light gray) and back face (black). The projections of the front and back faces on the image plane are shown as thick light gray and black lines respectively. The linetree cell covers exactly those pixels onto which both its front and back face project (shown in medium gray). On the right, the viewpoint has changed from **eye** to **eye'**. Different pixels are covered by the cell in the new image plane (shown in medium gray).

Consider the projection of the front segment of L on the image plane with **eye** as the center of projection (shown as the light gray line on the image plane). Similarly, the pixels onto which the back segment projects are shown by the thick black line on the image plane. The pixels covered by L are the pixels onto which *both* the front and back segment of L project. Therefore, the pixels covered by L are the intersection of the pixels covered by both the front and back segment (shown by the medium-gray segment in the figure). On the right in Figure 5-1, the same cell is shown projected onto the image plane from a new viewpoint, **eye'**. Notice that L covers different (in fact, more) pixels in the new frame.

To determine which pixels are covered by L, the intersection of pixels covered by its front and back segments is computed as follows: using the viewpoint as the center of projection, the front segment of L is projected onto the line containing its back segment, and is then clipped against the back segment. When this clipped back segment is projected onto the image plane it covers exactly the same pixels that L covers. This is clear from the geometry in Figure 5-2.

Extending this discussion to 3D, each linetree cell represents all the rays that enter its front face and leave its back face (see Figure 5-3). To determine the pixels covered by a linetree cell L, the front face of L is projected onto the plane of the back face of L and clipped against the back face. This clipping operation is inexpensive because the projected front face and back face are

101
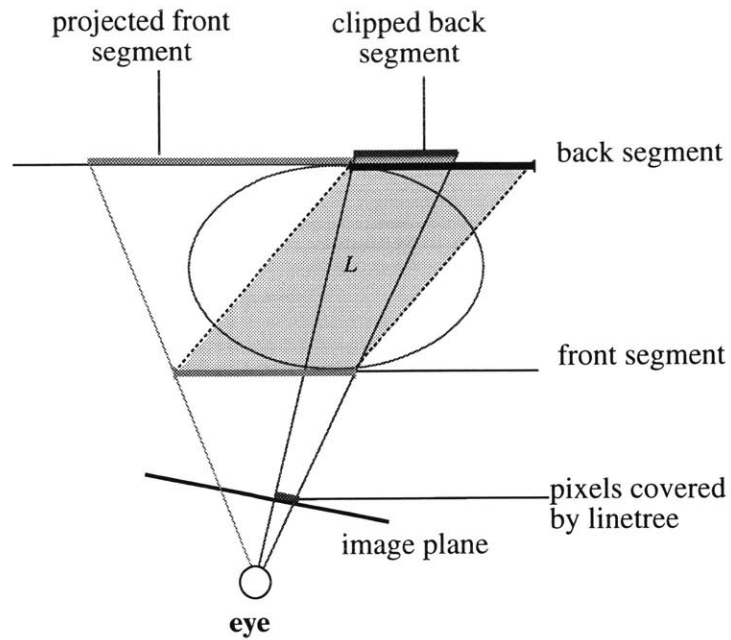
Figure 5-2: Reprojection in 2D. The front segment is projected on and clipped against the back segment. The medium gray segment shows the pixels covered by the linetree cell.
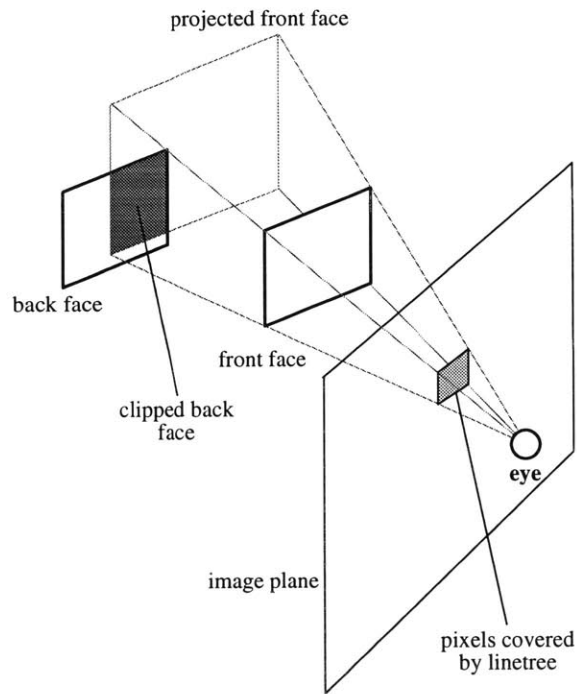
Figure 5-3: Reprojection in 3D. The front face is projected on and clipped against the back face. The medium gray region shows the pixels covered by the linetree cell.
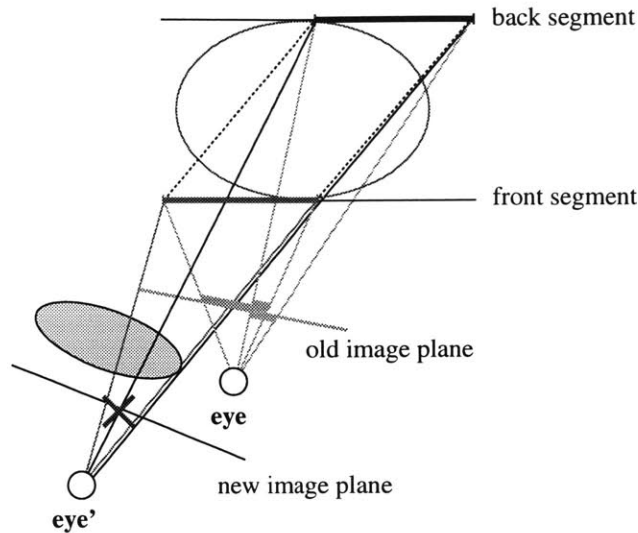
Figure 5-4: Reprojection correctness. The shaded ellipse occludes visibility to the linetree cell from the new viewpoint **eye'** but not from **eye**. Therefore, it would be incorrect to reproject the linetree cell to the new viewpoint.

both axis-aligned rectangles. The pixels covered by the projection of the clipped back face onto the image plane are exactly the pixels covered by L: in the figure, the medium-gray shaded region on the image plane.

When a new frame is rendered, the system clips and projects the faces of linetree cells visible in the previous frame. This process is accelerated by exploiting the projection capabilities of standard polygon-rendering hardware. The clipped back faces are rendered from the new viewpoint using a unique color for each linetree cell; the color assigned to a pixel then identifies the reprojected linetree cell that covers it. The frame buffer is read back into a *reprojection buffer* which now identifies the reprojected linetree cell, if any, for each pixel in the image. A pixel covered by a linetree cell is rendered using the interpolant of that cell; no intersection or shading computation is done for it.

5.1.2 Reprojection correctness

The reprojection algorithm described in the previous section identifies the pixels covered by a linetree cell; however, it does not guarantee correct visibility determination at each pixel. Figure 5-4 illustrates a problem that can arise due to changes in visibility; an object that was not visible in the previous frame (the shaded ellipse) can occlude reprojected linetrees in the current frame. Similarly, two linetree cells from the previous frame could reproject to the same pixels in the current frame.

103
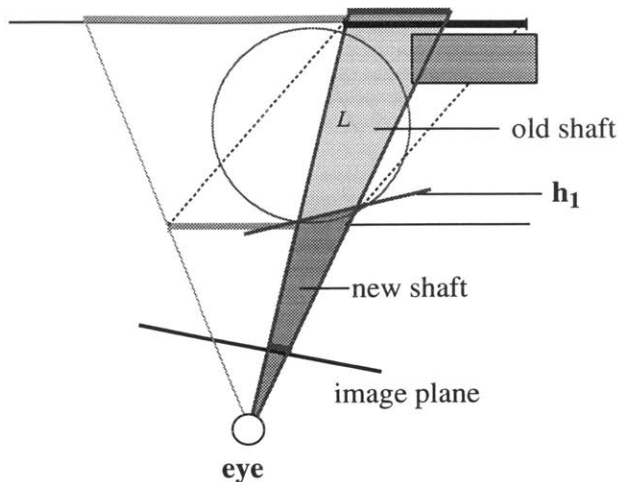
Figure 5-5: Shaft cull for reprojection correctness. The shaft cull using the back plane of the linetree cell L prevents reprojection of L because the shaded cube is included in the shaft. Using the more accurate shaft, shown in dark gray, permits the interpolant to be reprojected while guaranteeing correct results.

To guarantee that the correct visible surface is found for each pixel, the reprojection algorithm conservatively determines visibility by suppressing the reprojection of linetree cells that might be occluded. This occlusion is detected by shaft-culling [HW91] each clipped back face against the current viewpoint. The shaft consists of five planes: four planes extend from the eye to each of the edges of the clipped back face, and the fifth back plane is the plane of the back face of the linetree cell. If any object intersects the shaft, the corresponding linetree cell is not reprojected onto the image plane. If no object intersects the shaft, reprojecting the linetree's clipped back face correctly determines the visible surface for the reprojected pixels. Note that the least-common-ancestor optimization presented in Section 4.2.4 can be used to improve the performance of the shaft cull.

The interpolant ray tracer uses an additional optimization to make the shaft cull less conservative. This scenario is shown in Figure 5-5. In the figure, the old shaft using the planes discussed above (shown in light gray) includes the shaded cube. Therefore, the old shaft prevents reprojection of the linetree cell L. However, the region of space from the eye to the surface of the object for which the interpolant is built is free of occluders. Therefore, reprojecting L would not result in errors; the old shaft is too conservative. To produce more accurate shafts, the interpolant ray tracer uses the plane $\mathbf{h}_1$, described in Chapter 4, as the back plane of the shaft (see Figures 4-23 and 4-24). Using this new shaft, shown in dark gray in Figure 5-5, improves the accuracy of the shaft cull, which improves performance by increasing the number of pixels covered by reprojected

**Render frame
with viewpoint at *eye***

**For each L from previous frame
cp = project and clip L's front face on back face
if (ShaftCull(cp, *eye*)) Draw(cp with L-*id* as color)
Read back reproject buffer RB**

for each y

(x,y)

Reproject Path

Start — **Reprojected data available
RB[x,y] == L** → **Quadrilinear
Interpolation** → **x++** → **Start**

No reprojected data available

Interpolate Path

**Determine visibility: object *o*,
Check if interpolant
available for *o*** — **Yes** → **Quadrilinear
Interpolation** → **x++** → **Start**

No interpolant available

Slow Path

**Build interpolants if cost-effective
Shade pixel using base ray tracer** → **x++** → **Start**

Figure 5-6: Reprojection algorithm.

linetrees.

Reprojection accelerates visibility determination by correctly assigning a linetree cell to each pixel. For pixels covered by reprojection, no visibility or shading operation is needed. Only one shaft cull is required per linetree cell. For the museum scene in Figure 5-8, the shaft cull is faster than intersecting a ray for each pixel for linetree cells covering at least 24 pixels.

Note that other systems (see Chapter 2) that use reprojection to determine visibility can only support reprojection of polygonal objects, because reprojection of non-polygonal object silhouettes is difficult. The interpolant ray tracing system does not suffer from this restriction because while objects may have non-polygonal silhouettes, the error bounding algorithm guarantees that linetree cells with valid interpolants do not include these silhouettes.

105

The rendering algorithm with reprojection is summarized in Figure 5-6. Before a frame is rendered, all linetree cells that contribute to the previous frame are clipped and shaft-culled against the new viewpoint, obtaining a list of conservatively unoccluded linetree cells. These cells are reprojected using the polygon-rendering hardware. The frame buffer is read back into the reprojection buffer (RB) which identifies the linetree cell (if any) that covers each pixel in the image. The frame is rendered using the reprojection buffer to determine visibility when possible. For each pixel, the reprojection buffer is checked for the availability of a reprojected linetree cell. If such a cell exists, radiance for the pixel is quadrilinearly interpolated using the linetree cell. If no reprojected linetree cell is available, visibility at the pixel is determined by tracing the corresponding eye ray through the scene. If the closest visible object o along the eye ray has a valid interpolant for the eye ray, radiance for that pixel is quadrilinearly interpolated; this is the *interpolate path* referred to in Section 1.5.1. If no interpolant is available for the pixel, the eye ray is ray traced using the base ray tracer: the *slow path*. On the slow path, interpolants are built only if deemed cost-effective (see Section 3.5.4).

5.1.3 Optimizations: adaptive shaft-culling

The reprojection algorithm shaft-culls linetree cells from the previous frame. If an object is completely visible, it is wasteful to shaft-cull each of its linetree cells separately. This is also true if some significant number of linetree cells associated with the object are unoccluded. To avoid redundant work, the interpolant ray tracer uses clustering to amortize the cost of shaft-culling over multiple linetree cells. The algorithm clusters all the linetree cells of an object and shaft-culls the cluster. If the shaft cull succeeds, a significant performance improvement is achieved by eliminating the shaft cull for each individual cell. If the shaft cull fails, the cluster is recursively subdivided spatially along its two non-principal axes, and the four resulting clusters are shaft-culled. This recursive subdivision is repeated until the cluster size is reduced to a single linetree cell. For the museum scene shown in Figure 5-8, clustering decreases the number of shaft culls by about a factor of four.

Another problem with the reprojection algorithm is that it could be too conservative because large linetree cells that are only partially occluded by some occluder are not reprojected. To address this problem, when the interpolant ray tracer subdivides a cluster down to a single linetree cell, it uses a cost model similar to that used for subdividing linetrees (see Section 3.5.4) to compute the number of pixels covered by the single cell. If the number of pixels covered by the cell is significant (at least 24 for the museum scene in Figure 5-8), the linetree cell in turn is recursively subdivided and shaft-culled. The portions of the faces that are not blocked are then reprojected. This adaptive

106

subdivision technique improves the effectiveness of reprojection when there are some large linetree cells that are partially occluded. Without adaptive subdivision, the performance of reprojection is less predictable because a small intervening occluder can cause large areas of the image to not be reprojected.

5.2   Image-space coherence

A simple scan-line algorithm can exploit image-space coherence by using reprojected linetree cells to further accelerate the ray tracer. When rendering a pixel, this algorithm checks the reprojection buffer for a reprojected linetree cell (if any) associated with the pixel. If a reprojected linetree cell is available, the reprojection buffer is scanned to find all subsequent pixels on that scan-line with the same reprojected linetree cell. These pixels are said to form a *span*. The radiance for each pixel in the span is then interpolated in screen space. Note that the algorithm uses perspective correction when interpolating texture coordinates.

Using screen-space interpolation eliminates almost all of the cost of ray-tracing the pixels in the span. No intersection or shading computations are required, and interpolation can be performed incrementally along the span in a tight loop. One effect of screen-space interpolation is that speedup increases with image resolution because reprojected linetree cells cover larger spans of pixels in high-resolution images. The current perspective projection matrix can be considered by the error bounding algorithm (see Section 4.3), yielding an additional *screen-space* error term. Thus, unlike other systems that exploit image coherence [AF84, Guo98], the interpolant ray tracer can exploit image coherence while producing correct results. For linetree cells that are not close to the viewpoint, the additional screen-space error is negligible and can be ignored. In practice, no observable artifacts arise from screen-space interpolation.

The reprojection algorithm with screen-space interpolation is shown in Figure 5-7. In the figure, if a reprojected pixel is available for some pixel (x, y), the algorithm builds a span for all subsequent pixels on the scan-line with the same reprojected linetree cell. Radiance for all pixels in the span is interpolated in screen-space; this is the *fast path* referred to in Section 1.5.1. Figures 5-6 and 5-7 differ only in the reproject path; the interpolate and slow path are the same in both figures.

Figure 5-8 shows the reprojection buffer and the pixels covered by reprojection for the museum scene. The color-coded image in the top right shows how image pixels are rendered: purple pixels are span-filled (fast path), blue-gray pixels are interpolated (interpolate path), green and yellow pixels are not accelerated (slow path). The pale lines in the span-filled regions mark the beginning and end of spans. Note that objects behind the sculpture are conservatively shaft-culled, resulting
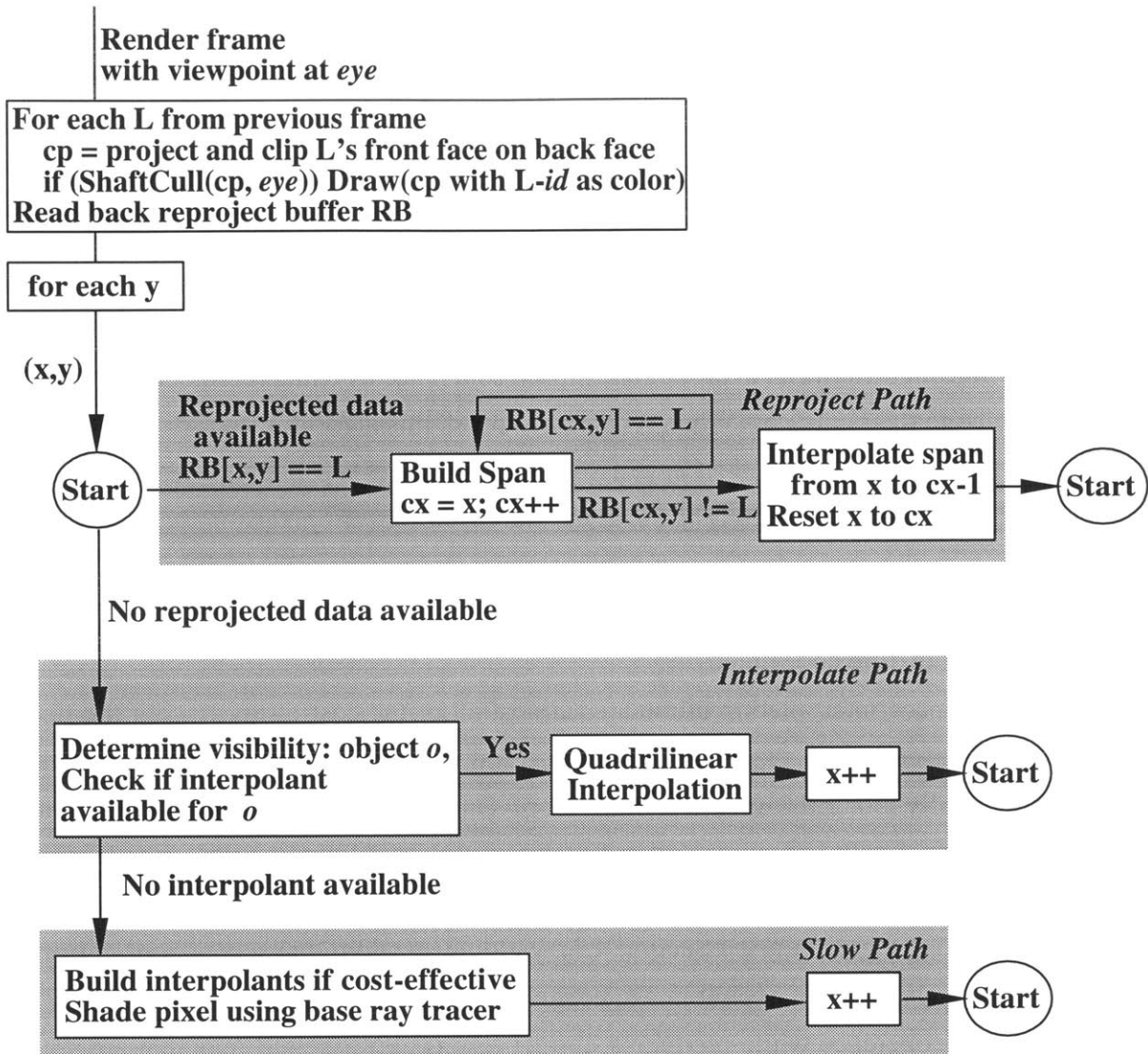
Figure 5-7: Reprojection algorithm with screen-space interpolation.

in a significant number of pixels around the sculpture not being reprojected. More accurate shaft-culling techniques would improve the reprojection rate.

5.3   Progressive image refinement using extrapolation

As mentioned in the beginning of this chapter, once shading is accelerated using interpolation, the cost of rendering a frame is dominated by the following three operations: visibility determination, quadrilinear interpolation and rendering of failed pixels. In the previous two sections, the first two of these problems have been addressed: reprojection decreases the cost of computing visibility, and screen-space interpolation decreases the cost of quadrilinearly interpolating pixels. Together
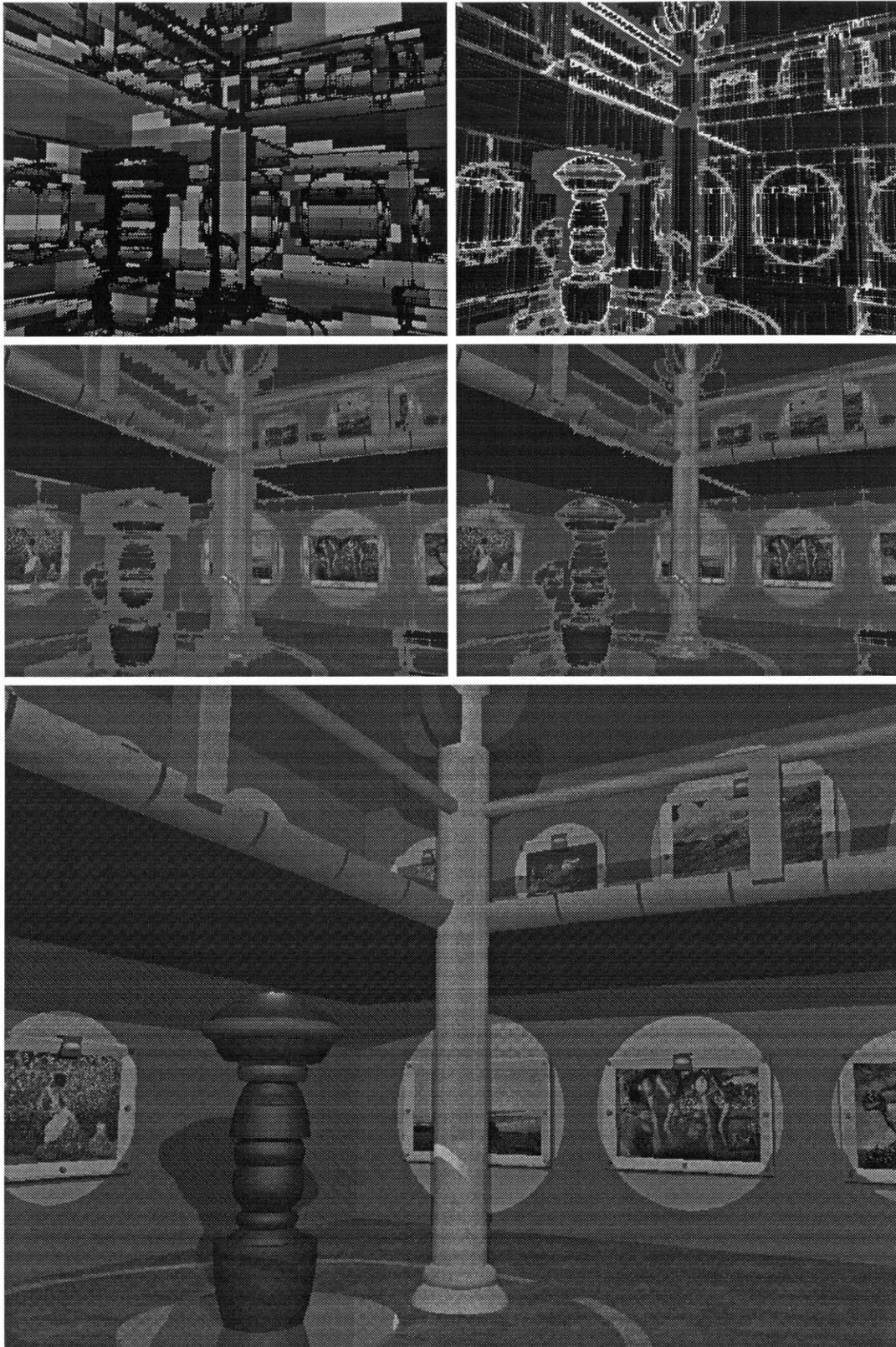
Figure 5-8: **Reprojection for the museum scene**. Top row (left to right): reprojection buffer, color-coded image. Middle row: span-filled pixels, span-filled and interpolated pixels. Bottom: final image.

these optimizations enable most pixels to be rendered rapidly. However, rendering pixels that are neither reprojected nor interpolated (failed pixels) now dominates the time to render a frame. If a guaranteed rendering frame rate is desired, it is necessary to eliminate the cost of ray tracing the failed pixels using some approximation for those pixels; however, this approximation cannot be expected to meet the error guarantees provided by the error bounding algorithm.

In this section, algorithms that approximate radiance for the failed pixels are presented. These algorithms extrapolate radiance computed for the reprojected or interpolated pixels. The reprojection algorithm is the same as shown in Figure 5-7; the interpolate and slow path of the algorithm are replaced by the extrapolation algorithm.

5.3.1 Algorithm 1: Simple extrapolation

The first and fastest extrapolation algorithm renders all the pixels in the scan-line that have a reprojected linetree cell available. The pixels that are not reprojected are then filled in by extrapolating radiance from the reprojected pixels. This algorithm is fast because it fills in the failed pixels without doing any shading or visibility; however, it extrapolates radiance between different objects, resulting in noticeable visual artifacts such as blurred object edges and color bleeding between different objects as can be seen in Figure 5-10.

5.3.2 Algorithm 2: Extrapolation with correct visibility

A second extrapolation algorithm uses both reprojection and interpolation to render pixels. This algorithm renders all the pixels in the scan-line that have a reprojected linetree or have an interpolant available. As before, all pixels that have reprojected linetrees are screen-space interpolated. If a reprojected linetree is not available for the pixel, the algorithm finds the closest visible object at the pixel. Then, if an interpolant is available, radiance is quadrilinearly interpolated for the pixel. The remaining failed pixels are filled in by extrapolating radiance from the reprojected or interpolated pixels. However, since the algorithm computes visibility at each pixel to check for the availability of a valid interpolant, this visibility information is put to use during extrapolation to guarantee correct visibility determination at each pixel.

This extrapolation algorithm is shown in Figure 5-9. The algorithm finds the closest two pixels, p and n, before and after the current pixel, that also intersect the same object. If p and n are reprojected or interpolated, radiance for all pixels between p and n (including the current pixels) are extrapolated. If p (or n) is neither reprojected nor interpolated, radiance for p (or n) is evaluated along the slow path. The radiance for all pixels between p and n is then extrapolated. Note that

End of scan-line


```
                              x = 0                        Extrapolation

        while (Reprojected(x,y) || Interpolated(x,y)) x++

        p = previous pixel that is reprojected or interpolated
        n = next pixel that is reprojected or interpolated
        c = current pixel, oc = object visible at c
        op = object visible at p, on = object visible at n

                           if (oc == op)

                Yes                      No

        if (oc == on)                         if (oc == on)

   Yes            No                      Yes            No

        Find m such that      Shade c      Find l,m such that
          om = object visible at m   p = c     om = object visible at m
          om == oc, m≥c, m<n                   ol = object visible at l
        Shade m                               ol == oc, l≤c
        n = m                                 om == oc, m≥c
                                            Shade l,m
                                            p = l, n = m

                        Interpolate span
                          from p to n
                        x = n+1
```

Figure 5-9: Algorithm 2: extrapolation with correct visibility determination.

this algorithm does not completely eliminate the slow shading operations of the base ray tracer, but the increased performance penalty is small (about 3% of the frame rendering time for the museum scene).

This algorithm is half as fast as the simple algorithm but it eliminates most of the visual artifacts produced by the simple algorithm since it guarantees correct visibility determination at each pixel. Some artifacts still remain because the algorithm interpolates between light and dark regions of the image. Figure 5-10 shows the museum scene rendered with both extrapolation algorithms. The relative merits of these two algorithms are discussed in detail in Chapter 7.
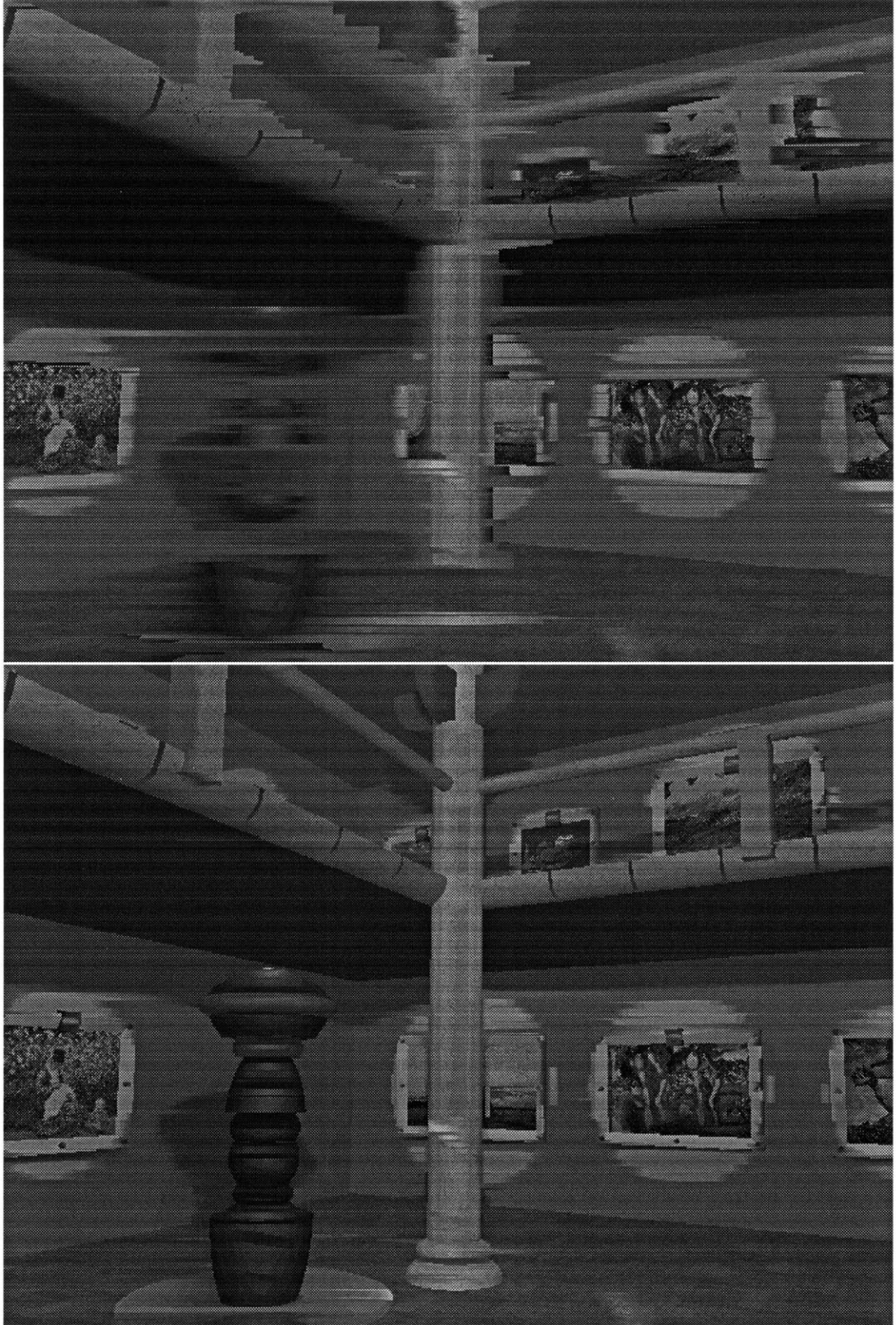
Figure 5-10: **Extrapolation for the museum scene**. Top: Algorithm 1 (simple extrapolation), Bottom: Algorithm 2 (extrapolation with correct visibility).

5.3.3 Algorithms 3 and 4: Progressive refinement

For interactive performance, several complementary techniques can be used to provide the user with a progressively refined rendered image. The pixels that are not reprojected are filled in by interpolating between reprojected pixels in various ways: the system uses two algorithms to produce progressively higher image quality than that produced by Algorithm 1 (the simple extrapolation algorithm), while being faster than Algorithm 2 (the extrapolation algorithm that guarantees correct visibility). Both these algorithms are faster because they use a binary search [CLR90] of the scan-line to find the previous and next pixels p and n described in Figure 5-9. However, neither of these algorithms guarantee correct visibility, since the binary search might miss small intermediate objects in the scan-line.

Algorithm 3: Progressive refinement with visibility check. This algorithm finds p and n using a binary search of the scan-line such that the object visible at p and n are the same. This test is similar to that done by the Algorithm 2, except that correct visibility is not guaranteed. If the maximum length of a span is not restricted, this algorithm produces results that are only slightly better (visually) than Algorithm 1. However, if the maximum length of a span is restricted, the results produced are as shown in Figure 5-11. (In the figure, the maximum span length is set to 20.) Note that there are some visual artifacts due to erroneous interpolation across shadows (as in Algorithm 2) and artifacts due to incorrect visibility determination, which are particularly visible at the frames of the paintings. However, the results are visually similar to those produced by Algorithm 2, while being computed much faster.

Algorithm 4: Progressive refinement with ray tree comparisons. This algorithm uses binary search to find the previous and next pixels p and n such that these pixels have the same ray tree as the current pixel. Comparing ray trees causes increased subdivision of the scan-line when compared to Algorithm 3, but also produces substantially improved image quality as shown in Figure 5-11. The images produced using this algorithm are often nearly indistinguishable from the images using the interpolant ray tracer with error guarantees, though some visual artifacts are still visible on the sculpture. This algorithm uses the fact that both reprojection and interpolation look up interpolants that have ray trees associated with them; these ray trees are used to obtain improved image quality.
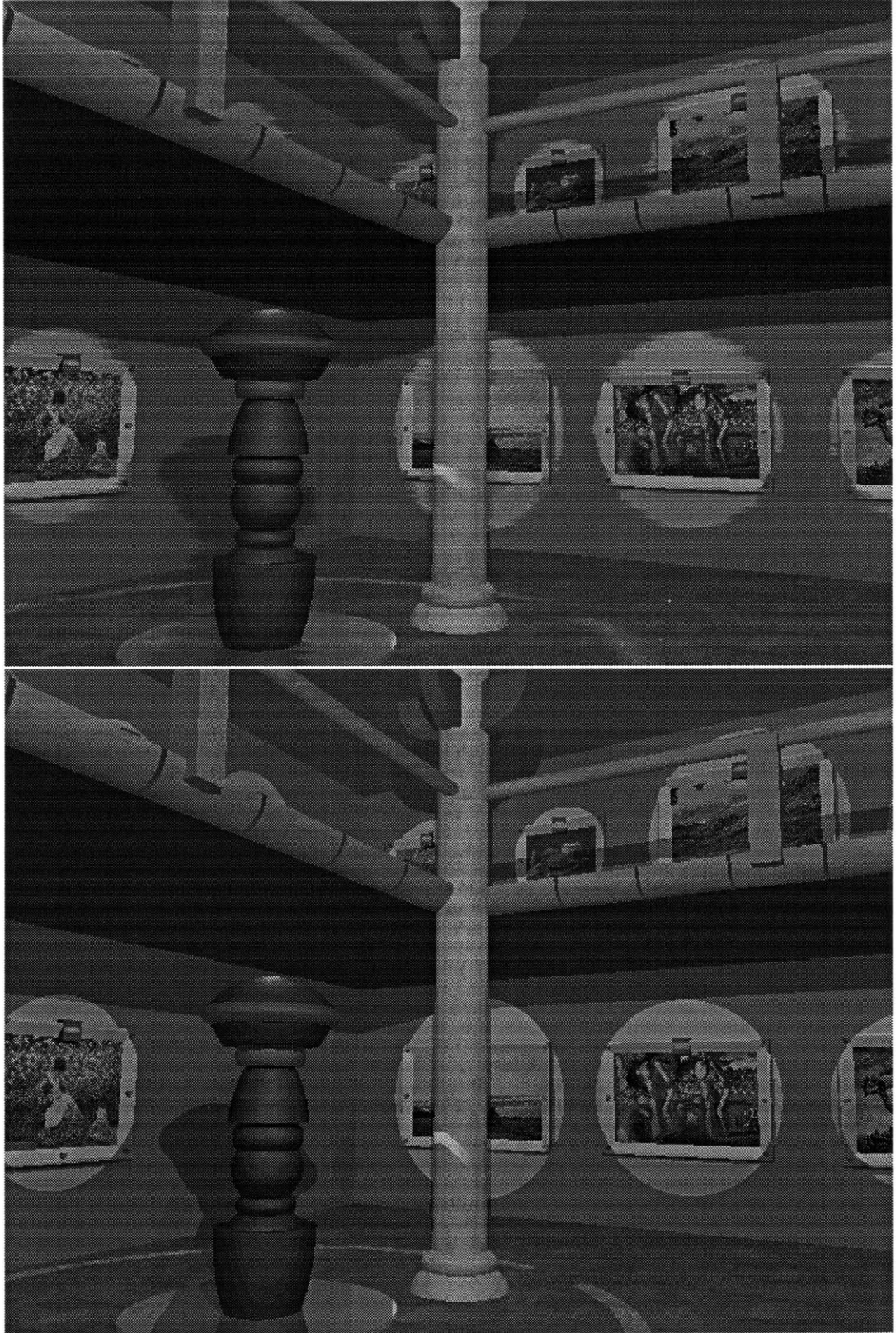
Figure 5-11: **Extrapolation for the museum scene**. Top: Algorithm 3, matching visibility. Bottom: Algorithm 4, matching ray trees.

Chapter 6

Scene Editing

Ray tracing is not used in interactive applications such as editing and visualization because of the high cost of computing each frame. An important application that would benefit from high-quality rendering is modeling; a user would like to make changes to a scene model and receive rapid feedback from a high-quality renderer reflecting the changes made to the scene. Ray tracers have been extended to support interactive editing using the localized-effect property described in Chapter 1. This property is exploited to give a modeler feedback quickly by *incrementally* rendering the part of the image that is affected.

However, to make incremental rendering tractable, existing systems impose a severe restriction: the viewpoint must be fixed. These systems are *pixel-based*: they support incremental rendering by maintaining additional information for each pixel in the image. This information is used to recompute radiance as the user edits the scene. The chief drawback of pixel-based approaches is that a change to the viewpoint invalidates the information stored for every pixel in the image. Therefore, rendering from the new viewpoint cannot be performed incrementally. Also, since information is maintained per pixel, the memory requirements can be large for high-resolution images. (A discussion of related work in this field is in Chapter 2.)

The previous chapters in this thesis describe the interpolant ray tracer, which accelerates ray tracing of static scenes with changing viewpoints. This chapter describes how the interpolant ray tracer is extended to support scene editing. This incremental ray tracer draws on ideas from Brière and Poulin [BP96] and Dretakkis and Sillion [DS97]. The important contribution of this work is its support for *incremental* rendering with scene editing *while permitting changes in the viewpoint*. It is the first ray tracer that supports scene editing with a changing viewpoint.

Radiance interpolants make viewpoint changes possible in an incremental ray tracer. Every interpolant depends on some regions of world space. When an object is edited, the interpolants that
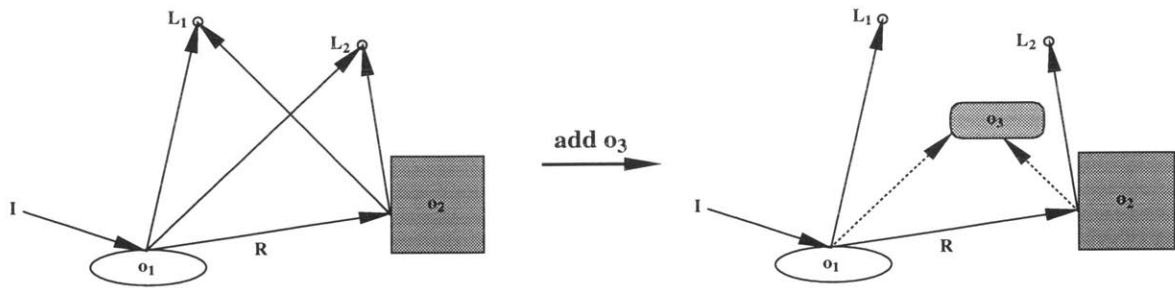
115

Figure 6-1: Effect of a scene edit.

depend on the region of space affected by the edit are invalidated. When a new frame is rendered from the same or a different viewpoint, interpolants that are still valid are reused to accelerate rendering.

To identify the interpolants that depend on a region of space, this thesis introduces the concept of *ray segment space*. Dependencies of an interpolant can be represented simply in this space. Space-efficient hierarchical *ray segment trees* are built over ray segment space and are used to track the regions of world space that affect an interpolant. When the scene is edited, these ray segment trees are traversed to rapidly identify and invalidate the interpolants that are affected by the edit.

This chapter is organized as follows. Section 6.1 describes why scene editing is a difficult problem and explains why interpolants are useful for scene editing. Section 6.2 introduces a parameterization of *global line space* and shows that edits affect a well-defined region of this space. Section 6.3 describes how global linetrees can be used to track the regions of line space affected by an interpolant. Section 6.4 introduces ray segment trees to address the limitations of global linetrees and describes how these trees are used to keep track of interpolant dependencies. Section 6.5 explains how these ray segment trees are used to rapidly find all interpolants that might be affected by a scene edit.

6.1 Goal

This section discusses the scene editing problem and presents some intuitions for why radiance interpolants are useful for solving this problem.

6.1.1 The scene editing problem

Interactive scene editing is difficult because radiance along a ray can depend on many parts of the scene. Figure 6-1 shows a ray **I** traced through the scene. Several sources contribute to the radiance

116

along **I**: the lights L_1 and L_2 contribute to radiance directly, and also indirectly through a reflection **R**. Various edits to this scene will change radiance along **I**. For example, if o_2 were deleted, the radiance along **R** would change, and indirectly the radiance along **I** would change. Recall that each ray has an associated ray tree (see Chapter 4). When an object o is edited, every ray whose ray tree has o in it could be affected by the edit. Therefore, finding the rays affected by some edits is straightforward: the affected rays are those whose ray trees mention the edited object.

However, updating rays whose ray trees mention the edited object is not sufficient for all edits. For example, if o_3 were added (as shown in the figure), the radiance along **R** would change since L_1 would become occluded; this would change the radiance along **I**. Also, L_2 would become occluded directly along **I**. Thus, even though o_3 does not appear in the ray tree for **I**, the scene edit makes o_3 affect the radiance along **I**. In general, a scene edit affects a ray **I** if some ray in the ray tree of **I** passes through the region of world space affected by the edit. In the figure, the ray from o_2 to light L_1 passes through the region of space affected by the edit (the volume of o_3).

To make the incremental ray tracer work well, it must address two goals:

- **Correctness:** All rays affected by a scene edit must be identified and updated; otherwise, the image rendered will be incorrect. However, some unaffected rays could also be conservatively flagged for update.

- **Efficiency:** For efficiency, the system should *accurately* identify the affected rays. When possible, the system should avoid updating rays that are not affected by the edit, because these updates are wasted computation.

6.1.2 Edits supported

The difficulty of supporting incremental rendering with scene editing depends on the kinds of edits allowed. There are several kinds of scene edits of interest for incremental ray tracing [BP96], which can be categorized usefully as follows:

- attribute changes, which include changes to the material properties of objects: for example, diffuse color, specular color, diffuse and specular coefficients, and reflective and refractive coefficients;

- geometry changes, which include adding, deleting, and moving objects;

- changes in viewpoint; and

- changes in lighting.

117

Brière and Poulin [BP96] support only the first two of these edits, because their system requires that the viewpoint be fixed. For a fixed viewpoint, the problem of identifying affected rays is easier because the set of rays being sampled is pre-determined. If the viewpoint is allowed to move, the set of sample rays changes, making it more difficult to identify rays affected by a scene edit. By using interpolants for scene editing, the incremental ray tracer described here is able to accelerate rendering with the first three kinds of scene edits.

A change to the lighting of the scene is more difficult to render incrementally because it violates the localized-effect property described in Section 1.2. A lighting change potentially affects the entire scene, making efficient incremental rendering difficult. The incremental ray tracer described here does not support lighting changes.

6.1.3 Why use interpolants for scene editing?

Radiance interpolants are crucial for incremental scene editing with changing viewpoints because of the following two properties:

- Interpolants represent radiance for a bundle of rays: *all* the rays represented by the interpolant. This representation offers advantages both in detecting changes to radiance and in updating radiance after an edit. Rather than detect changes to radiance of the individual pixels covered by an interpolant, the system detects changes to radiance at the granularity of an entire interpolant, which is more efficient. In addition, updating the 16 samples stored in an interpolant effectively updates all the rays it represents. As a result, interpolants provide an efficient way to update radiance correctly when a scene is edited.

- Interpolants do not depend on the viewpoint; therefore, the viewpoint can be changed freely without invalidating them. An interpolant that remains valid after the edit can be reused.

The benefits of interpolants for scene editing are illustrated in Figure 6-2. The figure shows line space representations of the samples collected by a pixel-based incremental ray tracer on the left, and the interpolant ray tracer on the right. (Note that this line space representation is similar to that used in Figure 3-5.) In a pixel-based incremental ray tracer, radiance along eye rays from a fixed viewpoint is sampled as shown by the light gray points. When the scene is edited, the radiance for every pixel affected by the edit is invalidated. However, when the viewpoint changes, new samples are required, shown as dark gray points. Because no information about the neighboring points in line space is available, pixel-based systems cannot support changes in the viewpoint. A new viewpoint requires a completely different set of samples.
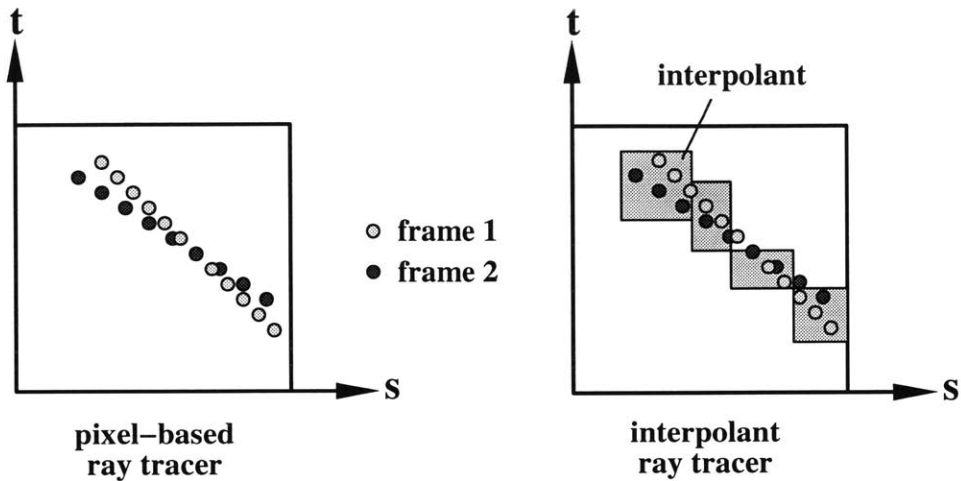
Figure 6-2: Interpolants for editing.

The interpolant approach builds interpolants that represent radiance for regions of line space, independently of the viewpoint (as shown by the rectangles in the figure). Therefore, when the viewpoint changes, interpolants can be reused. When the scene is edited, affected interpolants are updated, which effectively updates radiance of all rays represented by the interpolant.

6.2 Ray dependencies

This section describes how to identify the rays affected by an object edit. First, a *global* four-dimensional parameterization is presented of all rays intersecting the scene. When an object is edited, a portion of this *global line space* is affected. Conservatively, the radiance of rays in this portion of global line space should be recomputed after the edit.

6.2.1 Global line space parameterization

Global line space is the space of all directed lines that intersect the scene. In Chapter 3, an object-space four-dimensional parameterization of rays is presented. A similar parameterization is used for rays intersecting the scene, except that the face pairs (as shown in Figure 3-3) surround the entire scene, and $w \times l \times h$ is the size of the bounding box of the scene. As explained in Chapter 3, every ray intersecting the scene is associated with a face pair, and the ray is parameterized by the four intercepts it makes with the two parallel faces of the face pair. Note that per-object line space
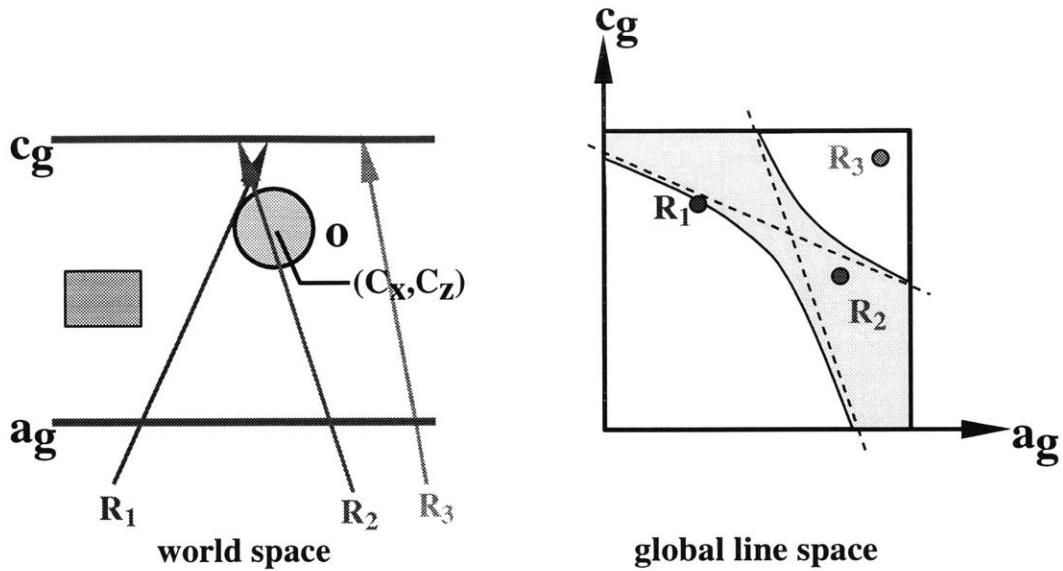
Figure 6-3: When the circle is edited, the hyperbolic region of line space (shaded, on the right) is affected.

coordinates for a directed line can easily be transformed into global line space coordinates for the line.

For simplicity, concepts are presented in 2D in this chapter; the extension of these ideas to 3D is straightforward. Each 2D ray is represented by two intercepts (a, c) that it makes with a pair of parallel 2D line segments (see Chapter 3). For example, in Figure 6-3, the horizontal lines surrounding the scene represent a 2D segment pair for *global line space*. Four such segment pairs are needed to represent all the rays that intersect the scene.

6.2.2   Line space affected by an object edit

A central intuition is that interpolants can be updated efficiently to reflect an object edit because an object edit affects a simple, contiguous subset of line space, as shown in Figures 6-3 and 6-4. On the left in Figure 6-3, a circle o in world space, a global segment pair, and rays associated with that segment pair are shown. On the right is a Cartesian representation of 2D line space. Every directed line in world space is a point in line space (see Chapter 3).

The region of line space affected by an object edit can be characterized straightforwardly: in 2D, the region of line space affected by an object edit is the interior of a hyperbola, and for an object edit in 3D, the region of 4D line space affected by the edit can be characterized by a fourth-order equation. These relations are derived in Appendix A.

When the circle is edited, the radiance of every ray in the interior of the hyperbola (shaded in

120

cg   cg

ag   ag

R

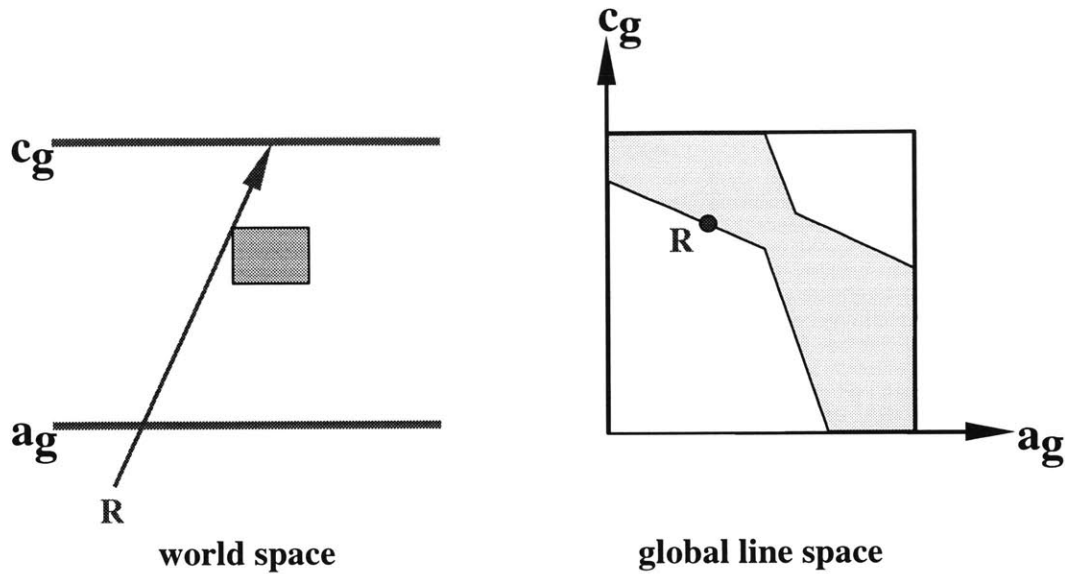**world space**   **global line space**

Figure 6-4: When the rectangle is edited, the hourglass region of line space (shaded, on the right) is affected.

Figure 6-3) could be affected. For example, in the figure, rays R_1 and R_2 are affected, but not R_3. If instead of a circle, a rectangle is edited (shown in Figure 6-4), an hourglass-shaped region (reminiscent of a hyperbola) of line space is affected by the edit.

The important point is that the region of line space affected by an edit is a well-defined subset of line space. In Chapter 3, it is shown that a hierarchical tree can be used to represent line space effectively; the same hierarchical tree approach can be used to efficiently identify the portions of global line space affected by an edit.

6.3   Interpolant dependencies

The global line space parameterization of the previous section can be used to determine whether a ray lies in the region of line space affected by an edit. Clearly, if an interpolant includes a ray in the shaded region of the hyperbola, the interpolant should be updated. However, as will be seen, an interpolant depends on a variety of rays other than those directly represented by it. Therefore, each interpolant depends on several regions of line space; if all these dependency regions of an interpolant do not overlap with the hyperbola in line space, the interpolant is unaffected by the edit and can be reused. This section describes how to identify these dependency regions of an interpolant. Once the dependencies have been identified, a hierarchical global linetree can be used to track the identified dependencies and to rapidly invalidate the interpolants affected by an object edit.
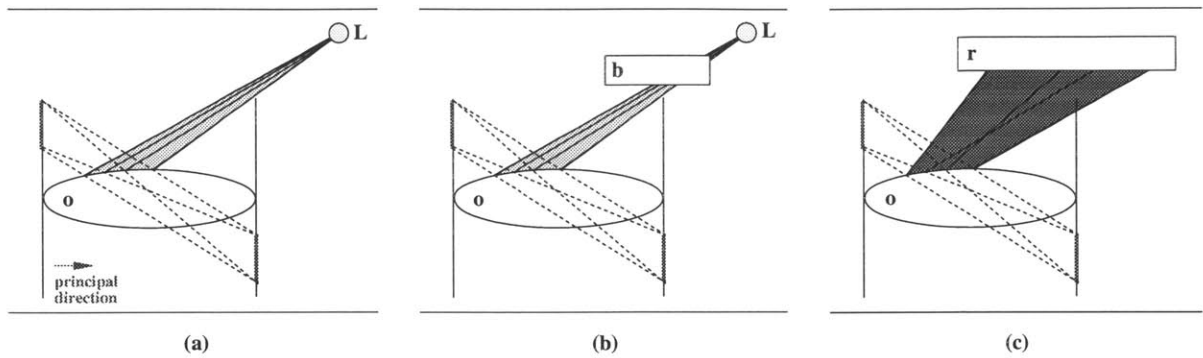
Figure 6-5: Rays that affect an interpolant: (a) light rays, (b) occluder rays, (c) reflected rays.

6.3.1 Interpolant dependencies in world space

In general, an interpolant depends on several regions of world space. When an edit affects a region of 3D space, the interpolants that depend on that region of space should be updated. The error bounding algorithm of Chapter 4 uses the sixteen radiance samples and their associated ray trees to determine if the interpolant approximates radiance to within a user-specified error bound over the region of line space that is *covered* by the interpolant. The error bounding algorithm ensures that the position-independent components of all rays represented by an interpolant are the same.

Consider an interpolant with its sixteen extremal rays. The sixteen extremal ray trees differ only in their position-dependent information (for example, their intersection points). Consider one set of sixteen corresponding arcs from the extremal ray trees; each arc is a ray segment. The error bounding algorithm ensures that the corresponding ray segment of every interior ray lies in the 3D volume bounded by the sixteen extremal ray segments. Therefore, when a scene edit affects that 3D volume of space, the interpolant should be invalidated to guarantee correctness. This 3D volume can be conservatively represented as a shaft [HW91]. The set of all shafts represented by an interpolant's ray trees is similar to the *tunnels* used by Brière and Poulin [BP96], although in that work, ray dependencies are captured only for a fixed viewpoint.

Now consider the different types of ray-tree arcs and the 3D volumes they cover. Figure 6-5 depicts three such arcs, corresponding to unoccluded light rays, occluded light rays, and reflected rays. In the figure, the ellipse o is the object for which an interpolant I is built. The interpolant is associated with the face pair shown as two vertical line segments surrounding o. The dotted lines show the four extremal rays (in 2D) that are used to build I. The two horizontal lines at the top and bottom of the scene show one of the face pairs of global line space. The volume that affects each arc (and therefore affects the interpolant) is shaded in each figure.

In Figure 6-5-(a), the four extremal rays intersect o, and their radiance is evaluated by shooting
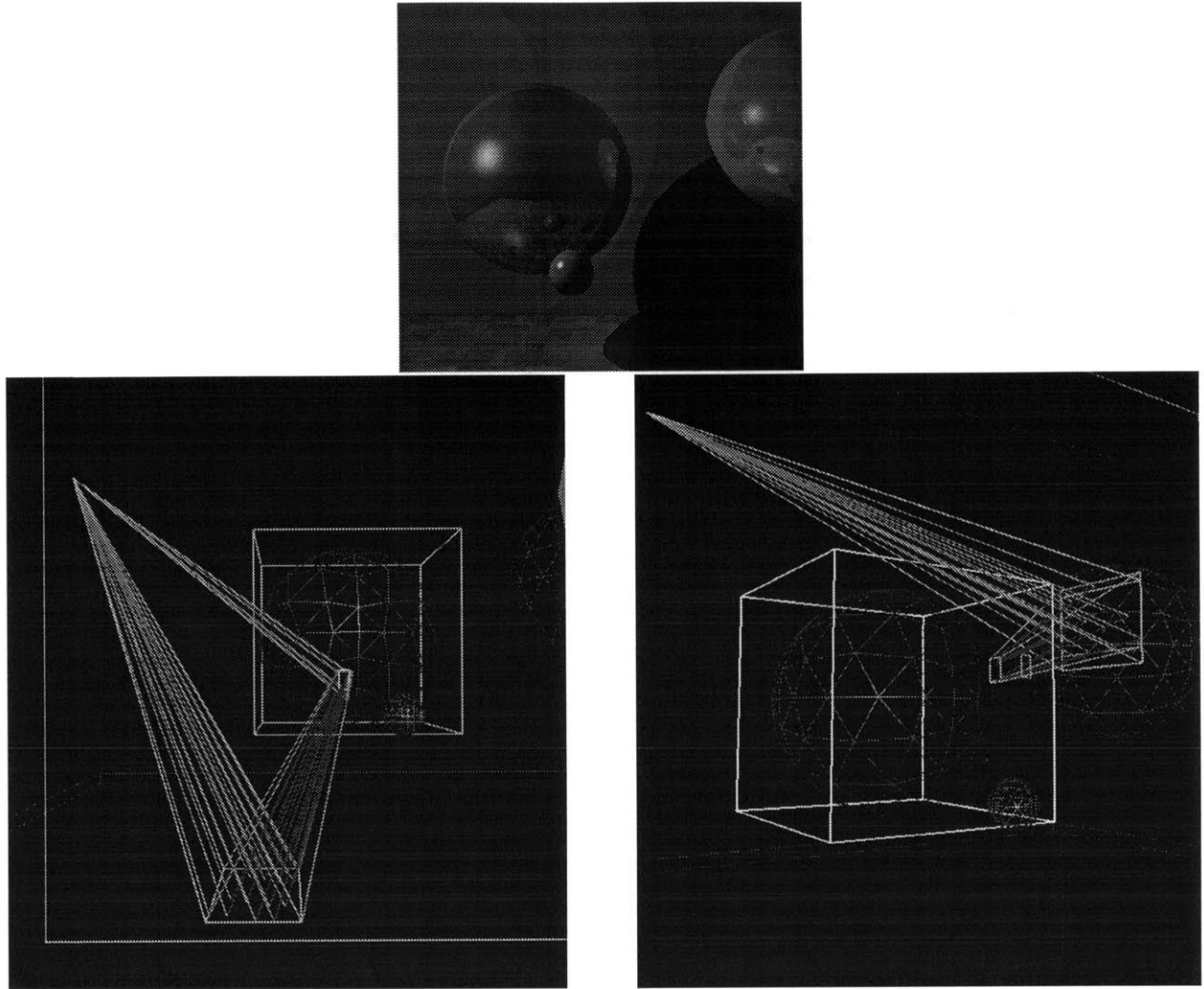
Figure 6-6: Tunnel sections of interpolants for the reflective red sphere.

rays to the light L, which is visible to every ray covered by I. Therefore, I depends on the shaded region shown in the figure. In Figure 6-5-(b), the light rays for the interpolant are all occluded by the same occluder b. If b is opaque, I depends only on the occluder b. If b is transparent, I depends on the shaded region shown in the figure. In Figure 6-5-(c), the volume of space that affects the arcs corresponding to reflections in the interpolant is shaded. Thus, the regions of world space that affect an interpolant can be determined using the ray trees associated with the extremal rays of the interpolant. An interpolant can become invalid only if the scene edit affects one of these regions.

In Figure 6-6, some tunnels associated with interpolants for the three-sphere scene are shown. The rendered image is shown in the top row. Two interpolants for the reflective red sphere (on the left of the image) and the world space regions the interpolants depend on are shown in the bottom row. The light is in the top left of the scene. On the left, an interpolant that reflects the ground plane is shown. The interpolant directly depends on the light and indirectly through the reflection
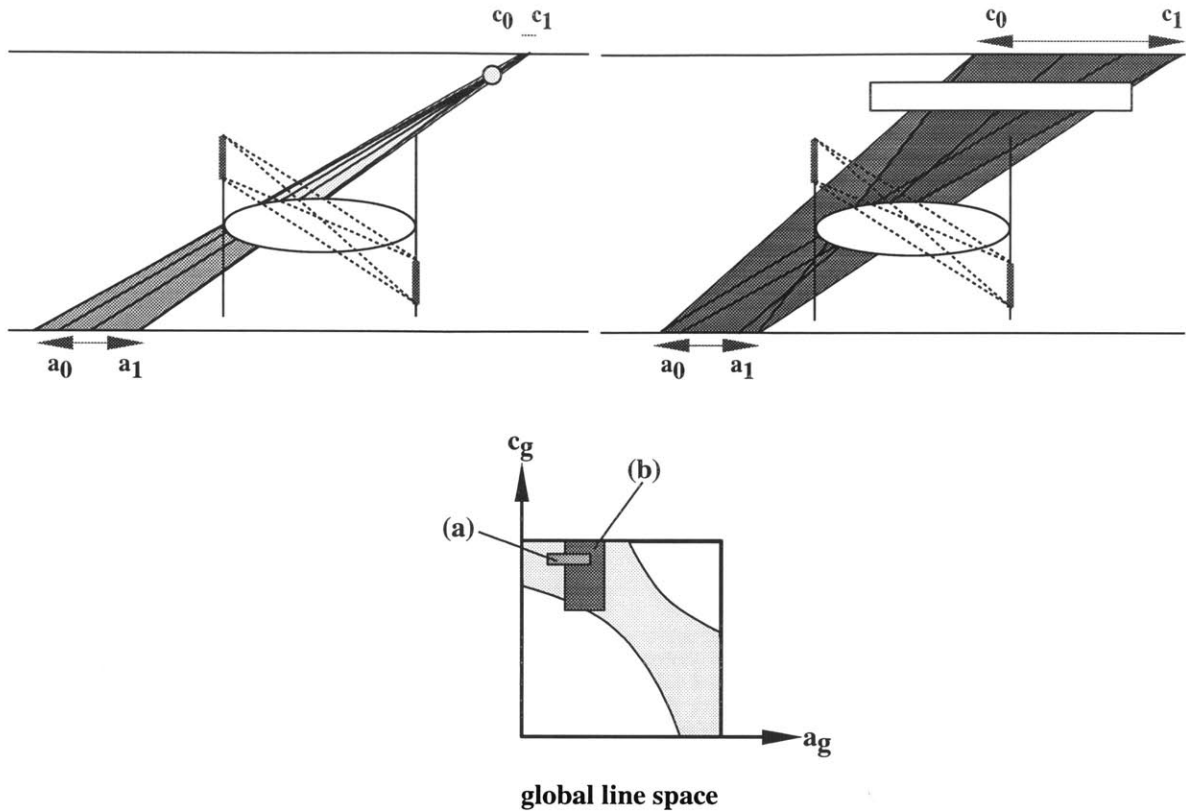
Figure 6-7: Global line space for: (a) light rays, (b) reflected rays.

off the ground plane. If a scene edits the indicated regions of world space, the interpolant will have to be invalidated or updated. On the right, an interpolant that covers the reflection of the green sphere in the red sphere is shown. The interpolant does not directly depend on the light, but it has a reflection which indirectly depends on the light.

6.3.2 Interpolant dependencies in global line space

Given a scene edit, the goal is to efficiently identify the interpolants that could be affected by the edit. This section describes how global line space can be used to track the regions of 3D space that affect an interpolant.

A scene edit affects a 3D volume; an interpolant depends on that 3D volume if any tunnel associated with the interpolant intersects the volume. Each of the tunnel sections of an interpolant is contained in some region of global line space. This region can be characterized conservatively by extending the extremal rays that define the tunnel section until they intersect the appropriate global face pair. For example, Figures 6-7-(a) and (b) show this computation in 2D. In Figure 6-7-(a), the four extremal rays from the object o to the light L are extended to intersect a global face

pair (shown as horizontal lines surrounding the scene). The a and c ranges of these intersections are computed. The corresponding rectangular region in line space, $[a_0, a_1] \times [c_0, c_1]$ (shown in the global line space depiction on the bottom), is a conservative characterization of the volume that affects the interpolant. In the figure, this region of line space is shown in medium gray. Similarly, in Figure 6-7-(b), the extremal reflected rays are intersected with the global face pair and the dark gray region shows the corresponding region of line space. This characterization is conservative because it covers a larger 3D volume than its tunnel section. In the next section this characterization is made more precise.

In 4D, each tunnel section of an interpolant is conservatively represented by 8 coordinates $(a_0, b_0, c_0, d_0)–(a_1, b_1, c_1, d_1)$ that define a 4D bounding box in line space. The tunnel sections affected by an object edit can be rapidly identified in the following manner: a linetree is constructed for each face pair of global line space. Each node of the linetree corresponds to a 4D bounding box in line space. A leaf node in the linetree contains pointers to every interpolant that *depends* on the region of line space represented by the node. In other words, for every interpolant included in the linetree node, the 4D bounding box of the linetree node intersects the 4D bounding box that conservatively represents at least one of the interpolant's tunnel sections. This hierarchical linetree can be used to rapidly identify the interpolants affected by an object edit.

6.4 Interpolants and ray segments

The previous section described a data structure that conservatively tracks the regions of line space that affect an interpolant. However, this representation is too conservative. This section introduces a 5D parameterization of rays to address this limitation, and describes *ray segment trees* that improve on the linetrees of the previous section.

6.4.1 Limitations of line space

The main disadvantage of the 4D representation of lines is that it is too conservative. This problem is illustrated in Figure 6-8-(a), which shows an interpolant for o. The tunnel section corresponding to reflected rays from o is shown in dark gray, while the corresponding conservative line space representation is shown in light gray. When the circles p and q are edited, they intersect the 4D bounding box represented by the tunnel section. Therefore, o's interpolant, stored in some leaf of the global linetree, is flagged as a potential candidate for invalidation. However, o's interpolant is only affected by changes in the dark gray region—this invalidation is unnecessary. This problem is addressed by introducing an extra parameter t for rays. Intuitively, this parameter represents
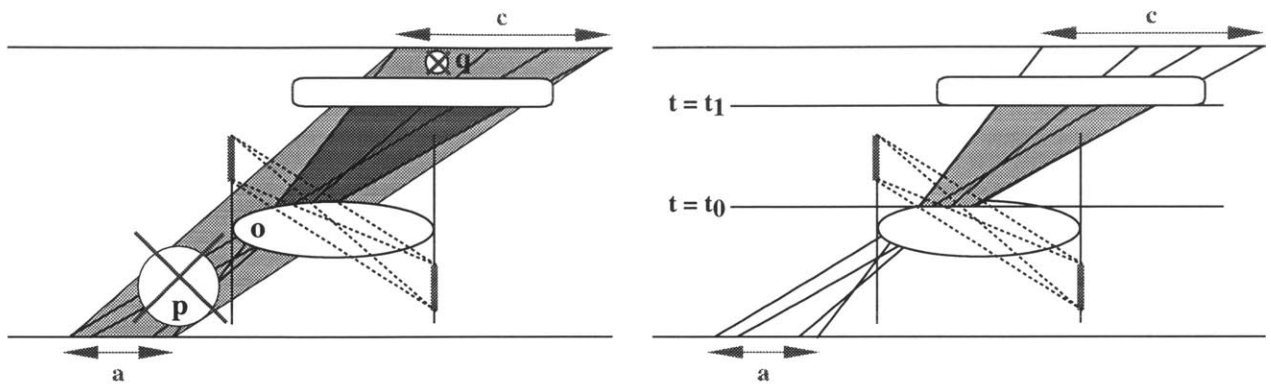
125

Figure 6-8: Line space vs. ray segment space. On the left, line space does not characterize dependencies accurately, causing unnecessary invalidations of unaffected interpolants. On the right, ray segment space characterizes dependencies more tightly than line space.

the distance along the 4D lines. In Figure 6-8-(b), the light gray line space region is bounded by $t = t_0$ and $t = t_1$. Using this extra parameter, o's interpolant is not flagged for invalidation when the circles are updated.

6.4.2 Ray segment space

The extra parameter t adds an extra dimension to line space: this new space is called *ray segment space (RSS)*. For 2D rays, RSS is a 3D space. For 3D rays, RSS is a 5D space. One important property of this space is the following: *an axis-aligned box in this space corresponds to a shaft in world space*. Therefore, shafts in 3D world space can be represented simply as boxes in ray segment space.

An interpolant has different dependency regions, corresponding to each tunnel covered by the interpolant. Each dependency region (or tunnel section) is conservatively represented by a 3D shaft, which is represented by a 5D bounding box in ray segment space. For example, in Figure 6-9, the interpolant on the left has 3 dependency regions. Each region is a box in RSS (shown on the right).

6.4.3 Global ray segment trees

To efficiently identify the interpolants that are affected by an edit, the system maintains six *global ray segment trees* (RSTs). Each ray segment tree node stores ten coordinates, $(a_0, b_0, c_0, d_0, t_0)$ to
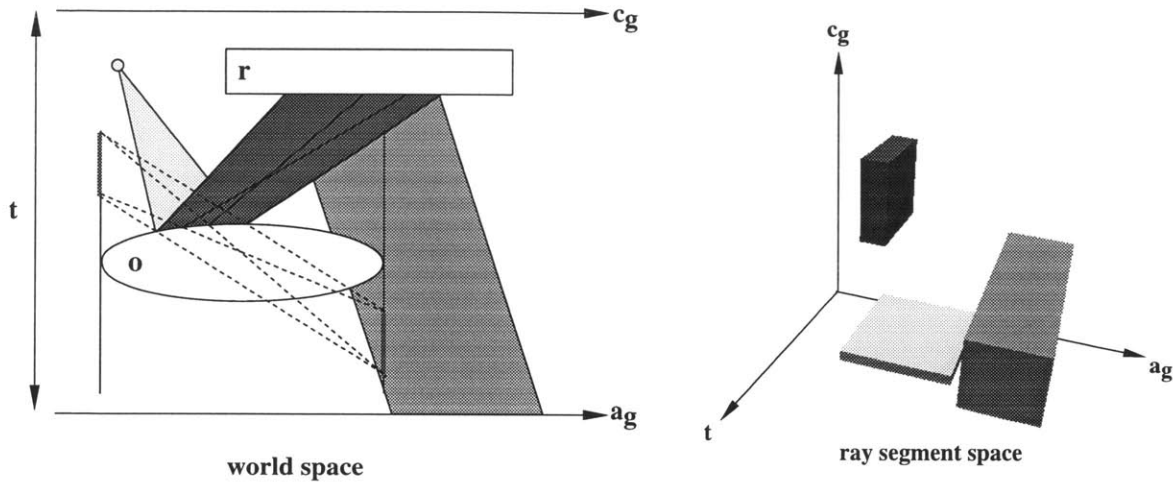
126

Figure 6-9: Interpolant dependencies in ray segment space.

$(a_1, b_1, c_1, d_1, t_1)$, that define a 5D bounding box in ray segment space. The t dimension represents the distance along the principal direction of the face pair. The front face of the face pair is at $t = 0$ and the back face is at $t = 1$. The root node of the tree spans the region from $(0, 0, 0, 0, 0)$ to $(1, 1, 1, 1, 1)$, and represents a shaft that encloses the scene. When an RST node is subdivided, each of its five axes is subdivided simultaneously. Each of the 32 children of the RST node covers the region of 5D ray space that includes the 3D shaft of all rays from its front face to its back face. While this branching factor may seem high, the tree is sparse, keeping memory requirements modest.

Figure 6-10 shows RST nodes for 2D rays. The parent node from (a_0, c_0, t_0) to (a_1, c_1, t_1) is shown on the top left, and a-c-t ray segment space (a three dimensional unit cube) is shown on the top right. The parent represents all rays entering its front face and leaving its back face. When the parent is subdivided, the rays represented by its eight children are as shown. Children 0 through 3 correspond to the ray segments that start at the front face at $t = t_0$ and end at the middle face at $t = \frac{t_0+t_1}{2}$. Similarly, children 4 through 7 start at the middle face and end at $t = t_1$. When the parent is subdivided, truncated segments of the parent's rays (shown in black in the figure) lie in different children. Together the eight children represent all the bounded ray segments in the parent.

6.4.4 Inserting interpolants in the ray segment tree

Ray segment trees are populated with interpolants by a recursive insertion algorithm that starts from the root RST node. For each tunnel section of the interpolant, its extremal rays are intersected with the current RST node to compute a 5D bounding box that includes the tunnel section. If this
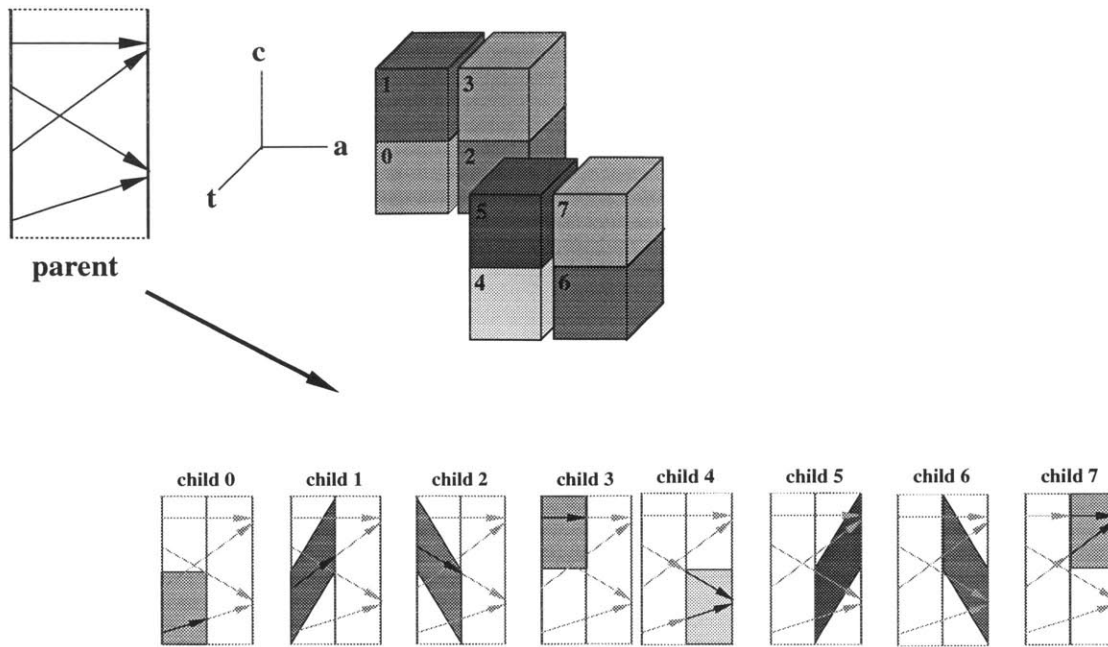
127

Figure 6-10: Subdivision of ray segment trees.

bounding box intersects a leaf RST node, a pointer to the interpolant is inserted in the node. For a non-leaf node, the algorithm recursively inserts the interpolant into the children of the RST node that intersect its 5D bounding box. As described in Section 6.2, the leaf node in an RST stores a list of pointers to every interpolant that *depends* on the region of ray segment space covered by that node and a list of the 5D bounding boxes of the interpolant's corresponding tunnel section. On the right in Figure 6-9, the three RSS bounding boxes corresponding to the interpolant on the left are shown. These boxes are inserted into the RST, which for 2D interpolants is an octree.

An RST node is split lazily when the number of entries in the node (tunnel sections of interpolants) exceeds a threshold. When split, the interpolants in the RST node are distributed to its children. This lazy approach is important for performance, because greedy splitting can result in excessive memory usage. For the results presented in Section 7, a maximum of 20 elements were permitted per RST leaf node. Another optimization was used for interpolants that intersect a significant fraction of the ray segment space represented by a parent RST node. If these interpolants were copied down blindly whenever the node is split, they would be replicated among many children of the RST node, wasting storage and computation. To avoid this problem, interpolants intersecting more than some threshold of children of a RST node are not copied down; instead they reside in the parent. For the results presented in Section 7, this threshold was set to 4. These settings performed well for a variety of scenes, though performance was not sensitive to their values.

128

6.5 Using ray segment trees

This section describes how interpolants affected by an object edit are rapidly identified and invalidated using RSTs. Brière and Poulin [BP96] describe two main categories of object edits: attribute changes (including changes to an object's color, specular or diffuse coefficient), and geometry changes (including insertion or deletion of an object). In their work, attribute and geometry changes are handled using different mechanisms, since attribute changes can be dealt with rapidly, while geometry changes require more time. Since the RSTs permit rapid identification of affected interpolants, the interpolant ray tracer uses the same mechanism to identify affected interpolants for both types of changes.

6.5.1 Identifying affected interpolants

When an object is edited, 3D shafts [HW91] are used to identify every region of ray segment space, and therefore every associated interpolant, that is affected by the edit. The identification algorithm is recursive and starts at each of the six root RST nodes with a world-space region v (the object's bounding box) that is affected by an object edit. For each RST node visited recursively, a shaft is built enclosing the 3D volume between the front and back face of the node. The shaft consists of six planes: four planes from each edge of the node's front face to the corresponding edge of its back face, and two planes that correspond to its front and back faces. If the shaft intersects v, the children of the RST node are recursively tested for intersection with v. When the shaft of a RST node does not intersect v, the descendants of that node are not visited. If the RST node is a leaf, it has a list of pointers to interpolants that depend on the 3D volume represented by the node's shaft, and the 5D bounding boxes of their corresponding tunnel sections. A 3D shaft is constructed for each such tunnel section. If that shaft intersects v, the interpolant is flagged as a candidate for update. Figure 6-11 shows the interpolants that depend on the reflective mirror at the bottom of the sculpture in the museum scene shown in Figure 5-8.

One class of interpolant dependencies (depicted in Figure 6-5-(c)), can be identified rapidly using a different mechanism. While building an interpolant for o, if a light is occluded by an opaque object b, that tunnel section of the interpolant can be affected when b moves. Therefore, a separate list of interpolants for occluders is maintained; when b is edited, its list of interpolants is marked for invalidation.
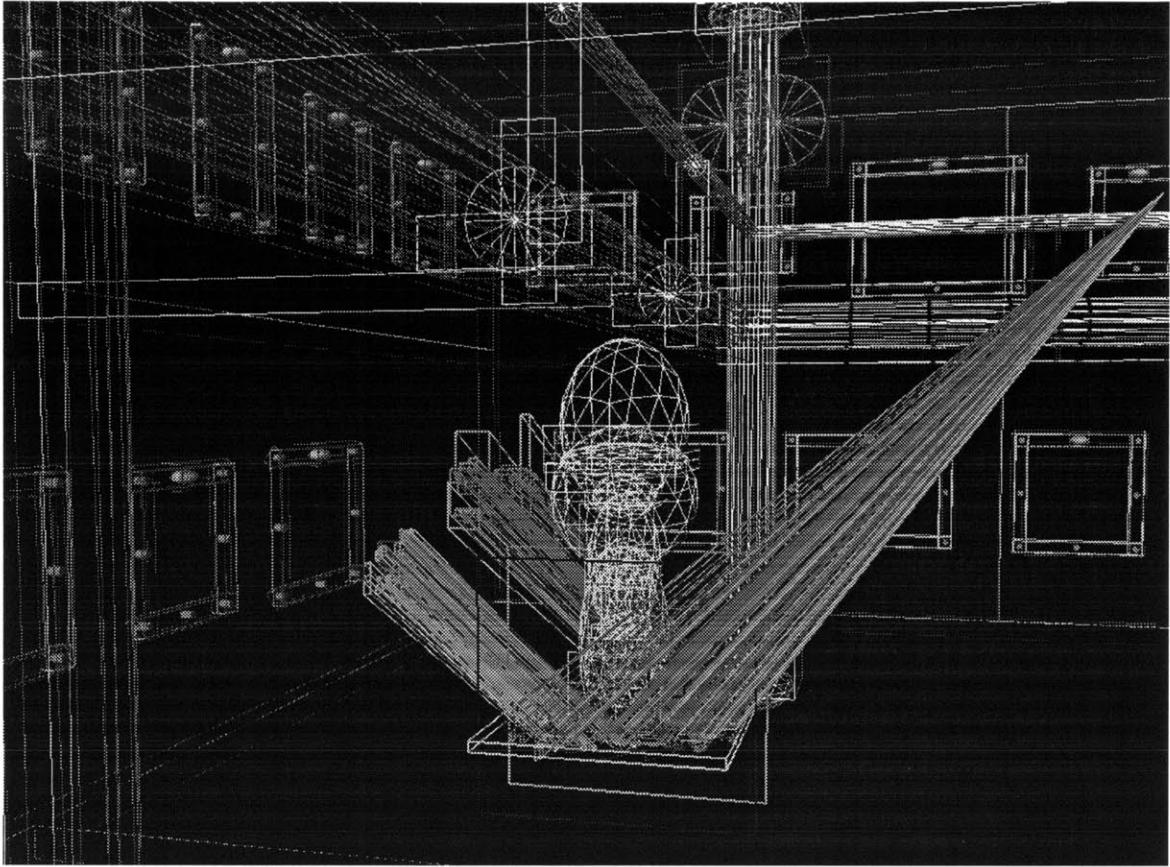
Figure 6-11: Dependencies for the reflective mirror in the museum scene.

6.5.2 Interpolant invalidation

The algorithm to identify affected interpolants is conservative: it might flag interpolants for update even if they are not affected by an object edit, because shaft culling against the edited object's bounding box is conservative. Therefore, an additional check is performed on the position-independent component of the interpolant's ray tree to determine if the interpolant is affected by the edit. For example, when o's color is edited, the edit affects an interpolant I if either I is o's interpolant, or I depends on o indirectly, for example through reflections. For a geometry change, such as the deletion of an object o, an interpolant I should be invalidated if I is o's interpolant, or o appears in the ray tree of I: for example, as an occluder or a reflection. Note that, as in [BP96], an object movement is treated as a deletion from its old position and an insertion to its new position.

When an interpolant is invalidated, the memory allocated to the corresponding object's linetree node is automatically garbage collected and the node itself is marked for deletion. If recursively

130

all that linetree node's siblings are also invalid, their space is reclaimed, and therefore, the parent is reclaimed. For example, consider an object o_1 that blocks the light to another object o_2, causing o_2's linetrees to be subdivided around o_1's shadow. If o_1 is deleted, o_2's interpolants are compacted, so that no unnecessary subdivision of o_2's linetrees takes place around the shadow that no longer exists.

To support rapid editing for attribute changes, interpolants could be augmented to include extra information such as the surface normal and point of intersection for each of the sixteen extremal rays. Using this extra information, the interpolants could be updated incrementally by computing the difference in radiance due to the change in o's material properties [BP96]. However, this extra position-dependent information increases the memory requirements of interpolants, without appreciable performance benefits. Therefore, the interpolant ray tracer invalidates interpolants for both attribute and geometry changes and lazily recomputes them as needed.

6.6   Discussion: pixel-based acceleration for scene editing

A potential optimization for scene editing is to use pixel-based techniques when the viewpoint is fixed. When extrapolation is not used, the time taken to re-render the scene is dominated by the time to render failed pixels that cannot be interpolated. In the special case when a user is making several edits without changing the viewpoint, the cost of rendering failed pixels can be further reduced by maintaining ray trees for each failed pixel. Because failed pixels account for only about 8-10% of the pixels in an image, as shown in Chapter 7, the cost of maintaining information for these pixels is correspondingly lower than in pixel-based scene editing systems.

Chapter 7

Performance Results

This chapter evaluates the speed and memory usage of my rendering system by comparing the interpolant ray tracer to the base ray tracer. The results demonstrate that the interpolant ray tracer can render images substantially faster than the base ray tracer: depending on the level of image quality desired, rendering is accelerated by a factor of 2.5 to 25. The memory usage of the system is modest and can be bounded using a cache management scheme. This scheme is effective, restricting total memory usage to 40MB with less than a 1% slowdown. This chapter also presents timing results for scene editing; it is shown that the ray tracer efficiently updates interpolants affected by a scene edit.

The rest of this chapter is organized as follows. Section 7.1 presents the base ray tracer and discusses some performance optimizations for the ray tracer. Section 7.2 describes the test scene used to evaluate performance. Section 7.3 presents timing results for the interpolant ray tracer, and Section 7.4 discusses a LRU cache management scheme to bound memory usage. Section 7.5 presents results for scene editing. Section 7.6 discusses how the various extrapolation algorithms presented in Chapter 5 perform for the museum scene. Section 7.7 discusses how the user can control performance-quality trade-offs. Section 7.8 discusses issues of interest for multi-processing the interpolant ray tracer and presents results.

7.1 Base ray tracer

The base ray tracer is a Whitted ray tracer extended to implement the Ward isotropic shading model [War92] and texturing. The ray tracer supports convex primitives (spheres, cubes, polygons, cylinders and cones) and the CSG union and intersection of these primitives [Rot82]. The base ray tracer is used by the interpolant ray tracer for non-interpolated pixels and for constructing

interpolants.

To make the comparison between the base ray tracer and the interpolant ray tracer fair, several optimizations were applied to both ray tracers. More precisely, the optimizations used in the base ray tracer when invoked by the interpolant ray tracer are also used by the base ray tracer when it is invoked as a stand-alone renderer. To speed up intersection computations, the ray tracer uses kd-trees for spatial subdivision of the scene [Gla89]. Marching rays through the kd-tree is accelerated by associating a quadtree with each face of the kd-tree cell. The quadtrees also cache the path taken by the most recent ray landing in that quadtree; this cache has a 99% hit rate. Therefore, marching a ray through the kd-tree structure is very fast. Also, shadow caches associated with objects accelerate shadow computations for shadowed objects.

7.2 Test scene

The data reported below was obtained for the museum scene shown in Figures 4-27, 5-8, and 7-1. The scene has more than 1100 convex primitives such as cubes, spheres, cylinders, cones, disks and polygons, and CSG union and intersection operations on these primitives. A coarse tesselation of the curved primitives requires more than 100k polygons, while more than 500k polygons are required to produce comparably accurate silhouettes. All timing results are reported for frames rendered at an image resolution of 1200×900 pixels. The camera translates and rotates incrementally from frame to frame in various directions. The rate of translation and rotation are set such that the user can cross the entire length of the room in 300 frames, and can rotate in place by 360° in 150 frames. These rates correspond to walking speed.

In Figure 7-1, rendered images from the scene appear on the left, and on the right, color-coded images show how various pixels were rendered. In the color-coded images, interpolation success (with or without reprojection) is indicated by a blue-gray color; other colors indicate various reasons why interpolation was not permitted. Green pixels correspond to interpolant invalidation due to radiance discontinuities such as shadows and occluders. Yellow pixels correspond to interpolants that are invalid because some sample rays missed the object. Magenta pixels correspond to interpolant invalidation because of non-linear radiance variations. Figure 5-8 differentiates between interpolated and reprojected pixels for the image on the bottom row in Figure 7-1.

134

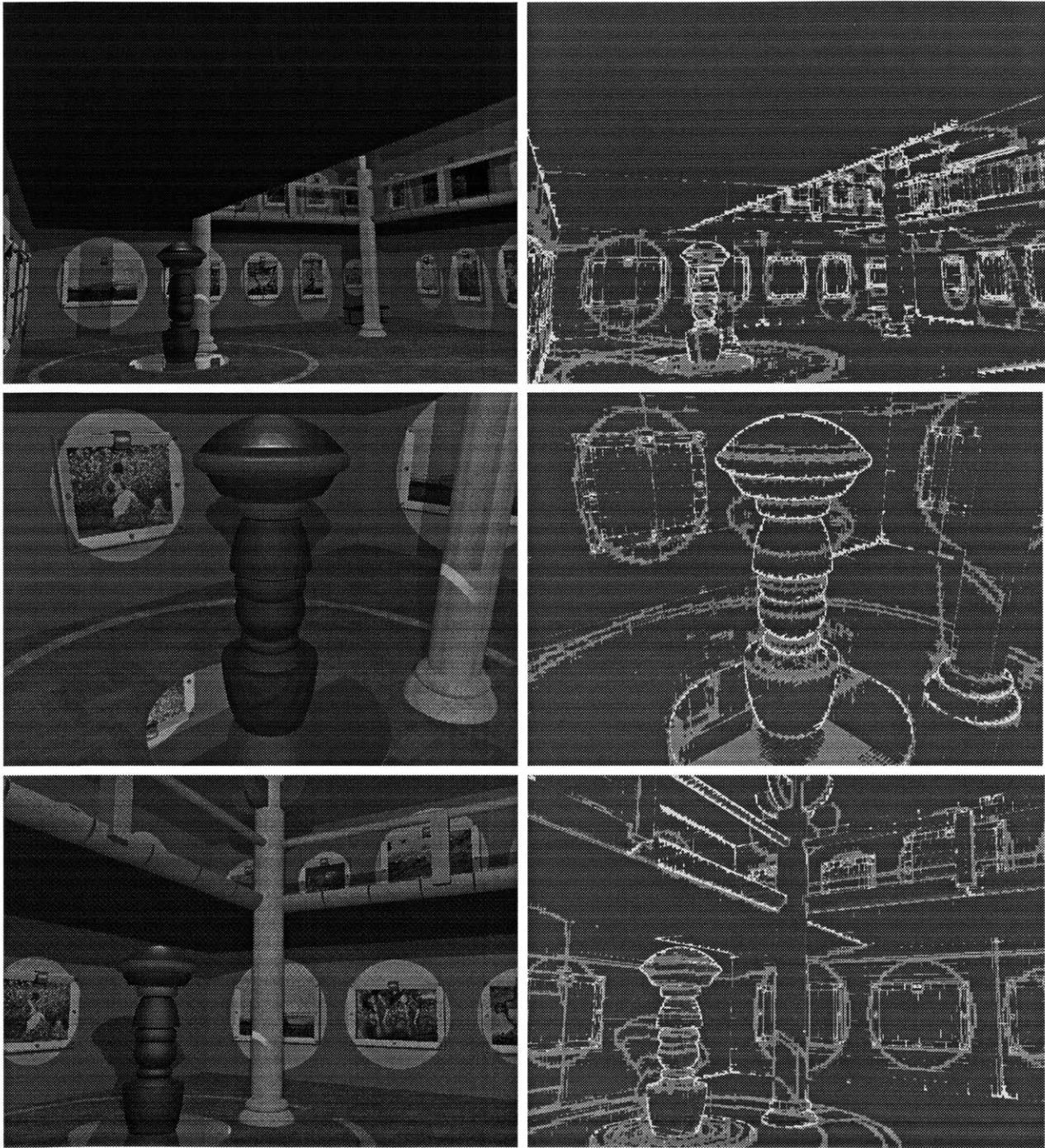Figure 7-1: **Museum scene**. Radiance is successfully interpolated for the blue-gray pixels. The error bounding algorithm invalidates interpolants for the green, yellow, and magenta pixels. Non-linearity detection is enabled for the bottom row. Green pixels: occluders/shadows. Yellow pixels: silhouettes. Magenta pixels: excessive non-linear radiance variation. Note the reflected textures in the base of the sculpture.

135

Path		Cost for path (μs)	Average fraction of pixels covered
Fast path	Span fill	1.9	75.2%
	Reproject	3.9	75.2%
	Total	**5.8**	**75.2%**
Interpolate path	Intersect object	24.1	16.88%
	Find linetree	4.5	16.88%
	Quad. interpolation	4.2	16.88%
	Total	**32.8**	**16.88%**
Slow path	Intersect object	24.1	7.92%
	Find linetree	4.5	7.92%
	Test subdivision	11.9	7.49%
	Build interpolant	645.5	0.43%
	Shade pixel (base)	160.6	7.92%
	Weighted total	**235.9**	**7.92%**
Interpolant ray tracer		28.5	100.0%
Base ray tracer		166.67	100.0%

Table 7.1: Average cost and fraction of pixels for each path over a 60 frame walk-through. The total time for the interpolant ray tracer, shown in the second to last row, is the weighted average of the time for each of the three paths. The last row reports the time taken by the base ray tracer.

7.3 Timing results

As described in Section 1.5.1, there are three paths by which a pixel is assigned radiance. These paths are shown in Figure 1-5 which is reproduced here in Figure 7-2 for ease of reference.

1. *Fast path*: reprojected data is available and used with the span-filling algorithm.

2. *Interpolate path*: no reprojected data is available, but a valid interpolant exists. A single intersection is performed to find the appropriate linetree cell, and radiance is computed by quadrilinear interpolation.

3. *Slow path*: no valid interpolant is available, so the cell is subdivided and interpolants are built if deemed cost-effective. If the built interpolant is invalid, the pixel is rendered by the base ray tracer.

Table 7.1 shows the costs of each of the three rendering paths. The data for this table was obtained by using the cycle counter on a single-processor 194 MHz Reality Engine 2, with 512 MB of main memory.
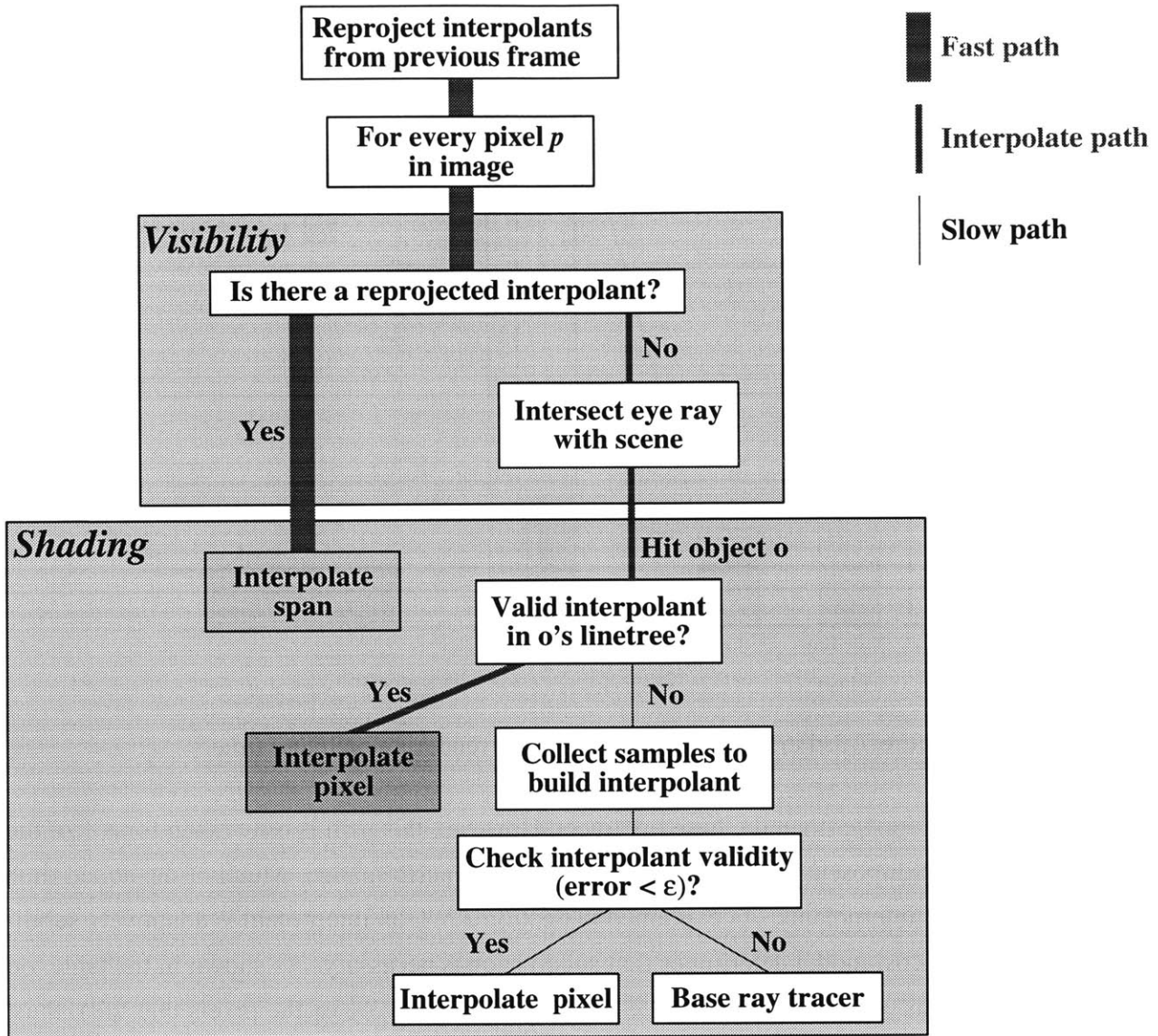
136

Figure 7-2: Algorithm overview.

In a 60-frame walk-through of the museum scene, about 75% of the pixels are rendered through the fast path, which is approximately thirty times faster than the base ray tracer for this scene. In this table, the entire cost of reprojecting pixels to the new frame is assigned to the fast path.

Pixels that are not reprojected but can be interpolated must incur the penalty of determining visibility. This interpolation path accounts for about 17% of the pixels. Quadrilinear interpolation is much faster than shading; as a result, the interpolation path is five times faster than the base ray tracer.

A pixel that is not reprojected or interpolated is rendered through the slow path, which subdivides a linetree, builds an interpolant (if deemed cost-effective), and shades the pixel. This path is
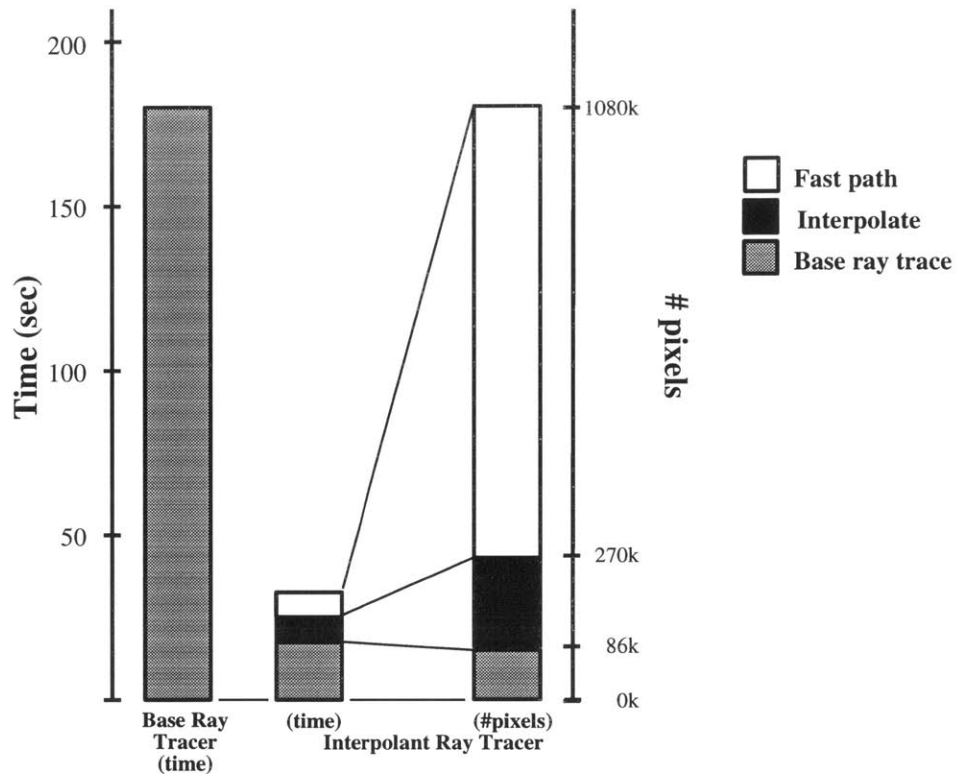
Figure 7-3: Performance breakdown by rendering path and time.

approximately 40% slower than the base ray tracer. However, this path is only taken for 8% of the pixels and does not impose a significant penalty on overall performance. Much of the added time is spent in building interpolants. As explained in Section 3.5.4, an interpolant is adaptively subdivided only when a cost model determines that subdivision is necessary. As shown in the table, on average, interpolants are built for only 0.4% of the pixels (about 5% of the pixels that fail); thus, the cost model is very effective at preventing useless work. The time taken to build interpolants could be further reduced in an off-line rendering application through judicious pre-processing.

In Figure 7-3, the average performance of the interpolant ray tracer is compared against that of the base ray tracer. The bar on the left shows the time taken by the base ray tracer, which for the museum scene is a nearly constant 180 seconds per frame. The middle bar shows the time taken by the interpolant ray tracer, classified by rendering paths. The bar on the right shows the number of pixels rendered by each path. Note that most of the pixels are rendered quickly by the fast path. Including the cost of reprojection, on average the fast path renders 75% of the pixels in 15% of the time to render the frame. Building interpolants and interpolating pixels (when possible) accounts for 19% of the time, and the remaining 66% of the time is spent ray tracing pixels that could not be interpolated.
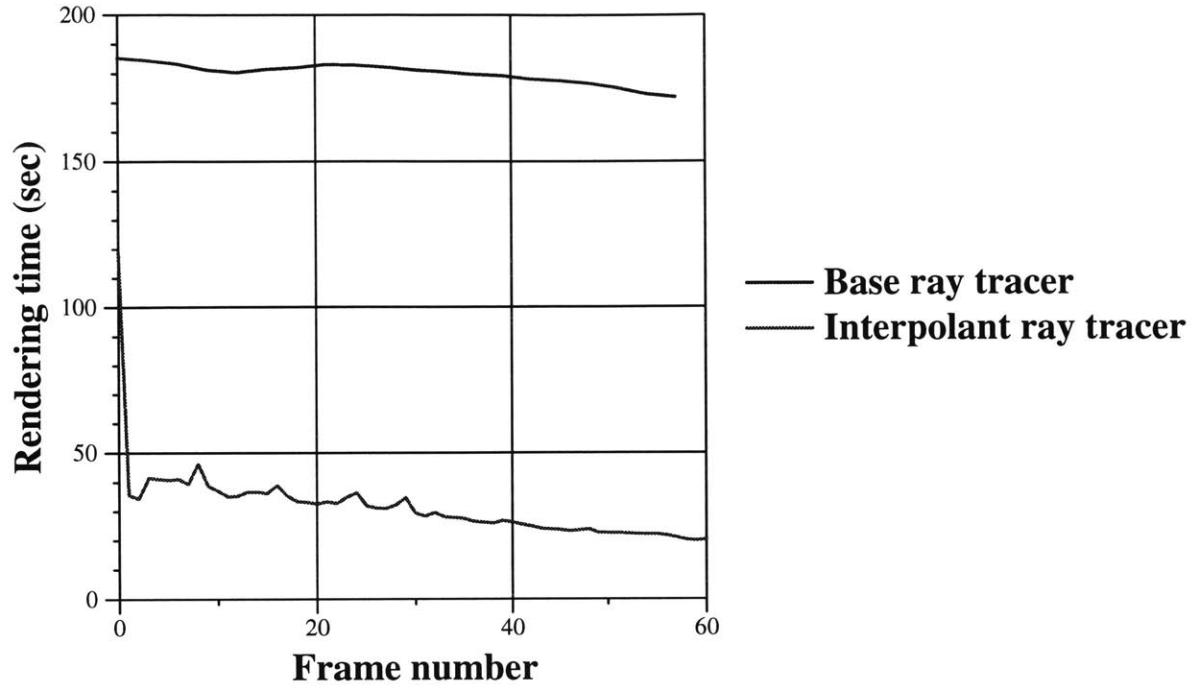
Figure 7-4: Timing comparisons for 60 frames.

In Figure 7-4, the running time of the base ray tracer and interpolant ray tracer are plotted for each frame. After the first frame, the interpolant ray tracer is 4 to 8.5 times faster than the base ray tracer. Note that even for the first frame, with no pre-processing, the interpolant ray tracer exploits spatial coherence in the frame and is about 1.6 times faster than the base ray tracer.

The time taken by the interpolant ray tracer depends on the scene and the amount of change in the user's viewpoint. Moving forward, for example, reuses interpolants very effectively, whereas moving backward introduces new non-reprojected pixels on the periphery of the image, for which the fast path is not taken. The museum walk-through included movements and rotations in various directions.

7.4   Memory usage and linetree cache management

One concern about a system that stores and reuses 4D samples is memory usage. The Light Field [LH96] and Lumigraph [GGSC96] make use of compression algorithms to reduce memory usage. The interpolant ray tracer differs in several important respects. The system uses an on-line algorithm that adaptively subdivides linetrees only when the error bounding algorithm indicates that radiance does not vary smoothly in the enclosed region of line space. Since this decreases the amount of redundant radiance information stored, the linetree data cannot be expected to be
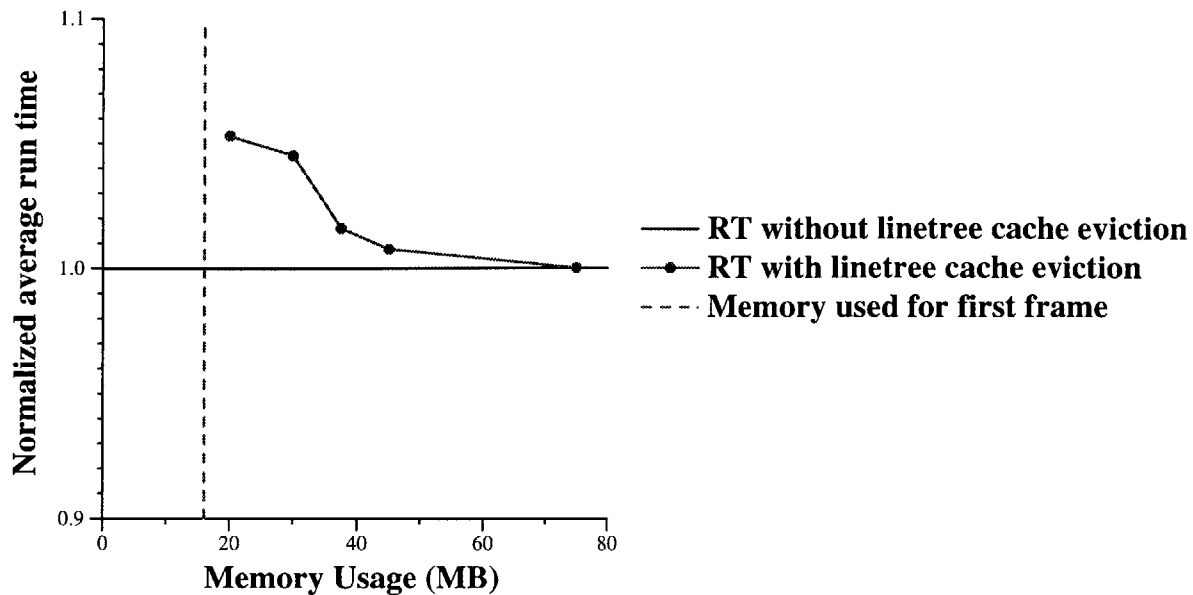
Figure 7-5: Impact of linetree cache management on performance.

as compressible as light fields or Lumigraphs. However, the memory requirements of the inter-polant ray tracer are quite modest when compared to these other 4D radiance systems. During the 60-frame walk-through, the system allocates about 75 MB of memory. As the walk-through progresses, new memory is allocated at the rate of about 1MB per frame.

Since the interpolant ray tracer uses an on-line algorithm, the system memory usage can be bounded by a least-recently-used (LRU) cache management strategy that reuses memory for line-trees and interpolants. The interpolant ray tracer implements a linetree cache management al-gorithm similar to the UNIX clock algorithm for page replacement [Tan87], though it manages memory at the granularity of linetree cells rather than at page granularity. The system allocates memory for linetrees and interpolants in large blocks. When the system memory usage exceeds some user-specified maximum block count, the cache management algorithm scans through entire blocks of memory at a time to evict any contained interpolants that have not been used recently. Each linetree cell has a counter that stores the last frame in which the cell was touched. If the linetree cell scanned for eviction is a leaf, and it has not been touched for n frames, where n is an *age* parameter, it is evicted. If all the children of a cell have been evicted, it too is evicted. Once the system recovers a sufficient amount of memory, normal execution resumes. Because scanning operates on coherent blocks of memory, the algorithm has excellent memory locality, which is important for fine-grained cache eviction strategies [CALM97].

In Figure 7-5, the performance of the LRU linetree cache management algorithm is evaluated. The horizontal axis shows the user-specified maximum memory limit. The gray vertical dashed

140

line shows the memory used when rendering the first frame (17 MB). The vertical axis shows the average run time of the interpolant ray tracer, normalized with respect to the average run time in the absence of memory usage restrictions (shown as a flat blue line). The green trace shows that the cache management algorithm is effective at preventing performance degradation when memory usage is restricted. Even when memory is restricted to 20 MB, the performance penalty is only 5%; at 45 MB, the penalty is only 0.75%. For long walk-throughs, the benefits of using cache management far outweigh this small loss in performance. Furthermore, it should be possible to hide the latency of the cache management algorithm by using idle CPU cycles when the user's viewpoint is not changing.

7.5 Scene editing

The part of the system that maintains and uses ray segment trees for scene editing is an optional module that can be activated selectively. In this section, timing results for scene editing are reported. All timing results are reported for frames rendered on a 250MHz single-processor of an SGI Infinite Reality. The results consider three edits to the museum scene, as shown in Figure 7-6: the top of the sculpture is deleted (Edit-(a)), the bottom of the sculpture is deleted (Edit-(b)), a green cube is moved in on the right (Edit-(c)). When the user changes the viewpoint, new interpolants are built as required.

Figure 7-6 shows the impact of these edits on interpolants. On the left, rendered images are shown, and on the right are color-coded images showing the regions of interpolation failure and success. As before, green, yellow pixels are not interpolated due to radiance discontinuities such as shadow edges and object silhouettes. Pixels that are successfully interpolated are shown in dark blue. The red pixels show the interpolants that are invalidated and rebuilt when the scene is edited. For example, after Edit-(a), the top of the sculpture and the shadow behind it are updated; the new interpolants lazily built to cover those pixels are shown in red. After Edit-(b), the interpolants associated with the bottom of the sculpture and its reflection in the mirror are found and invalidated.

Table 7.2 presents performance results for time and memory usage for scene edits. A change to the viewpoint is considered a scene edit, except that no interpolants are invalidated by the viewpoint change. This is because interpolants do not depend on the current viewpoint. For each of the edits, traversing the RSTs and invalidating the corresponding linetrees is fast: it takes about a tenth of a second. This is considerably faster than the invalidation process in pixel-based ray tracers supporting scene editing [BP96]. Depending on the type of edit, and its impact on interpolants, updating interpolants lazily while re-rendering a frame takes 4.5 to 14 seconds using the extrapo-
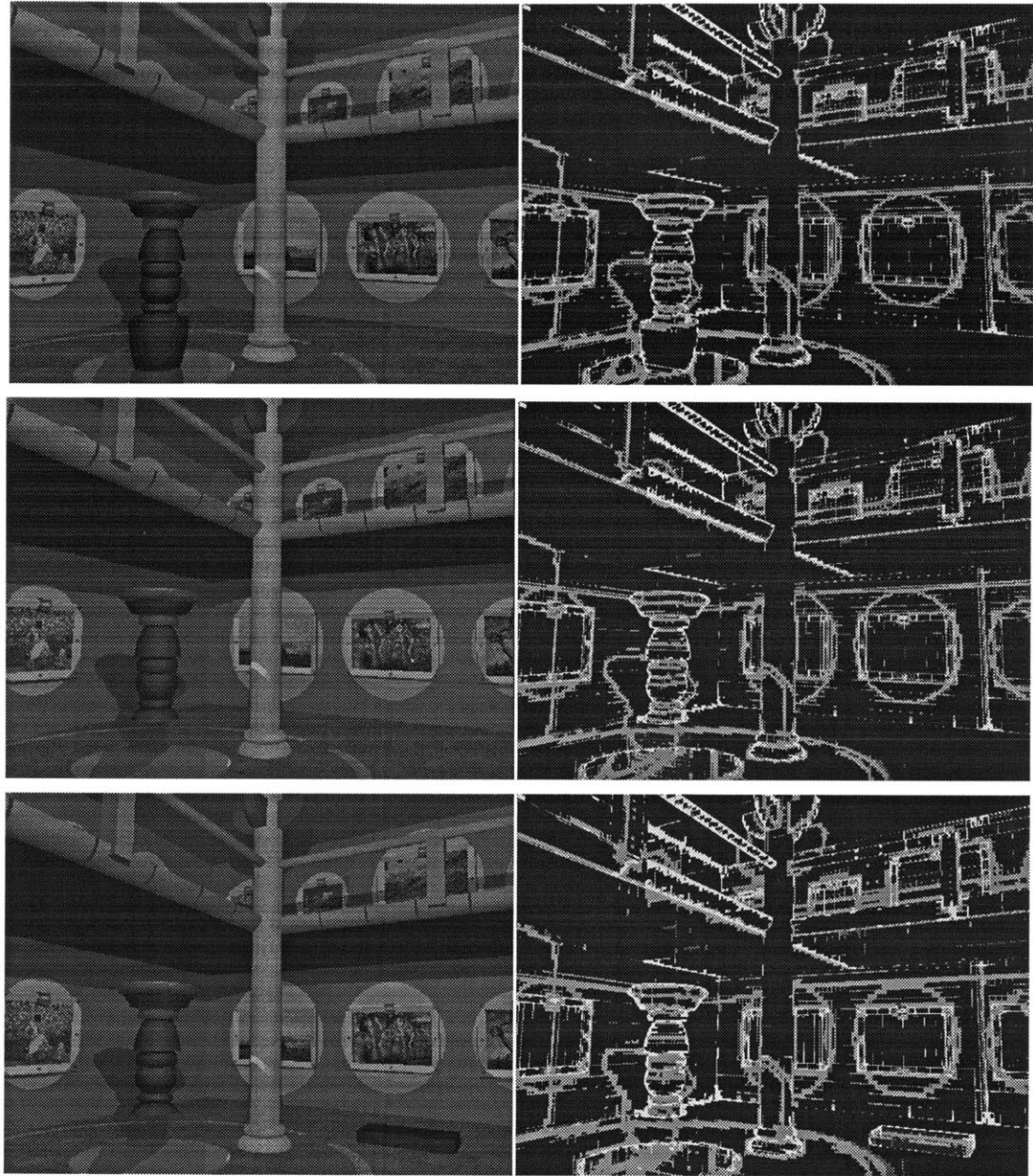
Figure 7-6: **Scene edits**. Top to bottom: Edit-(a), (b), and (c). Right: color-coded images; the red pixels are incrementally rendered.

lation algorithms described in Chapter 5; these extrapolation algorithms relax the error guarantees. Rendering with bounded error is done in 26 to 28 seconds. Of this time, building new interpolants lazily, shown in red in the plate, takes 1 to 3 seconds. Similar results are obtained when the object's material attributes (e.g., color) are changed. The fourth and fifth rows of the table show that as the viewpoint changes, frames are rendered in 4.5 to 14 seconds using extrapolation. When rendering with bounded error, camera changes result in rendering times of 26 to 31 seconds, depending on

Edit	Base ray tracer Time (s)	Interpolant ray tracer with RSTs			
		Time (s)			Memory (MB)
		Traverse RSTs and invalidate linetrees	Update and re-render		
			Extrapolation	Bounded error	
Edit-(a)	109.0	0.11	4.5–12	25.6	0.7 M
Edit-(b)	108.6	0.10	5.5–14	28.2	1.0 M
Edit-(c)	109.2	0.09	5.0–14	27.4	0.6 M
Pan	108.2	—	4.5–10	26.9	0.7 M
Forward	108.5	—	6.5–14	31.2	2.1 M

Table 7.2: Time and memory usage for edits and camera movements.

the camera movement; the greater the reuse of interpolants from the previous frame, the shorter the rendering time.

The memory requirements of this system are modest: each edit requires an additional 0.6 to 1 MB of memory. Camera movements typically require 0.7 to 2.1 MB of memory, depending on the type and extent of the movement. As described in the previous section, LRU memory-management is used to limit the memory usage to a user-specified maximum. For the first frame, RSTs require 5.5 MB of storage above the space required by the interpolant ray tracer. Subsequent frames require much less memory, as shown in Table 7.2. Note that this memory usage is much better than that of pixel-based systems. Since pixel-based systems store information on a per-pixel basis, memory overheads in these systems is reasonable only for lower-resolution images.

Unlike in other scene editing systems [BP96], the ray tracer using interpolants and updating the RST is faster than the base ray tracer even on the first frame. No pre-processing is needed to build RSTs; the time required to create RSTs in the first frame is small: less than 1 second.

7.6 Extrapolation

The time required to render a frame when the viewpoint changes can be improved further at the expense of image quality. This section presents results from the extrapolation algorithms of Section 5.3. These algorithms can be used to give the user feedback in a timely fashion. It should be noted that while none of these algorithms provide correctness guarantees; they give the user progressive, interactive feedback.

For the frame shown in Figure 5-10, the simple extrapolation algorithm renders a high-resolution image (1200 × 900) of the museum scene in 4 seconds using only reprojected pixels. Algorithm 3 takes an additional 1.5 seconds to produce images that have approximately correct visibility. Al-

gorithm 4 produces an image that is visually almost indistinguishable from the "correct" image, shown in Figure 5-11, in a total of 10 seconds.

Note that the extrapolation algorithm that guarantees correct visibility determination at each pixel of the image, Algorithm 2, takes a total of 9 seconds. In general, images produced by Algorithm 2 and Algorithm 3 are visually similar, though Algorithm 2 guarantees correct visibility determination at an increased cost, while Algorithm 3 achieves good performance with occasional errors due to incorrect visibility determination.

The final pass fills the failed pixels (the slow path) in about 18 more seconds, resulting in the image that the interpolant ray tracer produces. The advantage of this approach is that the user gets feedback rapidly, in 4 to 9 seconds, which is about 10 times faster than the base ray tracer for this image, with image quality comparable to the base ray tracer.

Although the results in this chapter are reported for images of 1200 × 900 pixels to allow a consistent basis for comparison, it is interesting to consider the performance of the renderer at lower resolution. Not surprisingly, the images at NTSC resolution (640 × 480 pixels) take less time to render. At this resolution, the simple extrapolation algorithm produces an image of the museum scene in 1.6 seconds. Algorithm 3 produces images in an extra 0.9 seconds; Algorithm 4 produces images in an additional 2.0 seconds. The failed pixels are then rendered in another 5-6 seconds. Thus, the user receives feedback quickly enough for practical interactive use.

Depending on the coherence in the scene, these progressive techniques provide rapid feedback (10× to 15× speedup over the base ray tracer) with good image quality.

7.7 Performance vs. image quality

The user-supplied error parameter ϵ allows graceful control of the computation expended per frame; a larger permitted error permits extended re-use of interpolants, and less computation expended per frame. Of course, this performance is achieved with lower image quality. A small permitted error results in longer inter-frame delays but produces higher image quality.

The interpolant ray tracer supports a number of different ways to trade performance for rendering quality. A comparison of these techniques is shown in Figure 7-7. The vertical axis of this plot shows the time required to render the museum scene. Note that the base ray tracer takes about 109 seconds to render this scene. Three different traces, marked by squares, diamonds, and circles, show the time required to accomplish three different rendering tasks with varying bounds on rendering error. For the trace marked by squares, the ray tracer is rendering the scene from a camera position forward from its previous position. For the trace marked by diamonds, the camera
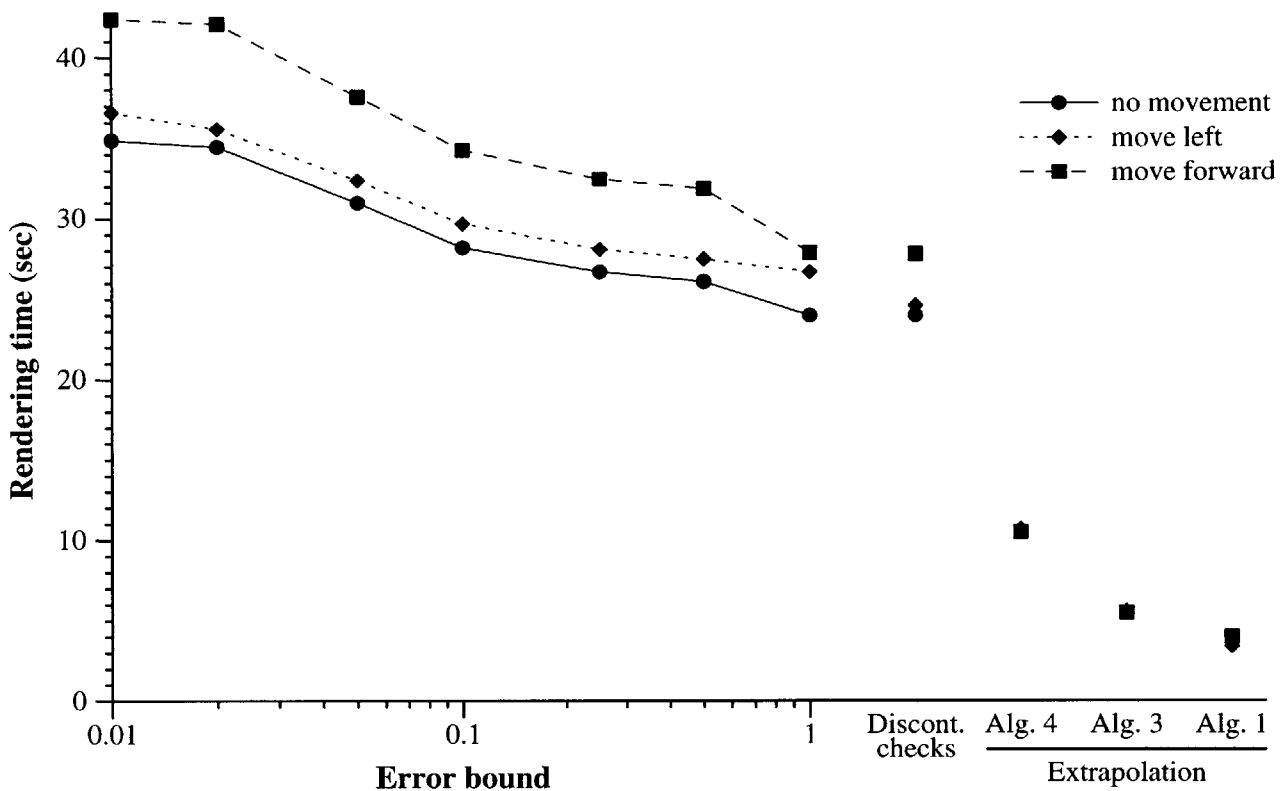
Figure 7-7: Performance vs. quality in the interpolant ray tracer

is turned to the right from the previous position. The trace marked by circles shows the cost of rerendering the scene from the same position as in the previous frame. The left side of the plot shows the time required to render the scene with detection of non-linear radiance variation turned on. The values along the horizontal axis are the relative error of radiance permitted. On the right side of the plot are timings for rendering methods with weaker quality guarantees. The "Discont. checks" cluster of timings measure the rendering time with discontinuity checking turned on, but non-linear checking turned off. The three points on the far right side of the horizontal axis provide results for three extrapolation rendering algorithms from Section 5.3. These rendering algorithms do not guarantee correct visibility determination or error bounds on radiance for the roughly 25% of the pixels that are not reprojected successfully.

The results show that the user has a wide spectrum of choices that trade performance for quality in rendering. Even when the error bound is set well below the limits of human perception (at 0.01 relative error), the interpolant ray tracer is 2.5 times faster than the base ray tracer. On the other end, extrapolation algorithm 4 offers a high-quality rendered image more than 10 times as quickly

as the base ray tracer; the other extrapolation algorithms offer speedup of up to $25\times$, though with more noticeable rendering artifacts.

Not shown in the figure is the time required to render the first frame. The rendering time for the first frame is faster in the interpolant ray tracer than in the base ray tracer for all the error settings except those in which $\epsilon \leq 0.05$. Even at the setting of $\epsilon = 0.01$, the interpolant ray tracer exhibits only a 16% slowdown rendering the first frame when compared to the base ray tracer. This slowdown occurs because the first frame requires the building of more interpolants than subsequent frames do. The fastest technique for rendering the first frame is to check only for discontinuity errors; the interpolant ray tracer is 1.6 times faster than the base ray tracer with this technique. Note that the extrapolation algorithms cannot be used to render the first frame because they rely on reprojected data from previous frames.

7.8   Multi-processing

Another technique for improving interactive performance is to use multiple processors to render the image. It should be noted that this technique also improves the performance of the base ray tracer. The interpolant ray tracer has been extended to run on a multiprocessor machine.

Two major issues should be considered when parallelizing a ray tracer: load balancing and memory contention. To achieve balanced loads when rendering a frame, the interpolant ray tracer divides an image into square chunks that are queued to the processors available. A work queue algorithm [BL94] is used to obtain balanced work-loads on each processor.

Several steps are taken to decrease memory contention between competing processors. The only data structure shared by the processors is the linetree. For example, each processor maintains its own common-ray hash tables to cache radiance samples, and performs all memory allocation using its own memory arenas. For the common-ray hash tables, it is less expensive to occasionally recompute radiance for some rays than to synchronize on every hash table access.

Because the linetree data structures are shared across all the processors, locks are placed in linetree nodes to prevent race conditions. However, the data structure is designed in such a way that interpolant lookups do not require any locking of linetree nodes. Locking is only required when inserting an interpolant into the linetree and when subdividing a linetree node. These optimizations greatly reduce the locking overhead, since multiple processors simultaneously read from the same linetree. Processors only block each other when updating the same linetree.

The shaft-culling phase of reprojection has not been parallelized, although it could be. The speedup for parallelizing shaft-culling should be nearly linear because workload balancing is

straight-forward and shaft culling is a computationally intensive (rather than memory-intensive) operation.

On a four-processor Reality Engine, rendering speedup is about 2.8× to 3.5× for the interpolant ray tracer. Speedup for the base ray tracer is slightly better, about 3.8×. This effect is to be expected because the interpolant ray tracer is a memory-intensive computation, and there is some memory contention between the processors. In addition, certain parts of the interpolant ray tracer are not parallelized in the current implementation.

Chapter 8

Conclusions and Future Work

This thesis presents the concept of radiance interpolants, which are used to approximate radiance while bounding approximation error. Interpolants allow ray tracing to be accelerated by exploiting object-space, ray-space, image-space and temporal coherence. The interpolant ray tracer described in this thesis uses radiance interpolants to accelerate both shading and visibility determination. The ray tracer also uses interpolants to support incremental ray tracing while permitting the user to edit the scene and the current viewpoint.

8.1 Contributions

Several new concepts and algorithms are introduced in this thesis:

- *Radiance interpolants:* This thesis demonstrates how radiance interpolants can be used to effectively capture the coherence in the radiance function. The thesis describes the interpolant construction mechanism that is used to sample the radiance function sparsely and reconstruct radiance. Hierarchical data structures over line space, called linetrees, are used to store radiance samples and facilitate efficient reconstruction of the radiance function.

- *Error bounds and error-driven sampling:* This thesis introduces novel geometric and analytical techniques to bound interpolation error. An error bounding algorithm is used to guide adaptive subdivision; where the error bounding algorithm indicates possible interpolation error, radiance is sampled more densely. Interpolation error arises both from discontinuities and non-linearities in the radiance function. The error bounding algorithm automatically and conservatively prevents interpolation in both these cases. Novel geometric techniques detect discontinuities. The thesis also describes how linear interval arithmetic can be applied to bounding non-linear radiance variations. To the best of my knowledge this is the

149

first accelerated ray tracer that bounds interpolation error conservatively. The error bounding algorithm is efficient and provides an accurate estimate of error; these properties are both important for its use in accelerating ray tracing. The thesis also demonstrates that error bounds can be used by the user to trade performance for quality. Even when the permitted error is very low, the interpolant ray tracer still accelerates rendering substantially.

- *Reprojection for visibility acceleration:* Determination of the visible surface for each pixel is accelerated by a novel reprojection algorithm that exploits temporal frame-to-frame coherence in the user's viewpoint, but guarantees correctness.

- *Interpolants for scene editing:* This thesis presents the first ray tracer that supports incremental ray tracing with scene editing while permitting changes in the user's viewpoint.

  Interpolants are shown to provide an efficient mechanism for incremental update of radiance when the scene is edited. The concept of ray segment space is introduced for scene editing; this five-dimensional space is useful because a bounding box in this space is a shaft in 3D space. This concept is used to identify the regions of world space that affect an interpolant. An auxiliary data structure, the ray segment tree, is built over ray segment space; when the scene is edited, ray segment trees are rapidly traversed to identify affected interpolants.

The performance results demonstrate that the interpolant ray tracer offers significant speedup. It successfully exploits coherence in radiance to accelerate ray tracing by a factor of $4\times$ to $15\times$. For the museum scene, the interpolant ray tracer accelerates 92% of the pixels, and only 8% of the pixels are rendered using the base ray tracer. For improved interactive feedback, the ray tracer also supports extrapolation algorithms that allow rendering of the scene without error guarantees in a few seconds. These extrapolation algorithms can be applied progressively in sequence, converging on an image with bounded error. For scene editing, the ray segment tree data structure allows identification of affected interpolants very rapidly; invalidation of these interpolants takes about 0.1 seconds in the museum scene. The additional overhead incurred when inserting information into the ray segment tree is less than 2%. Additionally, the thesis describes how a simple cache management algorithm can efficiently bound memory usage, keeping the memory requirements of the interpolant ray tracer modest.

8.2 Future work and extensions

The techniques presented in this thesis should be applicable to a variety of applications; some of these applications are discussed in this section. This section also discusses future avenues of

research that must be explored to support the extensions described in Section 4.5.

8.2.1 Animations and modeling

Animators should substantially benefit from the use of the interpolant ray tracer. An animator typically works in a model-render-model cycle in which he models the scene, previews his results by rendering the animation, and then uses these previewed animations to refine his model. Finally, once he has finalized his animation, he uses the ray tracer to produce high-quality images for final viewing. The interpolant ray tracer described in this thesis could be used to accelerate rendering and to improve the quality of the interactions that the animator has with the system in each of these phases of the creation of an animation.

There are several ways in which the interpolant ray tracer could be useful for this application. As the animator changes the scene, the interpolant ray tracer could incrementally render the scene to provide rapid feedback using the techniques developed in this thesis for scene editing. Once the animator is done modeling, the interpolant ray tracer could be used to rapidly compute images for previewing. The animator could use error bounds to trade performance for quality while previewing images. Finally, when the animator is ready to produce the high-quality animation, the techniques described in this thesis could be used to accelerate the rendering of the animation.

The following extensions to the interpolant ray tracer could further enhance the utility of the interpolant ray tracer for this application.

Persistence. A persistent store interface could be used to store interpolants as they are built for previews. These stored interpolants then could be reused from session to session as the animator refines the scene. As the animator edits the scene, the appropriate interpolants could be invalidated or reused appropriately. Once the animator is done modeling the scene and wants to create the final animation, he can invoke the interpolant ray tracer to render the animation with high quality (i.e., small ϵ). The interpolants stored in persistent storage could be reused to produce the final animation, provided they satisfy the error bound. Thus, the system could build and reuse interpolants from modeling sessions to final animations incrementally. There are several interesting systems issues that should be addressed to achieve this goal: for example, how to represent radiance in persistent storage and how to compress large radiance data sets effectively. Funkhouser et al. [FST92] address storage issues for large radiosity data sets; some of their techniques should be applicable to this problem. IBR systems [GGSC96, LH96] present techniques to compress 4D radiance information; these techniques should be applicable to the compression of radiance interpolants as well. However, since linetrees are not uniformly subdivided arrays, and interpolants already cap-

ture coherence in radiance, compression rates cannot be expected to be as high as in these previous systems.

Representing time explicitly. Animations typically have pre-defined trajectories for objects and the viewpoint. A useful extension would be to explicitly sample the temporal dimension when building interpolants. The domain over which samples are collected is then a five dimensional space, a temporal-line space. Glassner [Gla88] considers using a four dimensional spatio-temporal space to accelerate animations. The 5D temporal-line space described here is similar in spirit to Glassner's spatio-temporal space, although in this case, the interpolants would store time-varying radiance information. This approach opens an interesting avenue of research: translating error guarantees in 4D line space to meaningful error guarantees in 5D temporal-line space. It will be necessary to refine the invariant maintained by the error bounding algorithm, developing a notion of temporal error.

8.2.2 Architectural walk-throughs

Ray tracing is often used to produce high-quality imagery in large off-line animations for architectural walk-throughs and other visualizations. The techniques introduced in this thesis should be useful in accelerating both these pre-programmed animations and interactive walk-throughs. As described above, the interpolant ray tracer can be used directly for a pre-programmed animation where the user completely specifies a camera path. An interesting extension would be to support accelerated rendering when the user does not specify the entire camera position. Note that if the user provides absolutely no viewing information to the interpolant ray tracer, the ray tracer would start sampling the radiance function from all possible viewpoints. This could be prohibitively expensive. However, sampling could be limited usefully if the user provided an approximate description of the viewing trajectory; for example, the viewpoint could be restricted to a set of rooms in a building, or the user could provide a notion of the important features in the building for which interpolants could be built. This information would be used by the ray tracer to guide where samples are collected in the space of rays. This approach suggests several interesting areas of research.

8.2.3 Intelligent, adaptive sampling

When rendering high-resolution images, ray tracers typically must resolve a tension between sub-sampling the image to achieve good rendering performance, and super-sampling the image to achieve good image quality. While a ray tracer can achieve good performance by sampling an image sparsely, image quality may suffer because the ray tracer may miss small features, high-

lights, small reflections and shadows. These small features are important to the human perceptual system, particularly when animations are rendered; missing small features in some frames while capturing them in others results in disturbing speckling artifacts.

Existing algorithms that use adaptive sampling typically require hand tuning to ensure that good quality results are achieved with good performance. Also, these algorithms typically cannot accommodate varying sampling rates across an image: coarse sub-sampling is desired in the parts of the image where radiance varies smoothly, and super-sampling is needed where radiance changes rapidly. It is important to have quality assurances that are robust, automatically enforced without hand-tuning, and that permit sparse sampling where possible for good performance.

Independent of the interpolant mechanisms, the error bounding techniques described in this thesis should be applicable to this problem of adaptive sampling. Because the error bounding algorithm is able to characterize how the radiance function varies over ray space, this characterization could be used to guide intelligent sampling of images that provide good performance. The error bounding algorithm would allow computational resources to be focused automatically on the parts of the image that must be super-sampled at greater resolution, while identifying the parts of the image that can be sampled sparsely.

8.2.4 Perception-based error metrics

One area of research that is gaining prominence in computer graphics is the use of perception-based error metrics in rendering [FPSG96, FPSG97, PFFG98, BM98]. The error bounding algorithm presented in this thesis is used to bound either actual or relative error in radiance; however, since discontinuities are important to the visual system, they are treated as a special case. An interesting area of future research would be to generalize the error techniques presented in this thesis to capture other perceptually-important aspects of radiance variation. These perceptual techniques would complement the existing error bounding algorithm.

8.2.5 Generalized shading model, geometry and scene complexity

Section 4.5 describes several possible extensions to the system that extend its shading model and permit greater geometric, lighting, and scene complexity.

Non-convex and parametric surfaces. One limitation of the interpolant ray tracer is that it can only guarantee error bounds for convex primitives. Interpolants are not built for non-convex primitives; therefore, rendering of these primitives is not accelerated. The interpolation mechanism

remains the same for these primitives; the main research problem to be solved is extension of the error bounding algorithm to support these primitives.

Section 4.3 briefly sketches how interval arithmetic might be generalized to support non-convex objects described by parametric patches. The linear interval approach is easily applied to any surface defined by an implicit equation. To apply it to parametric surfaces requires the ability to solve for the surface patch parameters s and t in order to obtain accurate bounds on the surface normal. This can be accomplished using interval-based root finding, which generalizes to linear intervals [Han75].

Non-convex objects can be supported in a number of ways. One simple, conservative approach is to bound a non-convex object o on the inside and outside by convex objects. For complex non-convex objects, the object o can be broken into smaller pieces to allow these bounding convex objects to closely approximate the surface of o. For those parts of the error bounding computation that depend on convexity, such as the tests for shadow edge discontinuities, one or both of these convex objects can be used in place of o to ensure that error is bounded conservatively.

Textures. It would be useful to expand the support for textures in the interpolant ray tracer to include more general texturing techniques, such as bump maps and displacement maps. Bounds on perturbed surface positions and normals can be extracted for each interpolant from the region of the map corresponding to the object surface area covered by the interpolant. These bounds can then be applied in a straightforward manner to the linear interval analysis equations in Section 4.3. Other extended texturing techniques of interest include maps for specular and reflective surface coefficients. A similar bounding technique should be applicable for these maps as well.

Diffuse global illumination. Extending the ray tracer to compute diffuse inter-reflections and generalized BRDFs would be useful. The research question that must be addressed for this to be feasible is how to manage the increased complexity due to extra links to other sources of energy.

The invariant defined in Section 4.1.1 could be relaxed to permit interpolation across small discontinuities; understanding the implications of relaxing this invariant is an important research area. Importance-driven techniques [SAS92] could be used to track the important sources of light energy for each interpolant. Sources of energy that contribute light energy below the error threshold would be ignored. The error bounding algorithm would use this relaxed invariant of error, so a detected discontinuity would invalidate an interpolant only if the resulting interpolation error exceeds the user-specified bound. While the error guarantees will continue to be satisfied, the implication of this relaxed error invariant on perceived error deserves detailed study.

154

Clustered lights, area lights, large number of lights. Support for more general light sources, such as area light sources, clustered lights, and increased lighting complexity would be useful. As described above, in this case the invariant maintained by the error bounding algorithm could be relaxed to permit interpolation across discontinuities that are not important. While some researchers are studying the problems associated with clustered lights, area lights and their implications on illumination [PPD98, War91, SS98, WH98], computing error bounds with these forms of illumination is an open area of research.

Appendix A

Scene Editing: line space affected by an edit

This appendix characterizes the region of line space affected by an edit to a circular region of world space (in two dimensions) or a spherical region of world space (in three dimensions). As described in Section 6.2, in two dimensions the region of line space affected by a circular object edit is a hyperbola. In three dimensions, the region of line space affected by an edit can be characterized by a fourth-order equation. Gu et al. [GGC97] consider the relationship between points and lines in world space and line space. By considering points to be circles of zero radius, the treatment in this appendix can be seen as a generalization of those results.

world space   global line space
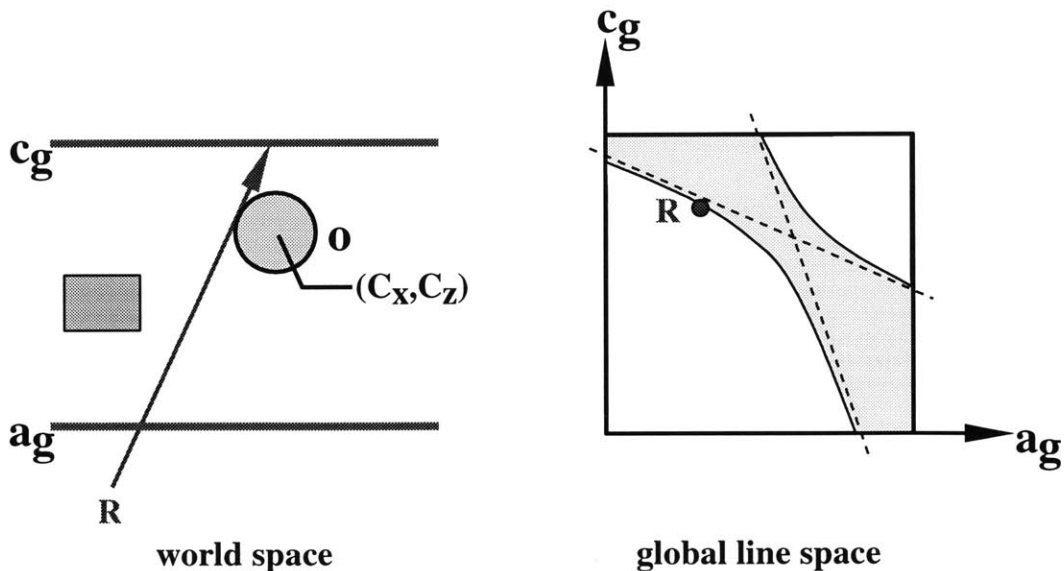
Figure A-1: A hyperbolic region of line space corresponds to a circular region of world space.

A.1 Edits in two dimensions

Consider a scene and its four global segment pairs. In Figure A-1, one of the four segment pairs (the pair of thick horizontal lines), with $+\hat{z}$ as principal direction, is shown on the left. When a circular object o is edited, every ray that passes through o is affected by the edit.

Claim: The region of line space (shown as a square on the right of the figure) affected by edits to o is the interior of a hyperbola in 2D.

Proof: A ray $\mathbf{R}$ is specified by its intercepts $[a, c]$ on its associated segment pair. Without loss of generality, we assume that the front segment is at $z = -\frac{1}{2}$, and the back segment is at $z = \frac{1}{2}$. Therefore, $\mathbf{R} = [c - a, 1]$. If $\mathbf{R}$ is a ray on the boundary of the region of line space affected by the edit, it satisfies two additional constraints: $\mathbf{R}$ intersects the circle o at some point $\mathbf{P} = [X, Z]$, and $\mathbf{R}$ is tangential to the circle at $\mathbf{P}$. There are three constraints: $\mathbf{P}$ lies on $\mathbf{R}$, $\mathbf{R}$ is perpendicular to the normal at $\mathbf{P}$, $\mathbf{P}$ lies on the circle.

$\mathbf{P}$ lies on $\mathbf{R}$.

$$
\begin{aligned}
[X, Z] &= [a, -\frac{1}{2}] + t[c - a, 1] \\
Z &= t - \frac{1}{2} \\
X &= a + t(c - a) \\
X &= a + (Z + \frac{1}{2})(c - a) \\
X &= \frac{a + c}{2} + Z(c - a)
\end{aligned}
$$

$\mathbf{R}$ is perpendicular to the normal at $\mathbf{P}$.

$$
\mathbf{R} \cdot \mathbf{N} = 0
$$

$$
\begin{aligned}
(c - a, 1) \cdot (X - C_x, Z - C_z) &= 0 \\
(c - a)(X - C_x) + Z - C_z &= 0 \\
(c - a)(\frac{a + c}{2} + Z(c - a) - C_x) + Z - C_z &= 0 \\
Z(1 + (c - a)^2) &= C_z + C_x(c - a) - \frac{(c - a)(a + c)}{2} \\
Z &= \frac{C_z + C_x(c - a) - \frac{(c-a)(a+c)}{2}}{1 + (c - a)^2} \\
X &= \frac{(C_z + C_x(c - a))(c - a) + \frac{a+c}{2}}{1 + (c - a)^2}
\end{aligned}
$$

158

P lies on the circle.

$$(X - C_x)^2 + (Z - C_z)^2 = R^2$$

Eliminating t, X and Z:

$$[(c - a)C_z + (\frac{a + c}{2} - C_x)]^2 - R^2[1 + (c - a)^2] = 0 \qquad \text{(A.1)}$$

Equation A.1 is a second-order equation in a and c. The discriminant of the equation satisfies the condition of a hyperbola [Som59]. Thus, when the circle o is edited, the region of 2D line space affected by the edit is the interior of a hyperbola—that is, the rays in the shaded region on the right in Figure A-1 are affected by the edit. The parameters of the hyperbola can be derived from o's location and radius. When the circle is edited, the radiance of every ray in the interior of the hyperbola (shaded in Figure A-1) could be affected.

A.2   Edits in three dimensions

A similar derivation identifies the region of 4D line space affected by an edit to a 3D sphere o. Each ray **R** associated with the face pair with principal direction $+\hat{z}$ is specified as $[c - a, d - b, 1]$. The region of 4D space affected by an edit to a 3D sphere is characterized by the following fourth-order equation:

$$[(c - a)C_z + (\frac{a + c}{2} - C_x)]^2 + [(d - b)C_z + (\frac{b + d}{2} - C_y)]^2$$
$$- R^2[1 + (c - a)^2 + (d - b)^2]$$
$$+ [(c - a)(\frac{b + d}{2} - C_y) - (d - b)(\frac{a + c}{2} - C_x)]^2 = 0$$

While the first two lines of the equation are exactly the 4D generalization of a 2D hyperbola, the third line in the equation introduces fourth-order cross terms. Thus, when a 3D sphere o is edited, the region of 4D line space affected by the edit is not a hyperboloid, but it is specified by a fourth-order equation. Every ray *inside* the surface represented by this equation could potentially be affected by the object edit.
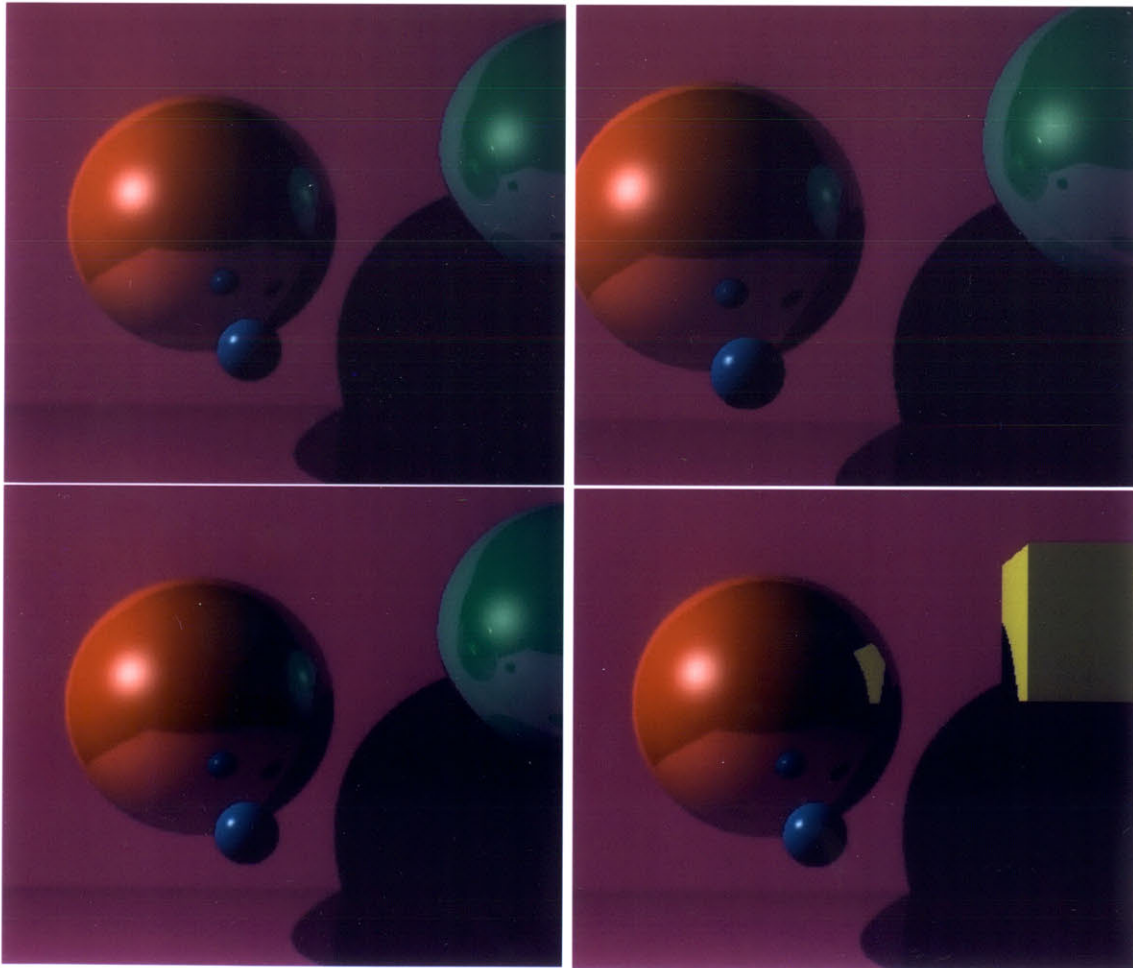
159

Appendix B
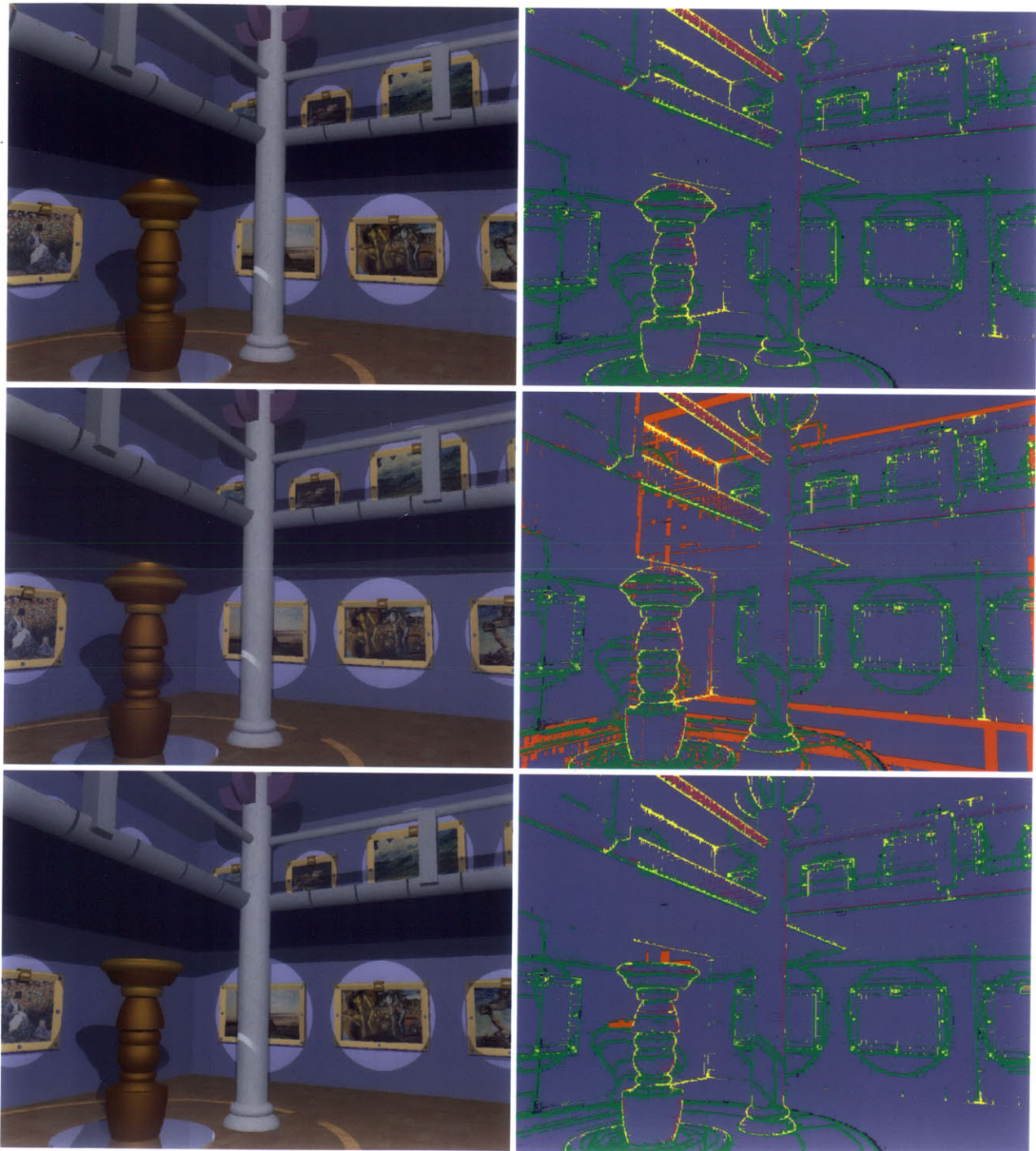
Color plates

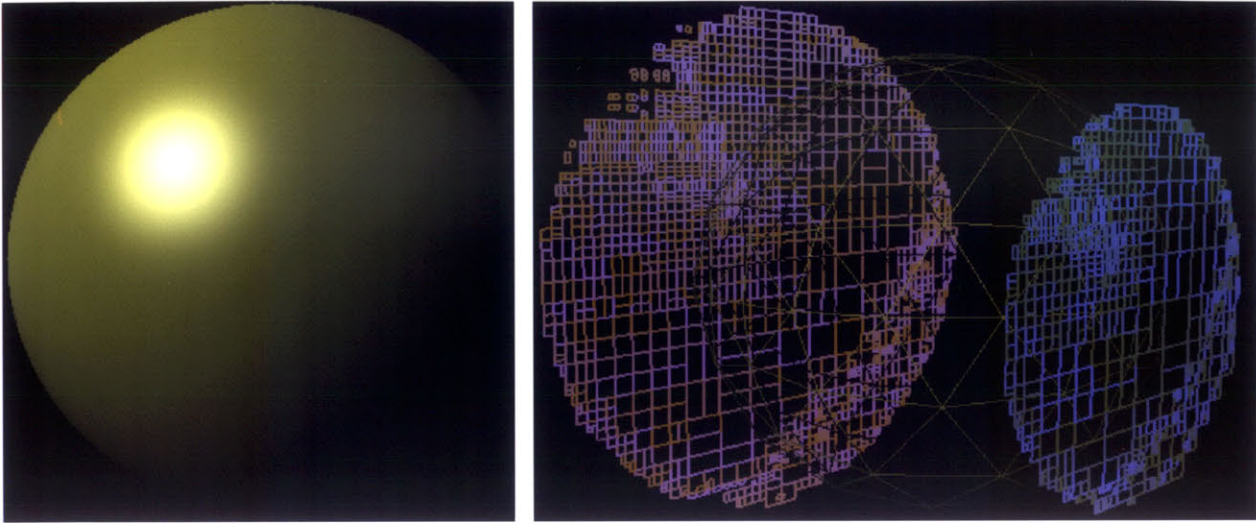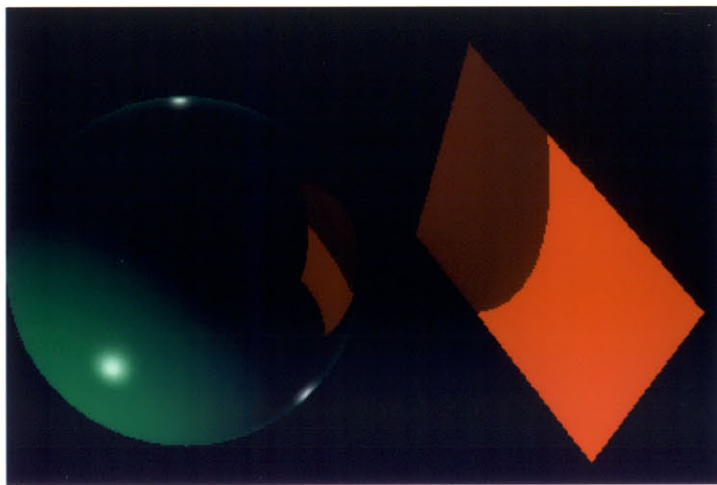Figure B-1: Figure 1-1 in color.

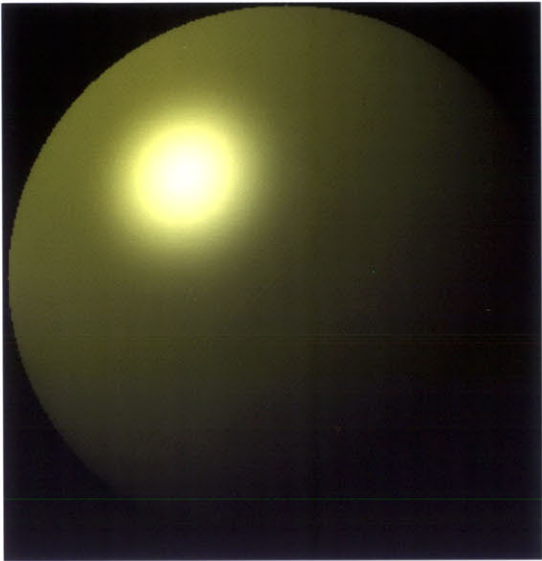Figure B-2: Figure 1-4 in color.

Figure B-3: Figure 3-9 in color.
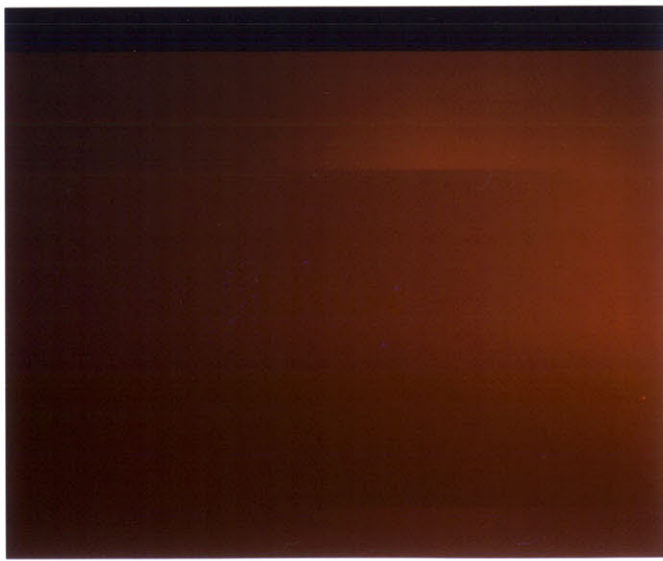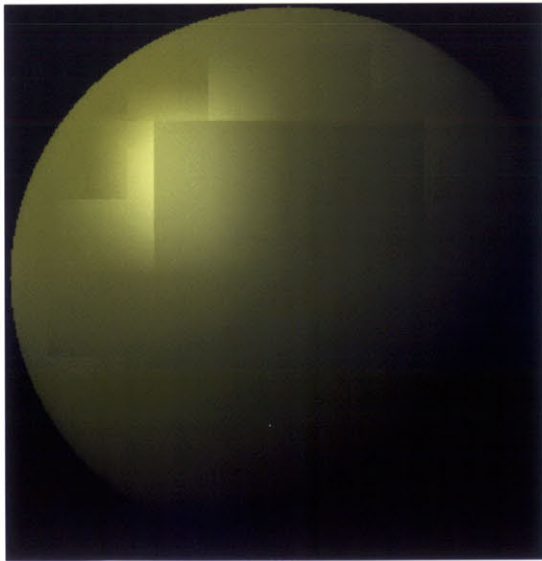

Figure B-4: Figure 4-9 in color.
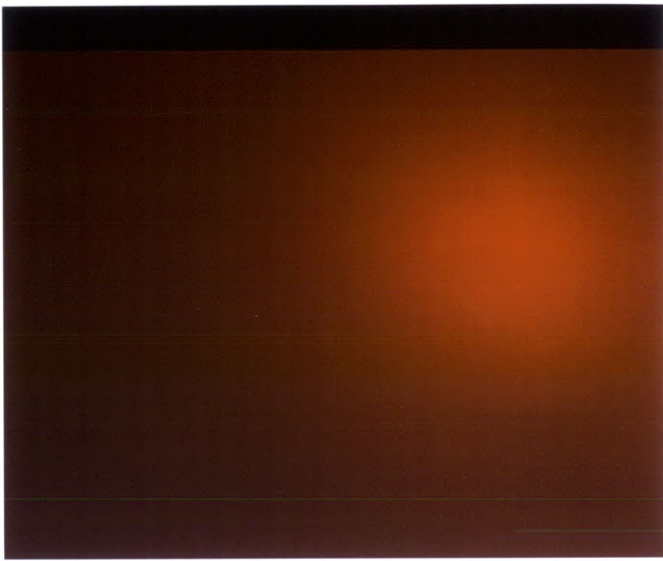
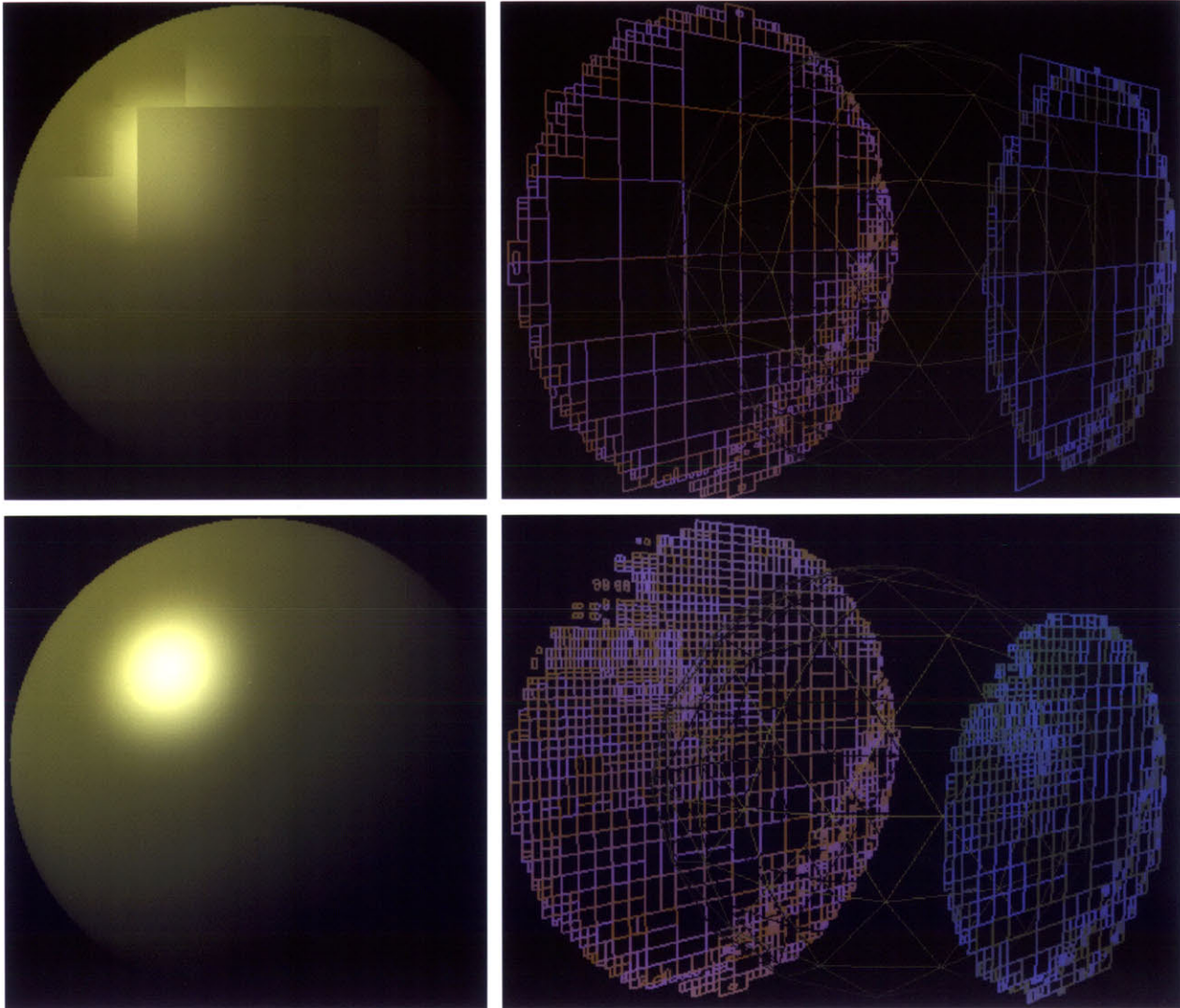**specular** **diffuse**

Figure B-5: Figure 4-16 in color.

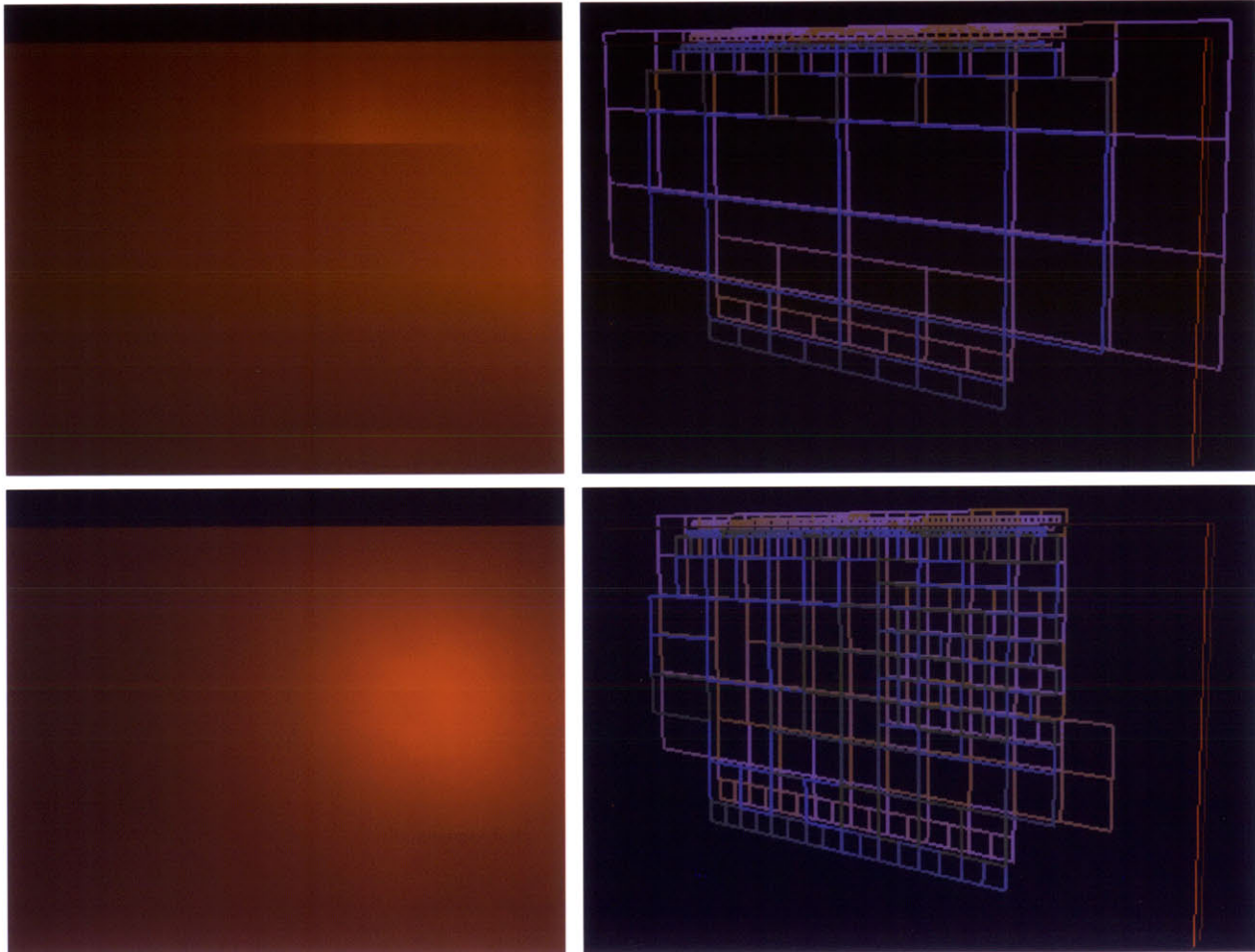Figure B-6: Figure 4-25 in color.

Figure B-7: Figure 4-26 in color.
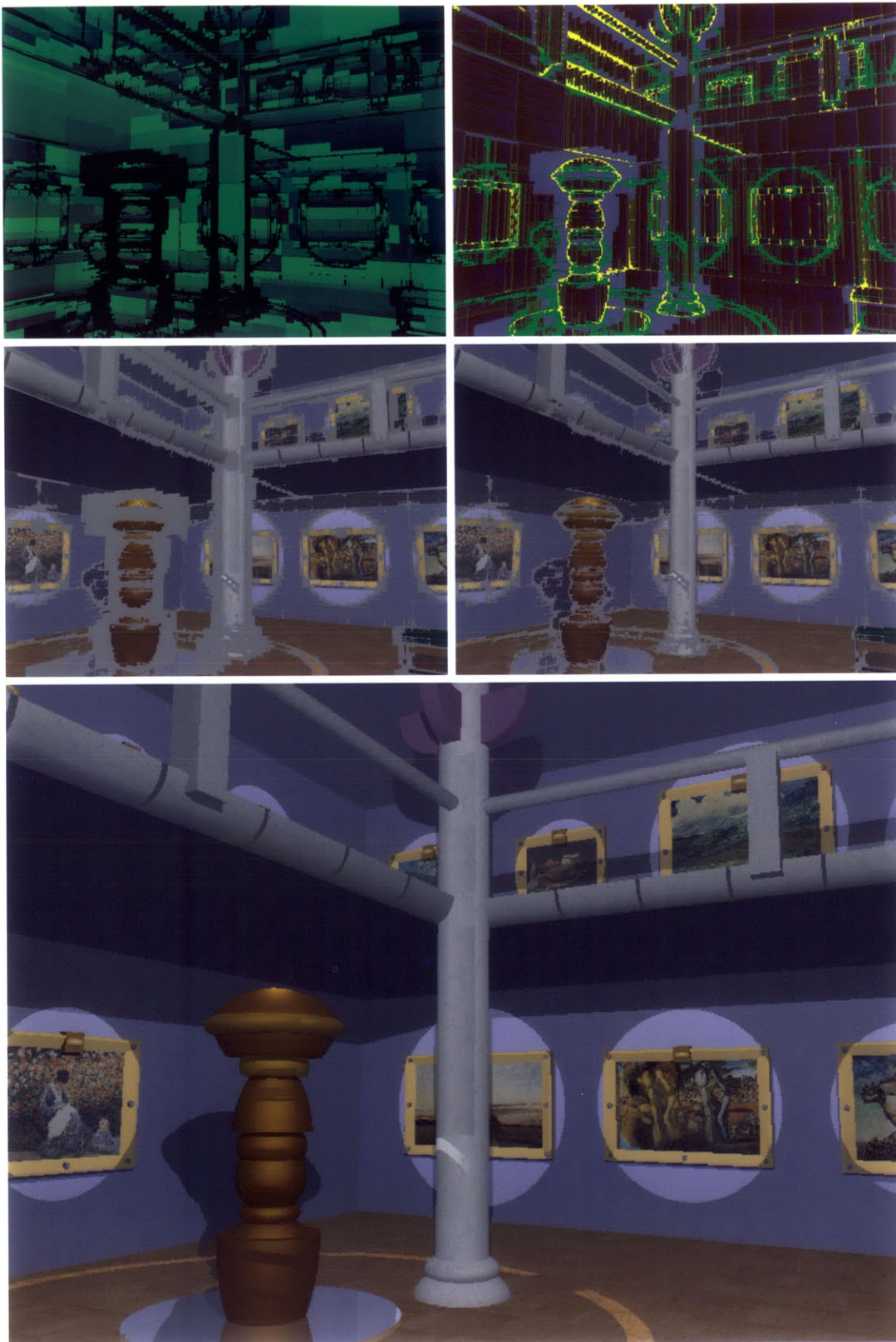
Figure B-8: Figure 4-27 in color.

Figure B-9: Figure 5-8 in color.

175

Figure B-10: Figure 5-10 in color.
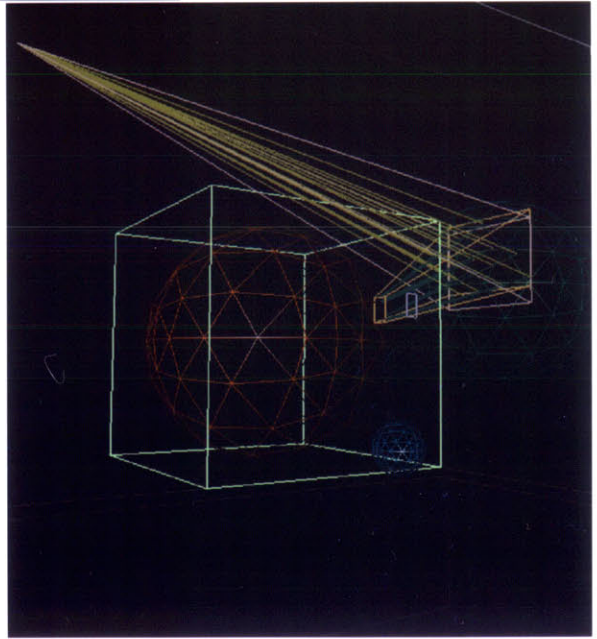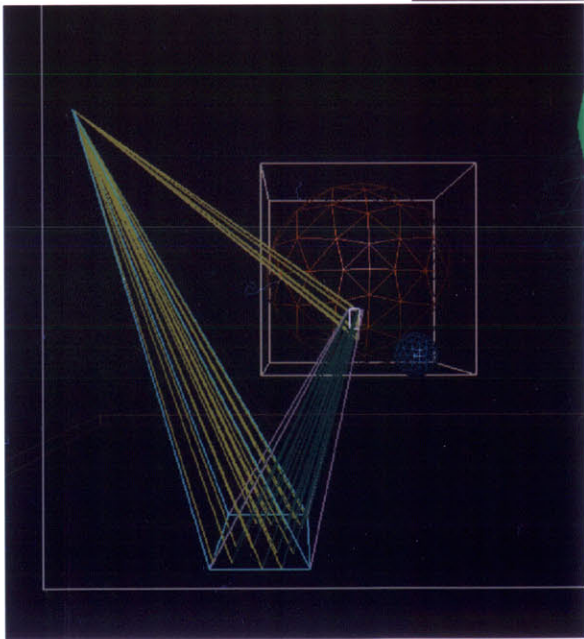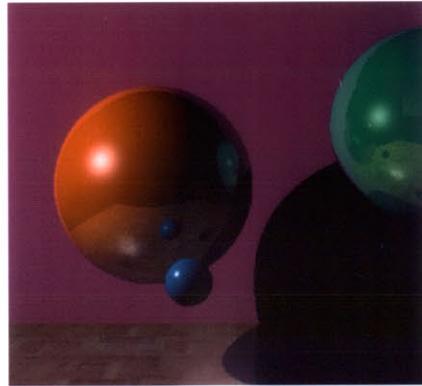
Figure B-11: Figure 5-11 in color.
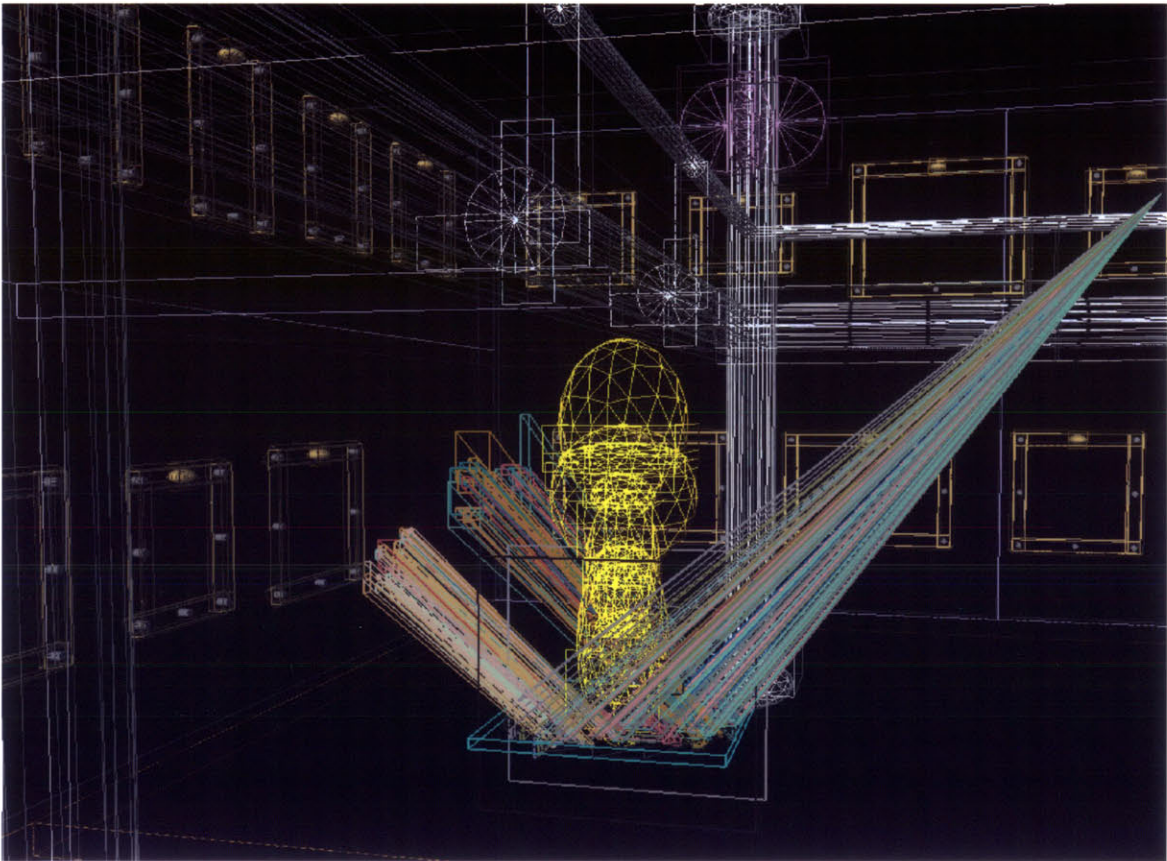
Figure B-12: Figure 6-6 in color.

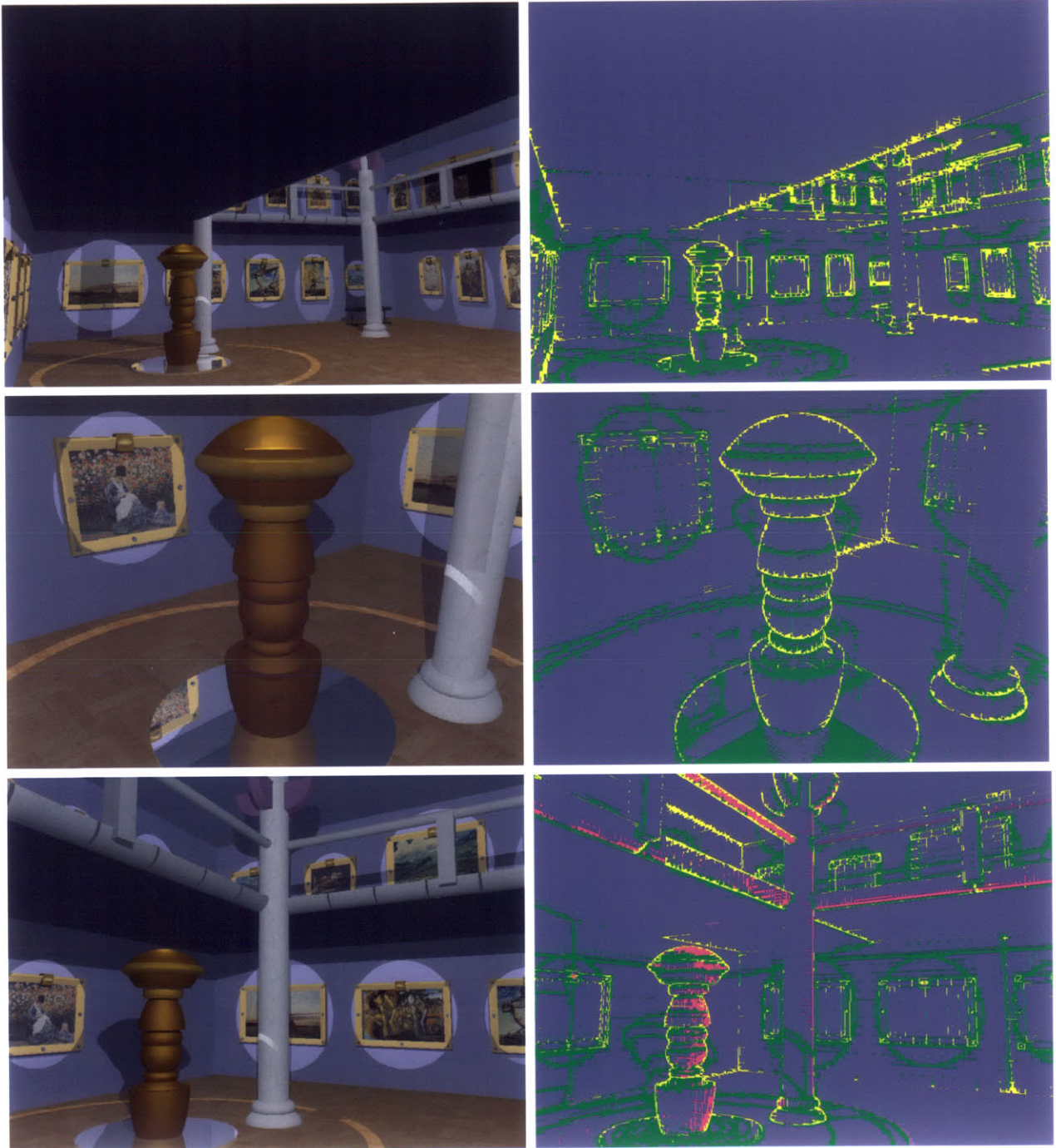Figure B-13: Figure 6-11 in color.

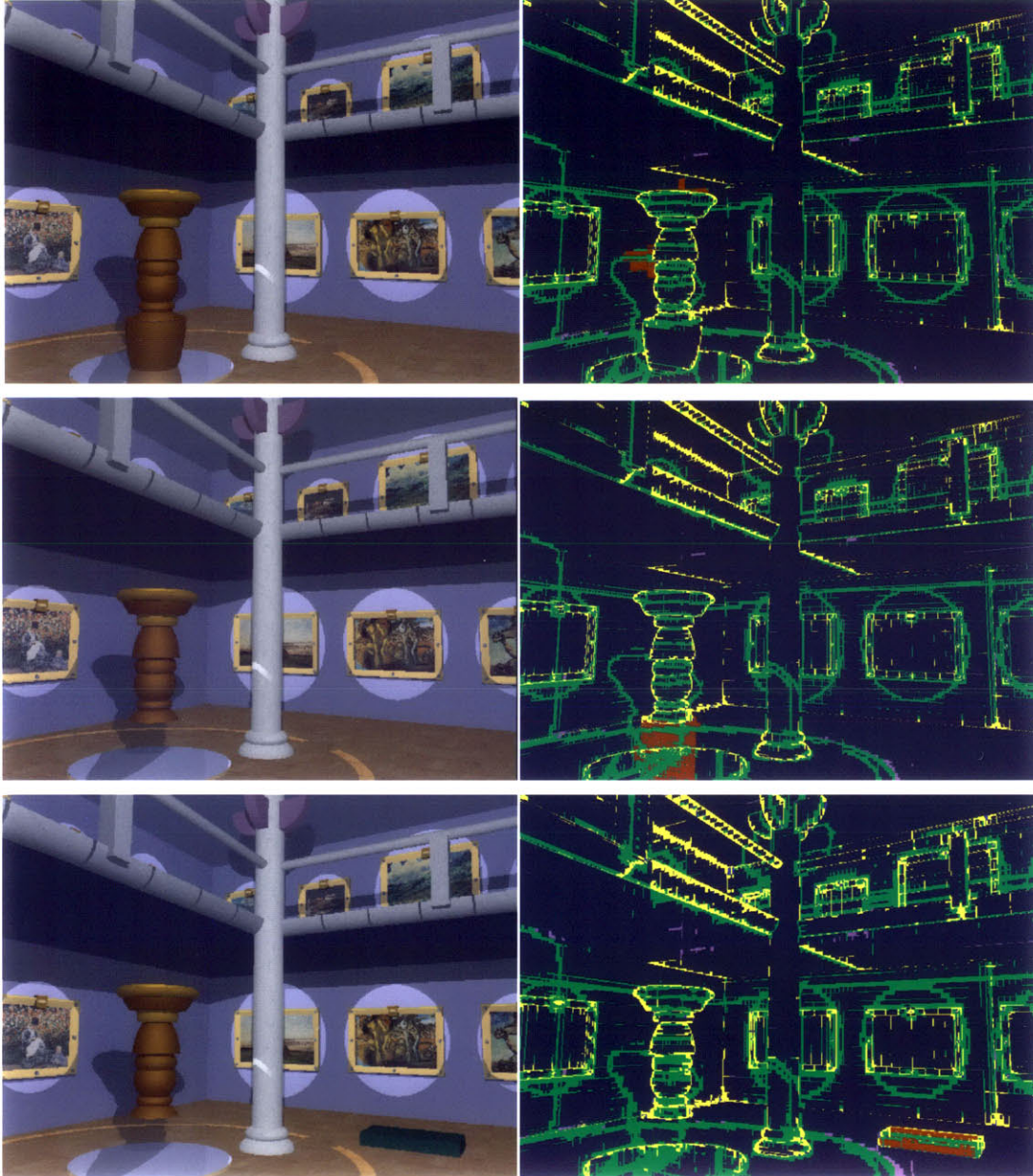Figure B-14: Figure 7-1 in color.

Figure B-15: Figure 7-6 in color.

Bibliography

[ACS94]   A Andrade, João Comba, and Jorge Stolfi. Affine arithmetic. In *Interval*, St. Peters-
          burg, Russia, March 1994.

[AF84]   John Amanatides and Alain Fournier. Ray casting using divide and conquer in screen
          space. In *Intl. Conf. on Engineering and Computer Graphics*. Beijing, China, August
          1984.

[AH95]   Stephen J. Adelson and Larry F. Hodges. Generating exact ray-traced animation
          frames by reprojection. *IEEE Computer Graphics and Applications*, 15(3):43–52,
          May 1995.

[AK87]   James Arvo and David Kirk. Fast ray tracing by ray classification. In *Computer
          Graphics (SIGGRAPH 1987 Proceedings)*, pages 196–205, July 1987.

[Ama84]   John Amanatides. Ray tracing with cones. In *Computer Graphics (SIGGRAPH 1984
          Proceedings)*, pages 129–135, July 1984.

[Bad88]   S. Badt, Jr. Two algorithms for taking advantage of temporal coherence in ray tracing.
          The Visual Computer, 4(3):123–132, September 1988.

[BDT98]   Kavita Bala, Julie Dorsey, and Seth Teller. Bounded-error interactive ray tracing.
          Technical Report Laboratory for Computer Science TR-748, Massachusetts Institute
          of Technology, August 1998.

[BDT99a] Kavita Bala, Julie Dorsey, and Seth Teller. Interactive ray-traced scene editing using
          ray segment trees. In *Tenth Eurographics Workshop on Rendering*, pages 39–52, June
          1999.

[BDT99b] Kavita Bala, Julie Dorsey, and Seth Teller. Radiance interpolants for accelerated
          bounded-error ray tracing. July 1999.

[BL94]   Robert D. Blumofe and Charles E. Leiserson. Scheduling multithreaded computations by work stealing. In *35th Annual Symposium on Foundations of Computer Science (FOCS '94)*, pages 356–368, November 1994.

[Bli78]   James F. Blinn. Simulation of wrinkled surfaces. In *Computer Graphics (SIGGRAPH '78 Proceedings)*, pages 286–292, August 1978.

[BM98]   Mark R. Bolin and Gary Meyer. A perceptually based adaptive sampling algorithm. In *Computer Graphics (SIGGRAPH '98 Proceedings)*, Annual Conference Series, pages 299–310, August 1998.

[BP96]   Normand Brière and Pierre Poulin. Hierarchical view-dependent structures for inter-active scene manipulation. In *Computer Graphics (SIGGRAPH 1996 Proceedings)*, pages 83–90, August 1996.

[CALM97]   Miguel Castro, Atul Adya, Barbara Liskov, and Andrew C. Myers. HAC: Hybrid adaptive caching for distributed storage systems. In *Symposium on Operating Systems (SOSP) 1997*, pages 102–115, Oct. 1997.

[CCD90]   John Chapman, Thomas W. Calvert, and John Dill. Exploiting temporal coherence in ray tracing. In *Proceedings of Graphics Interface 1990*, pages 196–204, Toronto, Ontario, May 1990. Canadian Information Processing Society.

[CCD91]   John Chapman, Thomas W. Calvert, and John Dill. Spatio-temporal coherence in ray tracing. In *Proceedings of Graphics Interface 1991*, pages 101–108, Calgary, Alberta, June 1991. Canadian Information Processing Society.

[Che90]   Shenchang Eric Chen. Incremental radiosity: An extension of progressive radiosity to an interactive image synthesis system. *Computer Graphics (ACM SIGGRAPH '90 Proceedings)*, 24(4):135–144, August 1990.

[Che97]   C. Chevrier. A view interpolation technique taking into account diffuse and specular inter-reflections. *The Visual Computer*, 13(7):330–341, 1997.

[CLF98]   Emilio Camahort, Apostolos Lerios, and Donald Fussell. Uniformly sampled light fields. In *Ninth Eurographics Workshop on Rendering*, June 1998.

[CLR90]   T. Cormen, C. Leiserson, and R. Rivest. *Introduction to Algorithms*. MIT Press and McGraw-Hill, Cambridge, MA, 1990.

190

[Coo84]   Robert L. Cook. Shade trees. In *Computer Graphics (SIGGRAPH 1984 Proceedings)*, volume 18, pages 223–231, July 1984.

[Coo86]   Robert L. Cook. Stochastic sampling in computer graphics. *ACM Transactions on Graphics*, 5(1):51–72, January 1986.

[Cox69]   H. S. M. Coxeter. *Introduction to Geometry*. John Wiley & Sons Inc., 1969.

[Cra98]   Tony Cragg. *Pillars of salt*. Sculpture of Goodwood, 1998.

[CRMT91]   Shenchang Eric Chen, Holly E. Rushmeier, Gavin Miller, and Douglass Turner. A progressive multi-pass method for global illumination. In *Computer Graphics (SIGGRAPH 1991 Proceedings)*, pages 165–74, July 1991.

[CT82]   Robert Cook and Kenneth Torrance. A reflectance model for computer graphics. *ACM Transactions on Graphics*, 1(1):7–24, January 1982.

[CW93]   Michael Cohen and John R. Wallace. *Radiosity and Realistic Image Synthesis*. Academic Press Professional, Cambridge, MA, 1993.

[DB69]   G. Dahlquist and Å. Björck. *Numerical Methods*. Prentice-Hall, New Jersey, 1969.

[DB97]   Paul Diefenbach and Norman Badler. Multi-pass pipeline rendering: Realism for dynamic environments. In *Proceedings of the 1997 Symposium on Interactive 3D Graphics*, pages 59–70, April 1997.

[DS97]   George Drettakis and Francois X. Sillion. Interactive update of global illumination using a line-space hierarchy. In *Computer Graphics (SIGGRAPH '97 Proceedings)*, pages 57–64, August 1997.

[FI85]   Akira Fujimoto and Kansei Iwata. Accelerated ray tracing. In Tosiyasu Kunii, editor, *Computer Graphics: Visual Technology and Art (Proceedings of Computer Graphics Tokyo 1985)*, pages 41–65, Tokyo, 1985. Springer-Verlag.

[FPSG96]   James A. Ferwerda, Sumant N. Pattanaik, Peter Shirley, and Donald P. Greenberg. A model of visual adaptation for realistic image synthesis. In *Computer Graphics (SIGGRAPH '96 Proceedings)*, pages 249–258, August 1996.

[FPSG97]   James A. Ferwerda, Sumant N. Pattanaik, Peter Shirley, and Donald P. Greenberg. A model of visual masking for computer graphics. In *Computer Graphics (SIGGRAPH '97 Proceedings)*, pages 143–152, August 1997.

[FST92]   T. Funkhouser, C. Séquin, and S. Teller. Management of large amounts of data in interactive building walkthroughs. In *Proc. 1992 Workshop on Interactive 3D Graphics*, pages 11–20, 1992.

[FvD82]   J.D. Foley and A. van Dam. *Fundamentals of Interactive Computer Graphics.* Addison-Wesley, 1982.

[FvDFH90] James D. Foley, Andries van Dam, Steven K. Feiner, and John F. Hughes. *Computer Graphics, Principles and Practice.* Addison-Wesley, Reading, Massachusetts, second edition, 1990.

[FYT94]   David Forsyth, Chien Yang, and Kim Teo. Efficient radiosity in dynamic environments. In *Proceedings 5th Eurographics Workshop on Rendering*, June 1994.

[Gar84]   M. Gardner. *The Sixth Book of Mathematical Games from Scientific American.* University of Chicago Press, Chicago, IL, 1984.

[GGC97]   X. Gu, S. Gortler, and M. Cohen. Polyhedral geometry and the two-plane parameterization. In *Eight Eurographics Workshop on Rendering*, pages 1–12, June 1997.

[GGSC96] Steven Gortler, Radek Grzeszczuk, Richard Szeliski, and Michael Cohen. The Lumigraph. In *Computer Graphics (SIGGRAPH '96 Proceedings)*, pages 43–54, August 1996.

[Gla84]   Andrew S. Glassner. Space subdivision for fast ray tracing. *IEEE Computer Graphics and Applications*, 4(10):15–22, 1984.

[Gla88]   Andrew S. Glassner. Spacetime ray tracing for animation. *IEEE Computer Graphics and Applications*, 8(2):60–70, March 1988.

[Gla89]   Andrew S. Glassner. *An Introduction to Ray Tracing.* Academic Press, London, 1989.

[Gla95]   Andrew S. Glassner. *Principles of Digital Image Synthesis.* Morgan Kaufmann Publishers, Inc., San Francisco, CA, 1995.

[GSG90]   David W. George, Francois X. Sillion, and Donald P. Greenberg. Radiosity Redistribution for Dynamic Environments. *IEEE Computer Graphics and Applications*, 10(4):26–34, July 1990.

[GTGB84]   Cindy M. Goral, Kenneth E. Torrance, Donald P. Greenberg, and Bennett Battaile. Modeling the interaction of light between diffuse surfaces. In *Computer Graphics (SIGGRAPH '84 Proceedings)*, pages 213–222, July 1984.

[Guo98]   Baining Guo. Progressive radiance evaluation using directional coherence maps. In *Computer Graphics (SIGGRAPH 1998 Proceedings)*, pages 255–266, August 1998.

[Han75]   E. R. Hansen. A generalized interval arithmetic. In *Interval Mathematics: Proceedings of the International Symposium*, pages 7–18, Karlsruhe, West Germany, May 1975. Springer-Verlag. Also published in Lecture Notes in Computer Science Volume 29.

[HH84]   Paul S. Heckbert and Pat Hanrahan. Beam tracing polygonal objects. In *Computer Graphics (SIGGRAPH 1984 Proceedings)*, pages 119–127, July 1984.

[HSA91]   Pat Hanrahan, David Salzman, and Larry Aupperle. A rapid hierarchical radiosity algorithm. In *Computer Graphics (SIGGRAPH '91 Proceedings)*, pages 197–206, July 1991.

[HTSG91]   Xiao D. He, Kenneth E. Torrance, Francois X. Sillion, and Donald P. Greenberg. A comprehensive physical model for light reflection. In *Computer Graphics (SIGGRAPH 1991 Proceedings)*, pages 175–86, July 1991.

[HW91]   E. Haines and J. Wallace. Shaft culling for efficient ray-traced radiosity. In *Proc. 2nd Eurographics Workshop on Rendering*, May 1991.

[Jan86]   Frederik W. Jansen. Data structures for ray tracing. In L. R. A. Kessener, F. J. Peters, and M. L. P. van Lierop, editors, *Data Structures for Raster Graphics*. Springer-Verlag, New York, 1986.

[Jev92]   David Jevans. Object space temporal coherence for ray tracing. In *Proceedings of Graphics Interface 1992*, pages 176–183, Toronto, Ontario, May 1992. Canadian Information Processing Society.

[LH96]   Mark Levoy and Pat Hanrahan. Light field rendering. In *Computer Graphics (SIGGRAPH '96 Proceedings)*, pages 31–42, August 1996.

[LL76]   L. D. Landau and E. M. Lifshitz. *Course of Theoretical Physics: Mechanics*. Butterworth-Heinemann, 1976.

[LR98]   Daniel Lischinski and Ari Rappoport. Image-based rendering for non-diffuse synthetic scenes. In *Rendering Techniques 1998*, pages 301–314, June 1998.

[LSG94]   Dani Lischinski, Brian Smits, and Donald P. Greenberg. Bounds and error estimates for radiosity. In *Computer Graphics (SIGGRAPH '94 Proceedings)*, pages 67–74, July 1994.

[MB95]   Leonard McMillan and Gary Bishop. Plenoptic modeling: An image-based rendering system. In *Computer Graphics (SIGGRAPH '95 Proceedings)*, August 1995.

[MH92]   Koichi Murakami and Katsuhiko Hirota. Incremental ray tracing. In K. Bouatouch and C. Bouville, editors, *Photorealism in Computer Graphics*. Springer-Verlag, 1992.

[MMB97]   William Mark, Leonard McMillan, and Gary Bishop. Post-rendering 3d warping. In *Proceedings of the 1997 Symposium on Interactive 3D Graphics*, pages 7–16, April 1997.

[Moo79]   Ramon E. Moore. *Methods and Applications of Interval Analysis*. Studies in Applied Mathematics (SIAM), Philadelphia, 1979.

[NDR95]   Jeffry Nimeroff, Julie Dorsey, and Holly Rushmeier. A framework for global illumination in animated environments. In *6th Annual Eurographics Workshop on Rendering*, pages 223–236, June 1995.

[OR98]   Eyal Ofek and Ari Rappoport. Interactive relfections on curved objects. In *Computer Graphics (SIGGRAPH '98 Proceedings)*, Annual Conference Series, pages 333–342, August 1998.

[PFFG98]   Sumant N. Pattanaik, James A. Ferwerda, Mark D. Fairchild, and Donald P. Greenberg. A multiscale model of adaptation and spatial vision for realistic image display. In *Computer Graphics (SIGGRAPH '98 Proceedings)*, Annual Conference Series, pages 287–298, August 1998.

[PH97]   Jovan Popović and Hugues Hoppe. Progressive simplicial complexes. In *Computer Graphics (SIGGRAPH '97 Proceedings)*, Annual Conference Series, pages 217–224, August 1997.

[PLS97]   F. Pighin, Dani Lischinski, and David Salesin. Progressive previewing of ray-traced images using image-plane discontinuity meshing. In *Rendering Techniques 1997*, pages 115–126, June 1997.

[PMS+99]   Steven Parker, William Martin, Peter-Pike Sloan, Peter Shirley, Brian Smits, and Chuck Hansen. Interactive ray tracing. In *Interactive 3D Graphics (I3D)*, pages 119–126, April 1999.

[PPD98]   Eric Paquette, Pierre Poulin, and George Drettakis. A light hierarchy for fast rendering of scenes with many lights. *Eurographics '98*, 17(3), September 1998.

[Pra91]   W. K. Pratt. *Digital Image Processing (2nd Edition)*. John Wiley & Sons, Inc., 1991.

[PS89]   James Painter and Kenneth Sloan. Antialiased ray tracing by adaptive progressive refinement. In *Computer Graphics (SIGGRAPH 1989 Proceedings)*, pages 281–288, July 1989.

[Rot82]   Scott D. Roth. Ray casting for modeling solids. *Computer Graphics and Image Processing*, 18(2), February 1982.

[SAS92]   Brian E. Smits, James R. Arvo, and David H. Salesin. An Importance-driven radiosity algorithm. *Computer Graphics (ACM SIGGRAPH '92 Proceedings)*, 26(4):273–282, July 1992.

[Som59]   D.M.Y. Sommerville. *Analytical Geometry of Three Dimensions*. Cambridge University Press, 1959.

[SP89]   Francois Sillion and Claude Puech. A general two-pass method integrating specular and diffuse reflection. In *Computer Graphics (SIGGRAPH 1989 Proceedings)*, pages 335–44, July 1989.

[SP94]   F. Sillion and C. Puech. *Radiosity and Global Illumination*. Morgan Kaufmann Publishers, Inc., San Francisco, CA, 1994.

[SS89]   Carlo H. Séquin and Eliot K. Smyrl. Parameterized ray tracing. In *Computer Graphics (SIGGRAPH 1989 Proceedings)*, pages 307–314, July 1989.

[SS98]   Cyril Soler and Francois X. Sillion. Fast calculation of soft shadow textures using convolution. In *Computer Graphics (SIGGRAPH '98 Proceedings)*, pages 321–332, August 1998.

[Tan87]   A. S. Tanenbaum. *Operating Systems: Design and Implementation*. Prentice-Hall, Inc., 1987.

[TBD96]   Seth Teller, Kavita Bala, and Julie Dorsey. Conservative radiance interpolants for ray tracing. In *Seventh Eurographics Workshop on Rendering*, pages 258–269, June 1996.

[TH93]   Seth Teller and Pat Hanrahan. Global visibility algorithms for illumination computations. *Computer Graphics (Proc. Siggraph '93)*, pages 239–246, 1993.

[Tup96]   Jeffrey Allen Tupper. Graphing equations with generalized interval arithmetic. Master's thesis, University of Toronto, 1996.

[War91]   Gregory J. Ward. Adaptive shadow testing for ray tracing. In *Second Eurographics Workshop on Rendering*, pages 11–20, 1991.

[War92]   Gregory J. Ward. Measuring and modeling anisotropic reflection. In *Computer Graphics (SIGGRAPH 1992 Proceedings)*, pages 265–272, July 1992.

[War98]   Gregory J. Ward. The Holodeck: a parallel ray-caching rendering system. In *2nd Eurographics Workshop on Parallel Graphics and Visualization*, 1998.

[WC88]   Turner Whitted and Robert L. Cook. A comprehensive shading model. In Kenneth I. Joy, Charles W. Grant, Nelson L. Max, and Lansing Hatfield, editors, *Tutorial: Computer Graphics: Image Synthesis*, pages 232–43. Computer Society Press, Washington, DC, 1988.

[WCG87]   John R. Wallace, Michael F. Cohen, and Donald P. Greenberg. A two-pass solution to the rendering equation: A synthesis of ray tracing and radiosity methods. In *Computer Graphics (SIGGRAPH 1987 Proceedings)*, pages 311–20, July 1987.

[WDP99]   Bruce Walter, George Drettakis, and Steven Parker. Interactive rendering using the render cache. In *Tenth Eurographics Workshop on Rendering*, June 1999.

[WH92]   Gregory Ward and Paul Heckbert. Irradiance gradients. In *Rendering in Computer Graphics (Proceedings of the Third Eurographics Workshop on Rendering)*. Springer-Verlag, May 1992.

[WH98]   H.-P. Seidel W. Heidrich, Ph. Slusallek. Sampling procedural shaders using affine arithmetic. 17(3):158–176, July 1998.

[Whi80]   Turner Whitted. An improved illumination model for shaded display. *CACM*, 23(6):343–349, 1980.

[WRC88]   Gregory J. Ward, Francis M. Rubinstein, and Robert D. Clear. A ray tracing solution for diffuse interreflection. In *Computer Graphics (SIGGRAPH 1988 Proceedings)*, pages 85–92, August 1988.